Etude locale de la thermique dans les piles à combustibles pour application automobile. Corrélation à la durée de vie

Fredy Nandjou

HAL Id: tel-01267255
https://tel.archives-ouvertes.fr/tel-01267255

Submitted on 4 Feb 2016

UNIVERSITÉ GRENOBLE ALPES

THÈSE

Pour obtenir le grade de

DOCTEUR DE L'UNIVERSITÉ GRENOBLE ALPES

Spécialité : **Mécanique des fluides, procédés, énergétique**

Arrêté ministériel : 7 août 2006

Présentée par

Fredy NANDJOU

Thèse dirigée par **Pr. Yann BULTEL** et
codirigée par **Dr. Jean-Philippe POIROT-CROUVEZIER**

préparée au sein du **Commissariat à l'Énergie Atomique et aux Énergies Alternatives**
dans l'**École Doctorale IMEP2**

Étude locale de la thermique dans les piles à combustible pour application automobile. Corrélation à la durée de vie.

Thèse soutenue publiquement le « **16 NOVEMBRE 2015** »,
devant le jury composé de :

M. Christian JALLUT
Professeur, Université Claude Bernard - Lyon 1, Rapporteur
M. Marc PRAT
Docteur, Institut de Mécanique des Fluides de Toulouse, Rapporteur
M. Marian CHATENET
Professeur, Grenoble INP, Examinateur
M. Pierre BOILLAT
Docteur, Paul Scherrer Institute, Villigen, Suisse, Examinateur
M. Yann BULTEL
Professeur, Grenoble INP, Directeur de thèse
M. Jean-Philippe POIROT-CROUVEZIER
Docteur, CEA LITEN, Grenoble, Encadrant
Mme. Marion CHANDESRIS
Docteur, CEA LITEN, Grenoble, Invité

Cette thèse est dédiée à ma grand-mère, *Mama Docta*, qui a rendu l'âme quelques jours avant la fin de rédaction du manuscrit.

ACKNOWLEDGEMENTS / REMERCIEMENTS

Il n'y a pas de solution basique dans une pile à combustible à membrane échangeuse de protons : non seulement les phénomènes physiques sont fortement couplés mais, en outre, le potentiel d'hydrogène est inférieur à 7.

ABSTRACT

One of the main challenges for Proton Exchange Membrane Fuel Cells development is the performance loss, which largely limits the durability. The study of the degradation phenomena of the different MEA components is a challenge addressed by many researchers, but a study at a stack scale is needed in order to better understand the ageing mechanisms. Indeed, in an industrial fuel cell the operating conditions are not homogeneous as for laboratory fuel cells, especially as regards thermal aspects. The heterogeneities are particularly emphasized for automotive fuel cells, because of the compactness constraint of the cooling circuit. Moreover, the requirements of cold start should be considered, as well as the inertial effects of the stacks and the increased heterogeneities during the driving cycles.

In this work, the effects of the temperature heterogeneities and hot spots on the automotive fuel cell performances and degradations are investigated. The study is conducted in different conditions: nominal conditions, load/thermal cycling and New European Driving Cycles (NEDC).

The work is composed of an experimental study, which consists of ageing tests on fuel cells and *on-line* diagnosis at both global and local scales. At the end of the tests, *post-mortem* analyses of the aged components are conducted. In parallel, a physic-based model is developed in order to predict the local temperature and humidity in the different components of the cell. Then, the impact of the reactive gases and cooling flow fields design on the thermal and water management of the cell is investigated. Finally, the experimental and modeling results are coupled in order to investigate the correlation between heat management, water management and degradations.

RÉSUMÉ

L'un des principaux freins au développement des piles à combustible de type PEMFC (Proton Exchange Membrane Fuel Cell) est lié aux phénomènes de dégradation des performances qui les pénalisent encore en termes de durée de vie. L'étude de ces phénomènes au niveau des composants de l'AME est un thème abordé aujourd'hui par de nombreuses équipes de recherche, mais une étude à une échelle d'un stack est nécessaire pour mieux comprendre les mécanismes en jeu. En effet, dans un stack les conditions de fonctionnement ne sont pas homogènes comme dans les cellules de laboratoire, notamment au niveau thermique. Ceci est particulièrement exacerbé dans les piles pour application automobile, dont la compacité contraint fortement la conception du circuit de refroidissement. De plus, les exigences en termes de démarrage à froid sont à prendre en compte, avec notamment la limitation de l'inertie thermique de l'empilement ou l'apparition d'hétérogénéités plus fortes pendant les phases transitoires.

Ce travail de thèse se propose d'étudier l'effet d'hétérogénéités de température sur la performance d'une pile en application automobile et sa dégradation. L'étude est menée dans différentes conditions de fonctionnement: fonctionnement nominal, cyclage thermique et cyclage NEDC (New European Driving Cycles).

Cette étude comporte une partie expérimentale, centrée sur des essais de vieillissement en pile et un travail sur le diagnostic électrochimique global et local. Elle est complétée par des expertises *post-mortem* des assemblages membrane-électrodes et des plaques testés. En parallèle, un travail de modélisation est mené pour relier les constatations expérimentales à une description des phénomènes en présence. L'influence du design des canaux de réactifs et de caloporteur sur le fonctionnement des piles est étudiée. Enfin, l'effet de la gestion thermique sur la dégradation des performances et sur la détérioration des composants de la pile est étudié.

SUMMARY

Chapter II - EXPERIMENTAL: METHODS AND TECHNIQUES

Chapter III - A THERMAL MODEL TO INVESTIGATE LOCAL TEMPERATURE AND HEAT TRANSFER PHENOMENA IN P.E.M. FUEL CELLS

Chapter IV - A PSEUDO-3D MULTIPHYSICS MODEL TO INVESTIGATE COUPLED HEAT AND WATER TRANSPORT IN LARGE AREA P.E.M. FUEL CELLS

Chapter V - CORRELATION BETWEEN TEMPERATURE, HUMIDITY AND DEGRADATIONS IN P.E.M. FUEL CELLS

LIST OF ACRONYMS AND NOMENCLATURE

ACRONYMS

BP	Bipolar Plate
CL	Catalyst Layer
CV	Cyclic Voltammetry
CW	Cooling Water
EIS	Electrochemical Impedance Spectroscopy
GDL	Gas Diffusion Layer
IR	InfraRed
LSV	Linear Sweep Voltammetry
MEA	Membrane Electrode Assembly
MPL	Micro-Porous Layer
NEDC	New European Driving Cycles
OM	Optical Microscopy
PEM	Proton Exchange Membrane
PEMFC	Proton Exchange Membrane Fuel Cell
SEM	Scanning Electron Microscopy
WLTC	Worldwide harmonized Light duty driving Test Cycle
XPS	X-ray Photoelectron Spectroscopy

NOMENCLATURE

c_i	Molar concentration of the species i	mol/m^3
D_{ij}	Binary molecular diffusivity between i and j	m²/s
D_h	Hydraulic diameter	m
e_n	Thickness of the component n	m
E_{rev}	Reversible potential of the cell	V
ECR	Electrical Contact Resistance	m²V/A
ECSA	Electrochemical Active Surface Area	m²
f_F	Fanning friction factor	
F	Faraday Constant	C/mol
h	Convective heat transfer coefficient	W/m²/K

H	Convective mass transfer coefficient	m/s
i	Current density	A/cm²
I	Total current	A
K	Permeability of the porous media	m²
K_1	Hydraulic permeability coefficient	m²
K_2	Hydraulic passability coefficient	
$\dot{m}$	Mass flow rate	kg/s
p	Pressure	Pa
Q	Heat power	W
R	Electrical resistance	Ω
RH	Relative Humidity	%
S_i	Species source	kg/s
S_m	Mass source	kg/s
T	Mean temperature along the thickness	K
TCR	Thermal Contact Resistance	m²K/W
u	Velocity	m/s
U	Potential	V
v	Bulk velocity	m/s
w_i	Mass fraction of the species i	
W_e	Electric power	W

GREEK LETTERS

ΔH	Total reaction enthalpy	J/mol
ΔS	Entropy change	J/mol/K
ε	Porosity	
θ	Temperature	K
λ	Thermal conductivity	W/m/K
λ_M	Electrolyte membrane water content	
μ	Dynamic viscosity	Pa s
ν	Kinematic viscosity	m²/s
ρ	Density	Kg/m³
σ	Electrical or proton conductivity	S/m

τ   Tortuosity

ADIMENSIONAL NUMBERS

Nu   Nusselt number

Re   Reynolds number

Sh   Sherwood number

Sc   Schmidt number

GENERAL INTRODUCTION

Hydrogen is considered to be a promising energy carrier for different applications in the future scenarios of energy mix. A move from hydrocarbon to hydrogen–carbon and finally to hydrogen economy is expected in the next decades [1]. The conversion of hydrogen energy into electrical and thermal energy in a fuel cell is a viable clean solution for the development of alternative solutions to fossil fuels and for the reduction of greenhouse gas emissions. Indeed, since the planet is severely enduring the impact of the fossil fuels combustion on global warming and climate change, environmental sustainability becomes a crucial factor in energy policies. Moreover, given the evolutions of the fossil fuels reserves estimations on the one hand, and the world consumption rate on the other hand, they will probably run out before the next century [2]. Nuclear energy could be an alternative, but its development is contested either for safety reasons, or for the radioactive waste management. In this context, alternative energy sources as much as appropriate energy carriers need to be developed urgently, with a deep integration of environmental and social aspects.

Hydrogen energy has the potential to become an earth-friendly energy because the only product of the conversion process of hydrogen chemical energy into electrical and/or thermal energy, via a fuel cell, is water. Hydrogen is a good energy carrier with a high energy density: $\sim 33 \; kWh/kg$. That means 1 kg of hydrogen is energetically equivalent to $2.8 \; kg$ of gasoline and $2.4 \; kg$ of natural gas. Finally, hydrogen is a sustainable alternative solution to fossil fuels because it represents a viable solution for energy storage. It can be used to make the connection between the place/time of energy production and the place/time of energy demand, allowing an efficient valorization of intermittent energy sources (solar power, wind power…).

Among the different fuel cell technologies, Proton Exchange Membrane Fuel Cells, which use a solid electrolyte, are particularly favorable for automotive application and many research works and industrials projects are underway regarding their commercialization. However, one of the main challenges for their development is the performance loss, which largely limits their durability. The local study of the degradation phenomena of the different Membrane Electrode Assembly components is a challenge addressed by many researchers, but a study at a stack scale, in real automotive conditions is needed in order to better understand the ageing mechanisms.

In this work, the effects of the temperature heterogeneities and hot spots on the automotive fuel cell performances and degradations are investigated. The work is composed of an experimental study, which consists of ageing tests on fuel cells with *on-line* and *post-mortem* diagnosis at both global and local scales. In parallel, a physic-based model is developed in order to predict the local temperature and humidity in the different components of the cell.

This manuscript is made up of five chapters and an appendix. The first chapter establishes the context of the study and sets out it main objectives. A literature review of the different studies of temperature distribution in PEMFCs and its impact on degradations is also presented.

The research study itself begins with the experimental study, presented in Chapter 2. It consists of durability testing of fuel cells in automotive related conditions, performed by applying different loads: nominal conditions, load/thermal cycles and New European Driving Cycles. During the ageing tests, specific instrumentations are used to investigate *in-situ* the evolution of local and global performances and identify the sources of performance loss. Those investigations are completed by *post-mortem* analyses of the different components of the aged fuel cells: membranes, electrodes and bipolar plates.

In parallel, modeling studies are performed in order to correlate the experimental results to the thermal conditions in the fuel cell. In particular, a dimensional continuum-based model, which consider the real design of the reactive gases as well as cooling water channels is developed, and validated with the experimental data. A thermal model, used for the study of temperature distribution in the cell is presented in Chapter 3. This model is extended to a multiphysics version for the study of coupled heat and water transport in the cells in Chapter 4. This model, which predicts simultaneously the heat sources and cooling flow heterogeneities, is used to predict the temperature and the water distributions in the cell in different operating conditions.

In the last part of the manuscript (Chapter 5), the experimental and simulation results are used simultaneously for a detailed study of the correlation between coupled heat/water management and degradations. Furthermore, a detailed study of each component's degradation is conducted and correlated to local temperature and humidity. That allows proposing ways and means for the improvement of heat and water management in the cell.

Finally, the study opens up new prospects about the study of some degradation mechanisms in the cell and the challenges related to the thermal modeling.

Chapter I

CONTEXT OF THE STUDY AND BACKGROUND

Summary

1. Hydrogen economy and Fuel Cells

The *hydrogen economy concept* considers hydrogen as a viable clean solution for energy storage and delivery. Hydrogen is the most abundant chemical element in the universe. Some studies [3] demonstrated the existence of natural hydrogen in submarine hydrothermal systems and researches are underway regarding its exploitation as an energy source. However, to date it is supposed that it exists freely (on the planet) only in negligible quantities. It needs to be produced by appropriate chemical processes like steam reforming of hydrocarbons, water electrolysis, photo-electrochemical water splitting, etc. [4].

In Fig.I.1, a graphic illustration of the long-term future of the hydrogen economy, from production to consumption, passing through storage and distribution, is presented.
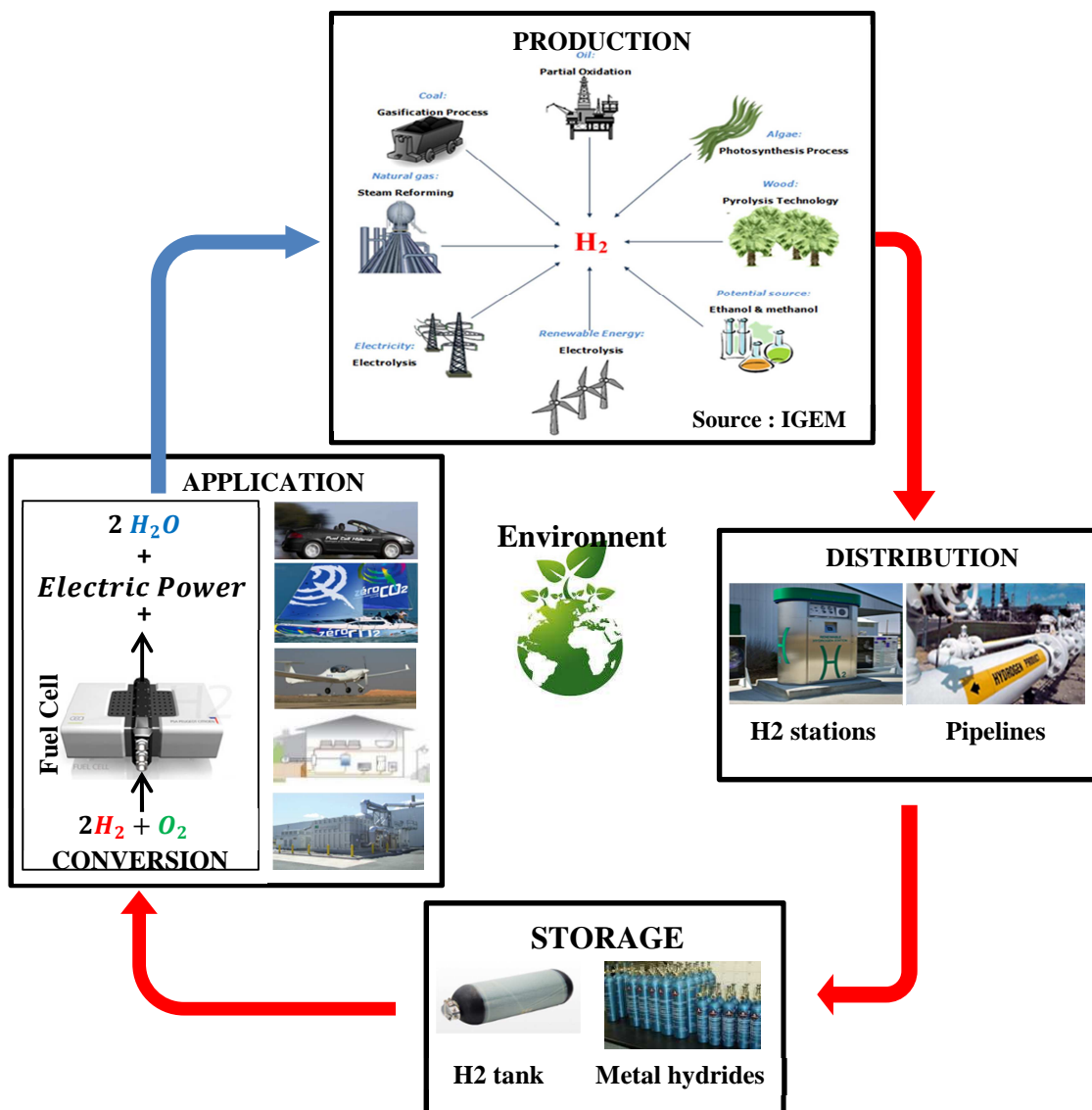
Figure I.1: Graphic illustration of the long-term future of the hydrogen economy

Nowadays, hydrogen, which is also used for chemical processes in industry, is mainly produced via steam reforming and partial oxidation of hydrocarbons. Only ~ 5% is produced via water electrolysis, which can be considered to be environmentally sustainable when the electric power is provided by a renewable process. Recently, there is a progressive move from natural gas steam reforming (which is the most commonly used method) to environmentally sustainable hydrogen sources, as illustrated in Fig.I.2.
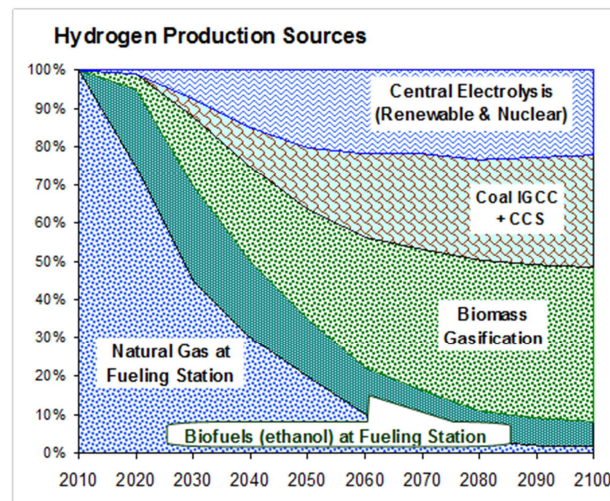
Figure I.2: Modeled transition from reformed natural gas to the other zero or near-zero carbon sources of hydrogen over the century [5]

Indeed, the production of hydrogen via steam reforming or partial oxidation of hydrocarbons can lead to higher emissions of greenhouse gases compared to their direct use in an internal combustion engine [6]. In the near future, other processes like photoelectrochemical water splitting or concentrating solar thermal, which convert solar energy into hydrogen energy, could also be implemented in the production mix.

Distribution infrastructures are needed to supply the produced hydrogen to the consumption sites. Currently, the installation of hydrogen pipelines or the injection of hydrogen in existing natural gas networks as well as the construction of hydrogen fueling stations for transportation application are expanding. Consecutively or alternatively to the distribution infrastructures, storage techniques are needed to make the connection between the production time/site and the demand time/site. Storage represents a crucial challenge regarding the development of hydrogen economy due, firstly, to its low volumetric energy content ($\sim 2\ kWh/l$) and secondly, to security reasons. Different technologies are used, depending mainly on the application: storage in gaseous phase (compressed hydrogen in tanks), in liquid phase (via liquefaction, in methanol or in formic acid), or in solid phase (in

metal hydrides). As with the production method, the distribution and storage methods presented in the Fig.I.1 are not exhaustive.

Hydrogen is a potential fuel for many applications, from transportation to stationary power generation: vehicles, boats, airplanes, residences and power stations. It can also serve as an energy storage medium, used to solve the discrepancies in time between the power stations production and the demand. This application, commonly called "*power to gas*" is a promising solution for managing the intermittency of renewable energy sources such as solar, wind and tidal power.

Regarding the energy conversion process, different researchers and industrials have worked on hydrogen conversion for decades and harnessed hydrogen for different applications, from fueling space shuttles to powering energy stations. There are different ways to convert hydrogen energy. The first one is the conversion into thermal and mechanical energy using Internal Combustion Engines. This technology has many disadvantages like the performance limitation, the difficulties in controlling the fuel in the combustion chamber and the significant emissions of nitrogen oxides (NO_x) related to the high combustion temperatures. For these reasons, there is an important push towards Fuel Cells in which hydrogen is converted into electrical energy through an electrochemical reaction. The main advantages of the fuel cell technology are the good electrical efficiency ($\sim 50\%$), and the environmental sustainability.

Historically, the fuel cell development is intrinsically coupled to the hydrogen production. In 1766, Henry Cavendish produced hydrogen (H_2) by dissolving metals in acids and identified its main characteristics. In 1839, Sir William Grove developed the fuel cell principle to convert the H_2 energy into electrical energy via redox reactions. As presented in Fig.I.3, a fuel cell consists of two Platinum electrodes (catalyst), separated by an ionic conductor (called electrolyte).
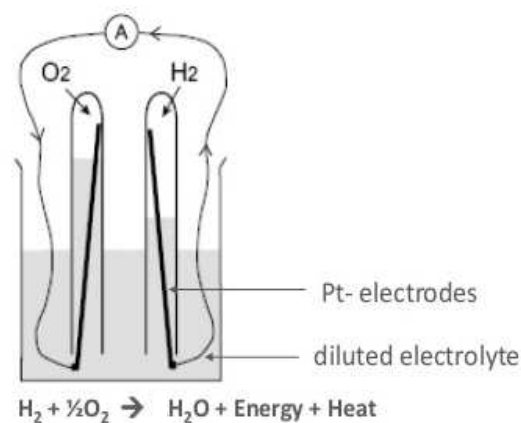
Figure I.3: Principle of the Grove Fuel Cell

However, the fuel cell technology had to wait until 1961 for its first industrialization, when General Electric developed and implemented a 1 kW fuel cell in the space capsules Gemini (NASA's spaceflight program). To date, different hydrogen fuel cell technologies have been developed: Proton Exchange Membrane Fuel Cells (PEMFC), Solid Oxide Fuel Cells (SOFC), Molten Carbonate Fuel Cells (MCFC), Alkaline Fuel Cells (AFC), Proton Ceramic Fuel Cells (PCFC) and Phosphoric Acid Fuel Cells (PAFC). Their main characteristics are reported in Tab.I.1.

Fuel Cell Technology	Anode reaction	Electrolyte/ charge carrier	Cathode reaction	Operating temperature (°C)	Application
PEMFC	$H_2 \rightarrow 2H^+ + 2e^-$	Acid polymer (solid) H^+	$\frac{1}{2} O_2 + 2H^+ + 2e^- \rightarrow H_2O$	60 -120	Transportation Distributed power
SOFC	$H_2 + O^{2-} \rightarrow H_2O + 2e^-$	Yttria–Stabilized Zirconia (solid) O^{2-}	$\frac{1}{2} O_2 + 2e^- \rightarrow O^{2-}$	500 – 1300	Distributed power APUs Power plants
MCFC	$H_2 + CO_3^{2-} \rightarrow H_2O + CO_2 + 2e^-$	$Li_2CO_3/K_2CO_3/$ Na_2CO_3 (liquid) CO_3^{2-}	$\frac{1}{2} O_2 + CO_2 + 2e^- \rightarrow CO_3^{2-}$	600 – 700	Distributed power
AFC	$H_2 + 2OH^- \rightarrow 2H_2O + 2e^-$	Alkaline polymer KOH (liquid) OH^-	$\frac{1}{2} O_2 + H_2O + 2e^- \rightarrow 2OH^-$	50 - 250	Portable power Backup power
PAFC	$H_2 \rightarrow 2H^+ + 2e^-$	H_3PO_4 (liquid) H^+	$\frac{1}{2} O_2 + 2H^+ + 2e^- \rightarrow H_2O$	160 - 220	Distributed power Transportation

Table I.1: Main characteristics of the different hydrogen fuel cell technologies

Among those technologies, PEM Fuel Cells (PEMFCs), which use a solid electrolyte, are particularly favorable for automotive application and many research works and industrials projects are underway regarding their development and commercialization.

2. PEM Fuel Cells in automotive application

The Proton Exchange Membrane Fuel Cell introduced above is a promising candidate for many applications, especially for transportation due to its:

➢ Excellent dynamic;

➢ High power density;

➢ Good electrical efficiency: ~ 50%;

➢ Solid polymer electrolyte;

As illustrated in Fig.I.4, a cell is composed of one Membrane Electrode Assembly (MEA) where the electrochemical reaction takes place and one Bipolar Plate (BP) for the distribution of the reactive gases. As its name indicates, the electrolyte, which exchanges the protons, is a polymer membrane. In order to produce the desired level of power, single cells are usually connected in series, forming a "stack". Different stacks are connected in parallel in high power systems for flexibility and modularity reasons.
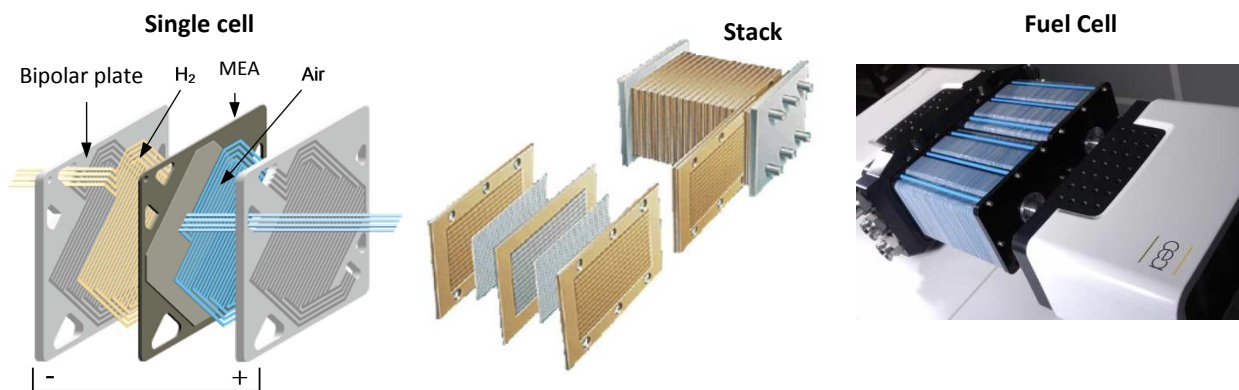
Figure I.4: Illustration of a single cell, a stack and a high power (80 kW) fuel cell

Fig.I.5 illustrates the configuration of a fuel cell with the related system in automotive application. The implementation of experimental fuel cells in vehicles started in 1959 with a modified Allis-Chalmers farm tractor, powered by a 15 kW fuel cell. It was followed by an upscaling in road vehicles by General Motors in 1966 (Chevrolet Electrovan). The development of fuel cell vehicles accelerated during the 2000s and since then many concepts have been presented: *Toyota FCHV-4 (2007), Peugeot 307cc Fisypac FCV (2008), Honda FCX Clarity (2008), Mercedes-Benz F-Cell (2009), Audi A7 h-tron quattro-FCEV (2014)*, etc. Many automakers are planning to enter the market and start the commercialization of next-generation fuel cell vehicles before 2017. For example, Toyota Motors Co. started the sales of its high performance fuel cell vehicle *Toyota Mirai* in early 2015. Hyundai Motor Co. is planning to produce 1000 units of the *Tucson Fuel Cell* by 2015.
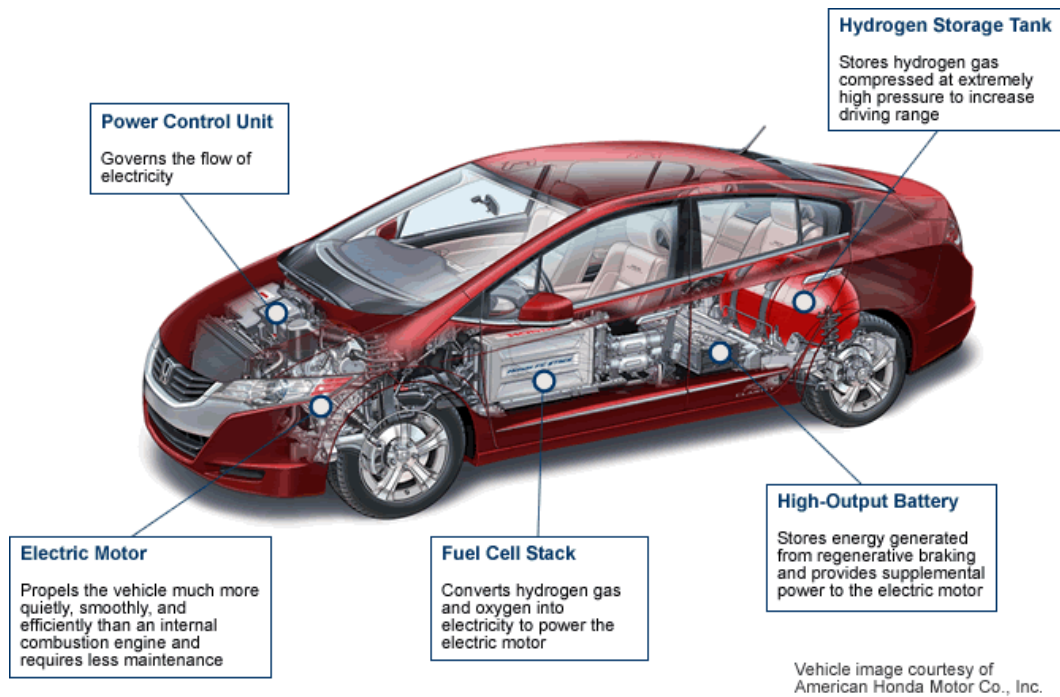
Figure I.5: Illustration of the main components of a Fuel Cell Vehicle (Honda FCX Clarity)

In parallel, many programs are underway regarding the development of the infrastructures and filling stations for fuel cell vehicles. The *California Hydrogen Highway* program is planning to install more than 100 H_2 filling stations in California in the next years [7]. A map of the stations in use and under construction is presented in Fig.I.6. *JX Nippon Oil & Energy* projects to install more than 100 H_2 filling stations in Japan before 2018 [8]. In Europe, the *H_2 mobility initiative* in Germany wants to raise the number of filling stations to 100 from 2015 to 2017 and to 400 by 2023 [9]. Many other programs are underway all over the world.
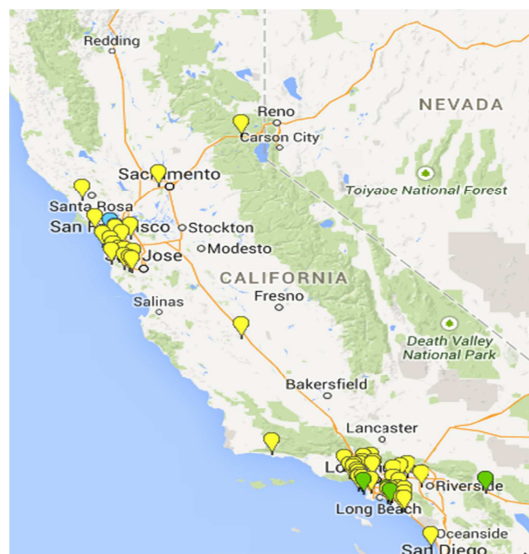
Figure I.6: Localization of the 60 filling stations in use (green) and under construction (yellow) in California [10]

As illustrated above, great investments and advances have been made on fuel cells for automotive application during the last years. However, their development and commercialization are still limited by the cost and lifetime. The Fuel cell technical status with respect of the target is presented in Fig.I.7, with the projected fuel cell system cost in the next years.
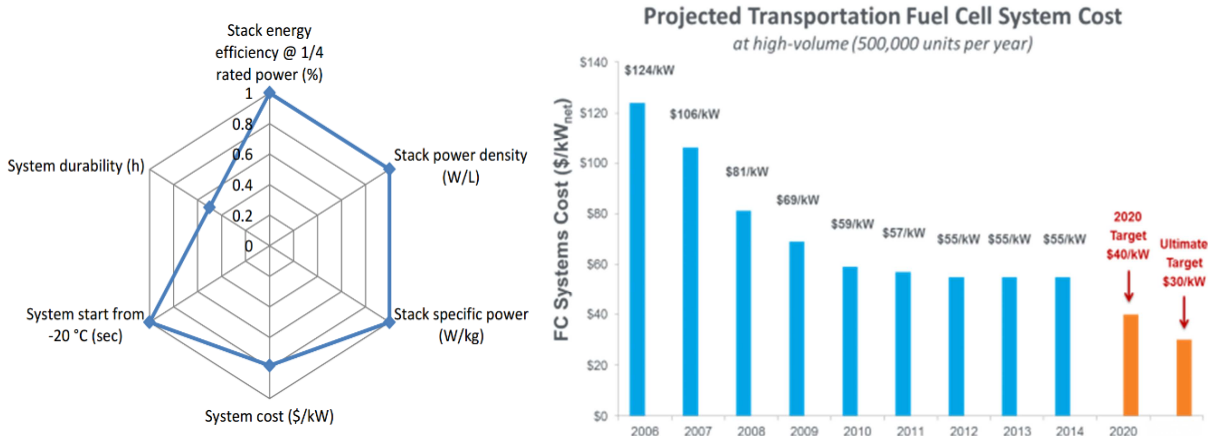
Figure I.7: Automotive fuel cell targets vs status (the blue line indicated the status as a fraction of the target) [11] - Projected fuel cell transportation system costs per kW (assuming a volume production 500 000 units per year) [12]

It is observed that tremendous advances have been achieved regarding the stack efficiency, specific power, cold start, etc. Nevertheless, a great deal of progress remains to be made regarding the cost and durability. In particular, in order to compete with the internal-combustion engines, a fuel cell should cost 30 $/kWe and present a lifetime of 5000 h. Both challenges are related to the thermal management of the stack, because the performance and the degradations are intrinsically linked to the local temperature and water management.

3.   PEM Fuel Cells: state of the art and heat sources

3.1.   Principle of operation and efficiency

The Proton Exchange Membrane Fuel Cell is an electrochemical device which converts the chemical energy of hydrogen into electricity and heat, via a redox reaction with oxygen. The principle of operation is illustrated in Fig.I.8. The fuel cell components illustrated in the figure will be presented in detail later.
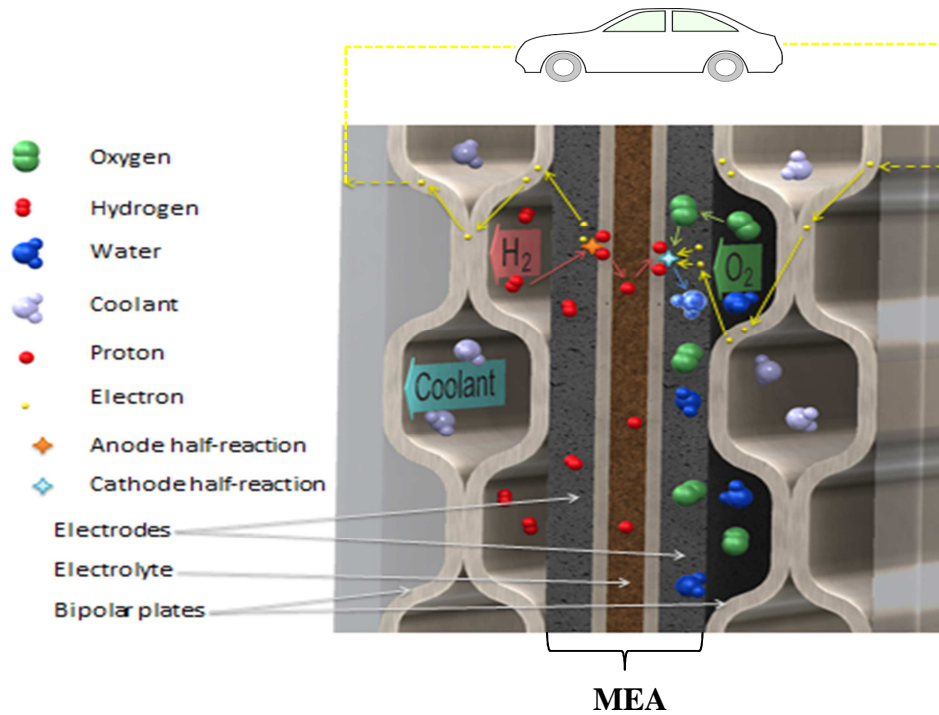
Figure I.8: Redox reactions occurring in the cell

The half-reaction which occurs at the anode electrode is:

$$H_{2\,(gas)} \rightarrow 2H^+ + 2e^- \qquad\qquad \text{[I. 1]}$$

The reversible potential of this electrode is:

$$e_{rev}^{anode} = -\frac{\Delta G_{anode}}{nF} \qquad\qquad \text{[I. 2]}$$

where ΔG_{anode}, n and F are respectively the Gibbs free energy, the number of electrons involved in the reaction and the Faraday constant. The produced protons (H^+) flow through the polymer electrolyte membrane meanwhile the produced electrons (e^-) flow through an electrical load, producing current. Once the protons and electrons arrive at the cathode electrode, they react with oxygen through the half reaction:

$$\frac{1}{2}O_{2\,(gas)} + 2H^+ + 2e^- \rightarrow H_2O_{(vap\ or\ liq)} \qquad\qquad \text{[I. 3]}$$
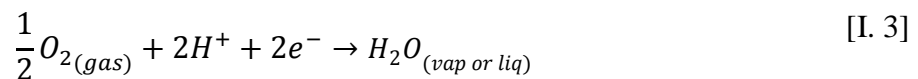
The reversible potential at the cathode electrode is:

$$e_{rev}^{cathode} = -\frac{\Delta G_{cathode}}{nF} \qquad\qquad \text{[I. 4]}$$

Water can be produced either in vapor or in liquid phase, depending on the operating conditions of the fuel cell. The global electrochemical reaction of the cell is:

$$H_{2(gas)} + \frac{1}{2}O_{2(gas)} \rightarrow H_2O_{(vap\ or\ liq)} \qquad\qquad \text{[I. 5]}$$
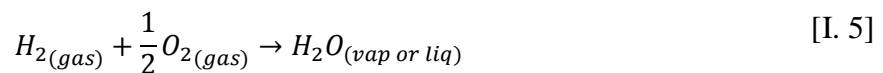
a)   Reversible potential of the cell

The Nernst reversible potential of cell is the difference between the cathode and anode potentials:

$$E_{rev} = e_{rev}^{cathode} - e_{rev}^{anode}$$
[I. 6]

In the Standard conditions for temperature and pressure ($T_0 = 25°C$, $P_0 = 1\ atm$), the Nernst reversible potential is $E_{rev}^0 = 1.23\ V$. However, the Gibbs free energy of the half reactions depends on the cell local temperature and operating pressure. The resulting Nernst potentials can be obtained through the expression:

$$E_{rev} = E_{rev}^0 + \frac{\Delta S}{nF}(T - T_0) + \frac{RT}{nF}\ln\left(\frac{P_{H_2}}{P_0}\left(\frac{P_{O_2}}{P_0}\right)^{\frac{1}{2}}\right)$$
[I. 7]

where ΔS is the change in entropy of the electrochemical reaction, T the temperature and P_i the partial pressure of the species i. Nevertheless, the actual cell potential is decreased from its ideal potential because of several types of irreversible losses. These losses are due to the electrochemical reaction (or charge transfer) at the electrode/electrolyte interface in the active layers, and the charge and mass transport in the other components. These losses are often referred to as overpotential or overvoltage, though only the ohmic losses actually behave as a resistance. They are named activation overpotential (η_{act}), Ohmic limitations (η_{ohm}) and concentration overpotential (η_{conc}). The resulting potential of the cell (U) is:

$$U = E_{rev} - \eta_{act} - \eta_{ohm} - \eta_{conc}$$
[I. 8]

b)   Overpotentials

➤   Activation overpotential: reaction kinetics

The activation overpotential is due to the limited interfacial redox reactions kinetics, because a part of the generated voltage is lost in order to force the transfer between the protons and the electrons on the reaction sites. The Butler-Volmer equation relates the electrical current density (i) of the cell to this overpotential (η_{act}):

$$i = i_0\left[\exp\left(\frac{\alpha nF}{RT}\eta_{act}\right) - \exp\left(\frac{-(1-\alpha)nF}{RT}\eta_{act}\right)\right]$$
[I. 9]

Where α is the charge transfer coefficient and i_0 is the exchanged current density, given by:

$$with \quad i_0 = n\,k_0\,exp\left(-\frac{A_0}{RT}\right)\left(\prod_{v_i>0}a_i^{\gamma_i}\right)^{1-\alpha}\left(\prod_{v_i<0}a_i^{-\gamma_i}\right)^{\alpha}$$
[I. 10]

A_0 is the activation energy; n is number of electrons involved in the reaction; k_0 is the standard rate constant; a_i are the activities of the reactive species; γ_i are the orders of the reactions; ν_i are the stoichiometric coefficients and α is the charge transfer coefficient.

➢ **Ohmic limitations**

Ohmic losses are caused by the ionic resistance in the electrolyte and electrodes as well as the electronic resistance in the electrodes and current collectors. The ohmic losses through the electrolyte can be reduced by decreasing the electrolyte thickness and enhancing the ionic conductivity of the electrolyte. Because both the electrolyte and fuel cell electrodes obey Ohm's law, the ohmic losses can be expressed by the equation:

$$\eta_{ohm} = (R_e + R_p)\, i$$
[I. 11]

Where R_e and R_p are respectively the electrical resistance of the cell and the proton transport resistance of the electrolyte.

➢ **Mass transport limitations**

The mass transport limitation is caused by the diffusion limitation of the reactive gases and flooding phenomena. It depends strongly on the current density, reactant activity, and electrode structure. As a reactant is consumed at the electrode by electrochemical reaction, it is often diluted by the products, when finite mass transport rates limit the supply of fresh reactant and the evacuation of products. As a consequence, a concentration gradient is formed, which drives the mass transport process. While at low current densities, mass-transport losses are not significant, under practical conditions (high current densities, low fuel and air concentrations), they often contribute significantly to the losses of the cell potential. Since, the rate of mass transport to an electrode surface in many cases can be described by Fick's law, the concentration overpotential can be defined as:

$$\eta_{conc} = \frac{RT}{nF} \ln\left(1 - \frac{i}{i_{lim}}\right)$$
[I. 12]

where i_{lim} is the limiting current density.

c) **Polarization curve**

The current flow increase in a fuel cell results in a decrease of the cell voltage because of the losses by electrode and ohmic polarizations. The polarization curve represents a plot of the cell potential versus the current density. An example of polarization curve is presented in Fig.I.9 (in blue). The Nernst equilibrium potential and the different overpotentials which limit the fuel cell performances are presented on the same plot. This plot is valuable in quantifying

the performance evolution and the sources of performance loss (irreversibilities) as a function of the operating current density.
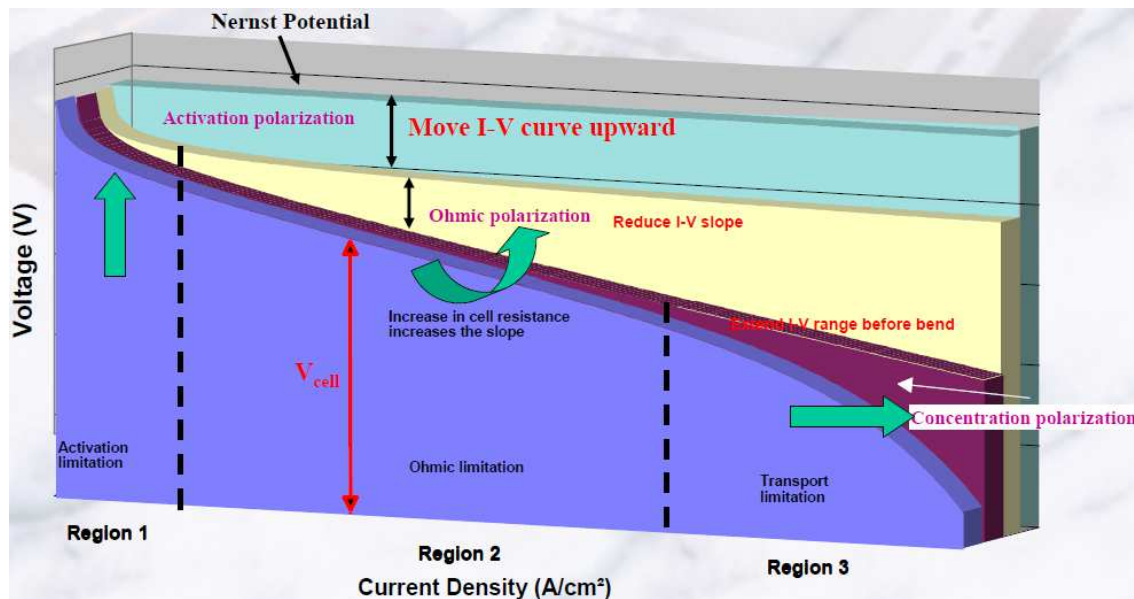
Figure I.9: Polarization curve and sources of potential loss

The reversible voltage of the cell, which is about 1.23 V in the Standard conditions for temperature and pressure, is degraded by the different overpotentials presented above:

➢ *The activation limitation (plot in light blue)* accounts most for the losses occurring at low current densities and depends on temperature as presented in Equation [I.9].

➢ *The ohmic limitation (plot in yellow)* is quite proportional to the current density. It is the cause of the linear shape of the polarization curve. As presented in Equation [I.11], higher is the electrical resistance, higher is the slope of the curve.

➢ *The mass transport limitation (plot in purple)* occurs at high current densities and is responsible for the cell potential drop.

Moreover, there is a deviation of the Open Circuit Voltage from the Nernst reversible voltage due to the permeability of the membrane to reactive gases. The measurement of that permeation is performed using an appropriate electrochemical characterization technique, which will be presented in the next chapter.

d)   Efficiency

The performance of fuel cells is affected by operating variables (e.g., temperature, pressure, gas composition, reactant utilization, and current density), cell design and other factors (impurities, degradations) that influence the ideal cell potential and the magnitude of the voltage losses described above. From a thermodynamics point of view, the fuel cell is an

energy conversion system in which the chemical energy of the fuel (total reaction enthalpy) is converted into electrical energy, generating entropy and waste heat.

$$Global\ reaction:\ H_2 + \frac{1}{2}\,O_2 \rightarrow Electric\ power + Heat\ power + Water \qquad \text{[I. 13]}$$
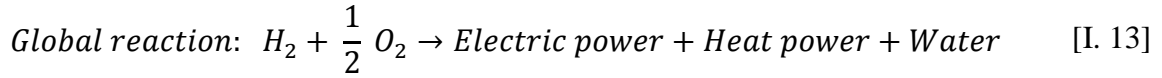
The total reaction enthalpy is:

- $\Delta H_{tot} = \Delta H_l = 285.8\ kJ/mol_{H_2}$ if water is produced in liquid phase;

- $\Delta H_{tot} = \Delta H_v = 242\ kJ/mol_{H_2}$ if water is produced in vapor phase;

The difference between them being the latent heat of water evaporation/condensation. From the first principle, the chemical power source is the sum of electric power (P_{e^-}) produced and heat power (P_{th}):

$$\dot{n}_{H_2}\Delta H_{tot} = P_{e^-} + P_{th} \qquad \text{[I. 14]}$$

Where $\dot{n}_{H_2}$ is the molar flow rate of the hydrogen consumed during the energy conversion process. The electric power (P_{e^-}) of the cell is the product of the cell potential (U) and the produced current (I):

$$P_{e^-} = U \cdot I \qquad \text{[I. 15]}$$

The fuel cell resulting thermodynamic efficiency is:

$$\varepsilon = \frac{P_{e^-}}{\dot{n}_{H_2}\Delta H_{tot}} = \frac{U \cdot I}{\dot{n}_{H_2}\Delta H_{tot}} \qquad \text{[I. 16]}$$

The fuel cell electrochemical efficiency is the ratio of the electrical energy output to the ideal energy output (if all the fuel chemical energy is converted):

$$\epsilon = \varepsilon\,\eta \qquad \text{[I. 17]}$$

$$\text{with } \eta = \frac{Reacted\ fuel}{Supplied\ fuel} \text{ the fuel utilization coefficient} \qquad \text{[I. 18]}$$

The evolution of fuel cell and automotive system (fuel cell and ancillaries) efficiencies as a function of the electric power is presented in Fig.I.10.
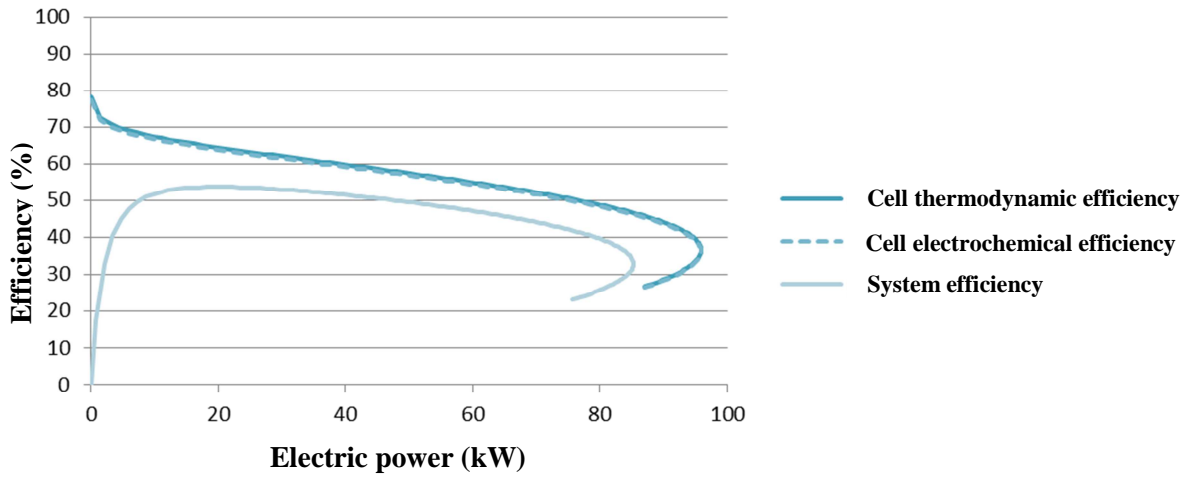
Figure I.10: Evolution of fuel cell efficiencies as a function of the electric power (CEA)

The efficiency of the cell decreases when the output electric power increases. There is a maximal operating point above which there is a performance drop. The cell thermodynamics and electrochemical efficiencies are quite the same, indicating that almost all the supplied hydrogen effectively reacts in the fuel cell. Taking into account the ancillaries of the fuel cell, the efficiency of the automotive system starts from zero. That means the output electrical power of the cell is not sufficient to power its ancillaries. There is a maximum operating point where the system efficiency reaches ~54%, followed by a shape which is similar to the cell efficiency.

The evolutions of the electric power and thermal power, as a function of the operating current is presented in Fig.I.11.
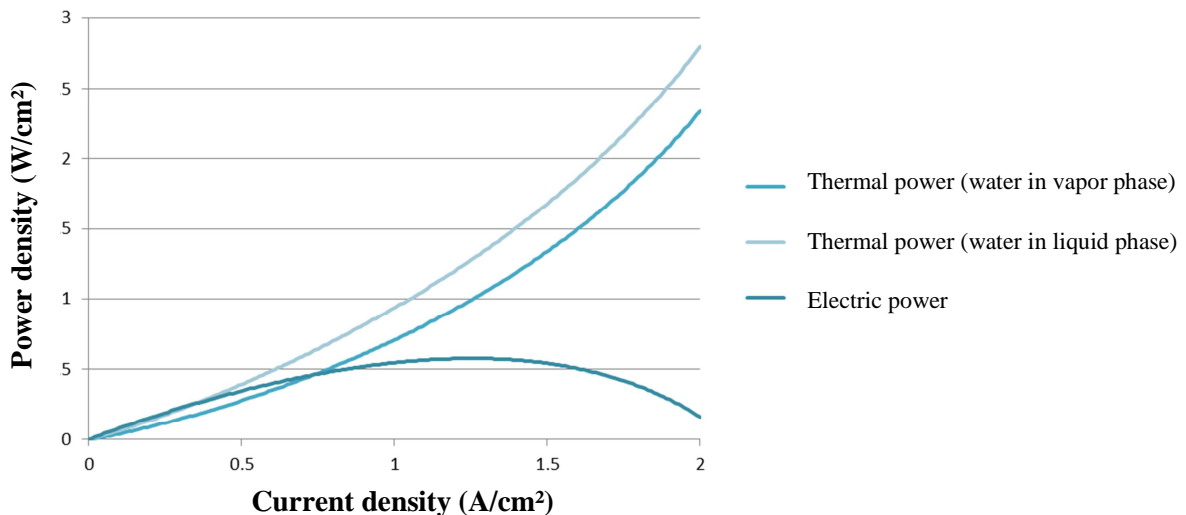
Figure I.11: Electric and thermal power as a function of the operating current (CEA)

There is a maximum operating point for the output electric power, which is obtained at $\sim 1.25\ A/cm^2$ in this case. The thermal power is lower than the electric power at low current densities $(< 0.75\ A/cm^2)$. At high current densities, the thermal power exceeds the electric power, following a quite quadratic evolution. This figure highlights the great importance of an appropriate heat removal strategy for the fuel cell design and optimization.

3.2. Heat sources in the cell

The heat production is governed by different generation mechanisms: thermodynamic irreversibility, electrode kinetic, ohmic losses and mass transport losses. In general, they can be classified in:

> *Half-reactions entropy (Peltier Effect)*

In the catalyst layers there is reversible heating due to the entropy change (ΔS) during the half reactions:

$$Q_{reac} = -T\ \Delta S(P,T) \hspace{2cm} \text{[I. 19]}$$

Different authors estimated the value of the half-reactions entropy change. Lampinen and Fominio [13] predicted *ΔS_{anode} =-0.104 J/mol/K* and *$\Delta S_{cathode}$ = 326.36 J/mol/K*. According to Ju et al. [14], it accounts for $\sim 35\%$ of the total heat release at (0.6V, 0.8A/cm², 80°C). According to Weber et al. [15], it accounts for 22% and 0.9% of the total heat generation (0.2V, 1.5A/cm², 80°C) respectively at the cathode and anode.

> *Electrochemical activation energy (Irreversibility)*

Standing to the activated complex theory, overpotentials are a consequence of the irreversibility of the reactions. The resulting heat source can be written:

$$Q_{act}^{a} = \eta_a\ i \hspace{2cm} \text{[I. 20]}$$

$$Q_{act}^{c} = \eta_c\ i \hspace{2cm} \text{[I. 21]}$$

The anode and cathode overpotentials (η_a and η_c) can be estimated using the electrochemical kinetic law. According to Ju et al. [14], it accounts for $\sim 50\%$ of the total heat release at (0.6V, 0.8A/cm², 80°C). According to Weber et al. [15], it accounts for $\sim 55.3\%$ and $\sim 8.6\%$ respectively at the cathode and the anode of the total heat generation at (0.2V, 1.5A/cm², 80°C).

> *Sorption/desorption heat*

In the catalyst layers, there is a water sorption phenomenon. Namely, water is liquid in the membrane and mainly in vapor phase in the pores of the CLs. The heat release during this process is given by:

$$Q_{sorp} = \dot{n}_{H_2O}\ \Delta H_{l\leftrightarrow v}(T) \qquad\qquad [I.\ 22]$$

where $\Delta H_{l\leftrightarrow v}$ is the enthalpy of phase change between liquid and vapor phases and $\dot{n}_{H_2O}$ is the flux of water phase change.

> *Phase change heat*

It can exist in all the subsystems of the MEA or in the gas channels. Phase change is determined by the equilibrium between the vapor partial pressure and the temperature. As a whole, water condensation may take place in the cold zones of the gas channels while water evaporation may occur close to the membrane in the hot zones. Weber et al. [15] quantified the impact of that phase change on heat source distribution and found a total amount of ~2.6% with saturated feed gases.

A global water balance of the fuel cells studied in this work was performed, assuming isothermal conditions in the cell (80°C). The operating range of the fuel cells studied in this work, with reference to the *T-v* diagram of water, is presented below in Fig.I.12.
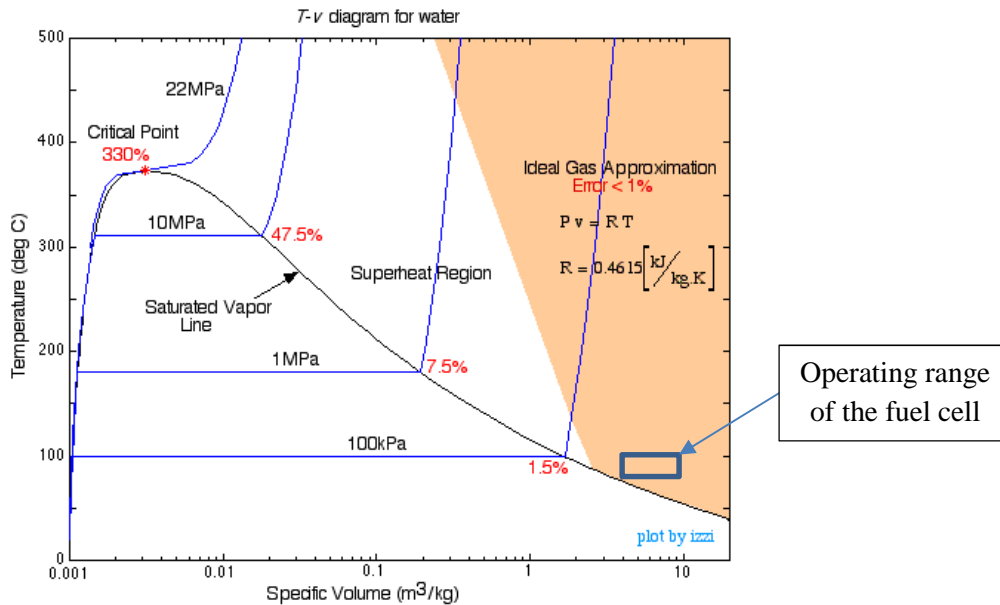
Figure I.12: Range of validity of ideal gas approximation for water vapor

It is observed that, at a global scale, water should not condense in the cell. However, the thermal heterogeneities may induce zones of local condensation, and that will be discussed in Chapter IV.

➢ *Joule effect*

In all the subsystems, there is Ohmic heating due to the resistance of the materials to charge transport:

$$Q_j = \frac{i^2}{\sigma}$$ [I. 23]

where σ is the electrical conductivity of the material.

3.3. PEM Fuel Cells components

As illustrated in Fig.I.8, a PEM fuel cell is composed of different layers, in order to:
- Supply the electrodes in reactive gases as uniformly as possible;
- Optimize the electrochemical reaction;
- Collect the produced electrical current;
- Ensure a good evacuation of the produced water and heat;
- Maintain a good mechanical stability of the system.

To this end, each cell is composed of one Membrane Electrode Assembly (MEA) and one Bipolar Plate (BP). The Membrane Electrode Assembly (MEA) is the multi-layered system in which the electrochemical reactions take place. As illustrated in Fig.I.13, it is composed of the Membrane and two Catalyst Layers sandwiched between two Micro-Porous Layers (MPL) and two Gas Diffusion Layers (GDL).
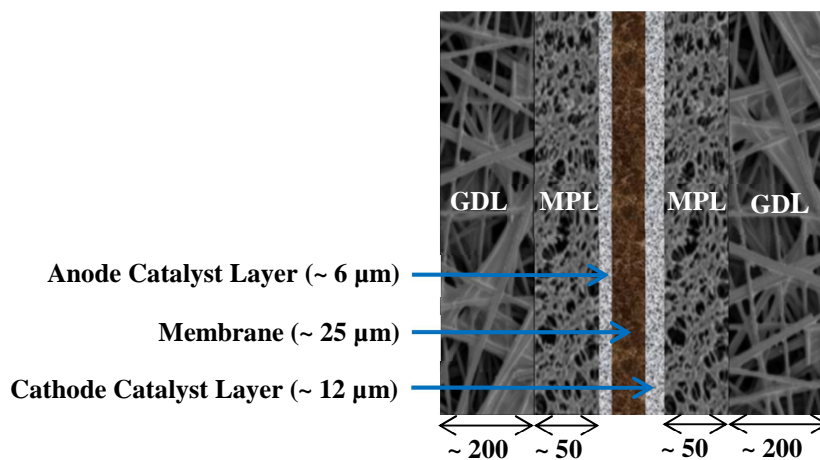
Figure I.13: Different components of the Membrane Electrode Assembly. The indicated thicknesses are in μm

a) Membrane (electrolyte)

The function of the membrane is to ensure protons transport and electronic insulation between the anode and the cathode while simultaneously inhibiting reactive gases transport. Different materials for the membrane have been studied in the past years (fluoropolymers, hydrocarbon-based polymers…) but the most well-known and the most commonly used is Nafion, a perfluorosulfonic acid polymer (trademark of *E.I. Dupont de Nemours*). As indicated in Fig.I.14, it is made of a perfluorinated polymer backbone with sulphonic acid side chains for protons transport.
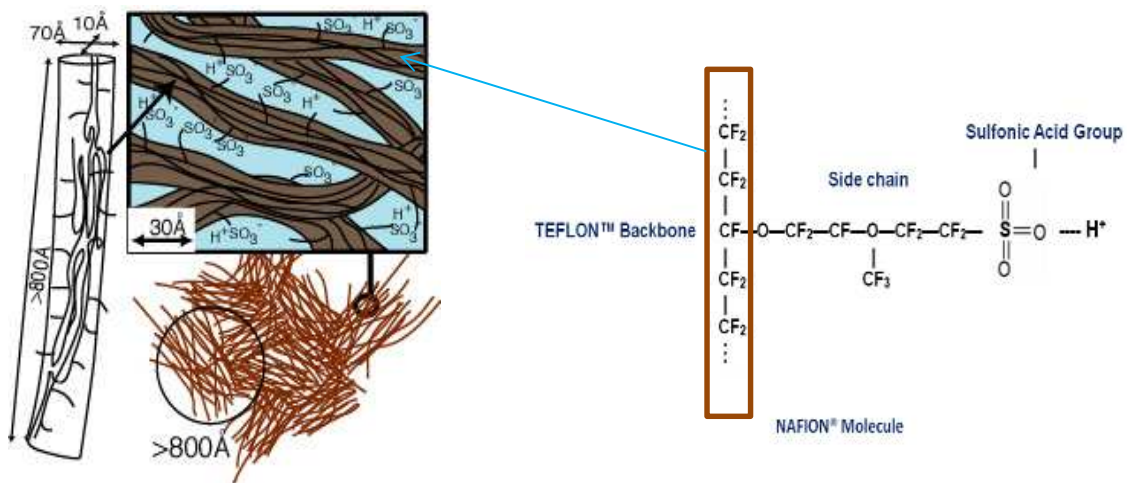
Figure I.14: Structure of the Nafion molecule [16]

When the Nafion membrane is humidified, there is a separation between the hydrophobic backbone and the sulphonic acid groups, which are clustered in hydrophilic regions. Water, which is located in those hydrophilic regions, allows the proton transport either via vehicle mechanism, or via Grotthus mechanism [17]. As a consequence, the *water content*, defined as the number of water molecules per sulfonic acid group, largely affects the ionic conductivity and so the performance of the fuel cell.

b) Catalyst Layers

As its name indicates, the catalyst layer is the component where is located the catalyst for the electrochemical reaction. This component has to ensure the delivery at the same time of the reactive gases, the electrons and the protons to the catalyst zones. A microstructure of the cathode catalyst layer, extracted from [18] is presented in Fig.I.15.
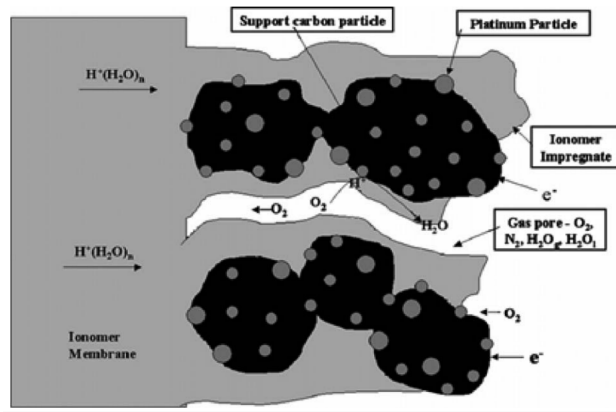
Figure I.15: Schematic illustration of the cathode catalyst layers in PEMFCs [18]

Usually, the platinum catalysts are deposited in the form of nano-particles on an electron conductive carbon support matrix, in order to maximize the flow of the electrons from the electrode to the reaction sites. The catalyst layer has a porous structure (porosity ~50%) for the transport of the reactive gases to the reaction sites. In parallel, Nafion is used for the transport of the protons from the membrane to the reaction sites. The hydrophobic properties of the PTFE included in the catalyst layer are also useful for the evacuation of produced water to the pores.

c) Gas diffusion Layers and Micro-Porous Layers

The main functions of the diffusion layers are to:

- ➤ Ensure a proper reactive gas distribution from the channel to the catalyst layer surface. To this end, they have a high porosity (~ 75%);
- ➤ Ensure a good electronic connection between the catalyst layers and the bipolar plate;
- ➤ Support mechanically the MEA in order to avoid stresses due to the clamping pressure and membrane swelling during water uptake.

GDLs are usually made of carbon fibers (diameter ~ 5 µm) pressed together either into a carbon cloth (GDL-CT, ELAT) or into carbon paper (Sigracet, Toray, Freudenberg). An image of a GDL obtained via Scanning Electron Microscopy is presented in Fig.I.16.
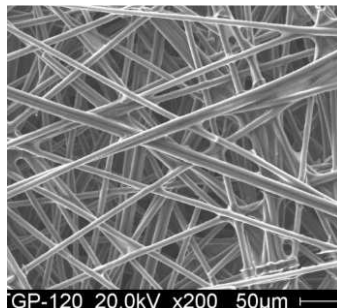
Figure I.16: Microstructure of the Gas Diffusion Layer

The GDLs have a hydrophobic treatment obtained by coating their bulk surfaces with PTFE in order to assist water management and avoid flooding. A microporous layer (porosity ~ 35%), which is made of carbon black powder with a hydrophobic agent (PTFE), is added between the GDLs and the CLs in order to:

➢ Smooth the surface heterogeneities of the GDL and improve the electronic contact between the GDL and the CL;

➢ Assist the water management of the cell by enhancing water removal from the catalyst layer and so avoiding flooding.

➢ Increase the mechanical protection of the MEA.

For this study, it is worth noting that the GDL is an extremely anisotropic component. The in-plane distribution of the carbon fibers induces electrical and thermal conductivities higher in the plane and lower across the plane (through plane). Moreover, in a stack the thermal and electrical conductivities of the GDLs highly depend on local compression.

d) Bipolar plates

The flow-field plates presented above are usually called "*bipolar plates*" because they ensure not only the anode and cathode gas distributions, but also the electrical connections between the individual cells. Usually, in order to eliminate the excessive heat in the system and maintain the optimal operating temperature, a coolant flows in the bipolar plates as indicated in Fig.I.8. So the Bipolar Plate is a multifunctional component which ensures a proper reactive gases distribution and products evacuation all over the cell, separates the different cells of the stack, collects the current from the cell, assists the heat and water management, and ensures the mechanical stability and the sealing of the stack.

The Bipolar plates are usually classified by the material used and the flow field design. The ideal characteristics of the bipolar plate's material are: high electrical and thermal conductivity; low weight; high corrosion resistance; low interfacial contact resistance; high mechanical strength; no brittleness. Different materials (Poco graphite, composite, metal) have been developed and tested by different researchers and industrials (see Fig.I.17), in order to optimize either the production cost or the durability in the fuel cell environment. Metallic bipolar plates (stainless steel, titanium, aluminum) are largely used in automotive application due to the good flexibility in manufacturing, the low volumetric power density and the low brittleness.
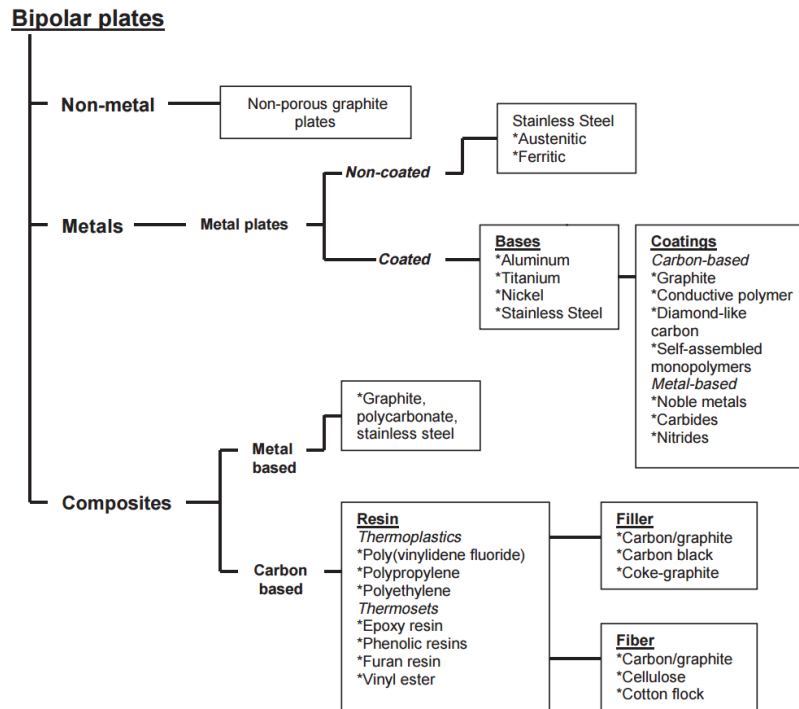
Figure I.17: Classification of materials for BPs used in PEM fuel cells [19]

Regarding the flow field design, conventional designs include *straight parallel*, *serpentine*, *parallel-serpentine* and *interdigitated flow fields*. Straight parallel channels are simpler in manufacturing and present the main advantage of low pressure drop. However, they are limited by the non-uniform distribution of the reactant gases in the channels and the accumulation of liquid water under the ribs. Serpentine channels help in overcoming these limitations by inducing forced-convective under-rib flows between adjacent channels which enhance the performances. But a direct consequence of serpentine is higher pressures drops. Multi-pass serpentine flow-fields (MPSFFs) are a combination of parallel and serpentine flow fields (see Fig.I.18), which allow obtaining the best trade-off between performance, pressure drop and drainage of condensed water. Interdigitated flow fields, in which the flow is forced to pass through the diffusion layers using dead-end channels design, can also be effective in removing liquid water.

Figure I.18: Illustration of serpentine, parallel (MGM-Carbon Industrial Co) and multi-pass serpentine flow-fields (Tech-Etch)

Bipolar plates design is a rapidly developing sector and with industrialization, innovative designs are continuously proposed. For example, Honda Motor Co. presented the *wave flow design* (see Fig.I.19.a) for the Honda FCX Clarity, and proved that it is effective in optimizing the performance and the volume of the fuel cell. Moreover, it uses gravity force to evacuate condensed water. Toyota Motor Co. proposed an innovative *3D fine-mesh flow-field* (see Fig. I.19.b) which uses a kind of non-symmetric corrugated plates in order to optimize the drainage of liquid water and the diffusion of reactive gases over the active area.
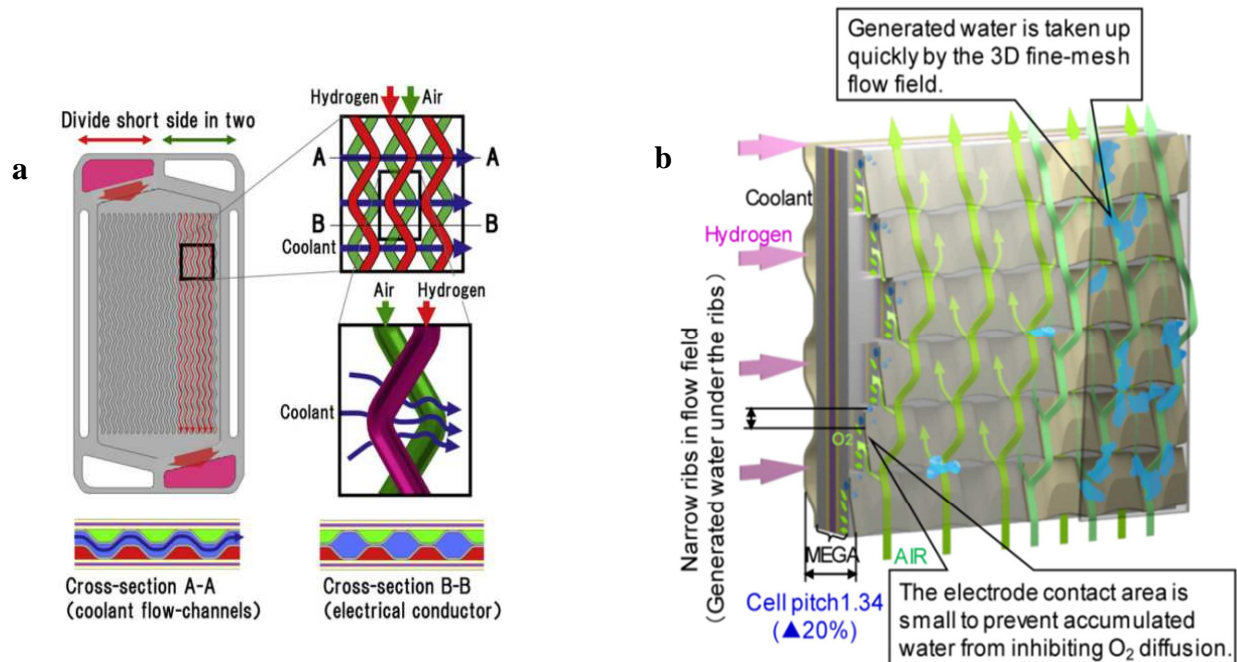
Figure I.19: (a) Wave flow BP of the Honda FCX Clarity with coolant flow field [20]
(b) 3D fine-mesh flow-field of the Toyota Mirai stack [21]

The coolant flow field (CFF) can be designed in an additional cooling plate, but nowadays there is an important push to use the channel network formed by the bipolar plate ribs for the cooling purposes (see Fig.I.19). With this solution, the reactive gases flow field design becomes a constraint for the coolant flow field design, which should be accurately controlled in order to avoid high temperature heterogeneities in the cell.

4. Thermal issues in automotive PEM Fuel Cells

One of the key parameters facing the technical barriers presented above is the *thermal management* of the fuel cell. Indeed, the electrochemical reaction produces electricity, water, as well as a huge amount of heat which is generated within the fuel cell by the highly exothermic redox reaction and the Joule effect. This waste heat accounts for 20 - 80% of the total reaction enthalpy depending on the operating current as presented in Fig.I.11.

On the one hand, the temperature of the cell should be maintained high enough in order to increase the kinetics of the electrochemical reactions, limit the voltage drop at low current densities, push maximal currents to higher values, improve the efficiency of heat rejection and increase the tolerance to CO (for hydrogen produced via steam reforming of hydrocarbons). On the other hand, the maximal temperature of the cell must be accurately controlled in order to limit the components ageing and prevent membrane drying (which limits it ionic conductivity). The issue of the balance between heat production and heat removal, called "*thermal management*" is a crucial factor regarding PEMFCs performance and durability. Different cooling methods have been studied by researchers and industrials [22]: liquid cooling, heat spreaders, air cooling, phase change cooling… The most commonly used method for automotive application is liquid cooling because of its efficiency and compactness. Liquid water is often used as coolant, and most of the time it is mixed with ethylene glycol or propylene glycol in order to avoid freezing problems at low temperatures. This kind of coolant shows the advantages of good heat capacity and thermal conductivity. As represented above in Fig.I.20, the liquid water flows in the stack via the bipolar plates, and evacuates the excessive heat in the fuel cell. The cooling water is in turn cooled in a radiator, generally associated to a fan which drives ambient air on this air/water heat exchanger in order to dissipate the heat in ambient air.
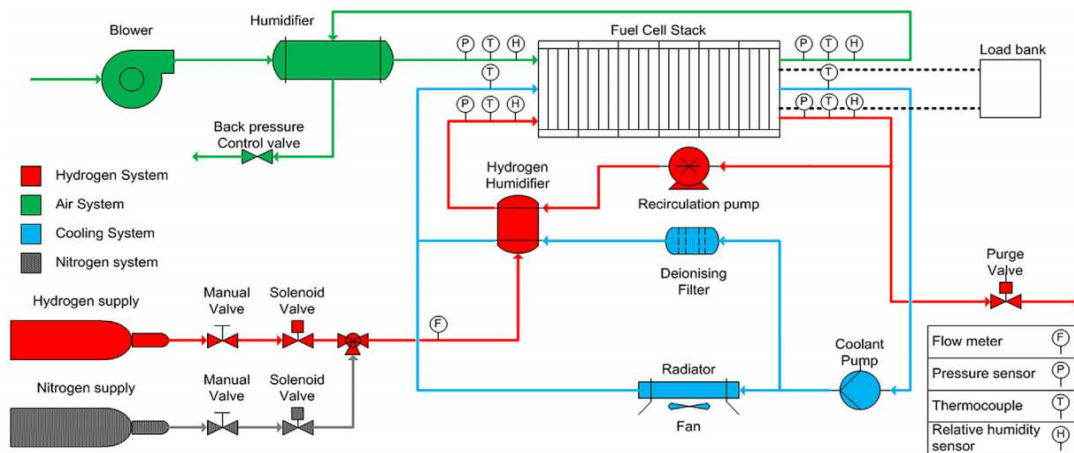
Figure I.20: Schematic of a fuel cell system with the cooling circuit in blue [23]

In the MEA, water can be produced in vapor or liquid phase depending on the local thermal and partial pressure conditions. On the one hand, water is necessary to ensure a good proton conductivity of the electrolyte. On the other hand, excessive water must be accurately removed through convection by the reactive gases in order to avoid flooding which significantly restrict the access of the reactive gases to the catalyst layers. The issue of the balance between water production (and supply) and water removal, usually called "*water management*", is also one of the key factors regarding PEMFCs development and commercialization. Coupled to the heat management issue via the phase change and the local humidity, water management is a technical challenge for the fuel cells design and optimization.

The technical barriers of PEMFCs development are greatly related to the temperature and water management of the stack, because the performance and the degradations are intrinsically linked to the local temperature and humidity. Nowadays, the reference temperature is 80°C and the reference humidity values varies between 30 and 50%. However, there is an important push to higher temperatures and lower humidity values. For example, the target of the *Japanese New Energy and Industrial Technology Development Organization* is to increase the fuel cell temperature at 120°C without external humidification by 2030 [24]. On the one hand, a high temperature can widely exacerbate the degradation mechanisms of the membrane, catalyst layer and bipolar plates. For example, according to Curtin et al. [25], a local temperature higher than 90°C can degrade the membrane due to the attack of free radicals such as OH* and OOH*. In addition, degradation mechanisms are known to be exacerbated by low humidity in the membrane. On the other hand, a low temperature can induce local flooding in the cell due to low water saturation pressures. In both cases these effects of temperature heterogeneities can significantly restrict the lifetime and the performances of the cell. For that reason, intensive investigations are needed to address the specific challenges of heat and water management in the cell as well as their impact on degradations.

The current study is put forward in that context. Its main objectives can be summarized as the study of temperature and humidity distributions in automotive PEM Fuel Cells and the investigation of the effect of local temperature as well as high temperature heterogeneities on performance evolution and degradations.

5. State of the art of the investigation of temperature distribution in PEMFCs and its effect on degradations

Since in a PEMFC the amount of heat released is of the same order of magnitude as the produced electrical energy, thermal management studies were performed with PEMFC development since the 1960s. The operating temperature was considered uniform in the fuel cell and was always limited by the material properties, especially by the membrane. The first detailed studies, introduced in early 1990s, were related to water management [26-27]. Those studies have been a spin-off for the studies of heat balance since it is intrinsically coupled to water transport. The pioneering studies of local temperature distribution within the cell were performed by Fuller and Newman [28]. After that, several studies have been conducted either via experimentation or via modeling in order to investigate local temperature and its effects on individual components degradation.

5.1. Experimental techniques for temperature measurement

As regards experimentation, conventional methods such as micro-thermocouples, thermistors and resistance temperature detectors (RTDs) have been used to get the temperature distribution inside a cell. Some researchers tried non-conventional techniques, which will be presented below: fiber bragg grating (FBG) sensors, bandgap temperature sensors, tunable diode laser absorption spectroscopy (TDLAS), phosphor thermometry, infrared imaging and capacitive polymer sensing elements (for humidity measurement).

Pei et al. [29] embedded 36 thermocouples into 4 cathode plates of a 46 cells stack (9 thermocouples for each 200 cm² active area cell) for the measurement of the temperature at the interface between the cathode plate and the MEA (Fig.I.21). At the cell scale, they found a parabola evolution of the temperature along the cell surface with maximal differences of 4.6 and 7.8°C respectively at 0.5 A/cm² and 0.7 A/cm².
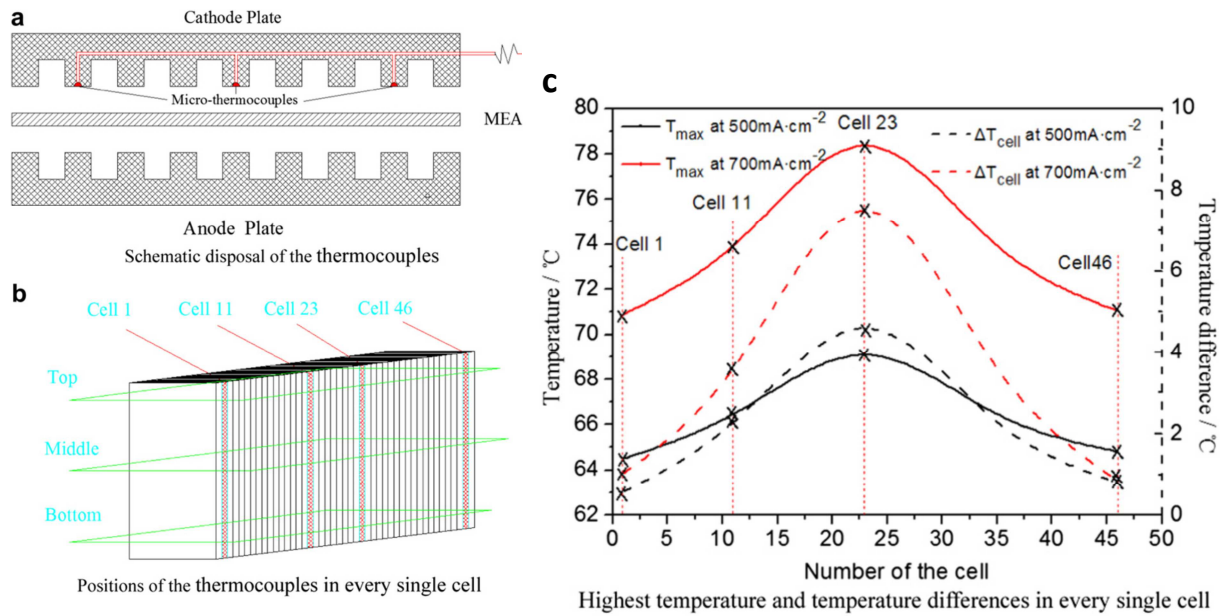
Figure I.21 : (a) Schematic disposal of the thermocouples in each cell used in [29] - (b) Position of the thermocouples in the stack – (c) Highest temperature and temperature differences in each cell

For the stack, they observe that the temperature reaches its maximal value in the middle of the stack and that temperature heterogeneities increase with the current density. In addition, measurements in different operating conditions allow concluding that the main parameters influencing the temperature heterogeneities are: (i) the coolant flow rate – (ii) the operating current.

Lee et al. [30] demonstrated the feasibility of using flexible thin-film sensors (2 μm thick) to measure at the same time local temperature (with RTDs) and humidity (with capacitive humidity technique) in a MEA. These thin-films were produced via micro-electro-mechanical-systems (MEMS) fabrication. The optical microscopy photographs of the sensors are presented in Fig.I.22.a, with a figure of their integration in a micro-fuel cell (Fig.I.22.b). A plot of the measured temperature evolution at the outer surface of the BP (measured with a thermocouple) and at the MEA (measured with the thin-film) surface is presented in Fig.I.22.c. It is clearly observed that the BP temperature follows the dynamics of the MEA temperature with a maximal temperature difference of 5.7°C. This technology was upscaled by the development of a micro-flexible thermocouple that can be placed anywhere between the MEA and the flow channels without support frame for local temperature measurement [31].
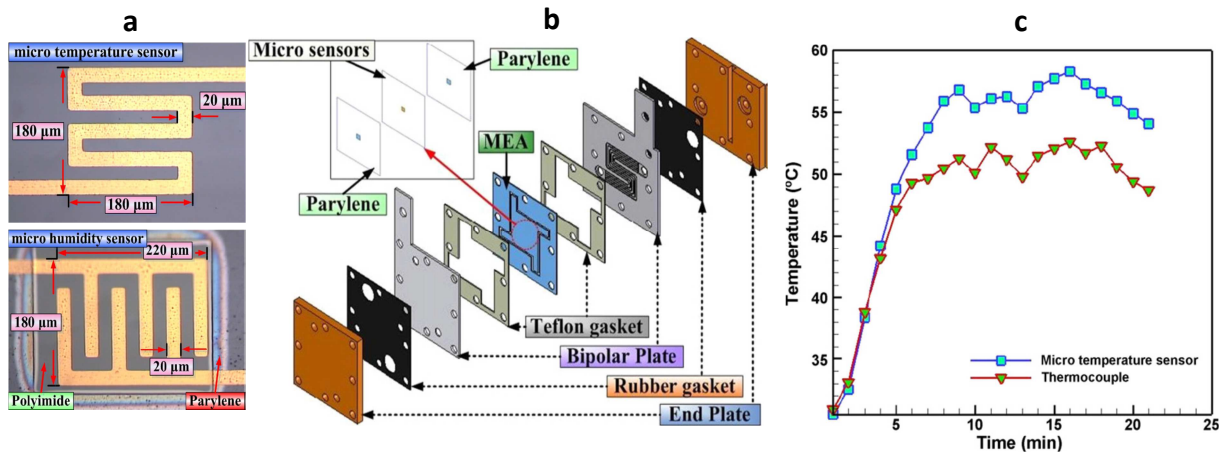
Figure I.22 : (a) Optical microscopy photographs of the sensors – (b) Integration of the sensor in a micro-fuel cell– (c) Comparison of measurements made at the outer surface of the BP and at the surface of MEA [30]

David et al. [32] implemented an optic fiber bragg grating (FBG) sensor for a simultaneous measurement of temperature and relative humidity inside the cell with high accuracy. Embedding two sensors along the cathode flow channel with serpentine design on a 30 cm² cell (Fig.I.23), they measured temperature variations of ~ 1.5°C and humidity variations of ~ 40% at 0.5 A/cm². Moreover, the sensor could be used to study the dynamics of water transport in the MEA since the time scale of the FBG sensor response is of the same order of magnitude as the time scale of water sorption/desorption into the membrane. The plots of the measured RH and temperature while incrementing current are presented in Fig.I.23.c. It is observed that increasing current leads to: (i) an increase of both temperature values and temperature differences along the active area; (ii) a large increase of the RH close to the air outlet, especially at low current densities.
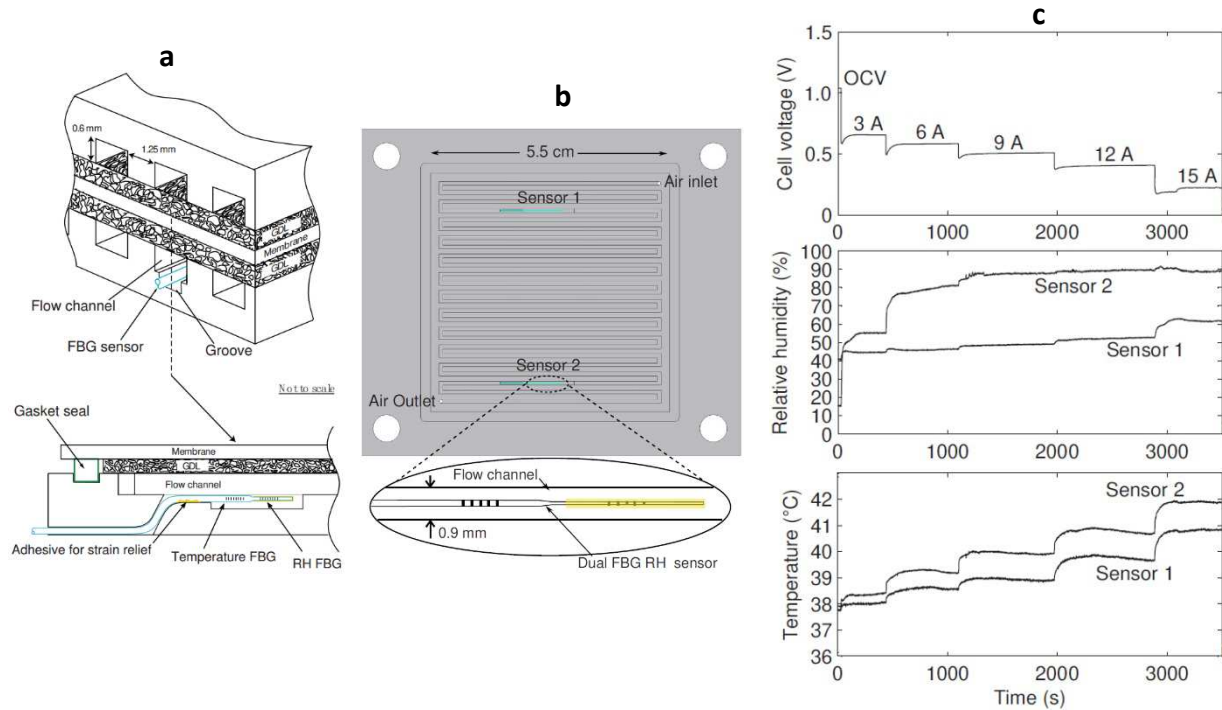
Figure I.23 : (a) Schematic of the in situ FBG sensor located in the bottom of the flow channel – (b) Side view of the positions of the sensors in the BP – (c) Measured relative humidity and temperature at while incrementing current [32]

Hinds et al. [33] used at the same time a miniature bandgap sensor for temperature measurement and a capacitive polymer sensing element for humidity measurement in a single cell. The sensors, incorporated into the flow field plates, can be used to study the humidity profile in the anode and cathode channels at the same time. However, eventual condensed water is not detected by the sensors.

Tunable diode laser absorption spectroscopy (TDLAS) has been proven to be effective in measuring gas temperature and partial pressure in the bipolar plate channels in the operating range of PEMFCs [34-35]. Inman et al. [36] implemented thermal sensors based on the principles of the lifetime-decay method of phosphor thermometry to measure temperatures between the MEA and the bipolar plates. Infrared imaging technology was also used by some authors [37-38-39] despite the constraint of using optical plates which are transparent to IR. For the measurement of the temperature distribution within the MEA with good sensitivity, He et al. [40] laminated in Nafion a thin film thermistor embedded in a 16 μm thick parylene. Over a 5 cm² fuel cell, they measured a temperature difference of ~ 1.5 °C at 0.19 A/cm².

5.2. Experimental techniques for current measurement

Since the measurement of current density distribution can be useful for the design optimization as well as the evaluation of local heat and water sources in the cell, some

researchers developed local current measurement techniques. Zhang et al. [41] used at the same time a current distribution measurement gasket and thin thermocouples between the cathode catalyst layer and gas diffusion layer (see Fig.I.24) to measure the in-plane current and temperature distributions (active area: 16 cm²).
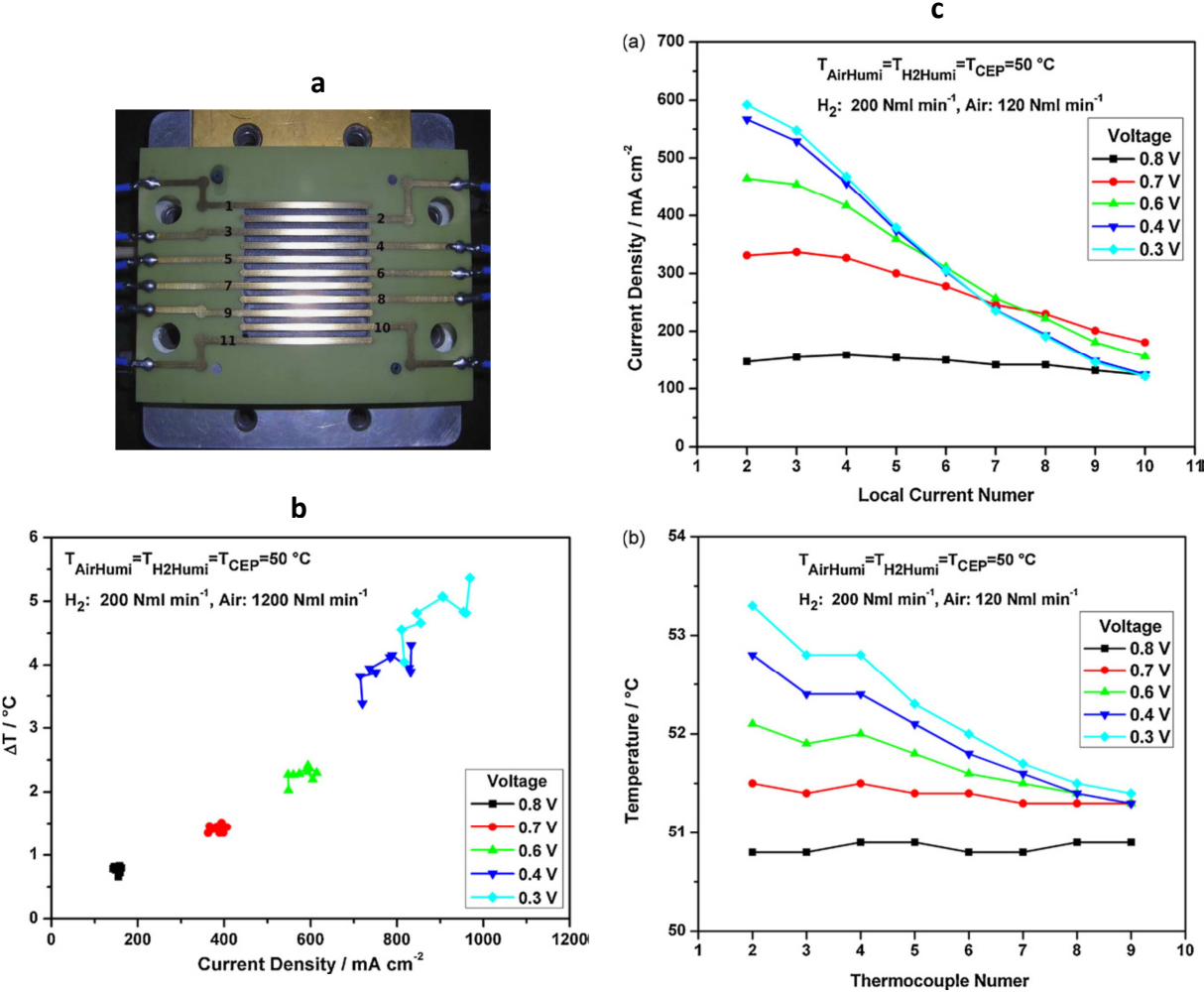
Figure I.24 : (a) Current distribution measurement gasket placed on the flow field plate – (b) Correlation between current distribution and temperature distribution at different cell voltages - (c) Current distributions and temperature distributions at different cell [41]

An interesting result of this study is the measured distribution of current density and temperature at different cell voltages. It is observed that increasing current (decreasing the cell voltage) leads to more heterogeneities of current density and temperature (Fig.I.24.c). Moreover the temperature difference over the active area significantly increases when the operating current increases (Fig.I.24.b).

Printed circuit boards like Current Scan Lin S++ device [42-45], inserted between two monopolar plates, can be used to map not only the temperature (using embedded RTDs) but also the current distribution (using hall effect sensors or shunts) in the stack with a good resolution. The main advantages of this technology are the accuracy, the relatively low

invasiveness and the simultaneous measurement of the current density and temperature over all the active area of the cell. Indeed, the sensor plate is positioned between two monopolar plates and so takes the place of one MEA in the stack (see Fig.I.25). Thus, there is no invasion of the reactive environment of the fuel cell by the sensor.
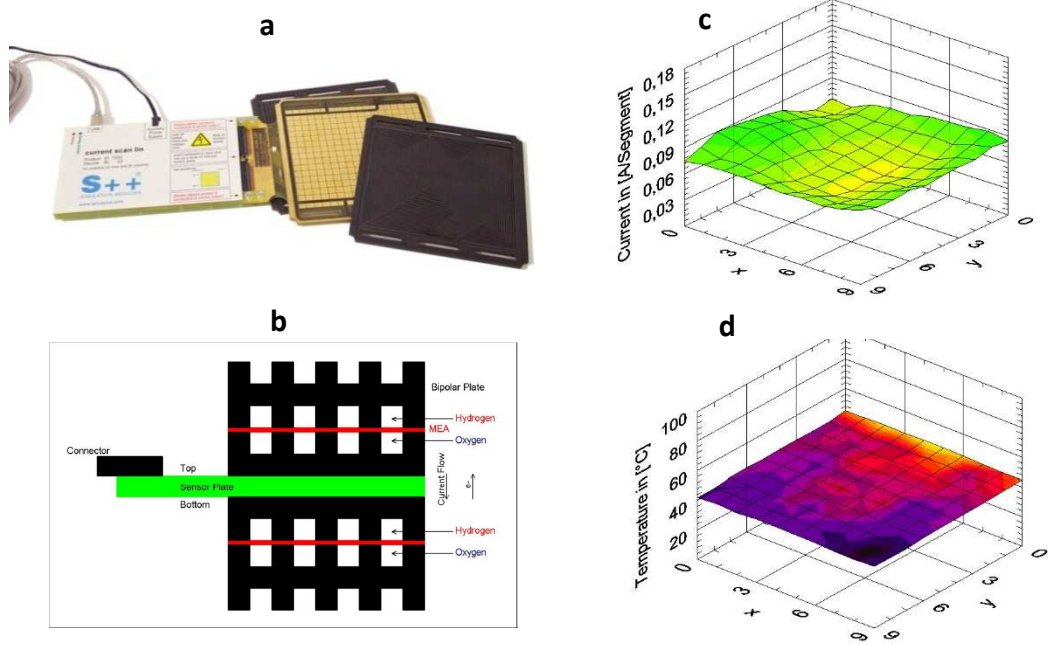
Figure I.25 : (a) Photography of a printed circuit board S++ Current Scan Lin between the flow field plates – (b) Position of the sensor plate in a cell – (c) Measured current and temperature [42]

More recently, Lee et al. [46] developed a flexible four-in-one micro sensor for the simultaneous measurement of temperature, voltage, current and flow in the cell. The micro temperature sensor uses the thermal resistance temperature detector (RTD) principle. However, this technology is limited by the resolution.

5.3. Experimental techniques for the investigation of liquid water distribution

Regarding liquid water distribution, Neutron Imaging is the most *in-situ* and non-invasive technique used in the area of PEMFCs. An example of experimental apparatus, used at the NIST (National Institute of Standards and Technology) is presented in Fig.I.26.a. The flow field geometry and the obtained colorized neutron image of liquid water distribution are also presented in Fig.I.26.b and I.26.c.
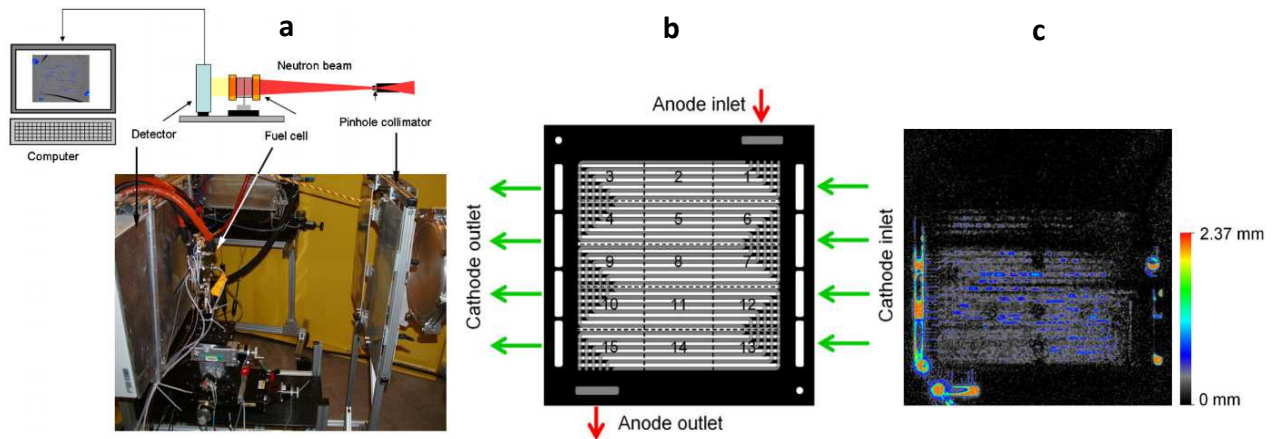
Figure I.26 : Experimental setup at NIST Center of Neutron Research – (b) Studied flow field geometry – (c) Colorized neutron image, which quantify the liquid water distribution [47[]

Small angle neutron scattering (SANS) is also a powerful *in-situ* technique for the determination of the water profile across the membrane, as demonstrated by Gebel et al. [48]. The experimental setup as well as some results of water distribution across the membrane are presented in Fig.I.27.
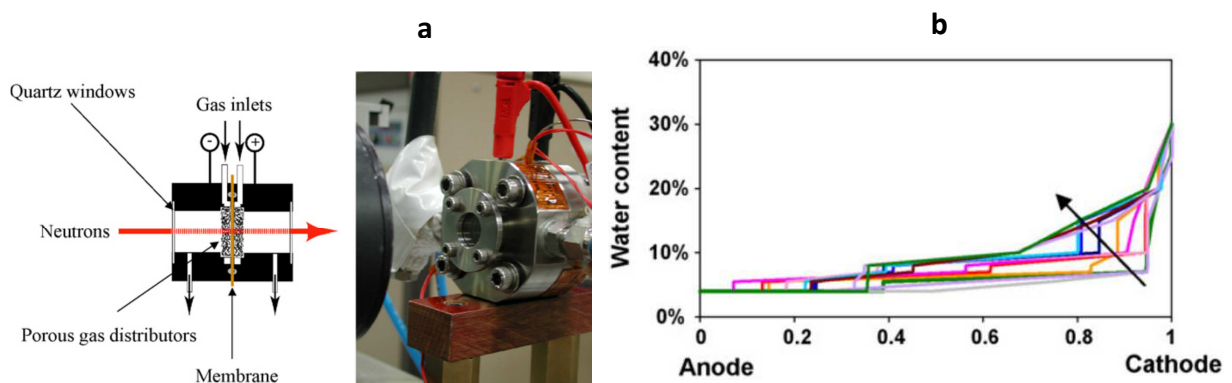
Figure I.27 : (a) SANS apparatus used by Gebel et al. [48] – (b) Distribution of water content in the membrane, the arrow indicates the profile evolution with time

From a general point of view, the measured temperatures presented above are mainly influenced by the coolant flow rate and the operating current. All these measurement techniques are limited either to in-plane investigations over the interfaces between the different layers of the cell, or to through-plane investigation at a reference point of the active area. At a reference current density of 0.5 A/cm², typical through-plane temperature differences are ~ 5°C and typical in-plane temperature gradients are ~ 0.6 °C/cm. However, this value highly depends on the coolant flow rate and flow-field design. The global in-plane distributions of temperature and related parameters in all the components of the cell cannot be determined experimentally, and can be estimated only through modeling. In this way, fuel cell

modelling allows determining the operating conditions in inaccessible zones of the MEA and bipolar plates with sensors.

5.4.   Models review

Several modeling studies have been conducted since the development of PEMFCs to investigate the thermal effects with the main scope of design improvement and optimization. Many computational heat and mass transfer PEMFC models have been developed during the last years from the channel/rib to the stack level (see Fig.I.28).
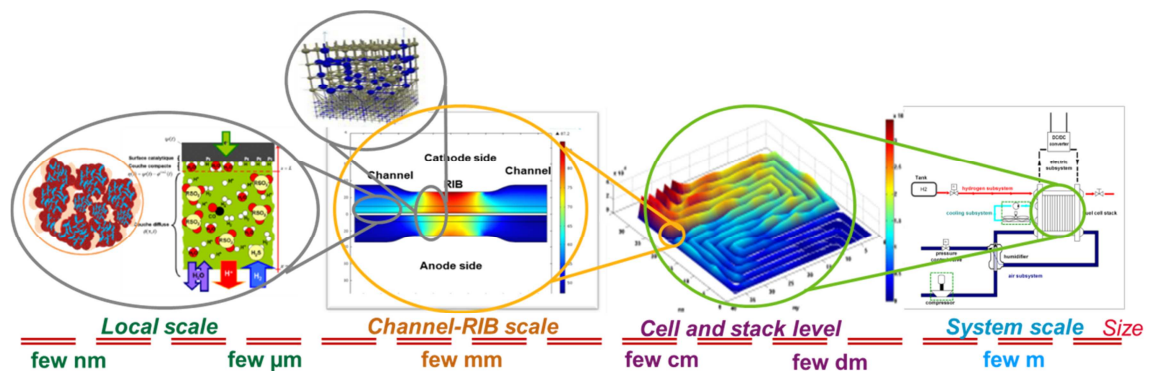
Figure I.28 : Description of the different modeling scales [49]

The great differences between the modeling approaches are the physics involved in the equations, the modeling scale and the dimensionality used to describe the system. Regarding the physics, the *theoretical modeling* is based on physical equations while *empirical modeling* is based on observation and experimentation. This latter is cheaper in computation time, but it requires appropriate experiments and detailed observations to implement the model. Two main types of approaches in PEMFCs theoretical modeling are found in literature:

- ➢ **Rule-based modeling** in which a set of physical rules is applied to simplified structures of the system. The models using this approach are:
  - ✓ **Full morphology models (FM)** which consider the detailed microstructure of the cell layers [50].
  - ✓ **Pore network modeling (PNM)** which appears to be very efficient in modeling water transport in the porous electrodes [51-54].
- ➢ **First-principle based modeling** in which governing partial differential equations of physical quantities obtained from established physics laws are solved.   Two sub-approaches are commonly used:

45

- ✓ *The bottom-up approach* which starts with the resolution of the equations at the atomistic scale and implements them at higher scales. This approach allows advanced multiphase fluid dynamics simulations, with a realistic representation of the cell components. However, its computational cost limits its applicability to a local scale (see Fig.28). The different models found in literature are: *lattice gas (LG) and lattice Boltzmann (LB)* equations [55-56]; *molecular dynamics (MD)* [57-58] and *off-lattice pseudo-particle* [59-60].

- ✓ *The top-down approach* which solves continuum-based equations in which homogeneous materials are considered with effective transport properties. This latter is the most adapted for this study, which is related to the heat and water transport phenomena at a macroscopic scale. Therefore, the following review is related to the thermal models solved using the "top-down approach". In general, one of the key factors facing computation with this approach is the dimensionality used to describe the transport phenomena. The Fig.I.29 shows the different dimensions used to describe transport phenomena in PEM Fuel cells.
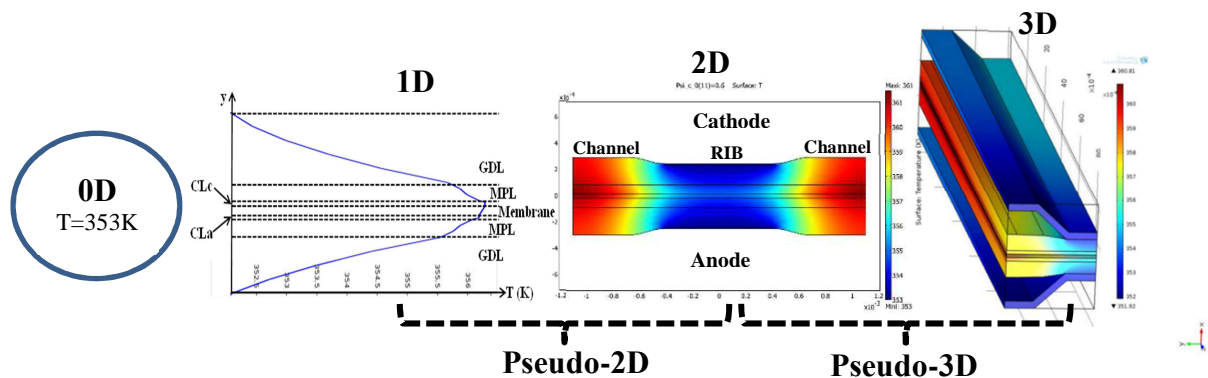
Figure I.29: Description of the different modeling dimensions at the channel/rib scale

0-D models use simple equations without any spatial resolution or geometry description. They can be extended to 0-D multi-zone models in which multiple zero-dimensional zones are considered. This approach is generally suitable to capture global heterogeneities and trends with limited computational resources.

1-D models solve the transport equations in one spatial dimension, either along or across the cell active area. Early 1D studies were performed by Fuller et al. [28] who studied the effect of heat removal rate on operation. Djilali and Lu [61] predicted a temperature difference along the cell thickness (through-plane temperature difference) of 1-5 °C, with a model developed at the channel scale. Weber et al. [15] highlighted the heat pipe effect in the cell with an innovative model at the channel/rib scale. Pharoah et al. [62] developed a similar

model and concluded that the catalyst layer temperature is 3-6°C higher than the bipolar plate temperature at 1 A/cm^2. Park et al. [63] developed a dynamic model on a 20-cells stack with resolution of heat transport in the coolant to study the transient behavior of the cells temperature. In all those models, the liquid/vapor phase change in the cell was considered. 2-D models have been very useful for the study of the transport phenomena in the active layers [64] and the channel/rib transport heterogeneities. The first 2-D thermal models were developed at the channel scale with a single phase approach. Hwang et al. [65] introduced a novel approach for the resolution of solid phase and fluid phase temperature in the porous structures of the MEA. Introducing a two-phase model, Siegel et al. [66] demonstrated that one-phase models overpredict the fluid temperature if there is phase change and that local hot spots position depends on the heat transfer coefficient. Birgersson et al. [67] predicted a ~ 9°C temperature difference across the cell at 1 A/cm^2 using a two phase model. Jung et al. [68] investigated the effect of membrane thickness on temperature distribution and concluded that increasing Nafion thickness results in higher temperature at cathode. Basu et al. [69] demonstrated that phase change and heat pipe effect are strictly linked to local heat transport phenomena, which can vary widely depending on the position of the gases and cooling water inlets. Shan et al. [70] developed a similar one-phase model on a 2 cells stack to predict the dynamic distribution of temperature.

For a complete analysis of the transport phenomena in the cell, some authors developed full 3D models. Shimpalee et al. [71] developed a two-phase model at the channel scale to study the impact of heat transfer consideration on performance prediction. Ju et al. [72] developed a similar model and concluded that GDL thermal conductivity plays an important role in coupled thermal and water management. Wang et al. [73] used a two-phase model to demonstrate that phase change accounts for 15–18% of the total heat generation. Nguyen et al. [74] developed a monophasic model on a cell segment and concluded that the temperature is highly dependent on the current density and that its difference across the cell increases from 4 to 7°C when the current density ranges from 0.3 to 1.2 A/cm^2.

Finally, some 3D models were implemented at the scale of an entire cell. Su et al. [75] developed a thermal model on a 5.29 cm^2-cell with CFD simulations and validated the model using micro-sensors. Le at al. [76] focused on liquid water transport and its effects on temperature distribution on a 2.6 cm^2 cell. Hwang et al. [77] developed a dynamic model to investigate the lag in heat transfer with respect to electrochemical phenomena on a 9 cm²-cell. Liu et al. [78] introduced a simpler approach for large scale fuel cell stack simulation, and applied it on a six 8 cm^2-cells stack. From a general point of view, the simulated temperature

distribution inside the cell in those papers was mainly governed by the local heat source and current density distribution. However, the temperature distribution also depends on the local heat removal rate, controlled by heat transfer rate with the coolant. Inoue et al. [79-80] developed a more complete two-phase model with simplified fluid dynamics equations on a 225 cm² cell using a simplified geometry. That model is powerful for optimizing the flow pattern of reactant gases and cooling water, in order to make the relative humidity as uniform as possible. A summary of these works on non-isothermal modeling of transport phenomena in the cell with the principal observations is presented below in Table I.2. The great differences between the models is the decomposition of the cell layers, the resolution or not of heat transfer in the coolant, the consideration or not of liquid/vapor phase change, and the boundary conditions considered.

Author	Scale	Dimension	Resolution of Heat transport in the coolant	Phases	Observations
Weber et al. [15]	Channel	1D	No	Two	Highlight of heat pipe effect in the cell
Djilali and Lu [61]	Channel	1D	No	Two	1 - 5°C temperature difference along the thickness of the cell
Pharoah et al. [62]	Channel / rib	1D	No	Two	The catalyst layer temperature is 3-6°C higher than the bipolar plate temperature at 1A/cm^2
Park et al. [63]	20-cell stack	1D	Yes	Two	Transient behavior of the cells temperature
Fuller et al. [28]	Channel	1D	No	Single	Effect of heat removal rate on operation
Birgersson et al. [67]	Channel	2D	No	Two	~9°C temperature difference across the cell at 1A/cm^2
Hwang [77]	Channel	2D	No	Single	Novel approach for resolution of solid phase and fluid phase temperature in the MEA
Siegel C. [66]	Channel /rib	2D	No	Single /Two	One-phase models always overpredicts the fluid temperature and local hot spot position depends on the heat transfer coefficient
Jung et al. [68]	Channel	2D	No	Two	Investigation of the effect of membrane thickness on temperature distribution: increasing Nafion thickness results in more heat accumulation in cathode
Basu et al. [69]	Channel	2D	No	Two	Phase change and heat pipe effect are strictly linked to local heat transport phenomena, which can vary widely depending on the position of the gases and cooling water inlets
Inoue et al.[79][80]	225 cm^2 Cell	2D	Yes	Two	Optimization of flow pattern of gas and cooling water that make the relative humidity higher and more uniform
Shan et al. [70]	2 cell stack	2D	Yes	Single	Dynamic distribution of temperature
Shimpalee et al.[71]	Channel	3D	No	Two	Impact of heat transfer consideration on performance prediction
Ju et al. [72]	Channel	3D	No	Single	GDL thermal conductivity plays an important role in coupled thermal and water management
Wang et al. [73]	Channel	3D	No	Two	Phase change could amount to 15–18% of total heat generation
Nguyen et al. [74]	Cell segment	3D	Yes	Single	The temperature is highly dependent on the loading conditions and the temperature difference across the cell rises from 4 to 7°C when the current density is changed from 0.3 to 1.2 A/cm^2
Su et al. [75]	5.29m^2	3D	No	Two	CFD simulation and validation with the use of micro-sensors

	Cell				
Le et al. [76]	Cell	3D	No	Two	Focus on liquid water transport and its effects on temperature distribution
Hwang et al. [77]	Cell	3D	No	Single	Investigation of lag in heat transfer with respect to electrochemical phenomena
Liu et al.[78]	Six 8cm^2 cell stack	3D	Yes	Two	Simpler approach for large scale fuel cell stack simulation

Table I.2 : Summary of the works on non-isothermal modeling of transport phenomena in the cell

5.5.   Review of the correlation between local parameters and degradation

Recently, a large number of studies has been conducted in order to study PEMFCs degradation with different approaches. Some of them are developed at the atomistic scale in order to understand the fundamentals of degradation mechanisms [81]. Other studies use macroscopic approaches by relating the operating conditions to global performance loss [82-83]. C. Robin et al. [84] introduced an efficient method to study the impact of local conditions on degradation by coupling performance models developed at the cell scale with degradation models developed at lower scales. J. Pauchet et al. [85] developed an innovative numerical method which couples a rule-based model and a performance model for the study of the impact of single component degradation on performance. Regarding experimentation, printed circuit boards can be useful to study the degradation heterogeneities [44-45] while the use of segmented cells [86] can also be efficient for understanding the local ageing conditions within the cell.[29] *Post-mortem* analyses of the aged components give also further information on the structure/properties of the different components for a better understanding of the degradations phenomena and their impact on the performances [87-88].

Pei et al. [89] reviewed the main factors influencing PEMFC degradation in automotive related conditions. It seems that coupled heat and water management is a probable driving force for many degradation mechanisms of membrane, catalyst layers, bipolar plates and gas diffusion layers. The review of the different degradation mechanisms of the cell components is presented in the following.

a) Membrane

The most common degradations of the membrane [90-91] can be classified in:

➢ *Chemical degradation.* It is due to chemical reactions of the membrane with species such as free radicals [92]. According to Sethuraman et al. [93], increasing the cell temperature leads to an acceleration of the membrane chemical degradation, which can be quantified in terms of fluorine release rate (FRR) or sulfur emission rate (see Fig.I.30). The measurements of the FRR is a good indicator for both the degradation state and the expected life of the membrane [94].
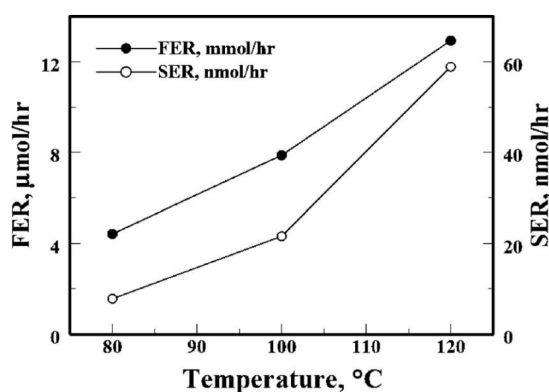
Figure I.30 : Total average fluorine and sulfur emission rates for a Nafion 112 membrane during OCV decay as a function of temperature [93]

➢ *Mechanical degradation.* There are membrane delaminations or fractures caused by fatigue stresses due to temperature and/or humidity cycling. Indeed, water is necessary for ion conduction, but a direct consequence of the Nafion hydration is swelling. Moreover, PTFE is a thermoplastic material which can suffer from temperature heterogeneities.

➢ *Shorting.* It is the local permeation to electrons, caused by a local overcompression and or creep of the membrane into the catalyst layers.

Since the membrane endures high hygrothermal stresses, some authors focused their studies on the impact of humidity cycling on membrane degradation [95-101]. According to Zhang et al. [102], a simultaneous coupling of high temperatures and low humidity values significantly accelerate the membrane degradation.

b) Catalyst layers

The catalyst layers ageing is usually quantified in terms of the remaining Electrochemically Active Surface Area (ECSA) because the main degradation mechanisms are the platinum dissolution and the carbon support corrosion. Bi et al. [103] studied the effect of temperature

(40-60-80°C) on platinum carbon (Pt/C) catalyst durability using potential cycling tests. They observed that increasing temperature results in higher degradations of the Pt catalyst ECSA and higher Pt deposition in the membrane. The obtained dissolution rate at different temperatures is presented in Fig.I.31.
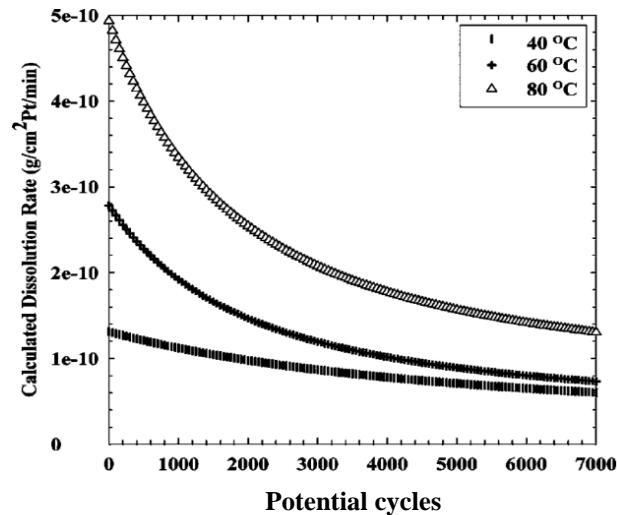
Figure I.31: Calculated Pt dissolution rate as a function of the potential cycles at different temperatures [103]

According to Dam et al. [104], the platinum dissolution rate strongly depends on both temperature and voltage as presented in Fig.I.32.
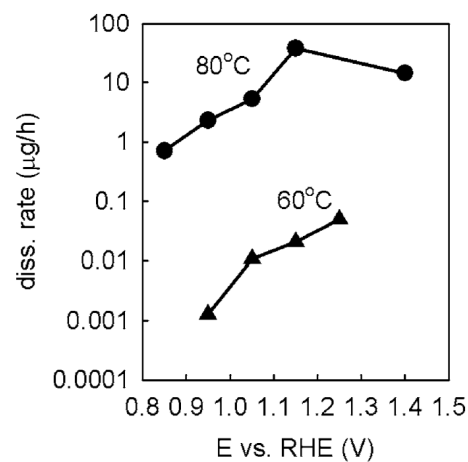
Figure I.32: Pt dissolution rate as a function of the potential, at different temperatures [104]

Borup et al. [105] conducted detailed studies of PEMFC electrocatalyst degradation and concluded that:

- The rate of ECSA loss increases with increasing temperature;
- Increasing the relative humidity induces at the same time an increase of the ECSA loss and a decrease of the carbon support corrosion.

c) Gas diffusion layers

The main degradation mechanisms of the diffusion layers are the hydrophobicity loss which induces changes in wetting behavior and changes in structure due to mechanical stress and carbon fibers corrosion. Mukundan et al. [106] studied the wetting behavior of GDLs aged at 80 and 95°C and concluded that the GDL hydrophobicity significantly decreases when the operating temperature is increased. Comparing *in-situ* the behavior the fresh and aged GDLs, they also observed that the new GDL performance increases with increasing the RH while the aged GDL performance decreases with increasing RH.

d) Bipolar plates

Regarding the bipolar plates, the main degradations listed in literature are corrosion, and deposits of corrosion products [107-111]. It is well known that corrosion increases with both temperature and humidity. Moreover, corrosion currents are higher at the anode compartment due to the acidity of the environment. However, it is observed that a passive layer, which stabilizes the corrosion current, can be developed on the BP surface [110]. Another effect of temperature on BPs degradation can be the large difference in the coefficient of thermal expansion (CTE) between the base metal of the BP and the coating material under the rib. It may induce thermomechanical failure in the hot zones by separation, microcracks and pinholes [112].

Conclusion

Fuel Cells are considered to be a viable solution for mitigating energy and environmental issues of the 21st century. Among the different types of fuel cells, Proton Exchange Membrane Fuel Cells (PEMFCs) are the focus of many works, especially for automotive application thanks to the advantages of good efficiency, excellent dynamics and high power density. However, heat and water management remain a global challenge for their development and commercialization.

Experimental methods can be very useful to study temperature and water distribution in the cell, but they are limited by the high cost and invasiveness of the measurement techniques. The most convenient technique for local measurements in this study appears to be the use of printed circuit boards because of their good resolution and accuracy while maintaining a relatively low invasiveness compared to the other existing technologies. Indeed, the other measurement devices presented above (resistive temperature detectors, fiber bragg grating sensors, bandgap temperature sensors, etc.) interact with the reactive environment and can significantly affect the results. The measurements of the printed circuit boards can also be used to validate models developed at the cell scale. The step between the existing models in literature and this study should be the development of a thermo-fluidic model, with the resolution at the same time of the heat sources and cooling water heterogeneities. The great challenge for this model is to find the best tradeoff between the dimensionality used to describe the model, the accuracy of the physics phenomena description and the computational scale. Ideally, the model should be developed at the cell scale, in order to capture all the global heterogeneities of the fuel cell components. Moreover, the model should allow the prediction of temperature, humidity and related parameters in each component of the cell.

Regarding the effects of local temperature on degradations, a first observation is that in PEMFCs, either temperature or water distribution are supposed to be driving forces for many degradation mechanisms, even if the coupling between local temperature, humidity and degradations remains a great challenge.

Chapter II

EXPERIMENTAL: METHODS AND TECHNIQUES

Summary

Introduction

In the previous chapter, the experimental techniques used to investigate local temperature in PEMFCs have been reviewed and printed circuit boards appeared to be the most adapted for this study. In this chapter, the methodology and experimental techniques used for the studies of temperature distribution and its impact on degradations are presented. First, the reference stack design and technology used is the study is presented with a detailed description of the single components of each cell. After that, the experimental test bench and control system is briefly described, as well as the different degradation tests performed in section 3. In section 4, the measurement and electrochemical characterization methods used to study the temperature distribution as well as global and local performance losses are presented. In the last section, the *post-mortem* analysis methods and devices used to study the degradation of each fuel cell component are illustrated.

1. Presentation of the stack design and technology

The studied stacks are composed of several cells with an active area of 220 cm^2, electrically connected in series. Each cell consists of one Membrane Electrode Assembly (MEA) where the electrochemical reactions take place and one metallic bipolar plate (BP). The configuration of a single cell is illustrated in Fig.II.1, with the main flow patterns of the reactive gases.
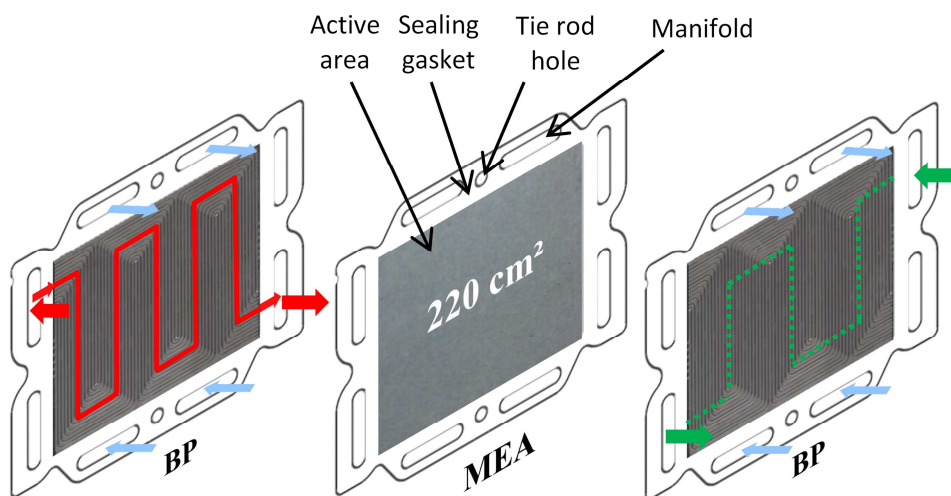
Figure II.1: Main components of each cell with the reactive gases main flow patterns. The red, green and blue colors are respectively related to hydrogen, air and cooling water

The cells are stacked between two end-plates designed to apply a homogeneous mechanical pressure of approximately 1 MPa at the interface between the MEA and the BP, and a localized pressure on the sealing gaskets to ensure the gas tightness of each circuit. The stack is assembled with tie-rod and nuts, then its leak tightness is validated and finally it is connected to the test bench.

1.1. Membrane Electrode Assemblies

A single MEA (CEA home-made) consists of a Nafion reinforced Proton Exchange Membrane (PEM), sandwiched between the anode and cathode Catalyst Layers (aCL and cCL), two MicroPorous Layers (MPL), and two Gas Diffusion Layers (GDL). The detailed description of the MEA components is presented in Tab.II.1.

Component	Thickness (μm)	Characteristics
PEM	25	Nafion, PTFE reinforced
aCL	6	Carbon supported Pt catalyst with 0.1 mgPt/cm^2
cCL	12	Carbon supported Pt-Co catalyst with 0.4 mgPt/cm^2
MPL	50	Carbon black powder (Sigracet)
GDL	246	Carbon paper GDL 24 BC (Sigracet)

Table II.1: Description of the MEA components

1.2. Bipolar Plates

The bipolar plate used in this study has a CEA homemade design, called "F" (see Fig.II.1), with multi-pass serpentine flow fields.

a) Material

The anode and cathode plates (aBP and cBP) are made of Stainless Steel 316 L Ni – Cr alloy. Its chemical composition is presented in Tab.II.2. In general, metallic bipolar plates have good advantages in fuel cell application like good electrical and thermal conductivities, the good mechanical stability, and the ease of manufacturing.

Chemical Element	Fe	Cr	Ni	Mo	Mn	Si	C	P	S	Nb
Percentage (wt%)	68.39	16.5	10.5	2.27	1.9	0.38	0.02	0.02	0.01	0.01

Table II.2: Detailed composition (mass fraction) of the stainless steel 316L used for the BP

The anode and cathode plates are stamped separately. Then, they are welded together to form the bipolar plate (see Fig.II.2) and coated in order to improve the electrical contact with the GDL, without worsening the corrosion resistance.
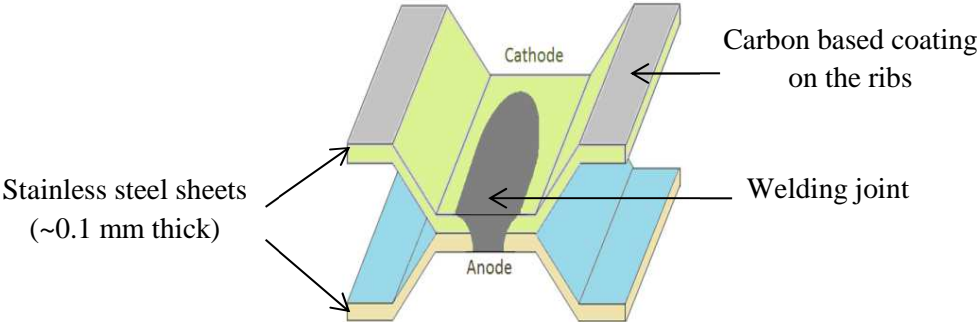
Figure II.2: Illustration of the bipolar plate elements at a channel/rib scale

b) Flow-fields design

The reactive gases flow field of the bipolar plates is multi-pass serpentine flow field (MPSFF) design with a different number of channels on both sides of the plate (Fig. II.3.a). In particular, there are:

- ➤ 12 channels doing 5-pass flow fields in the anode plate;
- ➤ 20 channels doing 3-pass flow fields in the cathode plate;
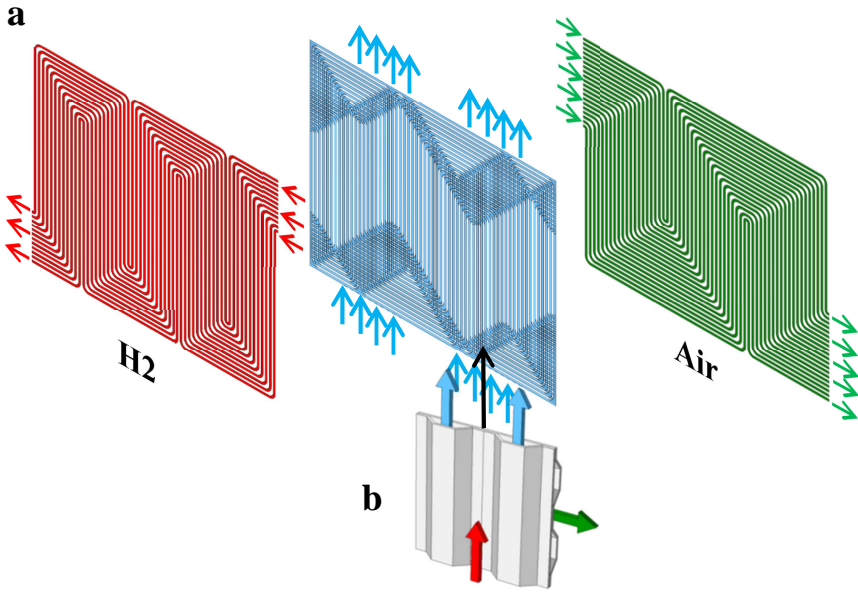
Figure II.3: (a) Presentation of the hydrogen, cooling water and air flow field designs

(b) Zoom of the BP geometry in a cross-flow zone

The cooling flow field is the resulting network between the two metallic sheets of the bipolar plate (see Fig. II.3.b). Thus, no additional cooling plate is needed.

c) Channels geometry

The gas channels section is trapezoidal due to design constraints of the flow field plates and liquid water drainage purposes. The resulting flow of the cooling water, at the back-side of the BP, has a hexagonal section in the parallel zones and a trapezoidal section in the cross-flow zones (Fig.II.4).
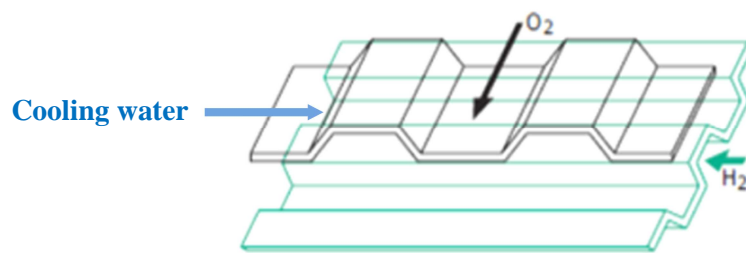
Figure II.4: Illustration of the channels design in a cross-flow zone

2. Presentation of the experimental bench

The test bench, presented in Fig.II.5, is designed to provide a management of the operating conditions, which are:

- The pressure of the reactive gases;
- The temperature of the cell;
- The relative humidity (RH) of the reactive gases;
- The stoichiometric coefficient, defined as the ratio of the supplied flow rate and the consumption flow rate of the reactive gases in the cell.

Figure II.5: Presentation of an experimental test bench

For the reactants, the main important parameters controlled with the experimental apparatus are the feed flows, the humidity, the pressure and the temperature. Their mass flow rate is fixed by the total current imposed in order to respect the stoichiometric coefficient set-point. The coolant used on the test bench is deionized water. The controlled parameters for the cooling circuit are the water mass flow rate and the temperature at the stack outlet. The components of the flow field circuits of the test bench are presented in Fig.II.6.
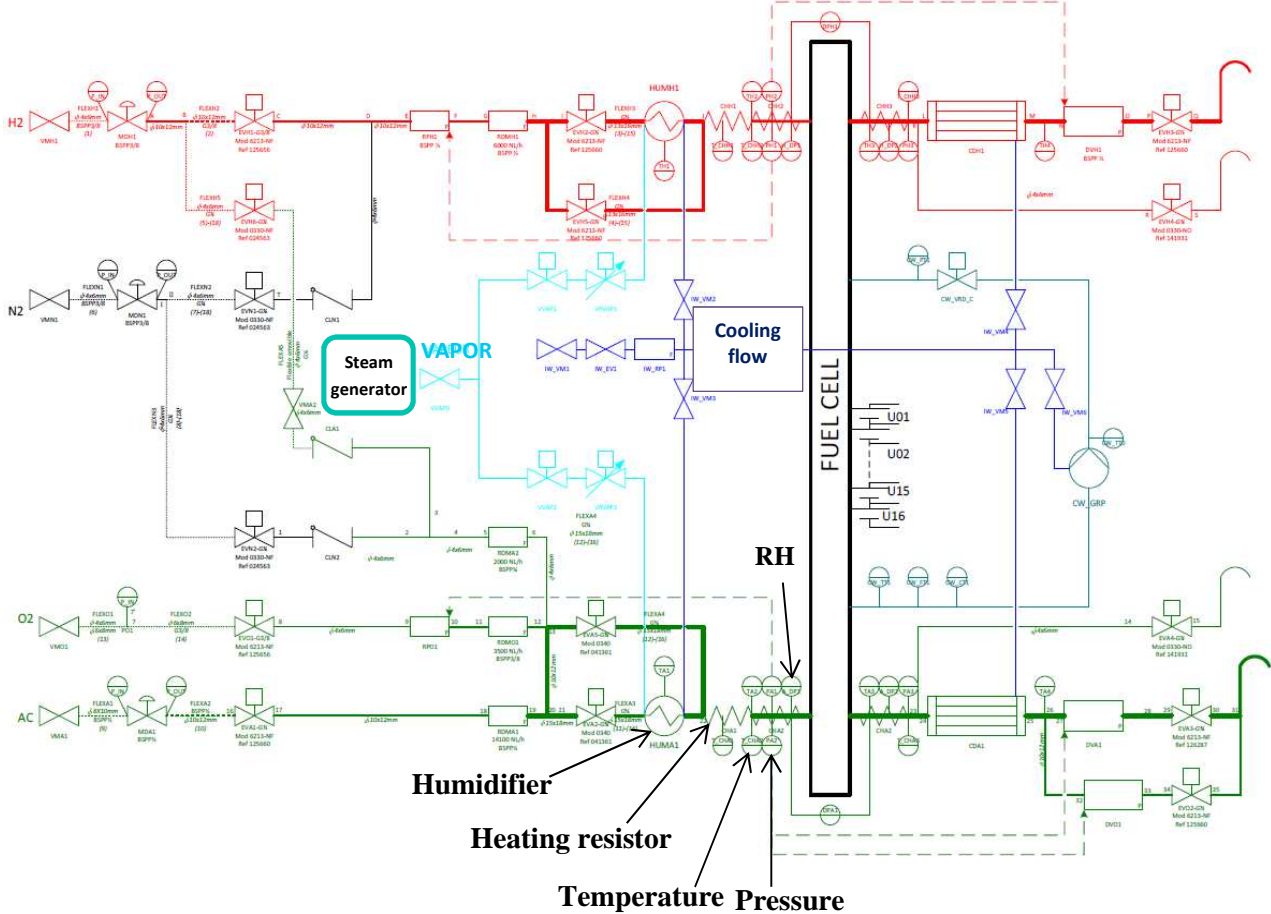
Figure II.6 : Fluid circuits of the laboratory test bench

A heating resistor is used in the reactant circuits at the stack inlet, after the reactive gases humidification, in order to avoid local water condensation in this zone. An electrical load, connected to the fuel cell current collectors, is used to monitor the total current setpoint. The laboratory test bench and its auxiliaries have a sufficient dynamic response for reproducing the cycling tests (which are presented below) in terms of pressure, relative humidity, cooling flow and current variations. However, there are some limitations in temperature variation rate due the limitations of the cooling system.

3. Ageing tests

The targeted ageing tests have to reproduce the local conditions occurring in an automotive fuel cell. From a thermal point of view, there are different typologies of stress:

➢ Thermal stresses under nominal operating conditions due to the history of local temperature (and humidity), even if the conditions are stationary. In addition, spatial heterogeneities in the MEA induce non-uniform stresses.

➢ Thermal effects due to high and/or rapid temperature variations induced by peaks in power demand, due to elevated accelerations of the vehicle, for example;

➢ Thermal effects due to humidity cycling between urban driving conditions (high humidity level) and highway driving conditions (dry conditions). Indeed, in highway driving, the combined effects of high temperature (due the radiator heat exchange limitations), high air flow rate (due to the high current) and low water vapor supplying (due to the humidifier limitations) induce dry operating conditions in the fuel cell;

➢ Occasional thermal stresses due to cold-starts at subzero temperatures leading to ice formation and growth in the fuel cell as described by Yan et al. [113]. Additionally, freeze/thaw cycles can induce significant degradations [100] [114] and many researches are underway on the topic. These conditions are of paramount importance for fuel cell vehicles, but are beyond the scope of this study.

This work focuses on reference operating conditions (around 80°C) of light-duty vehicles considering usual dynamic loads, cooling strategies and the fuel cell system constraints and limitations. Typically, there are different profiles of the dynamic load for light-duty vehicles depending on the country, the lifestyle and the vehicle performance. The commonly used are:

• The *New European Driving Cycle* (NEDC) which is a highly modeled cycle, adapted by the Motor Vehicle Emissions Group. It is commonly used in the area of fuel cell vehicles. It considers the driving cycle as a combination between an urban cycle and an extra-urban cycle with constant speeds, accelerations and decelerations. The main advantages of this cycle are its reproducibility and its repeatability. However, it suffers some criticism for not considering the real accelerations of a light-duty vehicle.

• The *Worldwide harmonized Light duty driving Test Cycle* (WLTC) which was designed from a statistical database provided by different countries all over the world, in order to determine the energy consumption and the greenhouse gases emission. It is more recent and more realistic than the NEDC.

The global durability tests used to study the thermal effects should be chosen bearing in mind at the same time the application, the need of isolating the root effect of each type of thermal loads (spatial heterogeneities, temporal heterogeneities, temperature/RH cycling) on degradations and the available timeframe for the experimental tests. The reference tests chosen for this purpose are listed in the following.

3.1. Test 1 - Nominal operating conditions (stationary)

The experiment consists of a stationary test over 2000 h in nominal operating conditions (0.4 A/cm², 80°C). The reference conditions of the ageing test are reported in Tab.II.3.

Experimental parameter		Setpoint
Current [A]		88 (0.4 A/cm²)
Outlet temperature cooling water [°C]		80
Inlet temperature reactant gases [°C]		85
Inlet pressure [bar]		1.3
Inlet relative humidity [%]	Hydrogen	50
	Air	30
Stoichiometric coefficient	Hydrogen	1.5
	Air	1.8

Table II.3: Reference conditions of the stationary ageing test

3.2. Test 2 - NEDC/RH cycling

The reference NEDC, which represents the evolution of the vehicle velocity over 1200 s, is presented in Fig.II.7. The NEDC was preferred to the WLTC because there is more database in literature concerning this cycle [44][115]. The firsts 800 s of the cycle repeat four low velocity urban cycles. The remaining 400 s represent a controlled-access highway driving with higher velocities.
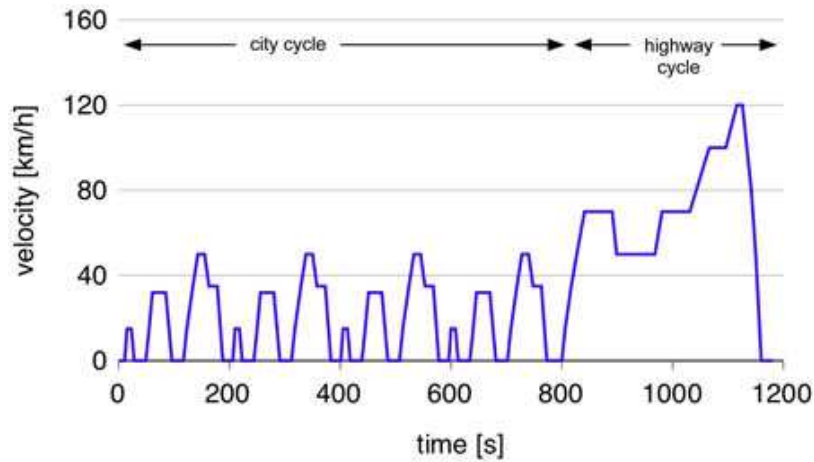
Figure II.7 : Reference NEDC cycle

In order to facilitate the control of the cycle, the reference NEDC speed cycle was adapted to a current cycle with different current steps as illustrated in Fig.II.8. This current cycle adaptation induces a squaring of the pulses and some loss of accuracy regarding the real dynamic loads of an automotive fuel cell, but it is commonly used in the area of automotive fuel cells [44][115].
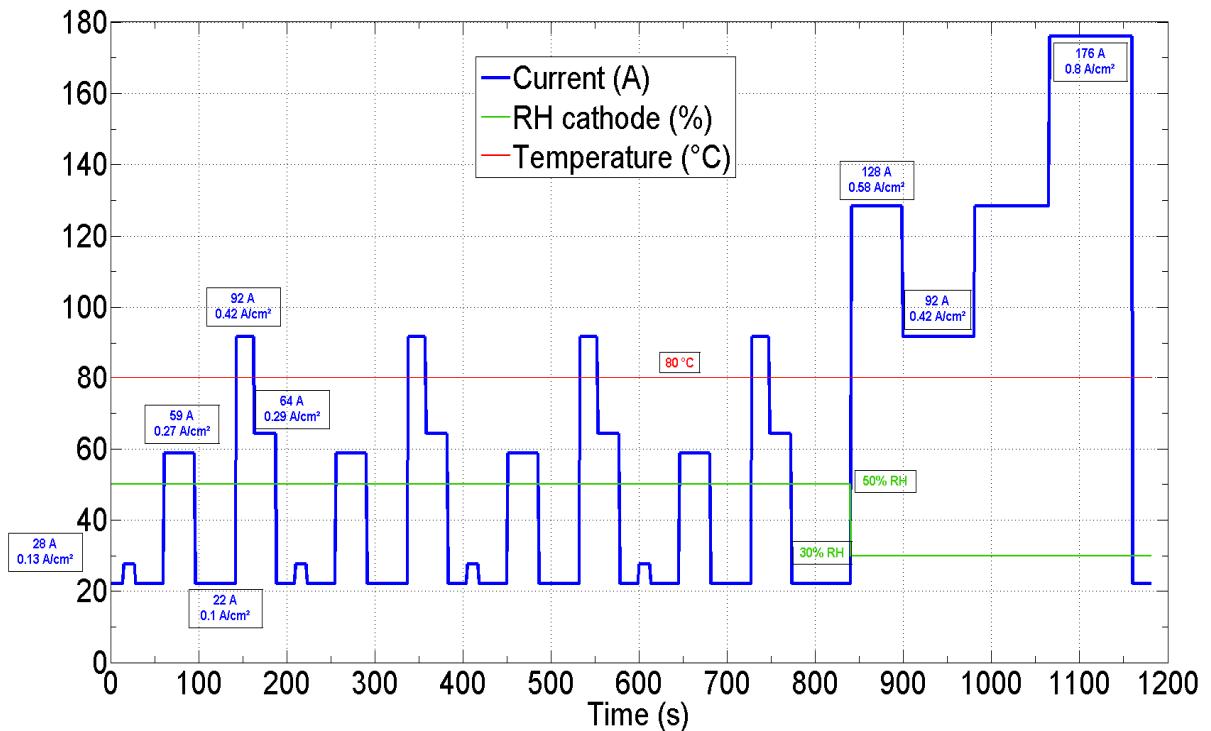
Figure II.8 : Adapted NEDC cycle

In order to take into account the humidifying system limitation at high currents, a lower RH (30% instead of 50%) is imposed during the controlled-access highway driving part of the cycle. The others parameters of the NEDC/RH cycling are the same as for the stationary test.

3.3. Test 3: Load/temperature cycling

The cycle simulates peaks in power demand (local accelerations) in automotive conditions. This operating condition induce quite huge heat source peaks located in the MEA and consequently a temperature increase with an evolution which depends on the heat capacity of the cell and the efficiency of the cooling system. To simulate this thermal behavior, a temperature increase from 80 to 95°C is imposed at the cooling water outlet, while the current density simultaneously changes from 0.5 to 0.77 A/cm² (see Fig.II.9). The period of the load/thermal cycles (~ 8 min) was limited by the test bench cooling system.
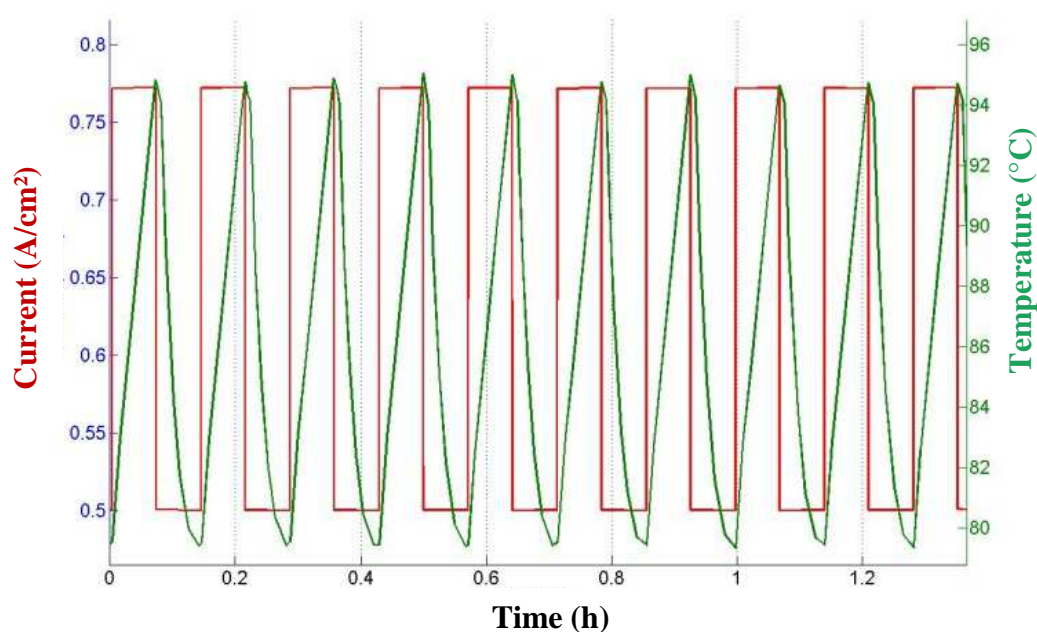
Figure II.9 : Imposed current and temperature during the load/temperature cycling

For comparison, the operating conditions of the three reference ageing tests are summarized in Tab.II.4.
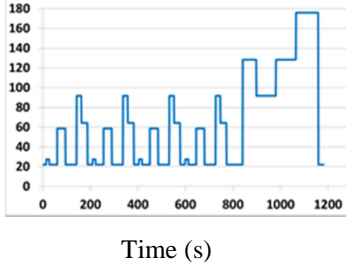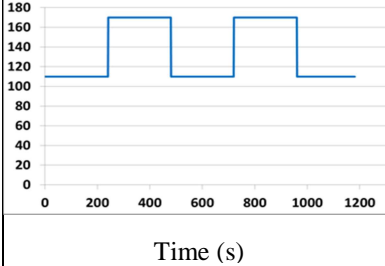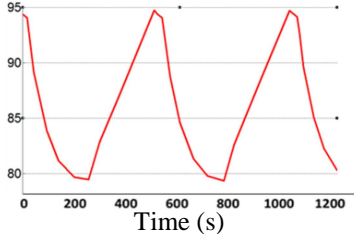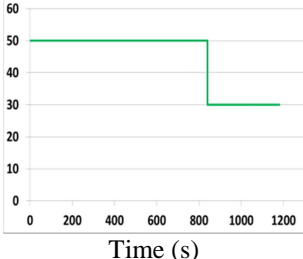
Experimental parameters	Stationary	NEDC/RH cycling	Load/thermal cycling
Number of cells	30	30	19
Duration	2000 h	~2000 h (6034 cycles)	~200 h (1500 cycles)
Current [A]	88 A (0.4 A/cm²)	Time (s)	Time (s)
Outlet temperature cooling water [°C]	80	80	Time (s)
RH Anode [%]	50	50	50
RH Cathode [%]	30	Time (s)	50
Inlet pressure [bar]	1.3	1.3	1.5
Stoichiometric coef. H_2	1.5	1.5	1.5
Stoichiometric coef. O_2	1.8	1.8	2

Table II.4: Operating conditions of the three reference ageing tests

It is worth noting that the maximal powers of the fuel cells stacks considered in the study (~ 3 kW) are not of the same order of magnitude as usual automotive fuel cells (~ 100 kW). The main difference between large-scale stacks (~ 500 cells) and laboratory-scale stacks (~5 cells) is the buckling phenomena after the assembly phase which can induce uneven

distributions of mechanical pressure on the active area. Carral et al. [116] demonstrated that for production-scale cells, increasing the number of cells enhance the uniformity of the mechanical pressure and 5 cells are sufficient to obtain negligible effects of buckling phenomena. So the numbers of cells used in this study (30 and 19) are sufficient to represent the real heterogeneities occurring in a large-scale stack.

4. Continuous diagnosis methods

A proper diagnostic protocol has been defined in order to observe the degradations and identify the main causes of performance loss. Nowadays, numerous diagnostic techniques are commonly used in PEM fuel cells area with the objective of isolating the root causes of degradation: I-V characteristics curves, Voltammetry, Electrochemical Impedance spectroscopy (EIS), Fluoride Release Rate (FRR), electrochemical heat pump, current interruption, high frequency resistance measurement (HFR), Tafel slope measurement etc. The methodology as well as the diagnostic techniques used specifically in this study could be summarized as:

➢ Punctual "*in-situ*" characterizations of the stack performance using polarization curves, cyclic voltammetry and linear sweep voltammetry;

➢ Punctual "*in-situ*" measurements of the Fluoride Release Rate for the study of the membrane chemical degradation;

➢ Continuous measurement of the temperature and current density distribution over the active area.

4.1. Global measurements

a) Polarization curves

The polarization curves are considered as the first step in studying the degradations and isolating the causes of performance loss. They are performed from the beginning to the end of test, in order to investigate the evolution of the global performance of the fuel cell. In most of the tests, the delay between the different polarization curves is 200 h, except for the load/thermal cycling in which the I-V curves were performed each 100 h. An example of polarization curves obtained for the stationary test is presented in Fig.II.10.
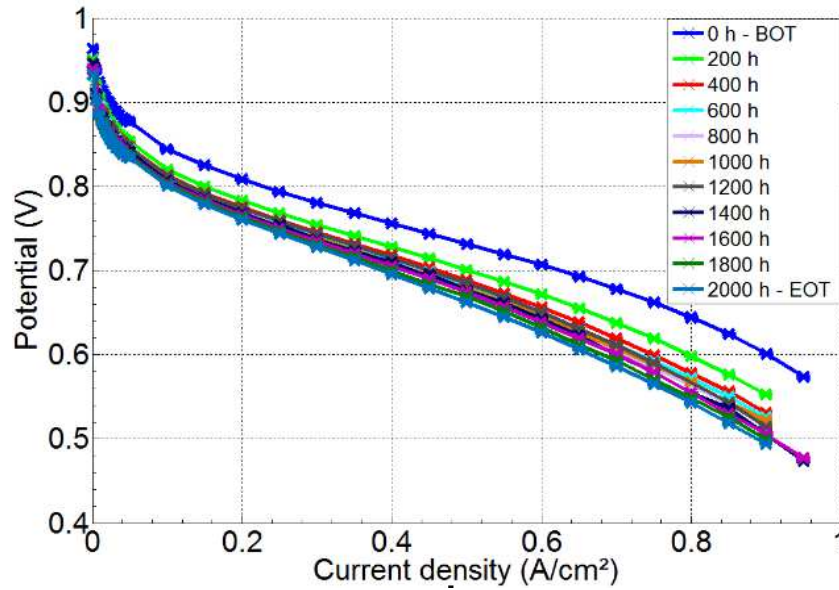
Figure II.10 : Example of polarization curves obtained for the stationary test

During the measurements, the current (*I*) is varies from ~ 198 A (~0.9 A/cm²) to 0 A, with 11 A steps when *I*>10 A (0.045A/cm²) and 1 A steps when *I*<10 A. The duration of each step is 2 min.

b)   Cyclic voltammetry (CV)

Cyclic voltammetry (CV) consists in determining the output current of an electrochemical system subject to a linear evolution of the cell potential between two values. Applied on a fuel cell, it is used to determine the electrochemical active surface area (ECSA). During this electrochemical characterization test, nitrogen flows over the working electrode (cathode) and hydrogen flows over the counter electrode (anode) which also works as the reference electrode. The voltage variation induces H_2 adsorption and desorption onto the catalyst layer interface. Thus, the cathode electrochemical active surface area can be determined. A potentiostat (Autolab) is used to apply the potential variation between the electrodes and a booster is used to provide an additional current range. The electrochemical active area can be calculated by integrating the current exchanged during the time under the peaks. The electroactive area of platinum particles (S) can be calculated as:

$$S = \frac{A}{v \, Q_{Pt}}$$

[II.1]

Where A is the area illustrated in the cyclic voltammogram (Fig.II.11); Q_{Pt} the hydrogen adsorption charge density (*C/cm²*) and v is the scanning speed.

66
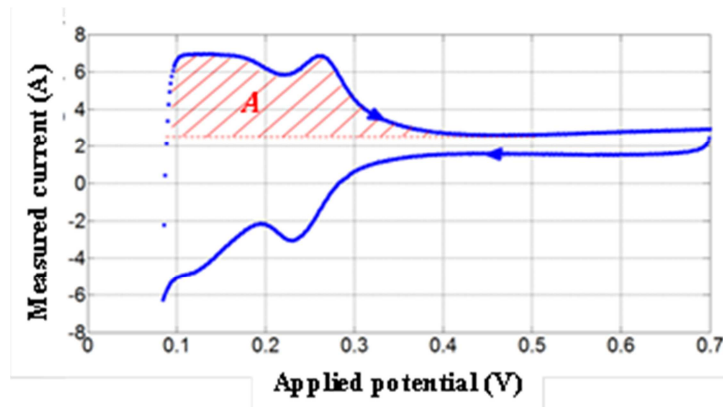
Figure II.11 : Current response of a cell under CV

The different peaks on the plots can add additional information like the charge-transfer reactions potential. During this electrochemical characterization test, three scanning speeds (v) are applied with 3 measurements for each speed in order to discard measurement dispersions.

However, the surface electrochemically active in the operating fuel cell is only the portion of that ECSA which is effectively accessible to reactive gases via the pores of the catalyst layers. There should be also a performance loss due to the anode electrochemical active area loss, but the main part of the platinum loss is generally located at the cathode due to the higher overpotentials. An example of the evolution of cyclic voltammograms from the beginning to the end of test (stationary test) is presented in Fig.II.12.
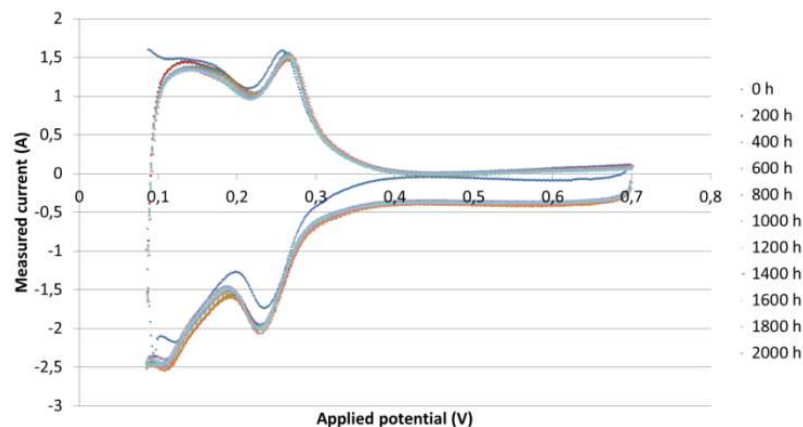
Figure II.12: Measured CV on a cell at different times

c)   Linear sweep voltammetry (LSV)

Linear sweep voltammetry (LSV) consists in applying a linear evolution of the potential to an electrochemical system between two values, and measuring the resulting current. Applied on

a fuel cell, it is used to study the evolution of the hydrogen permeation through the membrane. The measurement technique is almost the same as for the cyclic voltammetry, except the scanning velocity, which is sufficiently low in this case to allow the system stabilization. The quantity of hydrogen crossing the membrane is obtained from the expression:

$$Q_{H_2} = \frac{I}{2\,F\,S} \tag{II.2}$$

With I the mean value of the stabilized permeation current (indicated on the voltammogram of Fig.II.13). S the active are surface of the membrane (220 cm² in this study).
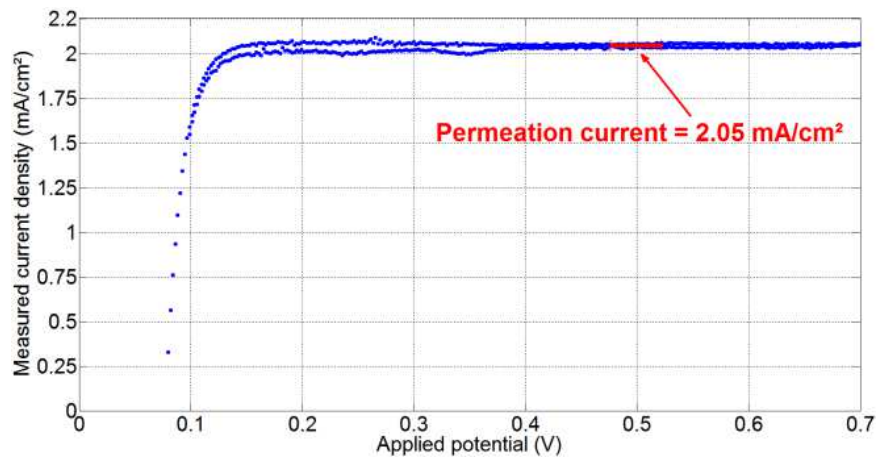
Figure II.13 : Current response of a cell under LSV

These LSV and CV characterizations are performed only on 6 different cells of each stack because of the high measuring time, which is about 30 min for each cell.

d)   Fluoride Release Rate

In order to investigate *in-situ,* the rate of the membrane chemical degradation, Fluoride Release Rate (FRR) measurements of the effluent water were performed every 200 h, by ion-exchange chromatography (*Thermo Scientific*[TM] *Dionex*[TM] *ion chromatography systems - ICS-5000+ HPIC*). It allows measuring the concentration of given anions (here F-) with a sensitivity about 50 ppb. The FRR (10^{-8}g/h/cm²) is calculated according to the mass flow rate of water collected at the outlet of the stack.

4.2.   Local measurements

a)   Presentation of the printed circuit board used in the study

Local *in-situ* diagnosis consisted of current density and temperature distributions measurements with a Current Scan Lin S++ sensor plate (see Fig.II.14). It is a custom-built segmented printed circuit board where the local current is measured using ring cores of a

magnetically soft material (ferrite). Because two ferrite ring cores are necessary for each measurement, the segments have a size of approximately 7 x 7 mm. Therefore, for a 220 cm^2 active surface, there are 480 measurement segments for current distribution.

Figure II.14 : Sensor plate out of the stack and inserted in the middle of the stack

➢ **Current measurement principle**

The current measurement principle is based upon the dependence of the permeability of a magnetically soft material (μ) on the magnetization H and the temperature T. As illustrated in Fig.II.14, the current I_m, which has to be measured, flows through the coil L$_1$ on a core made of magnetically soft material and causes its magnetization.
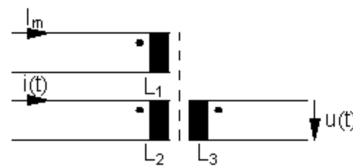
Figure II. 15 : Current measurement principle of the sensor plate

The magnetic field strength H depends upon the number of windings N and the magnetic length l:

$$H = \frac{I_m N}{l} \qquad \text{[II.3]}$$

A small alternating current $i(t)$ is generated through the coil L$_2$. This induces a voltage u (t) in the coil L$_3$ which is calculated with the formula:

$$u(t) = \mu(H, T, F)\, N^2 \frac{A}{l} \frac{di(t)}{dt} \qquad \text{[II.4]}$$

So the current I_m can be deduced from the induced voltage u(t) and compensated with the measured temperature since the permeability depends on temperature.

➢ **Temperature measurement principle**

The temperature measurement is based upon the dependence of the resistivity (R) of metals such as copper upon temperature (resistance temperature detectors):

$$R(T) = R(T_0)\,[1 + \alpha(T - T_0)]$$ [II.5]

with α the temperature coefficient of resistance and T_0 a reference temperature.

120 temperature sensors are embedded in the sensor plate to this end. There is a lower spatial resolution of the temperature measurement due to the limitations in space for the electronic circuit of the sensor plate. The precisions of the device are 0.02 A/cm² for the current density and 1 °C for temperature. The thickness of the sensor plate is mainly determined by the thickness of the ferrite ring cores and is approximately 3 mm. The apparatus, inserted between two monopolar plates in the middle of the stacks (in order to eliminate the side effects) is used to map simultaneously the temperature and current distributions in the cell. The specifications of the Current Scan Lin S++ device are summarized in Tab. II.5.

Current measurement	Range	$0 - 2.5$ A/cm^2
	Precision	0.02 A/cm²
	Measurement time	0.5 s for each 100 measurement segments
	Maximum current	3A/measurement segment
Temperature measurement	Range	Up to 180°C
	Precision	1°C
	Measurement time	2 s for each 100 measurement segments
	Maximum temperature	180°C

Table II.5: Specifications of the printed circuit board used for measurement

Examples of current and temperature map are illustrated in Fig.II.16. The local maxima observed on the current density distribution are induced by the welding points of the bipolar plates which are preferential paths for current flow. The hot zones observed on the temperature map are due to the heterogeneities of the cooling flow field. They will be studied in detail in the chapter dedicated to the thermal model.
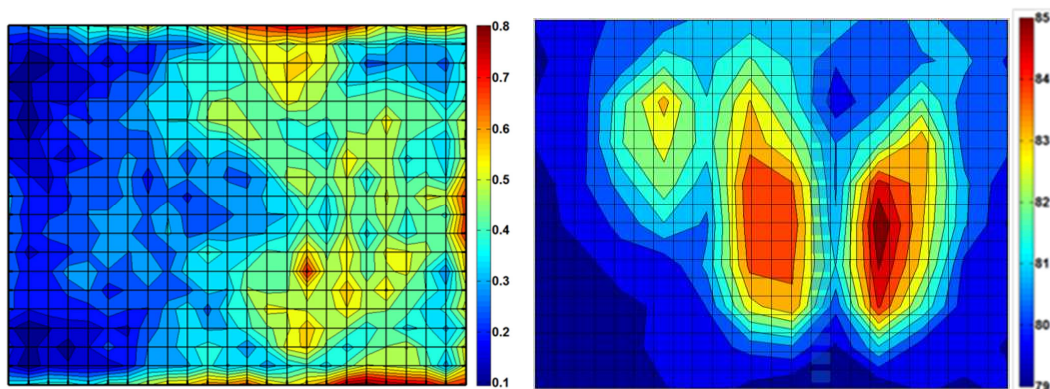
Figure II.16 : Examples of current density (A/cm²) and temperature (°C) distributions measured with the sensor plate

The measured current density needs a post-treatment since the contact between the measurements segments and the bipolar plate is not homogeneous.

b) Local data post-treatment

Given the Multi-pass serpentine flow field design of bipolar plates with curve corners, the contact area between the measurement segments of the sensor plate and the bipolar plate shoulders is not homogeneous at all as illustrated in Fig II.17.
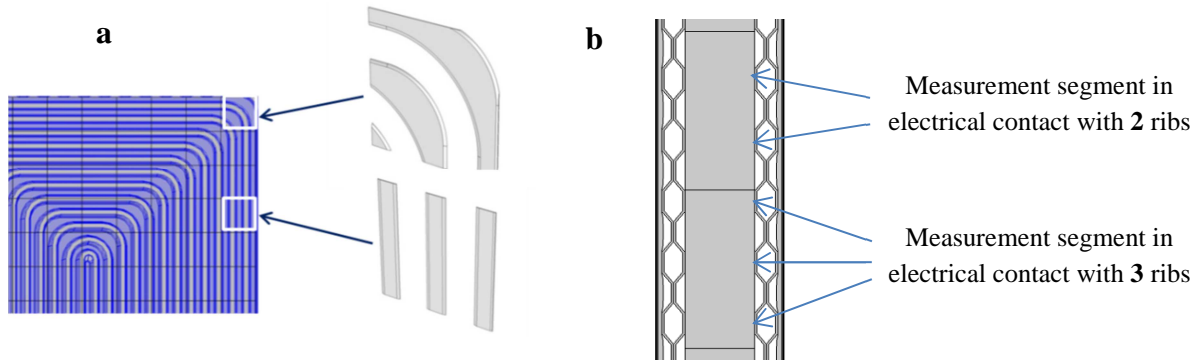
Figure II.17 : **(a) In-plane and (b) through-plane illustration of the heterogeneities of the contact area between the sensor plate segments and the bipolar plate ribs**

In order to take into account these contact area heterogeneities which can have a considerable impact on the current density distribution measurement, appropriate weighting factors inversely proportional to the contact areas are used in each segment as follows:

$$I_{mes}\,\overline{S} = I_{eff}\,S_{eff} \ \leftrightarrow \ I_{eff} = I_{mes}\,\frac{\overline{S}}{S_{eff}} = I_{mes}\,k \qquad [\text{II.6}]$$

Where I_{mes} and I_{eff} are respectively the measured and the effective current densities in each segment; $\overline{S}$ is the mean contact area between the BPs shoulders and each sensor plate segment; S_{eff} is the effective contact area between the BPs shoulders and the corresponding segment of the sensor plate. The weighting factors k, which consider the contact between the sensor plate and both the anode and cathode plate ribs (figure II.18) , varies from 0.75 to 1.25.
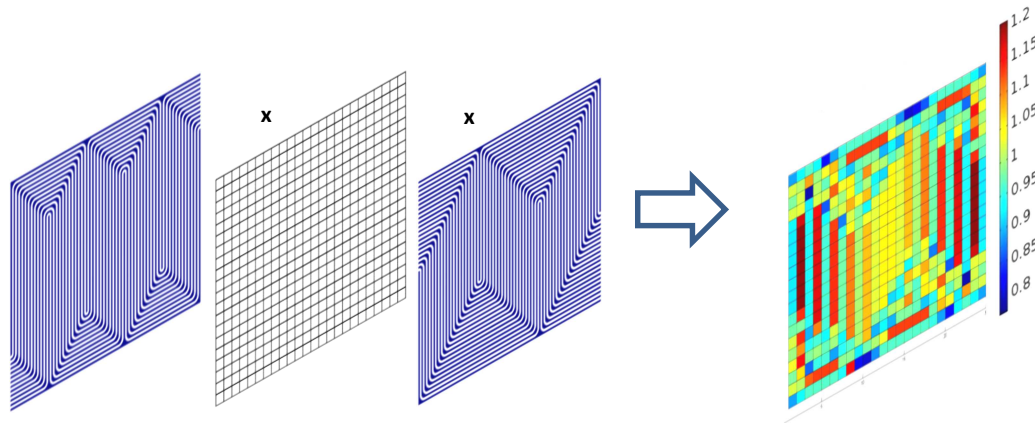
Figure II.18 : (a) Anode plate shoulders, scanning plate segmentation and cathode plate shoulders - (b) Post-treatment weighting factors matrix

As illustrated in Fig.II.19, the post-treatment of the current density using the weighting factors induces a smoothing of the current density distribution, even if the effect of welding points (local maxima on the post-treated current density) is still observed.
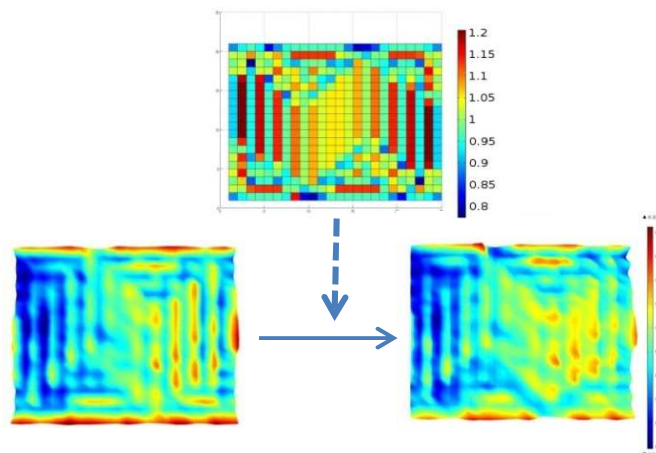
Figure II.19 : Effect of the post-treatment matrix on the current density distribution

c) Perturbations on the temperature measurement

The printed circuit board is sandwiched between two monopolar plates, replacing one MEA as indicated in Fig.II.17. As every plate contains a cooling circuit on the backside, the S++ temperature measurement is influenced by one additional cooling circuit. This configuration (Fig. II.20) may influence the absolute temperature measurement and its heterogeneity over the MEA surface. That induces a "double-cooling effect" and so a temperature heterogeneities smoothing with respect to the real heterogeneities along the active area. Moreover, given the relatively high thickness of the sensor plate with respect to the cell components (see Fig.II.20), there is a non-negligible heat exchanged between the sensor plate and the cooling water manifolds. As a consequence, the sensor plate is cooled on one side by the inlet cooling

water and heated on the other side by the outlet cooling water and that induces parasitic effects on the measurements.
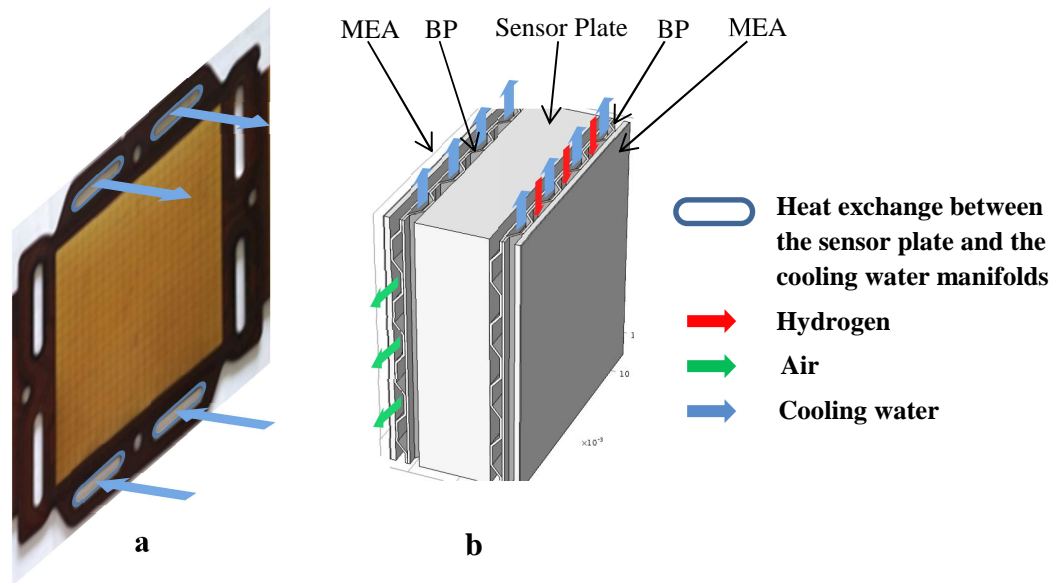
Figure II.20 : Illustration of: (a) the heat exchange between the sensor plate and the manifolds cooling water - (b) the double-cooling effect of the sensor plate sandwiched between two bipolar plates and two cooling circuits

The "double cooling effect" as well as the heat exchange with the cooling water flowing in the manifolds should be taken into account either during the interpretation of the temperature maps, or during the development of the thermal model.

5. *Post-mortem* analyses

The *post–mortem* analyses are used to study the degradation state and the change of atomic and molecular structure of the isolated components of the aged cells. The techniques and tools are defined depending on the information released by each technique, the characterization time and the cost while bearing in mind the necessity of linking the observed degradations to the physical root causes. To this end, the different techniques used in this study are: optical microscopy, X-ray photoelectron spectroscopy, scanning electron microscopy and Infrared camera.

5.1. Optical microscopy (OM)

Optical microscopy (*Digital microscope VHX 500-FE*) is used for the global analysis of the bipolar plates and membrane degradations at the cell scale. It is considered as the first step

before going toward the advanced characterization techniques. Examples of optical microscopy images are presented in Fig.II.21.
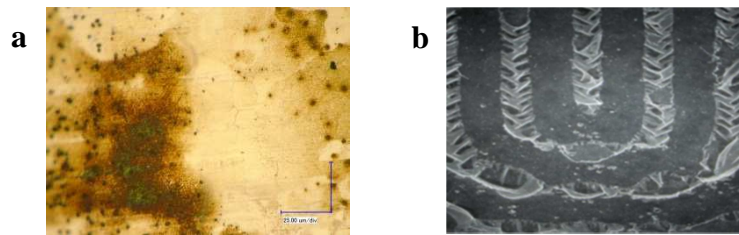
Figure II.21 : Visualization of (a) BP degradations and (b) membrane delamination using OM

5.2.   X-ray photoelectron spectroscopy (XPS)

X-ray photoelectron spectroscopy, sometimes named electron spectroscopy for chemical analysis (ESCA), is used for the local analysis of the chemical composition and state of oxidation of the bipolar plate surface. It consists in detecting the photoelectrons that are ejected from an inner-shell orbital of an atom by X-rays (see Fig.II.22).
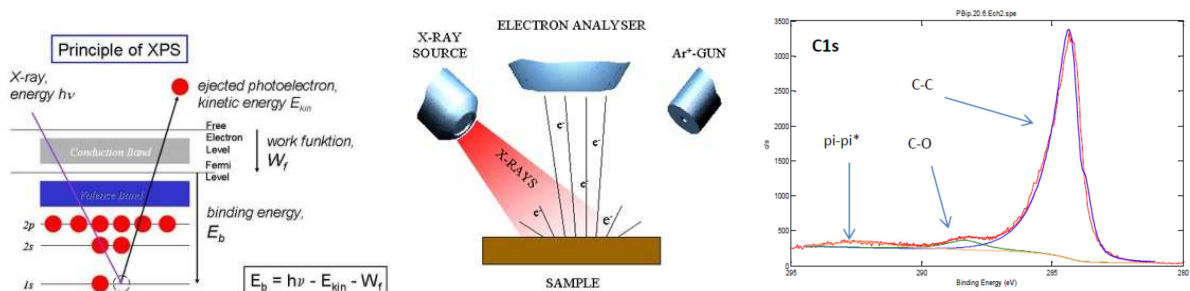
Figure II.22 : Principle of XPS, measurement system and example of a spectrum obtained on an aged BP

5.3.   Scanning Electron Microscopy (SEM)

Scanning Electron Microscopy (*SEM LEO, 40kV*) is used for a detailed study of the surface topography and microstructure of different components, from the bipolar plates to the MEA. It consists in making an interaction between a focus beam of electrons and the atoms that compose a region of the sample surface. The secondary electrons emitted back by the excited atoms reveal information about the morphology and microstructure of the sample. An example of SEM image of an aged MEA is presented in Fig.II.23.
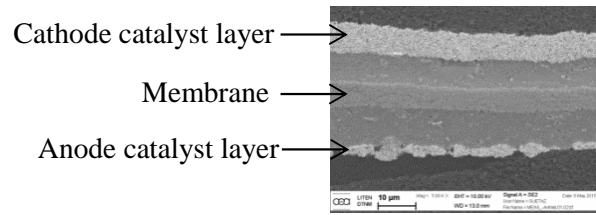
Figure II.23 : Example of SEM images obtained in back-scattered electrons on an aged MEA

5.4. Infrared (IR) Camera for local H$_2$ permeation

An IR camera (*FLIR® E-Series Advanced Thermal Imaging Camera*) is used to measure the temperature distribution over the active area of aged MEAs supplied by pressurized hydrogen (in a hydrogen box) on the frontside of the MEA, and ambient air on the backside. As the MEA permeation increases, more heat is generated over the MEA due to direct combustion of the reactants. Thus, observed variations in temperature distribution are related to changes in the rate of the reactants crossover through the MEA (Fig.II.24). This diagnostic tool is used to localize eventual pin-holes or local thinning of the membrane.
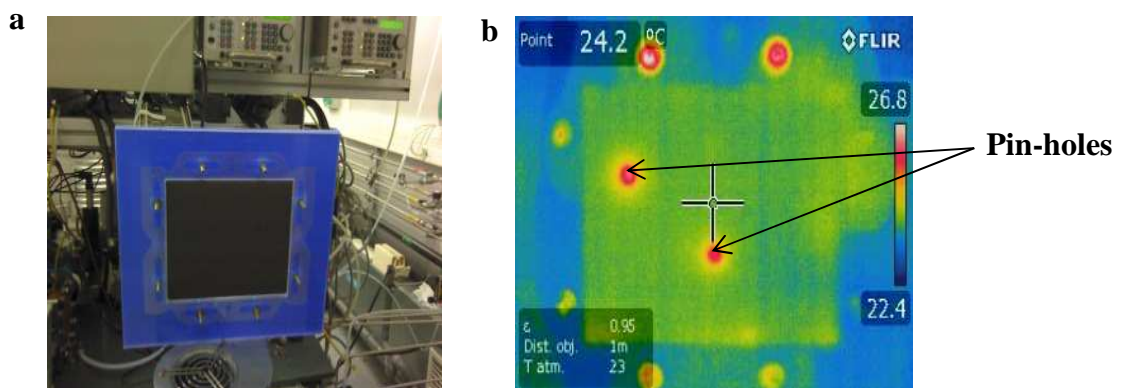
Figure II.24 : (a) MEA in the hydrogen box for the IR camera test

(b) IR image of a drilled MEA

Overview

The detailed ageing tests and diagnostics protocol used in the study are summarized in Tab.II.6.

Stationary	NEDC/RH cycling	Load/temperature cycling
30 cells	**30 cells**	**19 cells**

Stationary

Stack assembling

⬇

Conditioning

⬇

Beginning of Test

⬇

Characterizations: i-V, LSV, CV, S++

⬇

a | **200 h** ageing test, S++, FRR

⬇

b | Characterizations: i-V, LSV, CV, S++

⬇
⬇

Repeat **a** **b** x 9

⬇
⬇

End of Test

⬇

Stack disassembling

⬇

Post-mortem analyses : SEM, XPS, IR, OM

Load/temperature cycling

Stack assembling

⬇

Conditioning

⬇

Beginning of Test

⬇

Characterizations: i-V, LSV, CV, S++

⬇

100 h ageing test, S++, FRR

⬇

Characterizations: i-V, LSV, CV, S++

⬇

100 h ageing test, S++, FRR

⬇

Characterizations: i-V, LSV, CV, S++

⬇

End of Test

⬇

Stack disassembling

⬇

Post-mortem analyses : SEM, XPS, IR, OM

Table II.6: Overview of the ageing tests with the diagnostics protocol

Chapter III

A THERMAL MODEL TO INVESTIGATE LOCAL TEMPERATURE AND HEAT TRANSFER PHENOMENA IN P.E.M. FUEL CELLS

Summary

Introduction

In this work, a sensor plate is inserted between two monopolar plates of the stack in order to measure the temperature distribution over the cell area. Since this measurement device is limited to the investigation of the in-plane temperature distribution between two monopolar plates, through-plane temperature can be determined only via modeling. Modeling heat transport in a fuel cell is a multiphysics problem which involves the study of *in-situ* thermal properties of the cell components, computational fluid dynamics, thermodynamics of the electrochemical reactions and phase change. The different approaches used to solve this problem in literature were reviewed in Chapter I.

From a general point of view, the temperature distribution inside the cell is governed not only by the local heat source rate in the exothermic reaction zones and current density distribution, but also by the local heat removal rate, controlled by heat transfer rate in the coolant. Faghri and Guo [117] reviewed the thermal management issues related to fuel cell technology and modeling. They conclude that in order to optimize the components design and the thermal management of the fuel cells, 3D numerical analysis models are needed. Nevertheless, for large-scale fuel cells, full 3D simulations require high computational resources and appropriate fluid dynamics solvers. For this reason, 3D models are generally developed at the level of one single channel. In this chapter, a global 3D model is developed at the channel/rib scale in order to understand the exact temperature distribution in the cell and the associated channel/rib effects. The model is upscaled at the cell scale, with an appropriate dimensionality reduction in order to solve the tradeoff between accuracy and computational cost. The upscaled "pseudo-3D" model is validated using the temperature measured with the sensor plate inserted in the stack. In the following section, the thermal properties of the components, which are of fundamental importance in this study, are reviewed.

1. Thermal properties of the cell components

Understanding temperature distribution in PEM Fuel cells needs a deep and detailed analysis of the thermal properties (especially the thermal conductivity) of the MEA components and interfaces. Measured *ex-situ* data are useful for getting an idea of the thermal properties and their influence on an operating fuel cell. Nevertheless, these thermal properties can be very different during operation from those measured *ex-situ* due to local conditions (temperature, water content, local compression, etc.). So, local *in-situ* thermal properties are needed for an accurate study.

Many researchers focused on that challenge, especially via experimentation [118-120], even if some models can help making predictions in different operating conditions [121-122]. In the following, the impact of local conditions on thermal conductivity of every cell component is briefly reviewed for a proper definition of the model parameters.

1.1. Membrane

The membrane is a perfluorinated polymer backbone with sulphonic acid side chains for protons transport. Generally, for this type of thermoplastic material, the thermal conductivity varies with both temperature and water content.

a) Effect of temperature

It is commonly accepted that as the temperature increases, the thermal conductivity of the dry membrane decreases due to the phonon transport phenomena, as described by Choy et al. [123]. For dry Nafion, Khandelwal et al. [118] measured a decrease from 0.16 ± 0.03 to 0.13 ± 0.02 W/m/K when the temperature increases from 30°c to 65°C. With a linear extrapolation, they predicted a thermal conductivity of 0.11 ± 0.02 W/m/K at 80°C. These results are very similar to the results of Alhazmi et al. [120] who measured a decrease from 0.188 ± 0.015 to 0.135 ± 0.011 W/m/K when temperature changes from 35 to 65°C.

b) Effect of humidity

Water is necessary for the ionic conductivity of the Nafion. Water is supplied by humidifying the reactive gases and by using directly the water produced by the electrochemical reaction. When the Nafion is humidified, there is a separation between the hydrophobic backbone and the sulphonic acid groups, which are clustered in hydrophilic regions. This phenomenon strongly impacts on the thermal conductivity. In order to estimate it theoretically, Alhazmi et

al. [120] assumed that the wet membrane is a mixture of water, air, and membrane material. They observed that the thermal conductivity significantly increases as the membrane becomes wetter and explained it by the fact that thermal conductivity of water (0.66 W/m/K) is higher than the dry membrane one (0.18 W/m/K). They also noted that the thermal conductivity of a wet membrane slightly increases with increasing temperature: they observed an increase from 0.4 to 0.41 W/m/K when the temperature rises from 35 to 65°C. Burheim et al. [124] observed that the thermal conductivity of Nafion increases from 0.18 to 0.27 W/m/K when water content (λ_M) changes from 0 to 22. After exanimating experimentally its evolution as a function of the amount of water molecules per sulphonic acid group in the membrane (water content) using a conductivity meter, they proposed the law, which will be used in this study:

$$\lambda_{Nafion}\,[W/m/K] = (0.177 \pm 0.008) + (3.7 \pm 0.6) \cdot 10^{-3} \cdot \lambda_M \qquad \text{[III.1]}$$

1.2.   Catalyst layers

The catalyst layers are a mixture of carbon powder (~ 2 W/m/K), Nafion (~ 0.18 W/mK) and platinum particles (~ 71.6 W/m/K). So the thermal conductivity is supposed to increase when increasing platinum content. Alhazmi et al. [120] measured the thermal conductivity of the MEA in order to deduce the catalyst layer one. They concluded that it is almost independent of the temperature and is about 0.291 ± 0.018 W/m/K. It agrees with the measurements performed by Kandelwal et al. [118] who obtained 0.27 ± 0.05 W/m/K for a catalyst layer with catalyst loading around 0.5 mgPt/cm^2.

Standing to Burheim et al. [125], the thermal conductivity of catalyst layers containing water ranges from 0.10 to 0.15 W/m/K when the compaction pressure increases from 5 to 16 bars. In addition, they observed that the presence of the ionomer is supposed to increase the thermal conductivity as the catalyst layer absorbs water. For "supersaturated" catalyst layers, the thermal conductivity value can be expected to increase by 50%. The reference value of 0.15 W/m/K will be used in this study.

1.3.   Gas Diffusion Layer

The GDL is made of carbon fibers (diameter ~ 5-10 µm) pressed together into a paper. The in-plane orientation of the fibers makes it a highly anisotropic material. Different methods have been used in literature to predict its thermal conductivity [118][122][126]. In general, those studies agree that the through-plane thermal conductivity (W/m/K) are respectively

around 0.2 for ELAT GDL, 0.3-0.4 for Sigracet PTL and 0.3-0.8 for a Toray GDL. Regarding the in-plane conduction, Pfrang et al. [127] used X-ray computed tomography structure data as well as randomly computer-generated structures to compute the anisotropy of GDLs under different conditions. They concluded that the average in-plane thermal conductivity of all structures is by a factor 4 to 12 higher than the average through-plane thermal conductivity. They also presented in a table a comparison between 35 thermal conductivity predictions published in literature. Zamel et al. [128] used a slug calorimeter method to experimentally measure the through-plane thermal conductivity of Toray carbon paper for a temperature range from -50 to +120°C. They concluded that, due to the thermal expansion of the graphitized carbon fibers, the thermal conductivity increases with temperature. Given the operating temperatures of this study (between 78 and 100°C), it can be stated that the thermal conductivity of the GDLs is constant.

However, the microporous layer and the hydrophobic treatment, used to improve water management, greatly impact the *ex-situ* thermal properties of the GDL. The other parameters influencing *in-situ* thermal properties are the presence of liquid water in the pores and the inhomogeneous compression.

a)   Effect of PTFE content

In fuel cell application, in order to limit its wetting during operation, the GDL is treated with polytetrafluoroethylene (PTFE) also called Teflon, because of its hydrophobic properties. Owing to the low thermal conductivity of PTFE ($\sim 0.25\ W/m/K$), it insulates the carbon fibers (120 W/m/K) from each other, leading to a drop of the global thermal conductivity of the GDL.

Pfrang et al. [127] observed that the contact area between carbon fibers and the PTFE has a considerable effect on the thermal conductivity. According to Karimi et al. [119], the PTFE content influences more the GDL thermal conductivity at lower compression load. Khandelwal et al. [118] measured thermal conductivities of 0.48 ± 0.09, 0.31 ± 0.06 and 0.22 ± 0.04 W/m/K respectively when the PTFE content (wt.%) is 0, 5 and 20%. Sadeglifar et al. [122] proposed a statistically-based mechanistic model to predict the reduction of through-plane thermal conductivity of GDLs treated with PTFE.

b) Effect of MPL

The MPL, made of a mix of hydrophobic agents with black powder nanoparticles, is added between the GDL and the CL to improve water management and smooth the surface

heterogeneities of the GDL. According to Thomas et al. [129], temperature gradients across the MPL contribute to water transport and helps keeping the water in the MPL in the vapor phase.

Burheim et al. [130] measured the thermal conductivity of MPL at different pressures and PTFE contents and studied its impact on the temperature profile in the cell. They concluded that it can vary from 0.06 to 0.10 W/m/K depending especially on pressure. They also observed that the through-plane temperature difference significantly increases due to the MPL. So this component has to be considered for an accurate thermal modeling. Sadeghifar et al. [122] measured the thermal conductivity of SGL 24 BC MPL (which is used in this study) variations between 0.37 and 0.55 W/m/K depending on the compression.

c) Effect of humidity

The local humidity of the cell depends on water partial pressure and temperature. On the one hand, water partial pressure is supposed to be higher near the air outlet due to the production of water in the active layers. On the other hand, temperature is supposed to be higher near the coolant flow outlet. The coupling of both phenomena can induce high humidity variations in the cell. Moreover, at a more local scale, humidity is supposed to be higher under the BP ribs, where the temperature is lower and the GDL may contain residual water at the same time. In order to take into account those effects, Yablecki et al. [121] used a Thermal Lattice Boltzmann Model to determine the anisotropic thermal conductivity of GDL containing liquid water. They observed increases of 20.8% and 5.4% respectively for the through and in-plane thermal conductivities when the total saturation is changed from 0 to 24.4%. According to Burheim et al. [125], when considering wet GDL and moderately humidified CL, the PEMFCs maximum internal temperature difference increases by 33% when compared to the commonly assumed thermal conductivities. Wang et al. [131] highlighted that the heat pipe effect can be responsible of an apparent increase of the through-plane thermal conductivity of the GDLs by 20 – 40%.

d) Effect of inhomogeneous compression

There are two major causes of heterogeneous compression of the GDL:

- After the assembly phase, a deflection is observed at the center of the stack as demonstrated by Carral et al. [116]. The consequence is that the thermal resistance is higher at the center of the stack and lower close to the tie rods. The amplitude of the deflection depends on the number of cells and the position of the tie-rod nuts of the

assembly. Mechanical simulations and *in-situ* measurements showed that the effect of the deflection is negligible when the number of cells is higher than 10. Given that the experimental stacks tested in this study have 19 or 30 cells, the impact of deflection on the thermal study can be neglected.

- As shown in the Fig.III.1, the channel/rib structure of the BP induces different pressure distribution between the area of the GDL under the channel and the one under the rib.
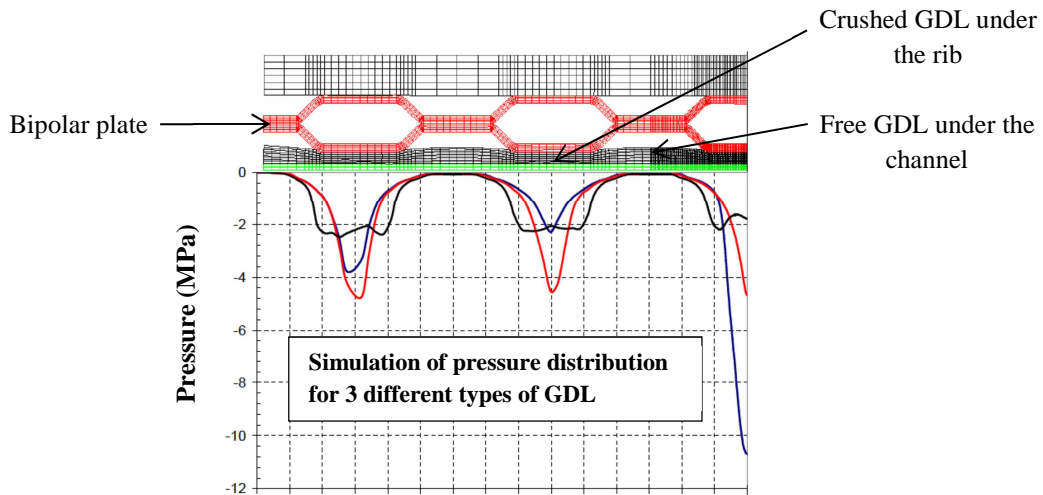
Figure III.1 : Simulation of the axial pressure distribution (MPa) in the GDL due to the channel/rib structure (CEA)

A comparative study of the effect of heterogeneous compression of the GDL under the channel/rib structure on the temperature distribution was achieved by Hottinen et al. [132], at the channel scale. They concluded that when heterogeneous compression is taken into account, a significant portion of the heat produced under the channel is conducted in the plane of the MEA and enters the GDL under the rib, where there is a smaller thermal resistance, causing a significant temperature gradient inside the electrode. The study showed that the in plane temperature differences between the area under the channel and the one under the rib can be multiplied by 8.5 from a homogeneous to a heterogeneous compression. Using a guarded heat flux meter device, Karimi et al. [119] measured variations from 0.26 to 0.7 W/m/K for Spectracarb GDL and from 0.25 to 0.52 W/m/K for Solvicore GDLs when the pressure rises from 0.7 to 13.8 bar, at a mean temperature of 70°C.

From these observations, the presence of the MPL as well as the variations in thermal conductivity due to the heterogeneous compression of the GDL are of paramount importance in modeling heat transfer and thermal effects in the cell. For the GDL, the values of 0.2 and 3.7 W/m/K, which were measured "*ex-situ*" at the CEA respectively for the though-plane and

in-plane thermal conductivities, will be considered as the references for this study. The MPL will be considered as a separate component, with an equivalent thermal conductivity of 0.4 W/m/K. The phenomenon of heterogeneous compression will also be considered, using a geometrical analogy (Fig.III.5).

1.4. Thermal contact resistances at the interfaces

Since the thermal contact resistances (TCR), especially between the GDL and the adjacent components, can have a great impact on temperature distribution, reliable estimations of their values are needed for this study. Karimi et al. [119] measured variations of TCR from 2.4 to 0.6 $10^{-4} \, m^2 K/W$ and 3.6 to 0.9 $10^{-4} \, m^2 K/W$ respectively for Spectracarb and Solvicore GDLs (in contact with iron surface) when the pressure is changed from 0.7 to 13.8 bar. Khandelwal [118] measured the TCR between Sigracet diffusion media and aluminium bronze material and found a quite constant value with varying PTFE content: $\sim 1.2 - 1.5 \cdot 10^{-4} m^2 K/W$, with a pressure of 2.2 MPa. Sadeghifar et al. [133] developed an analytical model to predict the thermal contact resistance between the GDL and a flat surface (representing the BPs rib). The obtained results largely depend on porosity and pressure. For the typical values of porosity and pressure used in this study, the TCR was $\sim 0.8 \cdot 10^{-4} m^2 K/W$. The values used in this study derive from literature: $1.5 \cdot 10^{-4}$ and $1.25 \cdot 10^{-4} \, m^2 K/W$ respectively for the GDL/BP and GDL/MPL thermal contact resistances.

It is worth noting that the thermal properties of the components evolve with ageing as observed by Burheim et al. [134]. Those ageing effects are not considered in this study, but could be of great importance for advanced fuel cell degradation models.

2. A 3D thermal model at the channel/rib scale

In this section, a 3D thermal model is developed at the channel/rib scale in order to investigate the real temperature distribution in the cell, as well as the impact of the thermal properties of the components and interfaces on heat transfer.

2.1. Geometry and hypothesis

a) Geometry

The reference modeled geometry is a 2 cm long channel of the fuel cell stack as presented in Fig.III.2. For symmetry reasons, the geometry is limited to ½ channel + ½ rib. A deformation

about 25% of the GDL under the rib is modeled to consider the heterogeneities in pressure due to the channel/rib structure.
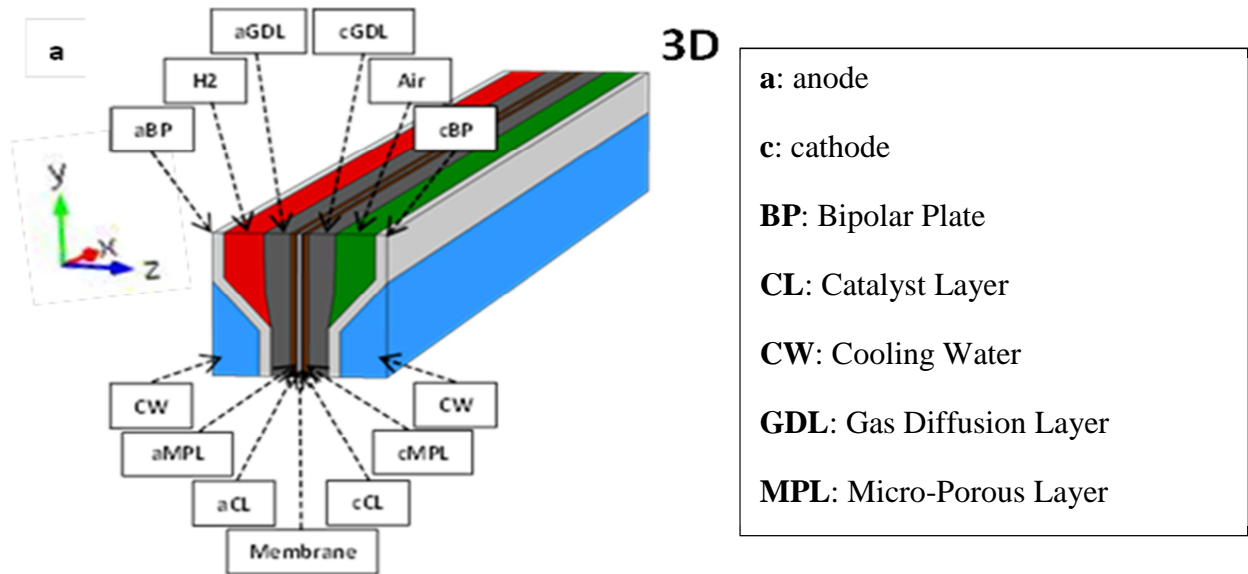
Figure III.2 : Reference channel/rib computational domain

b)   **Hypotheses of the model**

The hypotheses of the model are the following:

- Heat transfer in the porous layers is purely diffusive. In general, in porous media like GDL and MPL, heat is transferred by conduction and convection. The ratio of the two entities is given by the Péclet number. In this study, the Péclet number is sufficiently low ($\sim 10^{-3}$) to consider that the convective contribution to heat transfer is negligible. So the main heat transfer mechanism in the MEA is conduction.
- Single phase flows;
- Laminar flows in the channels ;
- Reactants are ideal gases;
- No mass transport through the membrane;
- The electrochemical reaction takes place at the interface between the catalyst layers and the membrane where a current density distribution is imposed.

2.2. Physical model: conservation equations

a) Continuity equation

Three equations of continuity are solved respectively in the anode compartment (aGC-aGDL-aMPL-aCL), cathode compartment (cGC-cGDL-cMPL-cCL) and cooling water channels (CW). The reference continuity equation is:

$$\frac{\partial \rho \varepsilon}{\partial t} + \nabla \cdot (\rho \, \boldsymbol{u}) = S_m \qquad \text{[III.2]}$$

where ρ and $\boldsymbol{u}$ are respectively the density and the velocity vector of the fluid; ε is the porosity of the medium (the porosity is 1 in the channels: aGC, cGC and CW). The mass source S_m is only located in the catalyst layers (aCL and cCL), where the electrochemical reactions take place. The equations of state for the fluids are: $\rho = P/RT$ in the gas channels, and $\rho = Cte = 976 \, kg/m^3$ for the water in the cooling channels.

b) Species conservation

The different species in the system are: H_2 and H_2O at the anode compartment; O_2, N_2 and H_2O at the cathode compartment. The global equation of species conservation is:

$$\frac{\partial \rho \varepsilon w_i}{\partial t} + \nabla \cdot (\rho w_i \boldsymbol{u}) = -\boldsymbol{\nabla} \cdot \boldsymbol{J_i} + S_i \qquad \text{[III.3]}$$

Where w_i is the mass fraction of the species i. One equation ($i=H_2$) is solved at the anode compartment and two equations ($i=O_2$ and $i=H_2O$) are solved at the cathode compartment. The remaining species (H_2O for the anode compartment and N_2 for the cathode compartment) are deduced from mass balance [III.2]. As for the mass balance, the species source S_i is only located in the catalyst layers (aCL and cCL), where the electrochemical reactions takes place. $\boldsymbol{J_i}$ is the diffusion flux, which is calculated using the generalized Fick's law of multicomponent gas diffusion:

$$\boldsymbol{J_i} = -\left[\rho w_i \sum_{k=1}^{n} D_{ik} \left(\boldsymbol{\nabla} X_k + \frac{1}{p} (X_k - w_k) \, \boldsymbol{\nabla} p \right) + D_i^T \frac{\boldsymbol{\nabla}\theta}{\theta} \right] \qquad \text{[III.4]}$$

Where D_{ik}, X_k, p, D_i^T and θ are respectively the binary molecular diffusivities, the mole fraction of the species k, the pressure, the thermal diffusivity and the temperature. In this model, the diffusion of species due to the thermal gradient is neglected, so the last term of the equation shown above is zero ($D_i^T = 0$). The molecular diffusivities D_{ik} are temperature and pressure dependent following the empirical correlation reported in Appendix 1.

$$D_{ik} = D_{ik}(p, T) \qquad \text{[III.5]}$$

In the porous media, the Bruggeman correction is considered in order to take into account the impact of porous and tortuous structures of the GDL and CL on effective molecular diffusivity:

$$D_{ik}{}^{eff} = D_{ik}\,\frac{\varepsilon}{\tau} \qquad \text{[III.6]}$$

c) Momentum

In the free flows domains (aGC – cGC – CW), the Navier-Stokes equations are solved:

$$\rho\left[\frac{\partial \boldsymbol{u}}{\partial t} + (\boldsymbol{u}\cdot\nabla)\boldsymbol{u}\right] = -\nabla\mathrm{p} + \nabla\left[\mu(\nabla\boldsymbol{u} + (\nabla\boldsymbol{u})^T) - \frac{2}{3}\mu(\nabla\cdot\boldsymbol{u})\cdot I\right] + \boldsymbol{F} \qquad \text{[III.7]}$$

Where μ is the dynamic viscosity of the fluid and $\boldsymbol{F}$ are the volume forces (gravity). $\left[\mu(\nabla\boldsymbol{u} + (\nabla\boldsymbol{u})^T) - \frac{2}{3}\mu(\nabla\cdot\boldsymbol{u})I\right]$ accounts for the viscous stress in the fluid, with $(\nabla\boldsymbol{u} + (\nabla\boldsymbol{u})^T)$ the rate of stress tensor and $\frac{2}{3}(\nabla\cdot\boldsymbol{u})\cdot\boldsymbol{I}$ the isotropic stress tensor.

In the porous domains (GDLa – GDLc – MPLa – MPLc – CLa – CLc), the Brinkman equations are used:

$$\frac{\rho}{\varepsilon}\left[\frac{\partial \boldsymbol{u}}{\partial t} + (\boldsymbol{v}\cdot\nabla)\frac{\boldsymbol{u}}{\varepsilon}\right] = -\nabla p + \nabla\left[\frac{1}{\varepsilon}\left(\mu(\nabla\boldsymbol{u} + (\nabla\boldsymbol{u})^T) - \frac{2}{3}\mu(\nabla\cdot\boldsymbol{u})I\right)\right] - \left(\frac{\mu}{K} + \frac{S_m}{\varepsilon^2}\right)\boldsymbol{u} + \boldsymbol{F} \qquad \text{[III.8]}$$

Where K is the hydraulic permeability of the porous medium.

d) Charge transport

Ohm's law is used for solving the electronic potential φ:

$$i = -\sigma\cdot\nabla\varphi$$

The calculation of the current density distribution in the different components is used in order to predict the local Joule heating.

e) Heat transport

The global heat transfer equation solved is:

$$\rho c_p\frac{\partial \theta}{\partial t} + \rho c_p\boldsymbol{u}\cdot\boldsymbol{\nabla}\theta = \boldsymbol{\nabla}\cdot(\lambda\,\boldsymbol{\nabla}\theta) + Q_s \qquad \text{[III.9]}$$

Q_s is the local heat sources in the cell, which are distributed depending on heat generation mechanisms.

f)   Local heat sources in the cell Qs

The calculation of local heat sources in the cell is obtained from the electrochemical reaction heat of overvoltage. Assuming that the produced water is in vapor phase, the total reaction enthalpy is (at 80°C): $\Delta H_{tot} = \Delta H_{tot}^{v} = 242\ kJ/mol_{H_2}$. The total reaction enthalpy is the sum of electrical energy leaving the system and waste heat:

$$\Delta H_{tot}\ \frac{i}{2\ F} = W_{e^-} + Q_{th} \qquad\qquad \text{[III.10]}$$

The local electric energy produced is: $W_{e^-} = V \cdot i$ where i is the current density distribution imposed at the interface between the catalyst layer and the membrane and V is the potential. So from the energy balance, the waste heat produced in the cell (heat of overvoltage) is the difference between the total energy and the electric energy produced:

$$Q_{th} = \left(\frac{\Delta H_{tot}}{2\ F} - V\right) i \qquad\qquad \text{[III.11]}$$

Moreover, the electrons and protons transport in the components create Joule heating source terms:

$$Q_j = \frac{i^2}{\sigma_j} \qquad\qquad \text{[III.12]}$$

Because of these uncertainties in heat generation mechanisms presented in Chapter I, section 3.2, the model assumes that all the entropy and electrochemical activation heats are located at the cathode catalyst layer/ membrane interface. The impact of that uncertainty about heat source localization on the temperature distribution will be evaluated in section 4.4.b. Standing to those heat generation mechanisms, the source terms used in this study for coupling the governing equations are:

Domain	S_m	S_i	Q_s
aCL	S_{H_2}	$S_{H_2} = -\dfrac{i}{2F}$	$0 \cdot \left(\dfrac{\Delta H_{tot}}{2\ F} - V\right) i$ at the anode catalyst layer/membrane interface.
cCL	$S_{O_2} + S_{H_2O}$	$S_{O_2} = -\dfrac{i}{4F}$ $S_{H_2O} = \dfrac{i}{2F}$	$1 \cdot \left(\dfrac{\Delta H_{tot}}{2\ F} - V\right) i$ at the cathode catalyst layer/membrane interface
Membrane	0	0	$\dfrac{i^2}{\sigma_m}$

88

MPLs	0	0	$\dfrac{i^2}{\sigma_{MPL}}$
GDLs	0	0	$\dfrac{i^2}{\sigma_{GDL}}$
BPs	0	0	$\dfrac{i^2}{\sigma_{BP}}$

<div align="center">Table III.1: Source terms used in the transport equations</div>

g)   Boundary conditions

The boundary conditions for the model are set as follows:

- Continuity at all internal boundaries;

- No slip boundary conditions at the channels walls: all the boundary layers are computed;

- Velocity, temperature and concentrations are defined at channels inlet (Figure III.3.a);

- Pressure and convective flux boundary (no viscous stress) conditions are defined at channels outlet (Figure III.3.b);

- The bipolar plate is set to electric ground on one side of the cell;

- The cell operation current density is fixed at the membrane/cathode catalyst layer interface;

- Thermal continuity across the cell, to consider the repeatability of the cells in the stack (Figure III.3.c);

- In-plane symmetry (Figure III.3.d);
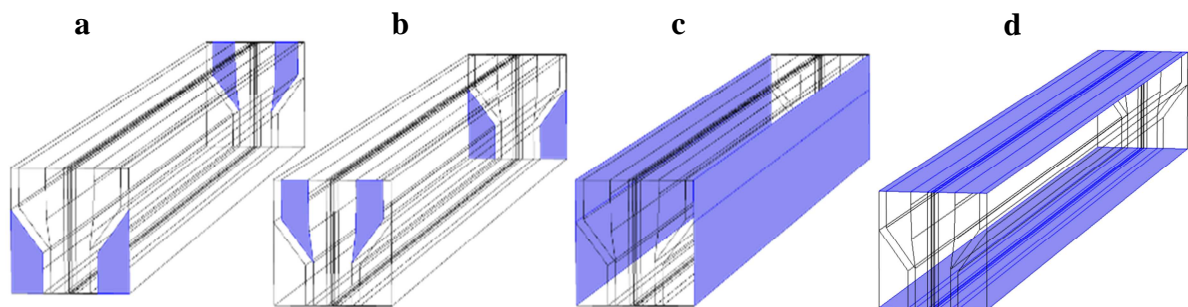
Figure III.3 : (a) Channels inlets - (b) Channels outlets - (c) Continuity and (d) Symmetry boundary conditions

2.3. Input parameters and physical properties of the components

The current density distribution at the interface between the membrane and the cathode catalyst layer is presented in Fig.III.4. It corresponds to a mean current density of 0.8 A/cm². The current density is higher under the channel due to the higher diffusion of reactive gases in that zone. This type of current density profile was obtained from an electrochemical model developed at CEA, which is beyond the scope of this study.
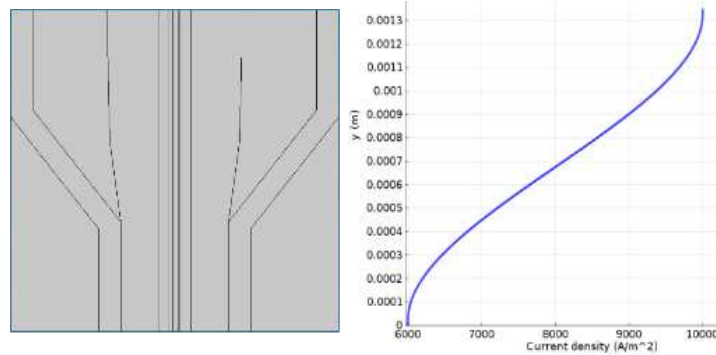
Figure III.4 : Current density distribution at the membrane/cathode catalyst layer interface

In the following table, the values of the physical properties of the cell components used in the study are presented. They are issued either from the literature review, or from local *"ex-situ"* measurements performed at the CEA as presented in Section 1.

Parameter	BP	GDL (Channel/rib variation)	MPL	CL	Membrane
Thickness [mm]	$2 \cdot 0.1$	$0.17 - 0.23$	0.05	aCL: 0.01 cCL: 0.015	0.025
Thermal conductivity λ [W/m/K]	16.1	In-plane: $3.7 - 5.4$ Through-plane: $0.2 - 0.3$	0.4	0.15	0.186
Electric conductivity σ [S/m]	$1.32 \cdot 10^6$	In-plane: $3460 - 4862$ Through-plane: $64 - 184$	50	1000	9.825
Porosity ε		$0.69 - 0.77$	0.35	0.47	
Permeability (m²)		*Kozeny-Carman correlation:* $$C \cdot \frac{\varepsilon^3}{(1-\varepsilon)^2}$$ With $C = 3 \cdot 10^{-14} \, m^2$	$2 \cdot 10^{-13}$	10^{-12}	
Tortuosity		1.165	1.7	1.3	

Table II.2: Physical properties of the cell components

The thermal contact resistances considered are:

- Thermal contact resistance GDL/BP: $1.5 \cdot 10^{-4} \; m^2 K/W$
- Thermal contact resistance GDL/MPL: $1.25 \cdot 10^{-4} \; m^2 K/W$

The channel/rib variations of the GDL thermal conductivities, used to consider the inhomogeneous compression, are presented in Fig.III.5. This profile is analogous to the geometrical deformation $e_v(y)$ which varies from 0 under the channel to 25% under the rib.
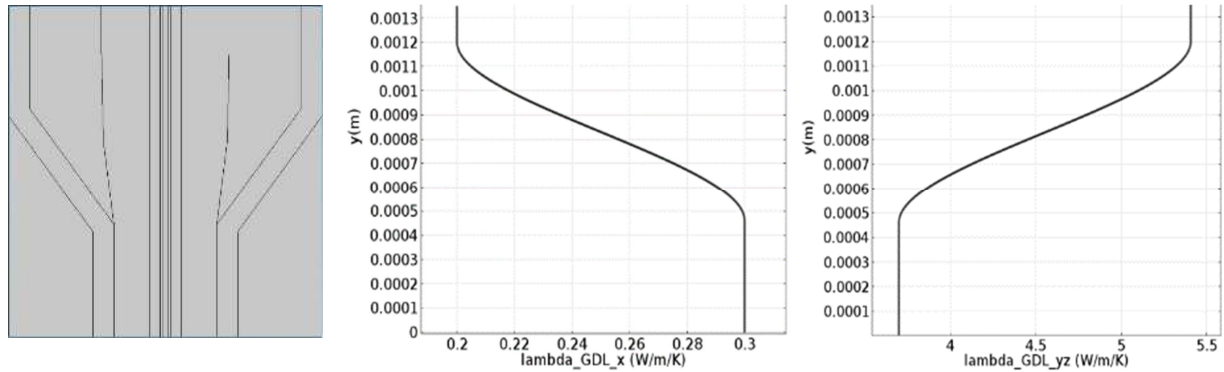
Figure III.5 : Distribution of the in-plane and through-plane GDL thermal conductivities used to take into account the inhomogeneous compression

The effect of the GDL deformation $e_v(y)$ on the porosity ε_{GDL} is taken into account considering the correlation [135]:

$$\varepsilon_{GDL} = \frac{\varepsilon_0 + e_v}{1 + e_v} \qquad \text{[III.13]}$$

In parallel, the hydraulic permeability used in the Brinkman equation is calculated using the Kozeny-Carman correlation:

$$k = C \cdot \frac{\varepsilon^3}{(1 - \varepsilon)^2} \qquad \text{[III.14]}$$

The other input parameters and properties of the model are summarized in Table III.3.

Description	Value
Inlet temperature of the reactive gases	$80°C$
Inlet temperature of the cooling water	$80°C$
Inlet velocity anode reactive gases	3.96 m/s
Inlet velocity cathode reactive gases	7.85 m/s
Inlet mass fraction H_2 - Anode	0.3
Inlet mass fraction O_2 - Cathode	0.2
Inlet mass fraction H_2O - Cathode	0.15
Inlet velocity cooling water	0.25 m/s

Table III.3: Input parameters of the model

2.4.   Numerical procedure

The model is implemented in the commercial software Comsol Multiphysics 4.3b and solved with Finite Elements Method. The mesh (see Fig.III.6) consists of triangular elements in the fluids and mapped elements in the solids, swept along the channel. The resulting 3D mesh is composed of 262 620 elements (151 200 prism elements and 111420 hexahedral elements). In order to reach a maximal relative error of 10^{-4}, the calculation time is about 28 minutes on an *Intel Xeon 2,67 GHz - RAM 32 GB*. For the computation, direct methods are used with a PARDISO solver.
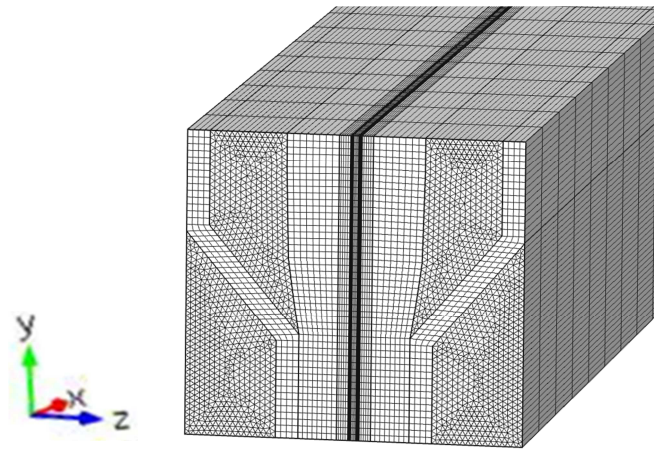
Figure III.6 : Swept mesh used for the computation

2.5.   Results and discussion

a)   Temperature distribution

The temperature distribution in the cell at a mean current density of 0.8 A/cm² is presented in Fig.III.7 using a 3D plot and a 1D plot at two different cut lines at the middle of the cell length, under the channel and under the rib. Firstly, it is observed that the temperature is higher in the cathode catalyst layer (~83.5°C) due to the exothermic oxygen reduction reaction, and lower in the bipolar plate (~79°C). The temperature difference across the cell is about 4.5°C under the channel and reduced to 3°C under the rib. Those results are in good agreement with the literature review results presented in the first chapter. No significant evolution of the temperature distribution is observed along the channel length, even if there is a global temperature rise from the inlet to the outlet of the cooling water.
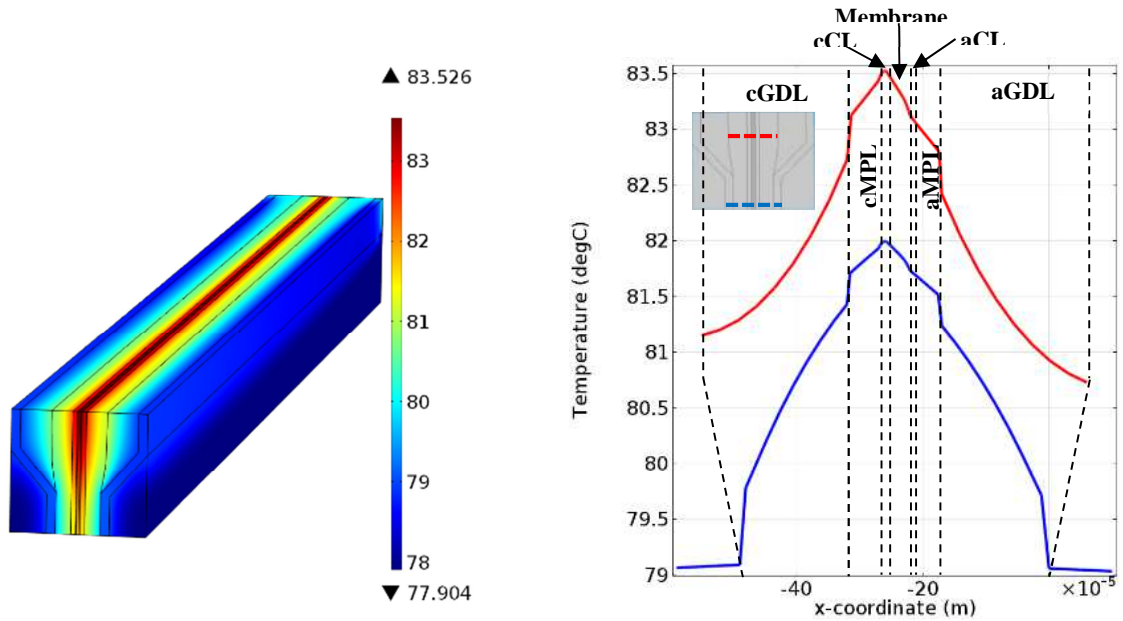
Figure III.7 : 3D Temperature distribution in the cell and 1D temperature distribution at the indicated cut lines

The temperature drop is higher in the GDLs (~ 1.5°C) and at the interfaces between the gas diffusion layer and the adjacent components. Typically, temperature drops of ~ 0.65 and ~ 0.4 °C are observed respectively at the GDL/BP and GDL/MPL interfaces. So the consideration of the thermal contact resistances is relevant for the temperature distribution prediction. In the other components, there is a lower temperature drop: ~ 0.4°C in the MPL, ~ 0.25°C in the membrane and ~ 0.1°C in the CLs.

The results also highlight the fact that considering the channel/rib heterogeneities is of paramount importance in modeling heat transfer in the cell: under the channel, there is a high heat production due to the high current density. Simultaneously, the heat flux to the channels flow is low due to the low heat capacity of the reactive gases. Under the ribs, the MEA is in direct contact with the cooling water which has a high heat capacity and the through-plane thermal conductivity is higher due to the elevated compression of the GDL. The combination of all these phenomena induces higher temperature variations between the zones under the channel and the ones under the rib. Moreover, the spatial variation of the temperature difference across the cell can induce heat pipe effect when there is phase change in the cell (for higher current densities) [68].

b)   Impact of reactive gases diffusion on heat transport

Fig.III.8 presents the evolution of the mass fractions of O_2 and H_2 distributions respectively at the cathode and anode compartments. These mass fractions distribution highlight the

significant impact of the channel-rib design. As expected, lower oxygen and hydrogen gas concentration are observed under the rib because of the diffusion limitation under the rib.
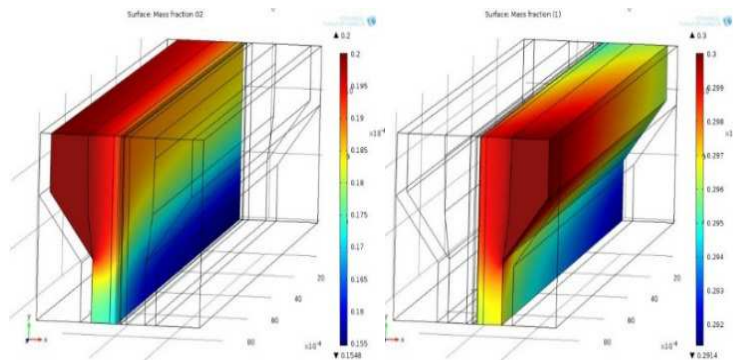
Figure III.8 : 3D H$_2$ and O$_2$ mass fractions evolution respectively at the anode and cathode compartments

A similar computation assuming constant physical properties for the reactive gases (no species source term in the active layers) showed quite the same results presented in Fig.III.8. Thus, it can be concluded that assuming constant physical properties for the reactive gases is a good approximation to save computational time in thermal modeling. However, it is worth noting that the consideration of water transport can be useful for a fuel cell operating in wet conditions, in which there could be a high amount of water condensation, especially under the ribs. As indicated in Fig.III.8, under the ribs there is not only a lower concentration of reactants species (and so a higher concentration of water), but also a lower hydraulic permeability of the GDL due to the higher compression. Additionally, the direct contact with the cooling water induces a cooler rib surface and so lower vapor saturation pressures in that zone. Before going to a deep analysis of temperature distributions, a candid discussion about the limitations and the dimensionality of the thermal model is needed.

3.   From 3D to Pseudo-3D modeling

3.1.   Limitations of the 3D channel/rib model

The 3D channel/rib model presented above is a kind of reference model, largely used in literature [71-73] thanks to the main advantages of full description of the channel/rib geometry and the capture of all the heterogeneities over the 3 dimensions. However, its main limitations are:

➢   The computational cost: the simulated geometry represents only ~1/1000 of the active area of the standard 220 cm² cell used in this study, despite of the computational time

of 28 minutes. Moreover, the boundary layers need to be accurately meshed in order to capture all the fluid/solid interactions.

➢ The local heat source: in large-area fuel cells, current density can show high variations over the active area due to the evolution of the reactive gases concentration and the local water content. As a consequence, there can be high variations of the heat source, which greatly impact the temperature distribution.

➢ The coolant flow field: the heterogeneities of the cooling flow field design can induce high flow rate heterogeneities in the cell, and consequently an uneven temperature distribution over the cell surface.

In the context of this study, which focuses on the analyses of the local heterogeneities and their correlation with degradations, full cell scale models are needed. For the development of a thermal model at the cell scale, the current density distribution can be either measured with the printed circuit board inserted in the stack (Chapter 3) or calculated by using a physic-based model (see Chapter 4). For upscaling the model while maintaining a feasible computational cost, the dimensionality used to describe the physics could be readjusted with appropriate pseudo-dimensional methods.

3.2. Multidimensionality effect in physic-based modeling of fuel cells

For a complete study of heat and water management, cell-scale models which take into account at the same time all the cell components and the channel/rib heterogeneities are needed. The best tradeoff between modeling scale, precision and computational time must be accurately studied. Indeed, for large-scale fuel cells, full 3D simulations require high computational resources and appropriate fluid dynamics solvers. Raj et al. [136] used concentration differences calculations to analyze the effect of multidimensionality in PEMFCs. From a physical point of view, they observed that differences between full 3D and 2D models mainly appear at high current densities ($> 1 \ A/cm^2$). From a computational point of view, they concluded that 3D models are almost ten times slower than 2D models and require three times more memory. In the same direction, Kim et al. [137] demonstrated that solving the transport equations in the 2D cross-section of the MEA with 1D integration along the channels is optimal in terms of both efficiency and accuracy for straight channels.

3.3.   Pseudo-3D concept

Actually, the thickness of the cell is very small compared to its length and width. The aspect ratio of the cell presented above: $Cell\ thickness/Cell\ width \approx 0.012$ is sufficiently low to consider each component as a plane layer. It can thus be appropriate to model the heat transport using a pseudo-3D approach, considering each component of the cell as a plane layer which exchanges heat out of plane with the adjacent components. The concept of the pseudo-3D approach, illustrated in Fig.III.9, is to consider each component of the cell as a plane layer which exchange heat out of plane with the adjacent components.
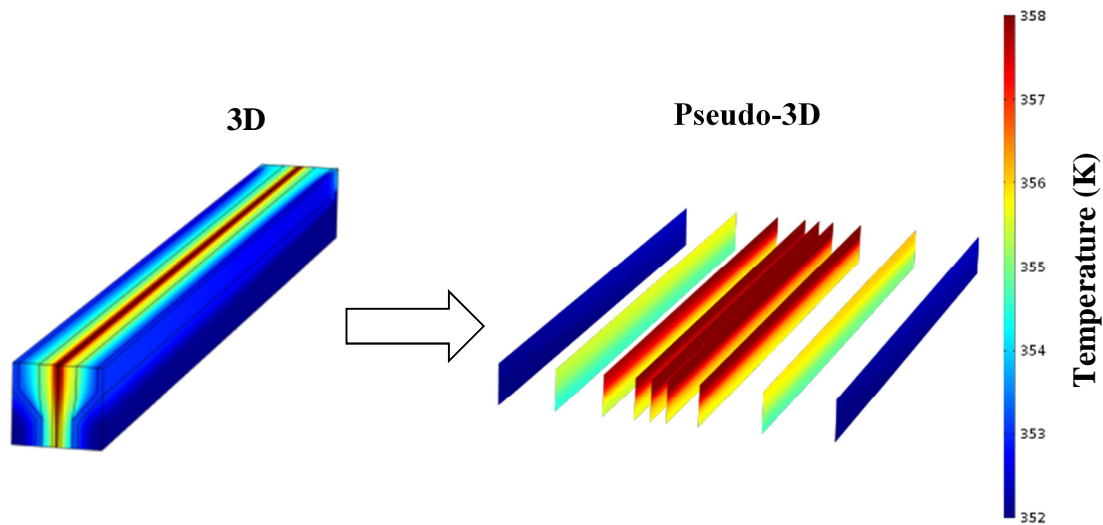
Figure III.9 : Temperature distribution (K) at the channel/rib scale from 3D to pseudo-3D

Applied at the cell scale, the pseudo-3D model can be validated experimentally with the printed circuit board Current Scan Lin S++ device [42] which, inserted between two monopolar plates of a 30 cells stack, is used to map the temperature distribution in the cell. Furthermore, the pseudo-3D concept developed at the cell scale allows predicting the in-plane temperature distribution in all the components of the cell with a low computation time, compared to full 3D model, while keeping a good precision. The thermal validation of the model is a first step of a multiphysics full predictive model which could take into account the species transport, the water content, the phase change effects, and the electrochemical behavior of the cell.

4. Development of a pseudo-3D model to investigate local temperature at the cell scale

In this section a pseudo-3D thermo-fluidic cell model is developed to investigate the temperature distribution in the different components of the large area (220 cm^2) Proton Exchange Membrane Fuel Cell. The main advantage of the model is the consideration of the real bipolar plate design and the detailed description of the studied geometrical domain while maintaining an acceptable computational time. The model is validated experimentally against local data obtained from a printed circuit board which, inserted between two monopolar plates of a stack, is used to map the current and temperature distributions. In this study, detailed heat transport equations are solved with thermal coupling by convection and conduction in order to predict the 2D distribution of the temperature in each cell component, from the membrane to the bipolar plate. The cooling water and gas flows in the bipolar plates are solved using a fluid dynamics model which is coupled to the thermal model. The current density distribution is implemented by using the S++ measurement device results. The model is implemented in the commercial software COMSOL Multiphysics.

4.1. Model development

a) Thermal model of the cell

The studied stack consists of 30 cells with an active area of 220 cm^2, connected in series. The configuration of the stack is shown in Fig.III.10 with a reduced number of cells for simplicity. The inlet and outlet manifolds for the reactant gases and cooling water are also indicated in Fig.III.10. The printed circuit board inserted between the 15th and the 16th cells allows measuring the in-plane current density distribution and the temperature in different operating conditions.
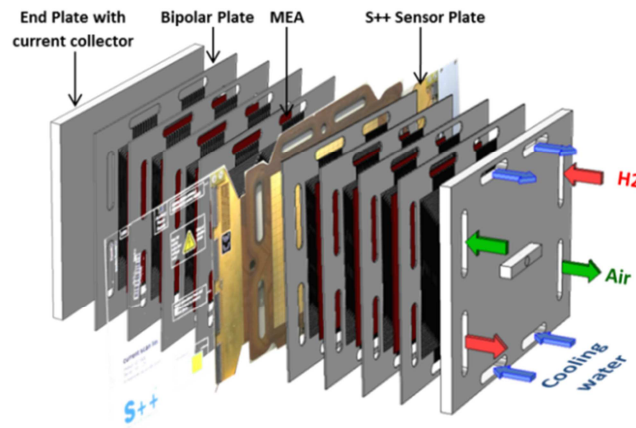
Figure III.10 : Configuration of the stack with the sensor plate

As presented in Fig.III.11.a, a single cell consists (*Reference cell*) of the Membrane and Catalyst Layers (CL) sandwiched between two microporous layers (MPL), two gas diffusion layers (GDL) and two bipolar plates (BP). Fig.III.11.b shows the different components and the configuration of the cell with the sensor plate (*Validation cell*). One reference cell consists of 9 solid and 3 fluid components. The S++ sensor plate, sandwiched between two monopolar plates, is introduced inside the stack replacing one MEA. As every plate contains a cooling circuit, the S++ temperature measurement is influenced by one additional cooling circuit. All of these additional components (including the S++ measurement device) need to be included in the cell description for the model's validation before going to the reference cell (Figure III.11.a). Thus, in this study, two cell configurations will be studied: the first one is the *validation cell* which includes the S++ measurement device for the model validation against experimental data. The second one is the *reference cell*, which is used for the cell temperature analysis, is the classical configuration without the measurement device.
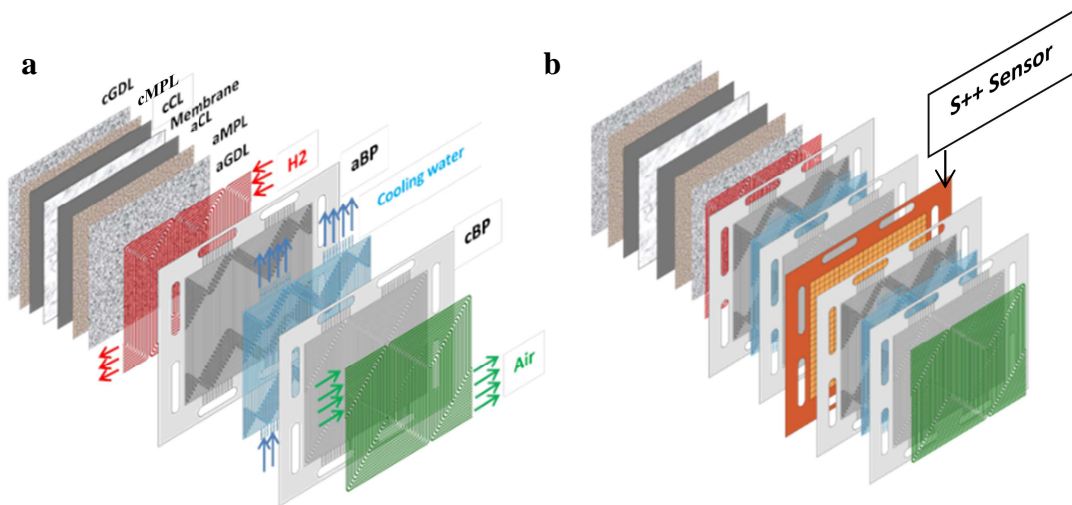
Figure III.11 : Reference cell (a) and validation cell with the sensor plate (b)

The governing equations of the model are derived with the following assumptions:

- Constant physical properties of the reactive gases.
- Uniform cell voltage.

With this pseudo-3D approach, the variables solved are the temperatures averaged over the thicknesses of the components, which will be called in-plane temperature and noted T_i. By coupling the in-plane temperatures through conduction and/or convection heat fluxes across the interfaces of the different components, it is possible to compute their 2D (in-plane) distribution in each component. So the in-plane temperature of each component from the MEA to the cooling water is calculated from the balance between local heat generation induced by the electrochemical reactions, the ohmic resistances and the local heat removal rate by cooling water and gases flows. The concept of the model, from the 3D geometry to the pseudo-3D approximation is presented below at the channel scale (Figure 9) and generalized to the cell.

To obtain the pseudo-3D formulation, the 3D heat balance equation in the component i is integrated along the thickness of each component. Assuming that the system is stationary, the 3D equation reduces to:

$$\left(\rho c_p\right)_i \boldsymbol{u_i} \cdot \boldsymbol{\nabla}\theta_i = \boldsymbol{\nabla} \cdot (\lambda_i \cdot \boldsymbol{\nabla}\theta_i) + Q_i \qquad [\text{III}.15]$$

The integration of the equation along the cell thickness leads to:

$$\int_0^e \boldsymbol{\nabla} \cdot (\lambda \cdot \boldsymbol{\nabla}\theta_i)dz + \int_0^e Q_i dz = \int_0^e \left(\rho c_p\right)_i \boldsymbol{u_i} \cdot \boldsymbol{\nabla}(\theta_i)dz \qquad [\text{III}.16]$$

The development of the equation considering Cartesian coordinates leads to:

$$\int_0^e \left(\lambda_x \frac{\partial^2 \theta_i}{\partial x^2} + \lambda_y \frac{\partial^2 \theta_i}{\partial y^2} + \lambda_z \frac{\partial^2 \theta_i}{\partial z^2}\right)dz + \int_0^e Q_i dz = \int_0^e \left(\rho c_p\right)_i \left(u_i^x \frac{\partial \theta_i}{\partial x} + u_i^y \frac{\partial \theta_i}{\partial y} + u_i^z \frac{\partial \theta_i}{\partial z}\right)dz \qquad [\text{III}.17]$$

Where e is the thickness of the components i of the cell. Given that the thermal conductivities of the components do not vary along their thicknesses, one gets:

$$\lambda_x \frac{\partial^2}{\partial x^2}\left(\int_0^e \theta_i dz\right) + \lambda_y \frac{\partial^2}{\partial y^2}\left(\int_0^e \theta_i dz\right) + \lambda_z \left[\frac{\partial \theta_i}{\partial z}\right]_0^e + Q_i \cdot e$$

$$= \left(\rho c_p\right)_i \left[\int_0^e u_i^x \frac{\partial \theta_i}{\partial x}\,dz + \int_0^e u_i^y \frac{\partial \theta_i}{\partial y}\,dz + \int_0^e u_i^z \frac{\partial \theta_i}{\partial z}\,dz\right] \qquad [\text{III}.18]$$

Then, the through-plane heat flux is discretized:

$$\lambda_x \frac{\partial^2}{\partial x^2} \left(\frac{1}{e} \int_0^e \theta_i \mathrm{d}z \right) + \lambda_y \frac{\partial^2}{\partial y^2} \left(\frac{1}{e} \int_0^e \theta_i \mathrm{d}z \right) + \frac{1}{e} \lambda_z \left[\frac{\partial \theta_i}{\partial z} \Big|_e - \frac{\partial \theta_i}{\partial z} \Big|_0 \right] + Q_i$$

$$= \frac{1}{e} \left(\rho c_p \right)_i \left[\int_0^e u_i^x \frac{\partial \theta_i}{\partial x} \, \mathrm{d}z + \int_0^e u_i^y \frac{\partial \theta_i}{\partial y} \, \mathrm{d}z + \int_0^e u_i^z \frac{\partial \theta_i}{\partial z} \, \mathrm{d}z \right]$$

[III.19]

Considering that:

$$\frac{1}{e} \int_0^e u \frac{\partial \theta_i}{\partial x} \, \mathrm{d}z = \frac{1}{e} \int_0^e u \, \mathrm{d}z \, \frac{1}{e} \int_0^e \frac{\partial \theta_i}{\partial x} \, \mathrm{d}z$$

[III.20]

And introducing the in-plane temperature T_i, the in-plane velocity $\boldsymbol{v_i}$ and the through-plane local heat-fluxes at the component interfaces J_T^+ and J_T^-:

$$T_i = \frac{1}{e} \int_0^e \theta_i \mathrm{d}z \ ; \ \boldsymbol{v_i} = \frac{1}{e} \int_0^e \mathbf{u_i} \mathrm{d}z \ ; \ J_T^+ = \frac{1}{e} \lambda_{i_z} \frac{\partial \theta_i}{\partial z} \Big|_e \ ; \quad J_T^- = - \frac{1}{e} \lambda_{i_z} \frac{\partial \theta_i}{\partial z} \Big|_0$$

[III.21]

2D heat transfer equations are obtained for the in-plane temperature of each component of the cell, assuming that the electrochemical heat source Q_i is uniform along the thickness:

$$\left(\rho c_p \right)_i \boldsymbol{v_i} \cdot \nabla_{xy} T_i = \boldsymbol{\lambda_{i_{xy}}} \cdot \nabla_{xy}{}^2 T_i + Q_i + \Sigma J_T^i$$

[III.22]

To solve this problem, it is necessary to determine the through-plane heat fluxes at all the interfaces, the local heat source in each component and the in-plane fluid velocity in the three fluid circuits.

b) Analytical model for through-plane heat flux J_T^i

The heat fluxes, which are related to the local temperatures θ_i, need to be described depending on the in-plane temperatures T_i, via the introduction of effective transfer coefficients. Those effective transfer coefficients can also be seen as equivalent thermal resistances between the layers. There are two typologies of interfaces (see Fig.III.12) in the system: solid/solid (ex: bipolar plate/GDL) and solid/fluid (ex: bipolar plate/cooling water). Heat conduction fluxes between the solid interfaces are estimated considering the half thickness of each solid component. Their derivation is given in Appendix 2. For solid/solid interfaces (see for example bipolar plate/GDL, $J_{1,3}$), the heat flux can be modeled as:

$$J_{1,3} = \frac{1}{e_1} \cdot \frac{1}{\frac{e_3}{2\lambda_{3_z}} + TCR_{1/3} + \frac{e_1}{2\lambda_{1_z}}} \cdot C_{1,3} \cdot (T_3 - T_1)$$

[III.23]

where $TCR_{1/3}$ is the thermal contact resistance between the two components. For solid/fluid interfaces (ex: bipolar plate/cooling water, $J_{1,12}$), it can be written:

$$J_{1,12} = \frac{1}{e_1} \cdot \frac{1}{\dfrac{1}{h_{12}} + \dfrac{e_1}{2\lambda_{1_z}}} \cdot C_{1,12} \cdot (T_{12} - T_1)$$

[III.24]
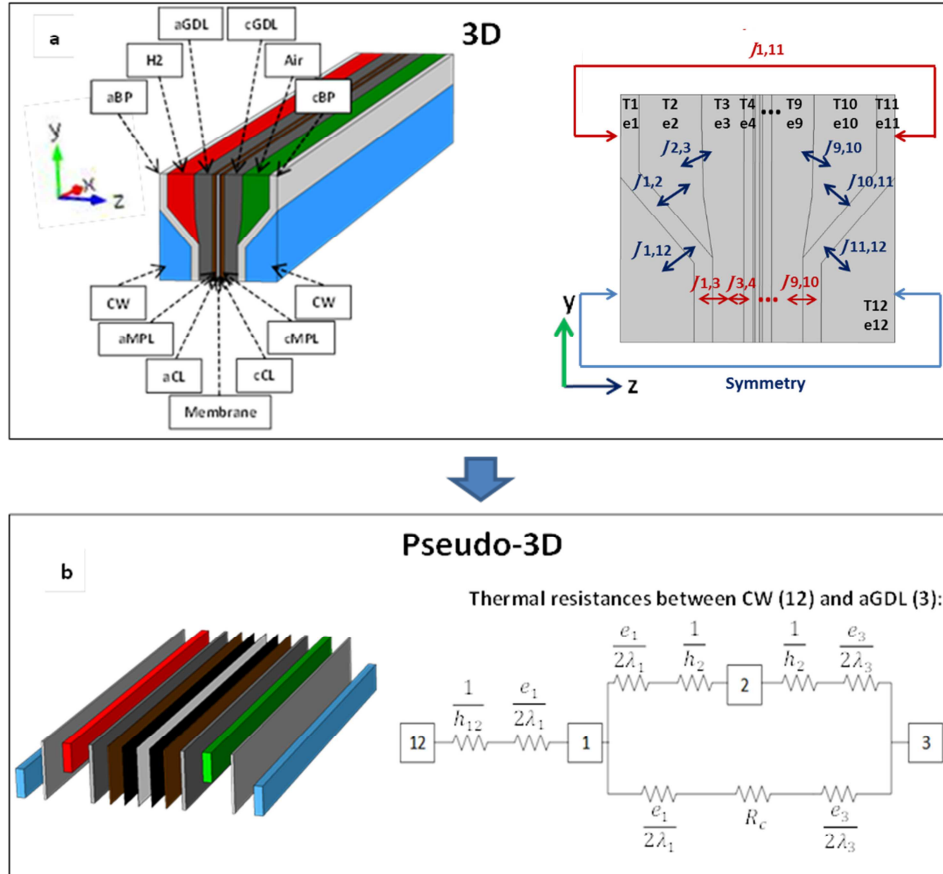
Figure III.12 : (a) Illustration of 3D geometry at the channel scale with the heat fluxes (Φ) - (b) Corresponding pseudo-3D concept with thermal resistances

where h_{12} is the convective heat transfer coefficient in the cooling water. Its calculation can be obtained via the Nusselt numbers which only depends on the geometry for laminar flows. The Nusselt numbers Nu in the channels will be calculated in the part dedicated to the fluid dynamics model. Note that $C_{i,j}$ are correction factors used to consider the change in heat exchange surface from the real 3D geometry to the 2D approximation. Indeed, as illustrated in Figure III.12, all the components of the cell are plane layers except the bipolar plates, which are stamped stainless sheets. Consequently, from the real geometry of the bipolar plates to the pseudo-3D geometrical model which assumes that the bipolar plate is a completely plane layer, there is a change in contact area between the bipolar plate and the adjacent components.

In order to consider the real exchange areas, the parameters C_{ij} are used. The C_{ij} parameters are defined as the ratio between the real exchange areas and the approximated exchange areas in the pseudo-3D approach. The corresponding values of C_{ij} are highlighted in Fig.III.13.

$$C_{1,2} = \frac{l_2}{l_1} = 1.6$$

$$C_{1,3} = \frac{l_3}{l_1} = 0.6$$

$$C_{2,3} = \frac{l_4}{l_1} = 1.4$$
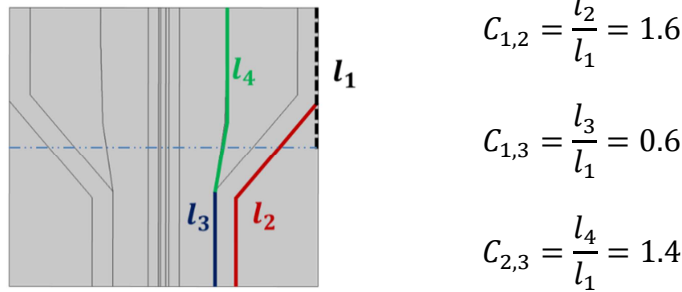
Figure III. 13 : Corresponding values of the heat fluxes correction factors

Thus, the thermal fluxes between the different components of the cell are evaluated by introducing effective transport coefficients in order to relate these fluxes to the mean temperatures averaged along the thickness of the components.

c) Heat sources distribution

Assuming that the produced water is in vapor phase, the total reaction enthalpy at 80°C is $\Delta H_{tot} = 242 \ kJ/mol_{H_2}$. It can be decomposed into produced electrical energy and heat source. The local produced electrical power $\dot{W}_{e^-}$ is estimated by considering the local current density distribution $i(x,y)$ and the cell potential V_{cell}, which are obtained from the experimental measurements:

$$W_{e^-}(x,y) = V_{cell} \ i(x,y) \qquad [\text{III.25}]$$

$i(x,y)$ can be obtained from Sensor plate measurement data. The heat of overvoltage is:

$$\dot{Q}_{th}(x,y) = \left(\frac{\Delta H_{tot}}{2\,F} - V_{cell}\right) i(x,y) \qquad [\text{III.26}]$$

In the components other than the catalyst layers, the heat sources density distribution (W/m^3) are exclusively the Joule effect due to the electric resistance:

$$\dot{Q}_i(x,y) = \frac{i(x,y)^2}{\sigma_i} \qquad [\text{III.27}]$$

and the energy balance is:

$$\frac{\Delta H_{tot}}{2\,F} i(x,y) = W_{e^-}(x,y) + \sum_i \dot{Q}_i(x,y) + \dot{Q}_{CL}(x,y) \qquad [\text{III.28}]$$

where $\dot{Q}_{CL}$ is the heat generated in the catalyst layer by the exothermic electrochemical reaction.

For sake of simplicity, in this study, it is assumed that all the irreversible reactions and entropic heat sources are located in the cathode CL. A parametric study of the heat repartition between the aCL and the cCL has been realized to estimate the impact of the uncertainty of heat sources localization on the temperature distribution. The results show that heat source repartition between the catalyst layers has a negligible effect on the MEA temperature and the deviation is about 0.05°C if 25% of the heat is generated in the aCL. So all the remaining heat source can be introduced in the cathode catalyst layer as follows:

$$\dot{Q}_{cCL}(x,y) = \frac{1}{e_{cCL}} \left[\left(\frac{\Delta H_{tot}}{2 \cdot F} - V_{cell} \right) i(x,y) - \Sigma \frac{i(x,y)^2}{\sigma_j} e_j \right] + \frac{i(x,y)^2}{\sigma_{CL}} \qquad \text{[III.29]}$$

So from the current density distribution which is obtained from experimentation, the local heat production inside each component of the cell can be deduced.

The geometric application of the pseudo-3D model at the channel/rib scale (for simplicity) is presented below in Fig.III.14 with the geometric indication of out of plane heat flux coupling at the interfaces of the subsystems. The detailed through-plane heat fluxes J_T^i of the different cell components are given in Appendix 2.

Heat transfer in Solids: $(\rho c_p)_{eq} \frac{\partial T}{\partial t} = \lambda_{i_{xy}} \cdot \nabla_{xy}{}^2 T_i + Q_i + \Sigma J_T^i$

Heat transfer in Fluids: $(\rho c_p)_{eq} \frac{\partial T_i}{\partial t} + (\rho c_p)_i v_i \cdot \nabla_{xy} T_i = \lambda_{i_{xy}} \cdot \nabla_{xy}{}^2 T_i + Q_i + \Sigma J_T^i$
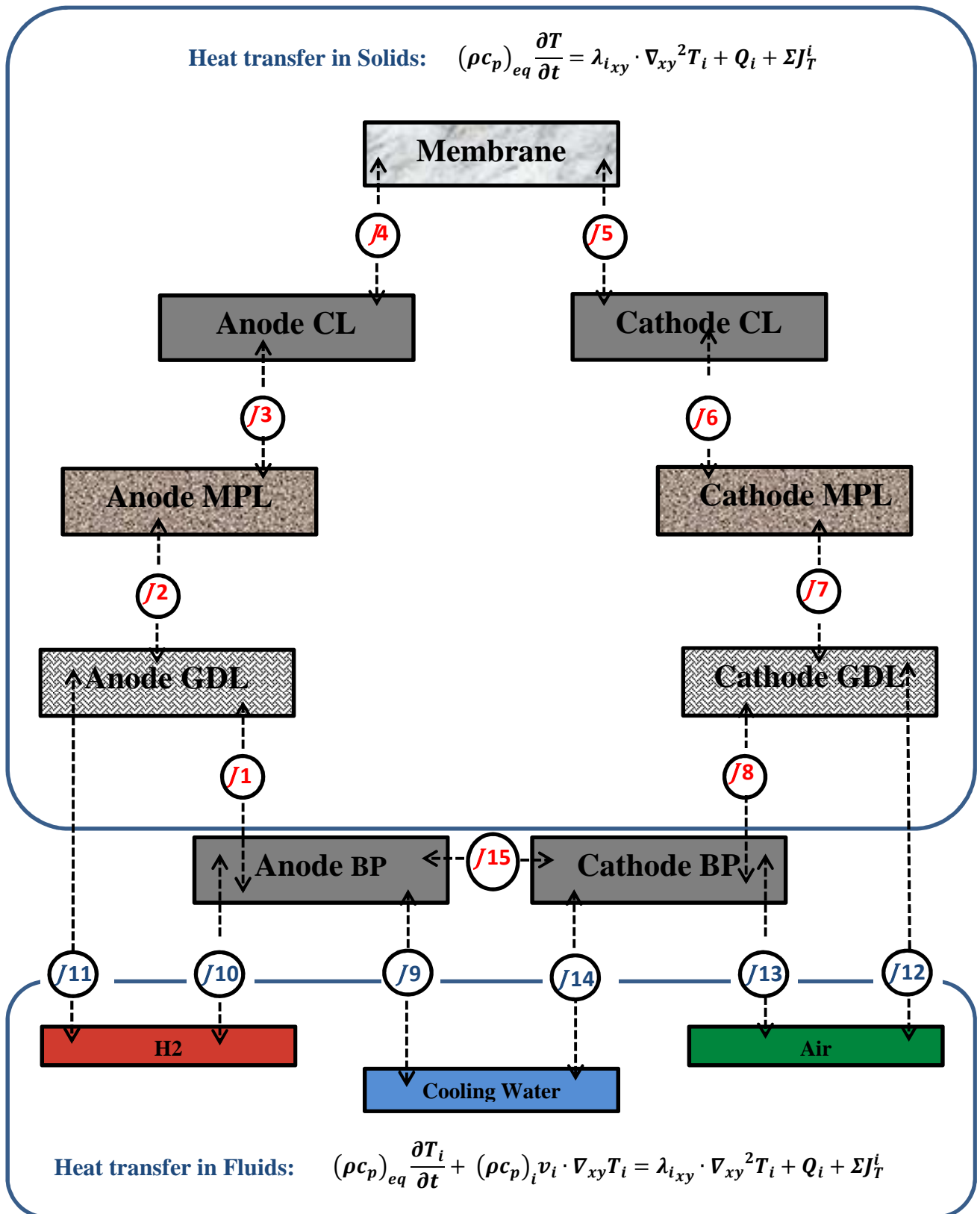
Figure III.14 : Out of plane heat flux coupling at the interfaces of the subsystems

The last physical variable needed to solve the heat transfer equations is the in-plane fluid velocity in the three fluid circuits because the local in-plane temperature is determined by the

balance between the local heat production and its removal, which is strongly related to the in plane velocity of the different fluids.

d) Fluid dynamics model of the cell

To study the heat transfer in the cell with an acceptable computation time, the simplest approach is to consider only the mean flow velocity in the channels. Indeed, the description of the temperature and velocity boundary layers inside the channels is not needed for the thermal balance since effective transfer coefficients have been introduced. The mass flow rate in the channel section, coupled with the use of effective convective transfer coefficient, h_i is sufficient to calculate the convective heat transfer considering the pseudo-3D equations of heat transport. Using such an approach, it is not necessary to mesh finely the boundary layer and compute the shear stress tensor in order to determine the mean flow velocity in the channels. The fluid dynamics equations are reduced to a Darcy-Weisbach like approach. As a consequence, computation time can be saved without affecting the accuracy of the results. A comparison between the results obtained using the Darcy-Weisbach and the Navier-Stokes approaches is presented in section 4.3.b for comparison.

The design of the two metallic plates is a parallel serpentine flow field technology with a different number of channels and passes for both plates. The general pattern of the gas circuit on a piece of the cell is presented in Fig.III.15. It consists of non-connected parallel serpentine channels for the two gas circuits. Thus the mean flow velocities in the gas channels will be easily deduced from the continuity equation. The cooling circuit results from the remaining space between both metal sheets and is a network of parallel straight channels in some zones and a network of chaotic connected channels in the other zones, where reactive gas channels cross each other. The local mean flow velocity in the different channels of the cooling circuit will be the result of the local pressure drops.
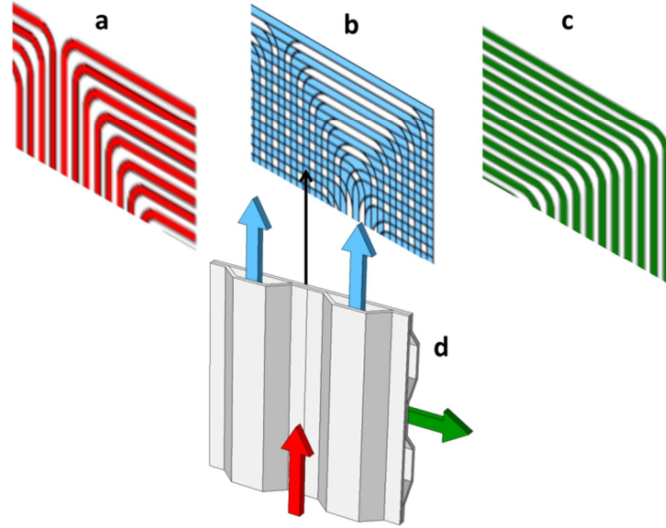
Figure III.15 : Hydrogen (a), cooling water (b) and air (c) channels respectively on a piece of the bipolar plate. Identification of the periodic cross flow (b) of the cooling water and illustration of the chaotic network in 3D (d)

Due to the fact that the channel section varies in the chaotic zones, specific formulations have to be developed for the 2D approach. In this approach, no-slip boundary conditions are considered at the walls and the mass and momentum conservation equations assimilate the channels as "porous" media. A permeability coefficient K_1 which accounts for the fluid/wall friction and a passability coefficient K_2 which accounts for the singular pressure drops due to section and direction variations in cross flow zones. The resulting continuity and momentum equations solved are:

$$\nabla \cdot \overline{v} = 0 \qquad \text{[III.30]}$$

$$0 = -\nabla p - \frac{1}{K_1}\mu\overline{v} - \frac{1}{K_2}\|\overline{v}\|\,\overline{v} \qquad \text{[III.31]}$$

where $\overline{v}$ is the mean velocity (bulk velocity) inside the channels, which will be called v in the following for sake of simplicity.

> ➢ **Distributed pressure drop: 1/K_1**

The permeability coefficient K_1 accounts for the distributed pressure drop due to the friction between the fluid and the wall. It is estimated using the Reynolds number Re, the hydraulic diameter D_h and the Fanning friction factor in the channel f_F. Thus, K_1 can be calculated from the Darcy-Brinkman equation:

$$\frac{\Delta p}{L} = 4 \cdot f_F \cdot \frac{\rho v^2}{2} \cdot \frac{1}{D_h} = \frac{1}{K_1} \cdot \mu \cdot \boldsymbol{v} \qquad \text{[III.32]}$$

The resulting permeability coefficient is:

$$K_1 = \frac{D_h^2}{2 \cdot (f_F \cdot Re)} \qquad \text{[III.33]}$$

For laminar flows, $f_F \cdot Re$ is only geometry dependent and its value is given in the next section (4.2).

> ➤ **Local/singular pressure drop: $1/K_2$**

The passability coefficient K_2 is the singular pressure drop factor in the complex zones where reactive gas channels cross each-other. In that chaotic flow network, the geometry is almost periodic as presented in figure II.4. In one basic element of the periodic chaotic network represented in figure III.16, the geometric configuration imposes the following obstacles to the fluid flow: 1 growth in hydraulic section, 3 shrinkages in hydraulic section, 2 changes in direction and 2 cross-flows. The singular pressure drop factor is thus estimated assuming that in one basic element of the periodic chaotic network we have the following pressure drops:

- 1 increase in hydraulic section: $1 \cdot (1 - S_2/S_1)^2 \cdot (\rho/2L)$
- 3 decreases in hydraulic section: $3 \cdot 0.5 \cdot (1 - S_2/S_1) \cdot (\rho/2L)$
- 2 changes in direction: $2 \cdot 1.13 \cdot \rho/2L$
- 2 cross-flows: $2 \cdot \rho/2L$
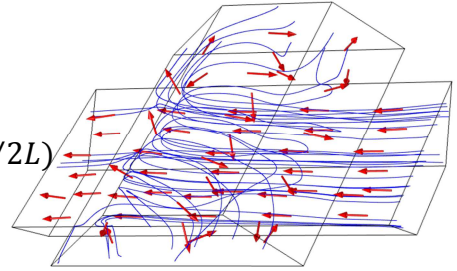
Figure III.16 : Simulation of velocity field in one basic element of the periodic chaotic network using the Navier-Stokes equations

The passability coefficient K_2 is then expressed as:

$$\frac{1}{K_2} = \left[1 \cdot \left(1 - \frac{S_2}{S_1} \right)^2 + 3 \cdot 0.5 \cdot \left(1 - \frac{S_2}{S_1} \right) + 2 \cdot 1.13 + 2 \right] \cdot \frac{\rho}{2L} = 5.26 \cdot \frac{\rho}{2L} \qquad \text{[III.34]}$$

where L is the length of the periodic element. In the reference bipolar plate configuration K_2 is about $2 \cdot 10^6 \ kg/m^4$. This value of the singular pressure drop coefficient is in good agreement with those reported in [138-140].

4.2. Input data and solution procedure

a) Friction factor and Nusselt number in the channels

The flows in the gas channels and in the cooling water are laminar. In order to optimize the diffusion of the reactive gases in the GDL, the gas channels section is trapezoidal. The resulting flow in the cooling water, between the anode and cathode plates, has a hexagonal section in the parallel zones and a trapezoidal section in the cross-flow zones.

Sadasivam et al. [141] used finite difference method to solve the Navier-Stokes equations for laminar flows and determine the friction factor and Nusselt number of these channels typology for a wide range of aspect ratio of the duct and different trapezoidal angles with good precisions. Venter et al. [142] used the finite element method to solve the appropriate momentum and energy equations in order to predict the same physical parameters. They found $(f_F \cdot Re, Nu) \approx (14, 4.3)$ and $(f_F \cdot Re, Nu) \approx (14.68, 3.5)$ respectively for hexagonal and trapezoidal geometries. These results are in a good agreement with those proposed by Sadasivam et al. [141] and Damean et al. [143]. So, they will be used to determine the appropriate friction factor and Nusselt number in this study. However, those results are effective for straight channels, where the flow is absolutely laminar.

In the chaotic zones, the geometry induces high perturbations of the hydrodynamic and thermic boundary layers which enhances mixing and thus promotes higher convective heat transfer. In particular, the geometry configuration in these zones (Fig.III.15.b) can be considered a C-shaped geometry, as initially introduced by Liu et al. [138]. So it is necessary to take into account the intensification of convective heat transfer due to the chaoticity of the flow. Lasbet et al. [139-140] used a finite volume method on the commercial software Fluent to solve the Navier-Stokes and energy equations in order to evaluate the thermal performances of mini-channels with a uniform flux condition on the closed surface of the channel for a C-shaped geometry. For a Reynolds number close to 200, they found a Nusselt number ratio of ~ 4.5 between the chaotic and the regular geometries. Given that the Reynolds number in this study is in the same order of magnitude and that those results are in a good agreement with those presented by C. Chagny-Regardin [144] for a similar type of chaotic geometry, the ratio of 4.5 is used in this study. According to all the references cited above, the corresponding parameters for this study are given in Table III.5.

Channel section	Friction factor $f_F \cdot Re$	Singular pressure drop $1/K_2$	Nusselt number Nu (uniform wall heat flux condition)
Trapezoidal	14.68	0	3.5
Hexagonal	14	0	4.3
Chaotic geometry	14 or 14.68	$2 \cdot 10^6$	$4.5 \cdot 3.5 = 15.75$

Table III.5: Fluid dynamics parameters for the study

b) Physical properties of the components

The thermal model presented above is implemented at the cell scale, including the sensor plate for model validation because its presence is thermally invasive. Indeed, the S++ sensor plate needs to be sandwiched between two monopolar plates and so induces the use of one additional plate to separate two cells and one additional cooling flow. All of these additional components need to be included in the model for its validation before going to the conventional configuration for the thermal study. The corresponding physical properties, presented in Table III.6, are issued from measurements and literature.

The inhomogeneous compression of GDL between the area under the channel and the one under the rib has a non-negligible impact on temperature distribution as illustrated with the 3D channel/rib model. Distinct values of the corresponding thickness and conductivities are considered as illustrated in Table III.6.

Parameter	BP	GDL	MPL	CL	Membrane	S++
Thickness [mm]	$2 \cdot 0.1$	*Under channel: 0.23* *Under rib: 0.17*	0.05	aCL: 0.01 cCL: 0.015	0.025	3
Thermal conductivity λ [W/m/K]	16.1	**In-plane** *Under channel: 5.4* *Under rib: 3.7* **Through-plane** *Under channel: 0.2* *Under rib: 0.3*	0.4	0.15	0.186	3
Electric conductivity σ [S/m]	$1.32 \cdot 10^6$	*Under channel: 64* *Under rib: 184*	50	1000	9.825	800

Table III.6: Physical properties of the cell components used in the study

c) Numerical procedure

The main numerical guidelines of the pseudo-3D thermal model are:

- ➢ The in-plane heat transfer is solved numerically through a 2D numerical model;
- ➢ The through-plane heat transfer is solved analytically with a flux continuity conditions at the interfaces between the components: 1D analytical model;
- ➢ Some correction factors are introduced to take into account the real geometry of the bipolar plate, which is considered a plane layer;
- ➢ The fluid dynamics model considers plug flows in the bipolar plates and the "bulk temperature" of the flow is considered for thermal coupling.

As illustrated in Fig. III.14, the global system computed in this simulation for the model validation consists of 12 equations of heat transfer in solids, 4 equations of heat transfer in fluids, with thermal coupling through conductive and convective heat fluxes at the interfaces. The fluid velocities are calculated in the gases and water cooling channels. For sake of simplicity, an electrochemical model of the cell is not proposed. The current density distributions are directly measured by the S++ sensor plate and the cell potential is recorded. The model is implemented in the commercial software Comsol Multiphysics 4.3b and solved with Finite Elements Method. The mesh (see Fig.III.17) is about $3 \cdot 10^5$ triangular shell elements and to obtain a relative error of 10^{-4}, the calculation time is about 6 hours on an *Intel Xeon 2,67 GHz - RAM 32 GB*. For the computation, direct methods are used with a PARDISO solver for fluid dynamics and MUMPS for heat transfer.
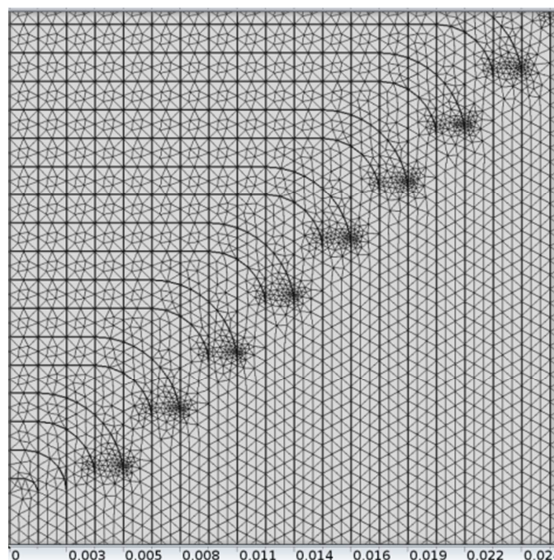
Figure III.17 : Zoom on the 2D shell mesh used for the computation

The results presented in the next section and the experimental validation were obtained for a total current of 110 A (mean current density: $0.5 \ A/cm^2$), corresponding to an average

cell voltage of 0.7 V at the conditions summarized in Table III.7. The inlet temperature of the cooling water, which is a boundary condition of the model, is fixed to 77°C. The corresponding flow rate (inlet boundary condition) is 20 $l/h/cell$.

Experimental parameters	H2	Air
Inlet temperature [°C]	80	80
Inlet relative humidity [%]	50	50
Inlet pressure [bar]	1,5	1,5
Stoichiometry	1,5	2

Table IVI.7: Inlet conditions of the reactant gases

4.3. Model validation

a) Local heat source

Figure III.18 shows the distribution of the measured current density and the corresponding local heat produced in the cathode catalyst layer. This local heat source is obtained through Eq. [III.29] based on the local current measured by the S++ Sensor Plate and the cell potential.
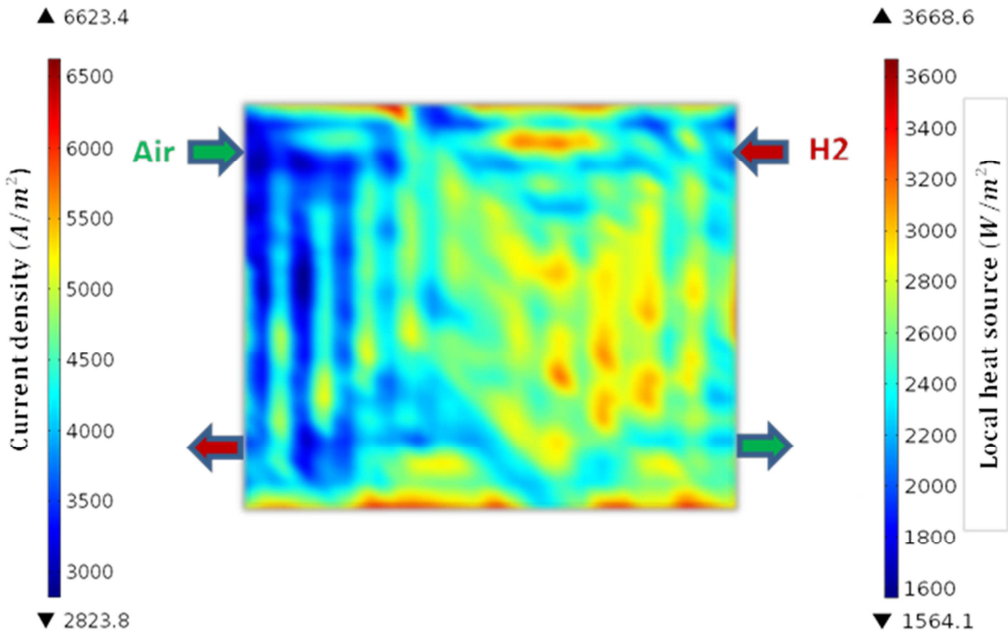
Figure III.18 : Current density and corresponding heat power density in the cell

The current density distribution and thus the heat source are higher close to the air outlet, because of the inlet conditions of the reactant gases and the GDL behavior. Indeed, the relative humidity at the air inlet in the reference conditions presented above is not sufficient to fully hydrate the membrane. As a consequence, current densities and corresponding heat sources remain rather small at the inlet part of the cell ($\sim 3500 \ A/m^2$). From the inlet to the outlet of the air flow, the progressive production of water because of the electrochemical reaction increases the water content of the membrane, and so increases its proton conductivity. This phenomenon induces an increase of the current density ($\sim 5500 \ A/m^2$) and the corresponding heat sources at the outlet because of irreversible and entropic losses.

It is also possible to observe local variations and oscillations of current density along the cell surface. This is due to the heterogeneities of the bipolar plates welding zones, which represent preferential paths for current.

b) Pressure distribution in the bipolar plate channels

Figure III.19 shows the pressure evolution in the anode, cathode and cooling water channels. For the reactive gases, a regular pressure drop and consequently a constant velocity is obtained in the channels. This is coherent with the non-connected parallel serpentine structure of the bipolar plates and the non-resolution of the species transport. This approximation is justified by the little impact of the concentration change on heat transport.
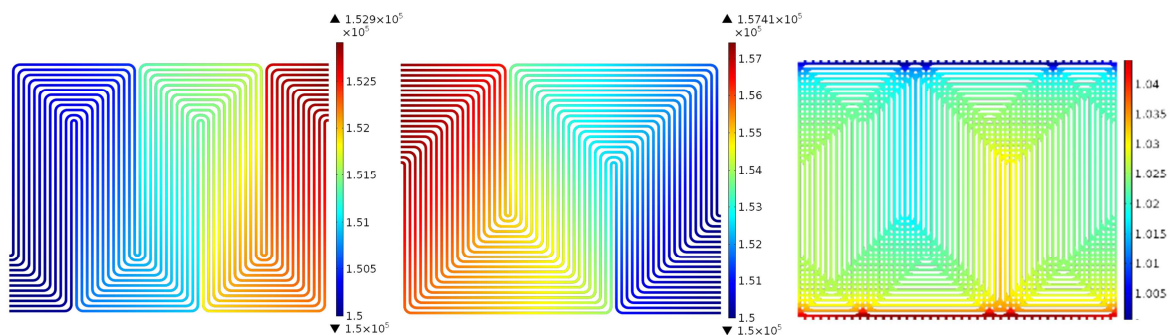
Figure III.19 : Pressure distribution (Pa) in the anode (left), cathode (middle) and cooling water (right) channels

For the cooling water, there are high pressure heterogeneities due to the complex geometry and the disposition of the channels as presented in Fig.III.15. Indeed, the cross flow zones which are heterogeneously distributed in the channels induce high singular pressure drops and so high velocity heterogeneities in the cooling flow. Nevertheless, the obtained symmetry of the pressure distribution is coherent with the geometry.

The fluid dynamic model is validated globally through a comparison of experimental and simulated overall pressure drop in the channels. In particular, for the cooling water which is the most complex flow, the experimental and simulated overall pressure drops are respectively 30 and 27 mbar. The small difference between these two values could be due to the fact that the pressure drop in the manifolds is not taken into account in the model.

Regarding the local validation, an experimental investigation of the local velocity is impossible because of the complex geometry of the flow field. Nevertheless, a local validation through a comparison with a full 3D Navier-Stokes model used for the design of the cell has been performed. The reference 3D Navier-Stokes model considers boundary layers and friction/wall interaction and is computed using Finite Volume Method. The comparison of the results obtained from the Darcy-Weisbach and the Navier-Stokes approaches at a reference cut line (see Fig.III.20) shows that the Darcy-Weisbach approach is able to capture the velocity distribution in the different channels of the cooling circuit.
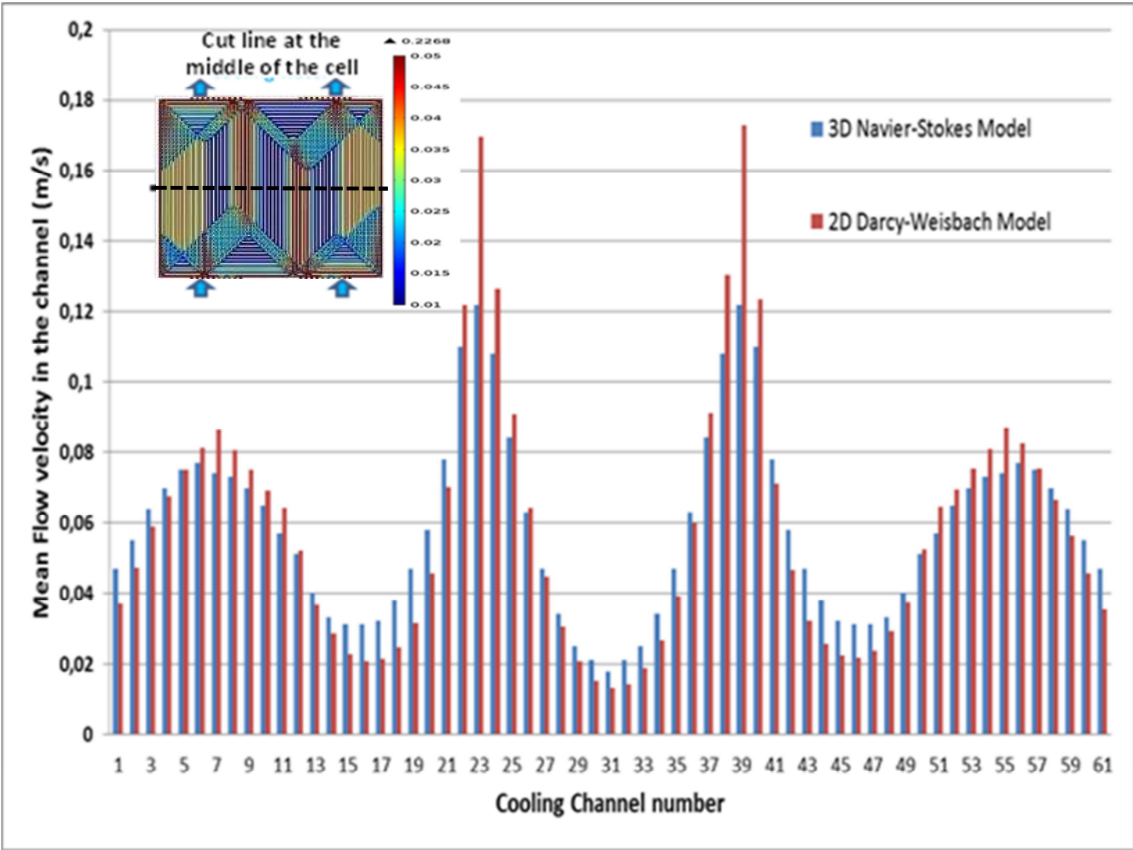
Figure III.20 : Comparison of the local velocities at the indicated cut line: 2D Darcy-Weisbach vs 3D Navier-Stokes model

In conclusion, the Darcy-Brinkman approach represents definitely a good method to resolve the compromise between the calculation time and the precision, especially in the cross

flow points. With the equivalent friction factors and Nusselt numbers in the channels it is no more necessary to compute the boundary layer gradients.

c) Thermal model validation

The thermal model including the Sensor plate is validated globally and locally. For the global validation, a comparison is made between the measured and simulated temperatures of the cooling water at the inlet and outlet of the cell. For an outlet temperature of the cooling water fixed at 353 K, the experimental and computed inlet temperatures are respectively 350 and 349.9 K. From these values, it can be stated that the model accurately predicts the global change in temperature of the cooling water from the inlet to the outlet of the stack.

For the local validation, a comparison between the measured and computed in-plane temperature distribution in the S++ sensor plate is presented in Fig.III.21.
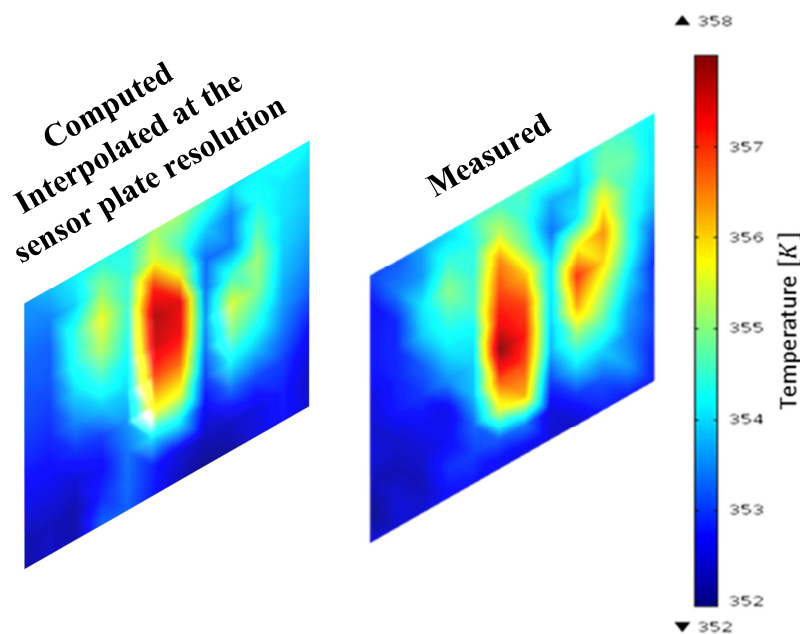
Figure III.21 : Comparison of the computed (left) and measured (right) temperature distributions in the sensor plate.

A very good agreement is observed between the simulated and the measured temperature. The heterogeneous temperature is well captured with a good localization of the hot zones over the cell surface and a good prediction of magnitude. Three hot zones are observed on the simulated and experimental temperatures. The measured temperature varies from ∼ 352 to ∼ 357.5 K meanwhile the computed one ranges from ∼ 352 to ∼ 358 K.

The temperature differences between the cathode catalyst layer and the bipolar plate ac vary from 3 to 6°C. This result is in a good agreement with the through-plane temperature simulated using the full 3D model at the channel/rib scale (see section 2.5.a).

4.4. Results of the pseudo-3D model and discussion

a) Temperature prediction at the cell scale

Once the model including the sensor plate is validated, the classical model is used to predict the temperature in all the components of a conventional cell, without the intrusive measurement device, from the bipolar plates to the membrane. The temperature distribution in some components of the cell is presented in Fig.III.22. The first observation is that there are more heterogeneities in the real temperature distribution of the bipolar plates than the temperature measured by the sensor plate. So the sensor plate just captures a part of the real temperature heterogeneities because of its in-plane thermal conduction and invasiveness. The hot zones in the middle and close to the air outlet are greater than the one close to the air inlet. First, their location can be related to the location of the three zones of very low cooling water velocity (Fig. III.20). Furthermore, the observed temperatures in the hot zones in the middle and close to air outlet are amplified by the high values of the current density distribution (Fig.III.18) in the corresponding zones.
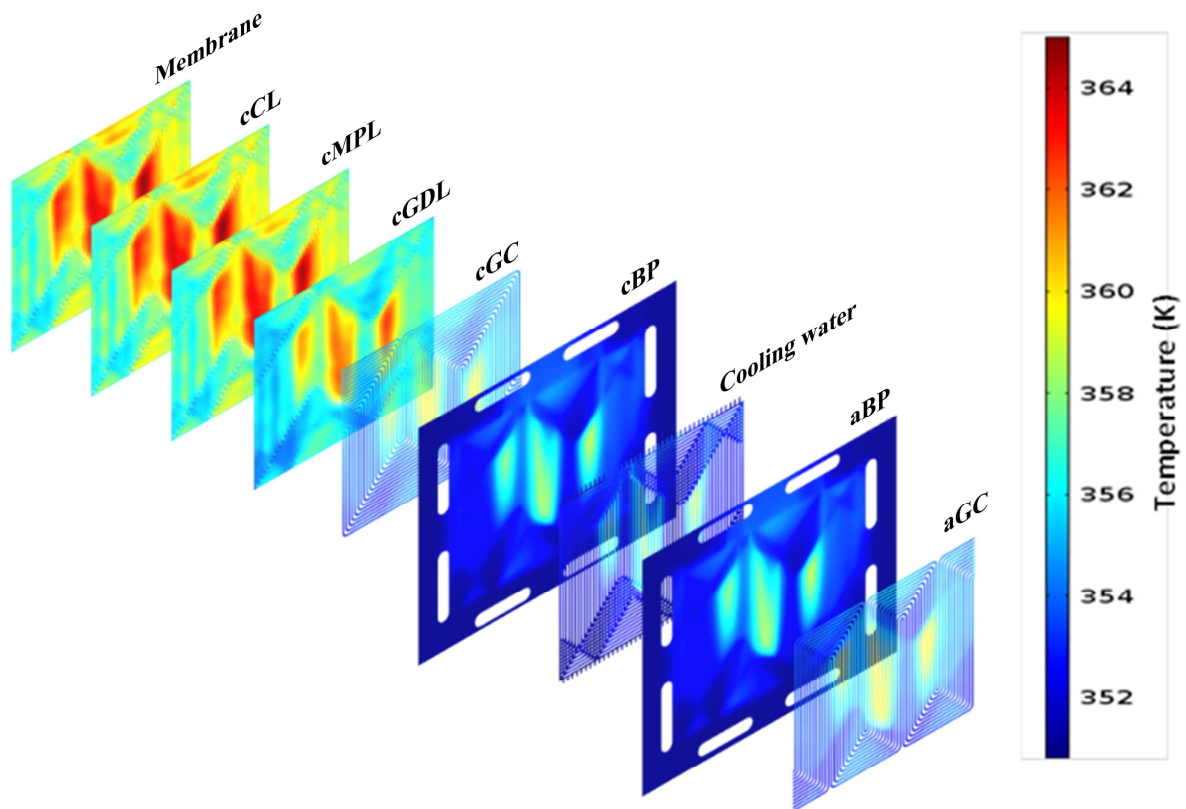
Figure III.22 : Temperature distribution in the components of the cell

The model allows predicting the in-plane temperature of each cell component and the through-plane temperature difference between the components. It is observed that despite the outlet temperature of cooling water is set to 80°C, there are some zones where the bipolar plate temperature reaches 85°C. As a consequence, in those hot zones the MEA temperature reaches 90°C. This value of local temperature can accelerate the degradation of the membrane due to the attack of free radicals [25].

The in-plane temperatures ranges are ~ 79 - 85°C, 81 – 87.5°C, 82 – 89°C, and 82.5 – 90°C respectively for the bipolar plates, GDLs, MPLs and MEA. Hot zones are systematically observed where the velocity of the cooling water is the lowest and where the current density is the highest. Nevertheless, the temperature variation is different between the components. In particular, the in-plane temperature variations are around 7.5°C for the membrane and catalyst layers meanwhile in the bipolar plates the variations are smoother and reduced to ~ 6°C. This means that the GDL and bipolar plate contribute to in-plane temperature homogenization. That observation is due to the high thermal conductivity of the bipolar plates and the anisotropy of the GDLs, which have an in-plane thermal conductivity higher than the through-plane thermal conductivity with a ratio about 20. For that reason, the GDLs thermal conductivity is essential in optimizing the heat management of the cell. This observation is in good agreement with the results presented by Ju et al. [72].

The temperature heterogeneities are mainly controlled by the coolant flow field design inside the bipolar plates because hot zones are located where the velocity of the cooling water is lowest. At the reference cut line at the middle of the cell (see Fig.III.23), it is observed that when the cooling flow velocity varies from 0.12 to 0.03 m/s (see Fig. III.20), the corresponding membrane temperature varies from 82 to 89 °C.

The local heat source heterogeneities (see Fig.III.18) also have a significant effect on temperature distribution. When the local heat source varies from ~ 1900 to ~ 3000 W/m^2, the membrane temperature in the corresponding zones varies from ~ 84 to 86°C. Note that the cooling flow velocity in both zones considered for the comparison is almost the same.

This simulation gives more precision on the decomposition of the temperature differences between the bipolar plates and the catalyst layers. The following values are obtained for the mean temperature differences between the components: 0.1 °C between the membrane and the cCL, 0.4 °C between the cCL and the cMPL, 1.7 °C between the cMPL and the cGDL, and 2.3°C between the cGDL and the cBP. The two monopolar plates (cBP and aBP) that compose the bipolar plate have almost the same in-plane temperature. That is due to the low thermal resistance between them because they are welded together.
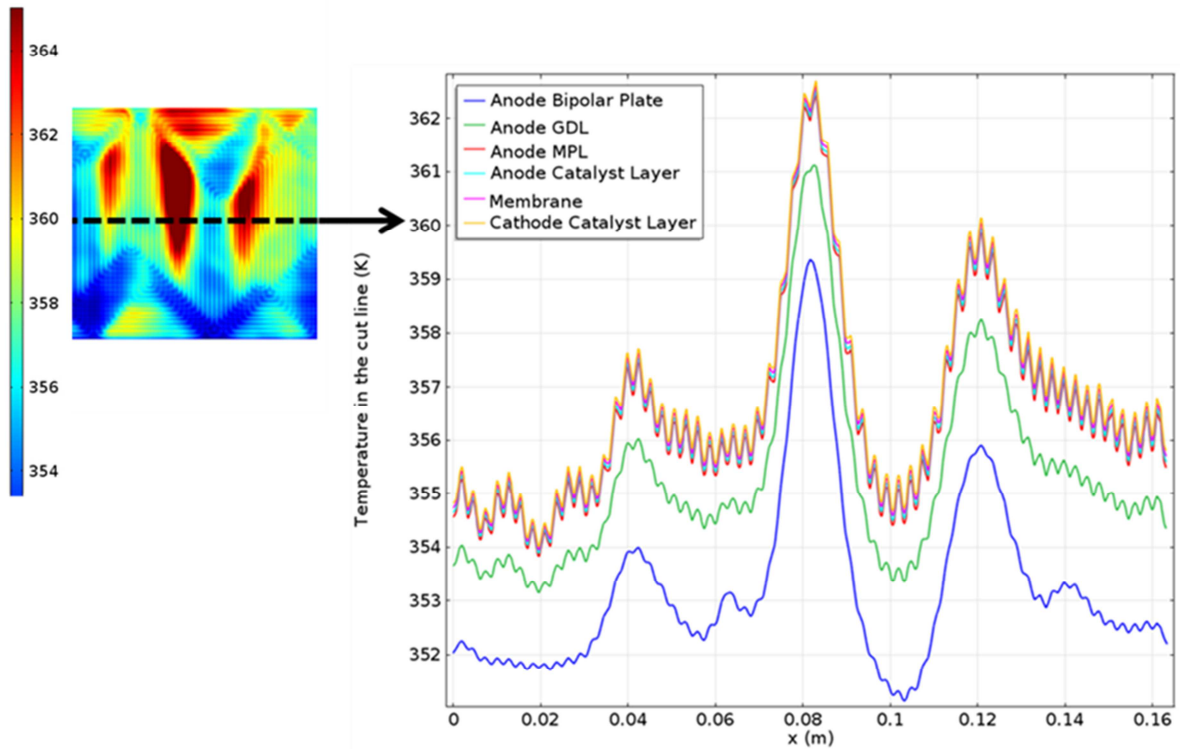
Figure III.23 : Temperature distribution in some cell components at the indicated cut line

b) Effect of uncertainty of heat sources localization on the temperature distribution

Since in the model it was assumed that all the entropy and electrochemical activation heats were located in the cathode catalyst layer, the impact of the uncertainty about heat source localization on the temperature distribution needs to be evaluated.

In the following figure, some results of this sensitivity analysis are presented for the anode compartment. In case 1, it is assumed that all the heat is generated in the cathode CL. In Case 2, it is assume that 25 % of the heat is generated in the anode catalyst layer. The results show that the heat source repartition has a small effect only on the catalyst layer temperature, for which the two curves are not perfectly superposed, the deviation being around 0.05°C. For all the other components, the difference cannot even be seen on this figure. The temperature distribution in the remaining components is almost insensitive to the heat source repartition between the catalyst layers.
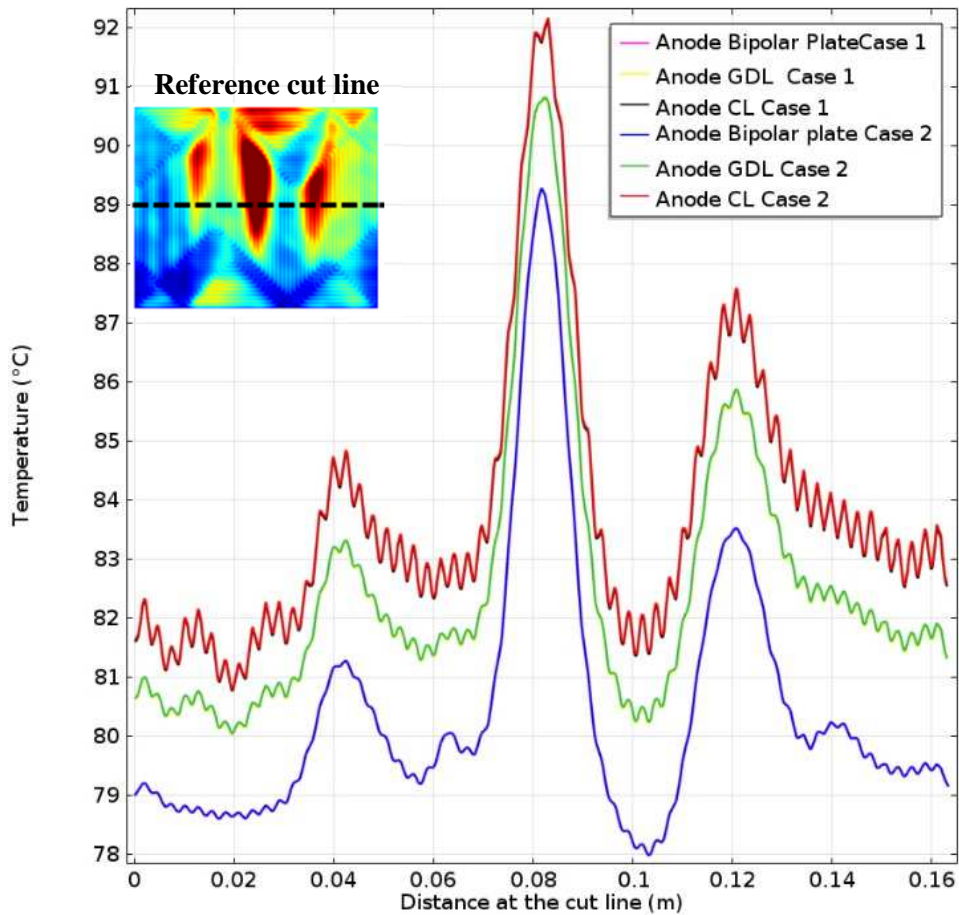
Figure III.24 : Temperature distribution in some cell components at the indicated cut-line: effect of uncertainty of heat sources localization on the temperature distribution

c)   Temperature prediction at the Channel/rib scale

The Fig.III.25 presents the temperature difference between the cathode catalyst layer and the bipolar plate on a segment of the cell active area. This temperature difference varies from ~ 3 to 6°C. The zones where the temperature differences are the lowest corresponds to direct thermal contact between the MEA and the cooling circuit. They are adjacent to high temperature difference zones, corresponding to thermal contact between the MEA and reactant gases channels. The spatial variation of this temperature difference can induce heat pipe effect when there is phase change in the cell (for higher current densities) [68]. Moreover, the difference in the current density distribution due to the fact that the diffusion is faster in the area under the channel is not taken into account in this study, but may intensify the channel/rib effect. The model predicts that the spatial variation of the temperature differences is not homogeneous over the cell active area and so the heat pipe effect may not be homogeneous. This can induce heterogeneities on the performance and MEA degradation.
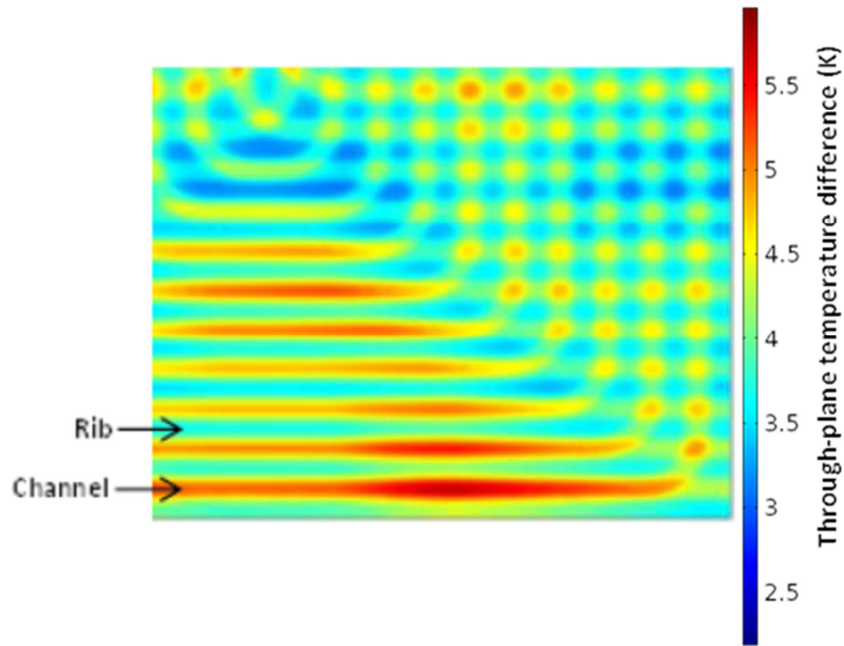
Figure III.25 : Temperature difference between cBP and cCL: visualization of the channel/rib heterogeneities on a piece of the cell

Conclusion

In this chapter, the thermal conductivities of the fuel cell components were reviewed and used to study temperature evolution in the cell via a 3D model at the channel/rib scale. In order to address the specific challenge of the balance between accuracy and computational time, a pseudo-3D thermo-fluidic model was presented to investigate the local temperature in the industrial large-area fuel cell used in this study (220 cm^2), with the resolution at the same time of the heat sources and heat removal. The model was first successfully validated against experimental data (S++) and then used for in-plane and through-plane temperature analysis in the cell. The main conclusions and discussions of the study can be drawn as follows: hot zones are observed in the cell due firstly to the heterogeneous flow velocity of the cooling water and secondly to the local current density heterogeneous distribution. It is worth mentioning that the flow regime is laminar and thus particularly unfavorable to intensive convective heat transfer. On the one hand, the heterogeneities of the local heat sources (current density distribution) depend on local concentration of reactants, water content of membrane, and local temperature. These local conditions are mainly controlled by the inlet conditions of the reactant gases, the gas channels design and the fluid dynamics. On the other

hand, the heterogeneities of the cooling water flow (local heat removal) depend on the cooling channels design. In other words, the local temperature is mainly controlled by the design of the bipolar plates and the inlet conditions of the reactant gases.

The pseudo 3D approach can be easily applied to other cell designs in different operating conditions. Indeed, the 2D (in plane) real geometry of the channels is considered in the model and the impact on temperature of other designs could be studied. The best advantage of this approach is that the thermal model developed is purely predictive. It allows a detailed study of the in plane temperature distribution in all the components of the stack and the pseudo-3D approach allows reaching a good precision with low computation time and resources.

Nevertheless, the limit of the applicability occurs when there is a considerable phase change in the cell because the local condensation/evaporation phenomena can have a non-negligible impact on the energy equation. Furthermore, the present model uses measured current densities for the calculation of the electrochemical local heat source. So for a completely predictive multiphysics model, the thermal model should be coupled with an electrochemical model in which the species transport and the electrochemical reactions are computed in order to predict the current density distribution (and heat source). Thus, the next step of this model could take into account the latent heat of condensation/evaporation. Nevertheless, solving the electrochemical equations means new assumptions and hypothesis as well as a pseudo-3D species transport model, which has to be very accurate in order to avoid lower precision on the heat source distribution calculation.

<div align="center">

Chapter IV

A PSEUDO-3D MULTIPHYSICS MODEL TO INVESTIGATE COUPLED HEAT AND WATER TRANSPORT IN LARGE AREA P.E.M. FUEL CELLS

Summary

</div>

Introduction

The pseudo-3D approach developed in the previous chapter has proven its worth as an efficient way in modeling the in-plane temperature heterogeneities in the different cell components for industrial scale fuel cells. However, the model was limited firstly by its dependence on the sensor plate current measurement and secondly by the assumption of constant physical properties for the reactive gases. To become a completely predictive model, the proposed thermal model should be coupled to an electrochemical model in which the species transport and the electrochemical reactions are computed in order to predict the current density distribution in the cell. Furthermore, in the frame of the study of the correlation between thermal effects and degradations, an accurate study of water transport is necessary since temperature is intrinsically coupled to water transport. It is commonly known that humidity largely impacts on hydrothermal stresses in the membrane [96-97] [101] as well as metallic bipolar plates corrosion [145]. In general, coupling water management to heat management remains a global challenge for the development and commercialization of PEM fuel cells [146].

In this chapter, a hybrid physic-based model is developed and validated experimentally against the measured data obtained from the printed circuit board. The model considers the cell as a multi-layered system and each layer is accurately in-plane discretized to allow the simulation of local heterogeneities. The transport equations are solved using a pseudo-3D approximation and coupled to an analytical electrochemical model for the current density prediction. The main advantage of the model is the prediction of the current density, species concentrations, water content and temperature distributions in all the components of the cell with a low computation time compared to full 3D model, while keeping a good precision. It represents a potent instrument for the study of the correlation between local temperature, humidity and degradations.

1. Model development and governing equations

The studied stack has the same configuration as the one presented in Chapter III, section 4.1.a. It is a 30 cells stack, with a printed circuit board inserted between the 15th and the 16th cells for the measurement of the in-plane current density and temperature distributions.

1.1. Pseudo-3D formulation of the conservation equations

In this model, the equations of the continuity, momentum, species and heat balance for each component n of the cell under steady state conditions are built with the same methodology as the 3D thermal model presented in Chapter III. The model considers ideal gases for the reactants and uniform cell voltage along the cell surface.

Given the aspect ratio of the different cell components, the idea of the pseudo-3D approach is to consider each component as a plane layer, which is coupled to the other components through appropriate exchange conditions, like the pseudo-3D thermal model presented in Chapter III. With this approach, it is thus possible to compute the 2D (in-plane) distribution of the different physical parameters (temperature, species concentration…) in each cell component (active layers, gas diffusion layers, membrane, bipolar plates, cooling circuit…) at a reasonable cost. The transformation from the full-3D to the pseudo-3D formulation is presented in the following for each equation. The nomenclature is the same as used in the Chapter III.

a) Continuity

Considering de pseudo-3D approach, which integrates the conservation equation over the thickness of the component, one gets in stationary conditions:

$$\nabla_{xy} \cdot (\rho \, \vec{v}) + \frac{1}{e_n} \int_{z_{n-1}}^{z_n} \frac{\partial}{\partial z}(\rho u_z) dz = S_m \qquad [IV.1]$$

with $\vec{v} = u_x \vec{i} + u_y \vec{j}$ the in-plane velocity and u_z the through-plane velocity. ρ and S_m are respectively the mean density and mass source along the thickness of the component. The integration of the through-plane mass transport term leads to:

$$\frac{1}{e_n} \int_{z_{n-1}}^{z_n} \frac{\partial}{\partial z}(\rho u_z) dz = \frac{\rho(z_n) u_z(z_n) - \rho(z_{n-1}) u_z(z_{n-1})}{e_n} \qquad [IV.2]$$

The mean density can be discretized as:

$$\rho(z_n) = \frac{\rho_n e_n + \rho_{n+1} e_{n+1}}{e_n + e_{n+1}} \quad and \quad \rho(z_{n-1}) = \frac{\rho_n e_n + \rho_{n-1} e_{n-1}}{e_n + e_{n-1}} \qquad [IV.3]$$

The mass transport equation becomes (*Pseudo-3D formulation*):

$$\nabla_{xy} \cdot (\rho \vec{v}) = S_m + \phi^+ + \phi^- \qquad [IV.4]$$

with the following through-plane mass fluxes:

$$\phi^+ = \frac{\rho(z_n) u_z(z_n)}{e_n} \quad and \quad \phi^- = -\frac{\rho(z_{n-1}) u_z(z_{n-1})}{e_n} \qquad [IV.5]$$
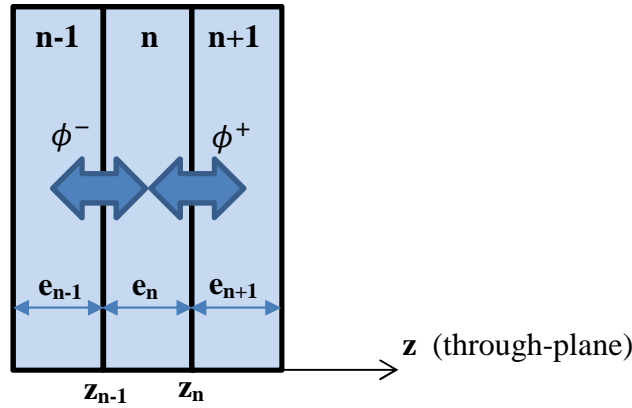
Figure IV.1 : Reference coordinates and fluxes used in the equations for the conservation equations in the component *n*, which exchanges with the components *n-1* and *n+1*

b)   Momentum equation

The global equation of momentum, considering no singular pressure drop and no momentum diffusion across the cell is:

$$\nabla p = \frac{1}{K_1} \mu \vec{u} + \frac{1}{K_2} \|\vec{u}\| \vec{u} \leftrightarrow \begin{cases} \nabla_{xy} p = \dfrac{1}{K_1} \mu \vec{v} + \dfrac{1}{K_2} \|\vec{v}\| \vec{v} \\ \dfrac{1}{e_n} \displaystyle\int_{z_{n-1}}^{z_n} \dfrac{\partial p}{\partial z} dz = -\dfrac{1}{K_1} \mu u_z \end{cases} \qquad [IV.6]$$

where p is the mean pressure along the thickness of the component. The discretization of the through-plane momentum equation leads to:

$$u_z(z_{n-1}) = -\frac{K(z_{n-1})}{\mu} \left[\frac{p_n - p_{n-1}}{\frac{(e_n + e_{n-1})}{2}} \right]; \qquad u_z(z_n) = -\frac{K(z_n)}{\mu} \left[\frac{p_{n+1} - p_n}{\frac{(e_{n+1} + e_n)}{2}} \right] \qquad [IV.7]$$

with the equivalent values of the hydraulic permeability discretized as follows:

$$K(z_{n-1}) = \frac{e_n + e_{n-1}}{\frac{e_n}{K_n} + \frac{e_{n-1}}{K_{n-1}}}; \qquad K(z_n) = \frac{e_n + e_{n+1}}{\frac{e_n}{K_n} + \frac{e_{n+1}}{K_{n+1}}}$$ [IV.9]

c) Species conservation

The pseudo-3D formulation for the species i conservation equation is:

$$\nabla_{xy} \cdot (\rho w_i \vec{v}) + \frac{1}{e_n} \int_{z_{n-1}}^{z_n} \frac{\partial}{\partial z}(\rho w_i u_z) dz = -\nabla_{xy} J_i - \int_{z_{n-1}}^{z_n} \frac{\partial}{\partial z}(J_{i_z}) dz + S_i$$ [IV.10]

where ρw_i, J_i and S_i are respectively the mean species concentration, diffusion flux and species source along the thickness of the component. The evaluation of the through-plane species transport terms is given by:

$$\frac{1}{e_n} \int_{z_{n-1}}^{z_n} \frac{\partial}{\partial z}(\rho w_i u_z) dz = \frac{\rho w_i(z_n) u_z(z_n) - \rho w_i(z_{n-1}) u_z(z_{n-1})}{e_n}$$ [IV.11]

with:

$$\rho w_i(z_{n-1}) = \frac{(\rho w_i)_n e_n + (\rho w_i)_{n-1} e_{n-1}}{e_n + e_{n-1}}; \quad \rho w_i(z_n) = \frac{(\rho w_i)_n e_n + (\rho w_i)_{n+1} e_{n+1}}{e_n + e_{n+1}}$$ [IV.12]

The Fick's law of diffusion for the through-plane species transport is discretized as:

$$\frac{\partial}{\partial z}(J_{i_z}) dz = \frac{\partial}{\partial z}\left(-D \frac{\partial(\rho w_i)}{\partial z}\right)$$

$$= -\frac{D(z_{n-1})((\rho w_i)_n - (\rho w_i)_{n-1})}{e_n{}^2} + \frac{D(z_n)((\rho w_i)_{n+1} - (\rho w_i)_n)}{e_n{}^2}$$ [IV.13]

Where D is the equivalent mass diffusivity of the reactive species and:

$$D(z_{n-1}) = \frac{e_n + e_{n-1}}{\frac{e_n}{D_n} + \frac{e_{n-1}}{D_{n-1}}}; \qquad D(z_n) = \frac{e_n + e_{n+1}}{\frac{e_n}{D_n} + \frac{e_{n+1}}{D_{n+1}}}$$ [IV.14]

Thus, the species transport equation becomes (*Pseudo-3D formulation*):

$$\nabla_{xy} \cdot (\rho w_i \cdot \vec{v}) = -\nabla_{xy} J_i + S_i + \phi_i^+ + \phi_i^- + J_i^+ + J_i^-$$ [IV.15]

With the through-plane convective fluxes:

$$\phi_i^+ = \frac{\rho w_i(z_n) u_z(z_n)}{e_n} \ and \ \phi_i^- = -\frac{\rho w_i(z_{n-1}) u_z(z_{n-1})}{e_n}$$ [IV.16]

And the through-plane diffusive fluxes:

$$J_i^+ = \frac{D(z_n)\big((\rho w_i)_{n+1} - (\rho w_i)_n\big)}{e_n^{\ 2}} \ and \ J_i^- = \frac{D(z_{n-1})\big((\rho w_i)_{n-1} - (\rho w_i)_n\big)}{e_n^{\ 2}} \qquad \text{[IV.17]}$$

d)   Heat transport

Pseudo-3D formulation (demonstrated in chapter 3, section 4):

$$\vec{v} \cdot \nabla_{xy}(\rho c_p T) = \lambda \cdot \nabla_{xy}^{\ 2} T + S_T + J_T^+ + J_T^- \qquad \text{[IV.18]}$$

Heat is transported via conduction in all the solid components and via convection in the bipolar plate channels. So, only one-phase (solid) heat transfer in considered in the porous media.

Discretization of the in-plane diffusive heat fluxes (see Chapter 3 for the demonstration):

$$J_T^- = -\frac{U(z_{n-1})(T_n - T_{n-1})}{e_n} \ \ and \ \ J_T^+ = \frac{U(z_n)(T_{n+1} - T_n)}{e_n} \qquad \text{[IV.19]}$$

With the global through-plane heat transfer coefficients:

$$U(z_{n-1}) = \frac{e_n + e_{n-1}}{\frac{e_n}{\lambda_n} + TCR_{n/n-1} + \frac{e_{n-1}}{\lambda_{n-1}}}; \quad U(z_n) = \frac{e_n + e_{n+1}}{\frac{e_n}{\lambda_n} + TCR_{n/n+1} + \frac{e_{n+1}}{\lambda_{n+1}}} \qquad \text{[IV.20]}$$

Where $TCR_{n/m}$ is the eventual thermal contact resistance between the components n and m. In particular, it plays an important role at the BP/GDL and GDL/MPL interfaces.

1.2.   Interfaces between the solid/porous components and the fluid flows in the channels

At the interfaces between the solids/porous and fluids subsystems (GDLs/reactive gases flow, BPs/cooling flow, BPs/reactive gases flow), appropriate exchange conditions are used. The model assumes plug flows in the channels (anode reactive gases, cathode reactive gases and coolant flows). The computed parameters in the flows are coupled at the interfaces with the adjacent cell components (GDLs and BPs) using the transfer coefficients presented in the following.

a)   Mass transfer coefficient

For the species transfer at the reactive gases flow/GDL interface, the convection mass transfer number used is:

$$H = Sh \cdot \frac{D}{D_h} \qquad \text{[IV.21]}$$

Where D, D_h and Sh are respectively the mass diffusivity, the hydraulic diameter and the Sherwood number. The Sherwood number is calculated using the Frössling correlation:

$$Sh = 2 + 0.552 \cdot Re^{1/2} \cdot Sc^{1/3} \qquad \text{[IV.22]}$$

Sc is the Schmidt number, which represents the ratio of momentum diffusivity and mass diffusivity:

$$Sc = \frac{\nu}{D} \qquad \text{[IV.23]}$$

b) Convective heat transfer coefficient

For the solid/fluid heat transfer, the convective heat transfer coefficient is calculated via the Nusselt number Nu which only depends on the geometry since the flows are laminar.

$$h = Nu \frac{\lambda}{D_h} \qquad \text{[IV.24]}$$

The appropriate Nusselt numbers adapted for the geometry in the laminar as well as in the chaotic zones are the same as presented in Chapter III.

The transport equations are coupled to the current density in the catalyst layers through appropriate source terms related to the electrochemical reaction.

1.3. Semi-empirical electrochemical model

The electrochemical model is obtained by inversing the Butler-Volmer equation presented in Chapter I:

$$\begin{aligned} U_{cell} = E_{rev} + \beta_1 + \beta_2 T + \beta_3 T ln(i) + \beta_4 T ln(P_{O_2}) \\ + \beta_5 T ln(P_{H_2O}) + \beta_6 T ln(P_{H_2}) - R_m i - R_{cell} i \end{aligned} \qquad \text{[IV.25]}$$

Where β_i are physical parameters which depend on the thermodynamics and kinetics of the electrochemical reactions.

The reversible potential of the cell is calculated as follows:

$$E_{rev} = a_1 + a_2 T + a_3 T ln(P_{O_2}) + a_4 T [ln(P_{H_2}) - ln(P_{H_2O})] \qquad \text{[IV.26]}$$

with

$$a_1 = \frac{\Delta G_0}{2F} = 1.4824 \, V \; ; \; a_2 = -\frac{\Delta S_0}{2F} = -1.593 \cdot 10^{-3} \frac{V}{K}; \; a_3 = \frac{R}{4F} = 2.154 \cdot 10^{-5} \frac{V}{K} \; ; \; a_4 = 2 \, a_3 \qquad \text{[IV.27]}$$

ΔG_0 (J/mol) and ΔS_0 (J/mol/K) are respectively the Gibbs free energy and the entropy variation of the electrochemical reaction in reference conditions.

R_m is the membrane protonic resistance defined as:

$$R_m = \frac{e_m}{\sigma_m} \qquad \text{[IV.28]}$$

where e_m and σ_m are respectivelly the membrane thickness and ionic conductivity, whose calculation will be presented below. R_{cell} is the electrical resistance of the cell. For its calculation, an electrical model of the cell resistance, will is presented in the next section, is used.

a) Electrical resistance of the cell R_{cell}

The local electrical resistance of the cell is evaluated considering the electrical architecture of the cell at the channel/rib scale and the heterogeneities of the welding zone positions over the BP active area which induce preferential paths for current transport. These zones are indicated in Fig.IV.2, where the welding points (blue) are superimposed on the cathode flow field geometry (white) and cathode ribs (grey):
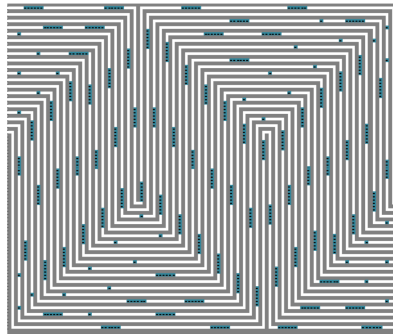
Figure IV.2 : Reference zones used for the electrical model

In the electrical model, two different zones are distinguished:

➢ BPs rough contact zones (grey on Fig.IV.2), in which there is a relatively low electrical conduction between the two sheets of the BP because of the rough contact:

$$R_{cell} = R_{MEA} + ECR_{GDL/BP} + R_{BP} + ECR_{BP/BP} \qquad \text{[IV.29]}$$

➢ BPs welded contact zones (blue on Fig.2), in which there is a relatively high electrical conduction between the two sheets of the BP thanks to the welding;

$$R_{cell} = R_{MEA} + ECR_{GDL/BP} + R_{BP} + ECR_{Welding} \qquad \text{[IV.30]}$$

Where $ECR_{BP/BP}$ is the electrical contact resistance between the rough BPs and $ECR_{Welding}$ is the electrical contact resistance on the welding zones of the BPs.

b) Membrane ionic conductivity σ_m

The membrane ionic conductivity is calculated using the Springer's law [26]:

$$\sigma_m = (33{,}75 \cdot \lambda_M - 21{,}41)e^{-\frac{1268}{T}}$$

[IV.31]

Where λ_m is the water content of the membrane obtained from an appropriate electrolyte water transport model.

1.4. Water transport through the membrane

Before presenting the membrane water transport model, it is worth reminding the water content of the membrane, defined as the number of water molecules per sulfonic acid group:

$$\lambda_M = \frac{c_{H_2O}}{c_f}$$

[IV.32]

Where c_{H_2O} is the water concentration (mol/m^3) and c_f is the molar concentration of sulfonate sites in Nafion:

$$c_f = \frac{\rho_M}{EW}$$

[IV.33]

with ρ_M the density of the membrane solid phase ($\rho_M = 2240 \ kg/m^3$) and EW the equivalent weight of Nafion ($EW = 1.1 \ kg/mol$). The water content at the interfaces between the Nafion and the pores of the catalyst layers (λ_{aCL} and λ_{cCL}) is obtained from the Springer's law:

$$\lambda(a) = \begin{cases} 0{,}043 + 17{,}81a - 39{,}85a^2 + 36a^3 & if \ a \le 1 \\ 14 + 1{,}4(a - 1) & if \ a > 1 \end{cases}$$

[IV.34]

with the activity a which is defined as:

$$a = \frac{P_{H_2O}}{P_{sat}(T)}$$

[IV.35]

So the discontinuity of the water content dependence on activity at the saturation point, resulting from the Schroeder's paradox, is considered in the model. However, in the numerical implementation, there is an interpolation at the saturation point in order to smooth the discontinuity and avoid numerical instabilities.

The water transport through the membrane is a resulting balance between electro-osmosis drag from anode to cathode and molecular diffusion from cathode to anode. The hydraulic permeation of water through the membrane due to the pressure gradient and the thermos-osmosis transport due to the temperature gradient are negligible.

a) Water electro-osmosis drag flux through the membrane

The water electro-osmosis drag flux is due to the polar attraction of the water molecules by the protons. The transport of protons from anode to cathode through the electrolyte induces a drag of water molecules at the same time. The flux of water dragged from anode to cathode is given by:

$$F_{eo} = \frac{a_{eo} M_{H_2O} i}{F}$$

[IV.36]

With a_{eo} the electro-osmosis drag coefficient, defined as the number of water molecules dragged per proton. It is well-known that it depends on water content, but there are different laws for this dependence in literature with large discrepancies. Springer et al. proposed a linear relationship [26], Hwang et al. [147] and F. Meier et al. [148] proposed a quadratic evolution. Zawodzinski et al. proposed a discontinuous relationship [149]. These laws are presented in Tab.I.1.

Author	Model
Springer [26]	$a_{eo} = \dfrac{2.5\,\lambda_M}{22}$
Hwang et al. [147]	$a_{eo} = -3.4 \cdot 10^{-19} + 0{,}05\,\lambda_M + 0{,}0029\,\lambda_M{}^2$
F. Meier et al. [148]	$a_{eo} = 1 + 0{,}028\,\lambda_M + 0{,}0026\,\lambda_M{}^2$
Zawodzinski et al. [149]	$a_{eo} = \begin{cases} 1 & if\ \lambda_M \leq 14 \\ 0.1875\,\lambda_M - 1.625 & if\ \lambda_M > 14 \end{cases}$

Table IV.1 : Different laws for the dependence of the electro-osmosis drag coefficient on water content

The law proposed by Zawodzinski is used in this study because it represents a kind of tradeoff for the discrepancies of the existing laws. For comparison, the different laws are plotted on the same graph on Fig. IV.3.
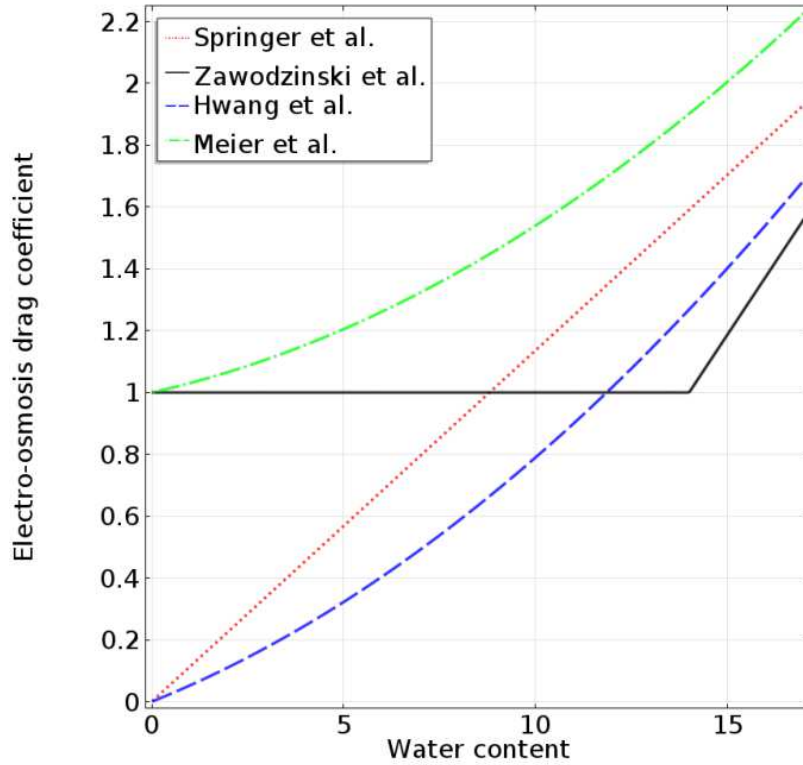
Figure IV.3 : Comparison between the different laws for the dependence of the electro-osmosis drag coefficient on water content

b) Diffusive flux through the membrane

The diffusion of water molecules in the membrane is caused by the water content gradient between the cathode catalyst layer where water is produced and the anode catalyst layer. The diffusive flux from the cathode to the anode catalyst layer is expressed by considering a Fick's law:

$$J_{H2O}^{-} = \frac{1}{e_{aCL}} \cdot \left(\frac{D_m}{e_m}\right) \cdot M_{H_2O} \cdot c_f \cdot (\lambda_{cCL}(a) - \lambda_{aCL}(a)) \qquad \text{[IV.37]}$$

Analogously, the diffusive flux from the anode to the cathode catalyst layer is:

$$J_{H2O}^{+} = \frac{1}{e_{cCL}} \cdot \left(\frac{D_m}{e_m}\right) \cdot M_{H_2O} \cdot c_f \cdot (\lambda_{aCL}(a) - \lambda_{cCL}(a)) \qquad \text{[IV.38]}$$

The membrane equivalent water content is evaluated as:

$$\lambda_M = \frac{\lambda_{aCL}(a) + \lambda_{cCL}(a)}{2} \qquad \text{[IV.39]}$$

It is commonly admitted that the membrane water diffusivity D_m depends on water content and temperature. The different models for such dependence found in literature are summarized in Table IV.2.

Author	Model
Fuller [150]	$D_m = 2.1 \cdot 10^{-7} \lambda_M \cdot \exp(-\dfrac{2436}{T})$
Nguyen and White [151]	$D_m = (1.94 \cdot 10^{-8} \lambda_M + 1.76 \cdot 10^{-9}) \cdot \exp(-\dfrac{2436}{T})$
Zawodzinski et al. [152]	$D_m = (6{,}707 \cdot 10^{-8} \lambda_M + 6{,}387 \cdot 10^{-7}) \cdot \exp\left(-\dfrac{2416}{T}\right)$
Hwang et al. [147]	$D_m = D(\lambda_M) \cdot exp\left[2416\left(\dfrac{1}{303} - \dfrac{1}{T_m}\right)\right]$ With $D(\lambda_M) = \begin{cases} 10^{-10} & if\ \lambda < 2 \\ 10^{-10}[1 + 2(\lambda - 2)] & if\ 2 \le \lambda \le 3 \\ 10^{-10}[3 - 1.67(\lambda - 3)] & if\ 3 \le \lambda \le 4.5 \\ 1.25 \cdot 10^{-10} & if\ \lambda \ge 4.5 \end{cases}$
Motupally [153]	$D_m = \begin{cases} 3.10 \cdot 10^{-7} \lambda_M [\exp(0.28\lambda_M) - 1] \cdot \exp(-\dfrac{2346}{T}) & if\ 0 \le \lambda_M \le 3 \\ 4.17 \cdot 10^{-8} \lambda_M [1 + 161 \cdot \exp(-\lambda_M)] \exp\left(-\dfrac{2346}{T}\right) & if\ 3 \le \lambda_M \le 17 \end{cases}$

Table IV.2 : Different laws for the dependence of the membrane water diffusivity on water content

As illustrated in Fig.IV.4, there are variations of the diffusivity reported in literature over several orders of magnitude due mainly to the difference in measuring methods and membrane material. In this study, the diffusivity's law used is Motupally one because of its agreement with experimental data (within 5%).
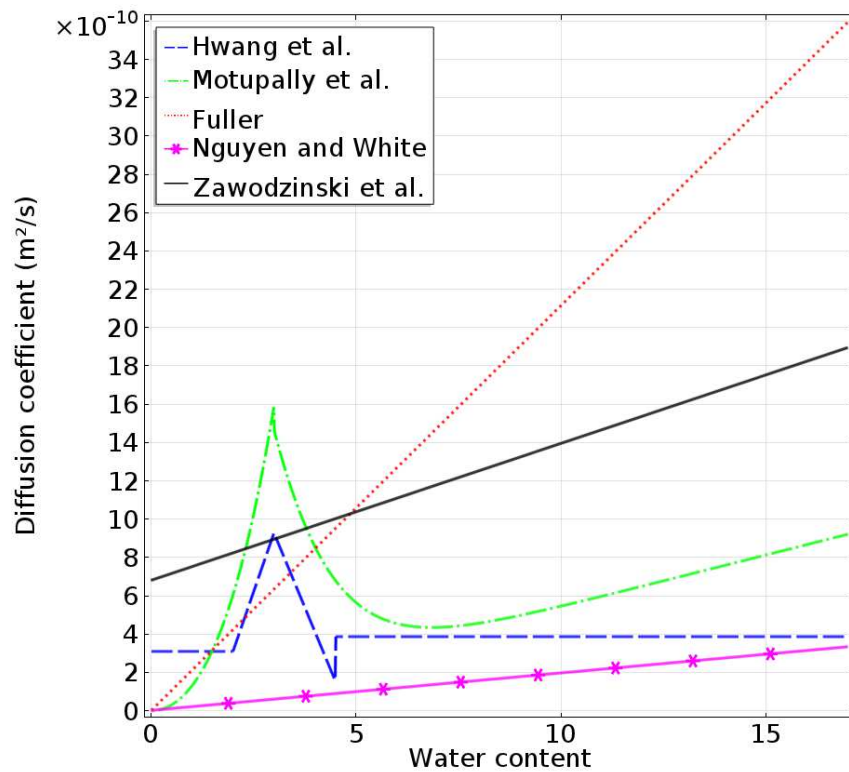
Figure IV.4 : Comparison between the different laws for the dependence of the membrane water diffusivity on water content

1.5. Summary of the equations

In summary, the global pseudo-3D model resolves 2D in-plane equations in each layer of the system with appropriate through-plane heat fluxes between the components. The global equations and related sources terms are summarized in Tab.IV.3.

Quantity	Equation
Mass	$\nabla_{xy}(\rho \cdot \vec{v}) = S_m + \phi_m^+ + \phi_m^-$
Momentum	$\nabla_{xy} p = \dfrac{1}{K_1}\mu\vec{v} + \dfrac{1}{K_2}\|\vec{v}\|\vec{v}$
Species	$\nabla_{xy} \cdot (\rho w_i \cdot \vec{v}) = -\nabla_{xy}J_i + S_i + \phi_i^+ + \phi_i^- + J_i^+ + J_i^-$
Heat	$\rho c_p \vec{v} \cdot \nabla_{xy}T = \lambda \cdot \nabla_{xy}{}^2 T + S_T + J_T^+ + J_T^-$
Current	$U_{cell} = E_{rev} + \beta_1 + \beta_2 T + \beta_3 Tln(i) + \beta_4 Tln(P_{O_2}) + \beta_5 Tln(P_{H_2O}) + \beta_6 Tln(P_{H_2}) - R_m i - R_{cell} i$

Table IV.3 : Global equations solved in the model for each component

The sources terms for the conservation equations in each subsystem are presented in Tab.IV.4:

Component	S_m	S_i	S_T
Channels	0	0	0
BPs, GDLs, MPLs (n)	0	0	$\dfrac{i^2}{\sigma_n}$
Anode CL (aCL)	$-\dfrac{1}{e_{aCL}} \cdot \left(\dfrac{M_{H_2}i}{2F} + \dfrac{a_{eo}M_{H_2O}i}{F}\right)$ $+$ $\dfrac{1}{e_{aCL}} \cdot \dfrac{D_m}{e_m} \cdot M_{H_2O} \cdot c_f \cdot [\lambda_{cCL}(a) - \lambda_{aCL}(a)]$	$S_{H_2} = -\dfrac{1}{e_{aCL}} \cdot \dfrac{M_{H_2}i}{2F}$	$\dfrac{i^2}{\sigma_{aCL}}$
Cathode CL (cCL)	$\dfrac{1}{e_{aCL}} \cdot \left(-\dfrac{M_{O_2}i}{4F} + \dfrac{M_{H_2O}i}{2F} + \dfrac{a_{eo}M_{H_2O}i}{F}\right)$ $+$ $\dfrac{1}{e_{aCL}} \cdot \dfrac{D_m}{e_m} \cdot M_{H_2O} \cdot c_f \cdot [\lambda_{cCL}(a) - \lambda_{aCL}(a)]$	$S_{O_2} = -\dfrac{1}{e_{cCL}} \cdot \dfrac{M_{O_2}i}{4F}$ $S_{H_2O} = \dfrac{1}{e_{cCL}} \cdot \left(\dfrac{M_{H_2O}i}{2F} + \dfrac{a_{eo}M_{H_2O}i}{F}\right)$ $+$ $\dfrac{1}{e_{cCL}} \cdot \dfrac{D_m}{e_m} \cdot M_{H_2O} \cdot c_f \cdot [\lambda_{aCL}(a) - \lambda_{cCL}(a)]$	$\dfrac{1}{e_{cCL}} \cdot \left[\left(\dfrac{\Delta H_{tot}}{2 \cdot F} - V_{cell}\right) \cdot i\right]$ $+ \dfrac{1}{e_{cCL}} \cdot \left[-\Sigma_j \dfrac{i^2}{\sigma_j}e_j\right] + \dfrac{i^2}{\sigma_{cCL}}$ Where j represents all the components of the cell, excepted the cCL
Membrane	0	0	$\dfrac{i^2}{\sigma_m(\lambda, T)}$

Table IV.4 : Sources terms used in the mass, momentum, species and heat balance equations

In order to consider the possibility of water vapor/liquid phase change in the cell at high currents, the total reaction enthalpy used is:

$$\Delta H_{tot} = \Delta H_l = 285.8 \; kJ/mol_{H_2} \; \text{if} \; P_{H_2O} = P_{sat}(T)$$

$$\Delta H_{tot} = \Delta H_v = 242 \; kJ/mol_{H_2} \; \text{if} \; P_{H_2O} < P_{sat}(T)$$

[IV.40]

Where P_{H_2O} is the water vapor partial pressure in the cathode catalyst layer and $P_{sat}(T)$ is the equilibrium vapor pressure, calculated with the Antoine equation:

$$P_{sat}(T) = 101325 \cdot \exp\left(11.6703 - \frac{3816.44}{T - 46.13}\right) \; [Pa]$$

[IV.41]

Thus, the enthalpy of phase change is considered, even if there is the assumption of ideal gases for the gas flows.

1.6. Input data and solution procedure

The calculation of the transport properties of the reactant species, which depend on temperature, is given in Appendix 3. The input data used in this study are presented in Table IV.5:

Parameter	BP	GDL (Channel/rib variation)		MPL	CL	Membrane
Thickness [mm]	$2 \cdot 0.1$	Channel: 0.23		0.05	aCL: 0.006 cCL: 0.012	0.025
		Rib: 0.17				
Thermal conductivity λ [W/m/K]	16.1	In-plane	Channel: 5.4	0.4	0.15	$0.177 + 3.7 \cdot 10^{-3} \cdot \lambda_M$
			Rib: 3.7			
		Through-plane	Channel: 0.2			
			Rib: 0.3			
Charge conductivity σ [S/m]	$1.32 \cdot 10^6$	In-plane	Channel: 4862	50	1000	$(33{,}75 \cdot \lambda_M - 21{,}41)e^{-\frac{1268}{T}}$
			Rib: 3460			
		Through-plane	Channel: 64			
			Rib: 184			
Porosity		Channel: 0.77		0.35	0.47	
		Rib: 0.69				
Permeability [m²]		$2.6 \cdot 10^{-13}$		$2 \cdot 10^{-13}$	10^{-12}	
Tortuosity		1.23		1.7	1.3	

Table IV.5 : Input data used in the model

The electrochemical model is calibrated globally on a 5 cm² active area laboratory cell using a set of 18 different polarization curves recorded at the different partial pressures, temperatures and humidity values in the cell. The obtained values of the calibrated parameters are given in Table IV.6.

β_1	β_2	β_3	β_4	β_5	β_6
$-0.75384 \; V$	$3.39 \cdot 10^{-4} \; V/K$	$-7.84 \cdot 10^{-5} \; V/K$	$1.298 \cdot 10^{-4} \; V/K$	$0 \; V/K$	$5.13 \cdot 10^{-5} \; V/K$

Table IV.6 : Parameters used in the electrochemical model

The electrical contact resistances between rough BPs and in the welding zones of the BPs are fixed respectively $ECR_{BP/BP} = 3.6 \cdot 10^{-6} m^2 V/A$ and $ECR_{Welding} = 1 \cdot 10^{-6} m^2 V/A$ [154].

Thus, the global electrical resistance of the cell is $R_{cell} = 4.9 \cdot 10^{-6} m^2 V/A$ under the welding contact zones and $R_{cell} = 7.5 \cdot 10^{-6} m^2 V/A$ under the rough contact zones.

2. Model validation

2.1. Electrochemical model validation

a) Global validation

The operating conditions used for these simulations are summarized in Table IV.7. The cooling flow rate of the cell is set to $\dot{m}_{cw} = 6 \ g/s$ (0.36 l/min) and cooling water temperature at the cell outlet is $T_{cw}^o = 80°C$.

Modeling parameters	Anode	Cathode	Cooling water
Inlet temperature [°C]	85	85	T_{cw}^o $-\dfrac{\left(\frac{\Delta H}{2F} - U\right) \cdot I}{\dot{m}_{cw} \cdot c_p}$
Inlet pressure P [bar]	1.5	1.5	1.5
Inlet RH [%]	50	50	
Stoichiometry Sto	1.5	2	
Species mass fractions	$w_{H_2} = \dfrac{1}{1 + X_a}$ $w_{H_2O} = 1 - w_{H_2}$ with $X_a = 9.01 \cdot RH \cdot \dfrac{P_{sat}(T_{cw}^o)}{P - RH \cdot P_{sat}(T_{cw}^o)}$	$w_{O_2} = \dfrac{0.222}{1 + X_c}$ $w_{H_2O} = \dfrac{X_c}{1 + X_c}$ $w_{N_2} = 1 - w_{O_2} - w_{H_2O}$ with $X_c = 0.622 \cdot RH \cdot \dfrac{P_{sat}(T_{cw}^o)}{P - RH \cdot P_{sat}(T_{cw}^o)}$	
Flow rate (kg/s)	$(1 + X_a) \cdot Sto \cdot \dfrac{I}{2F} \cdot M_{H_2}$	$\dfrac{1}{0.222} \cdot (1 + X_c) \cdot Sto \cdot \dfrac{I}{4F} \cdot M_{O_2}$	$6 \cdot 10^{-3}$

Table IV.7 : Reference nominal operating conditions used in the study

The electrochemical model is validated globally by comparing the predicted and the measured currents at different potentials, as presented in Fig.IV.5 on a polarization curve.
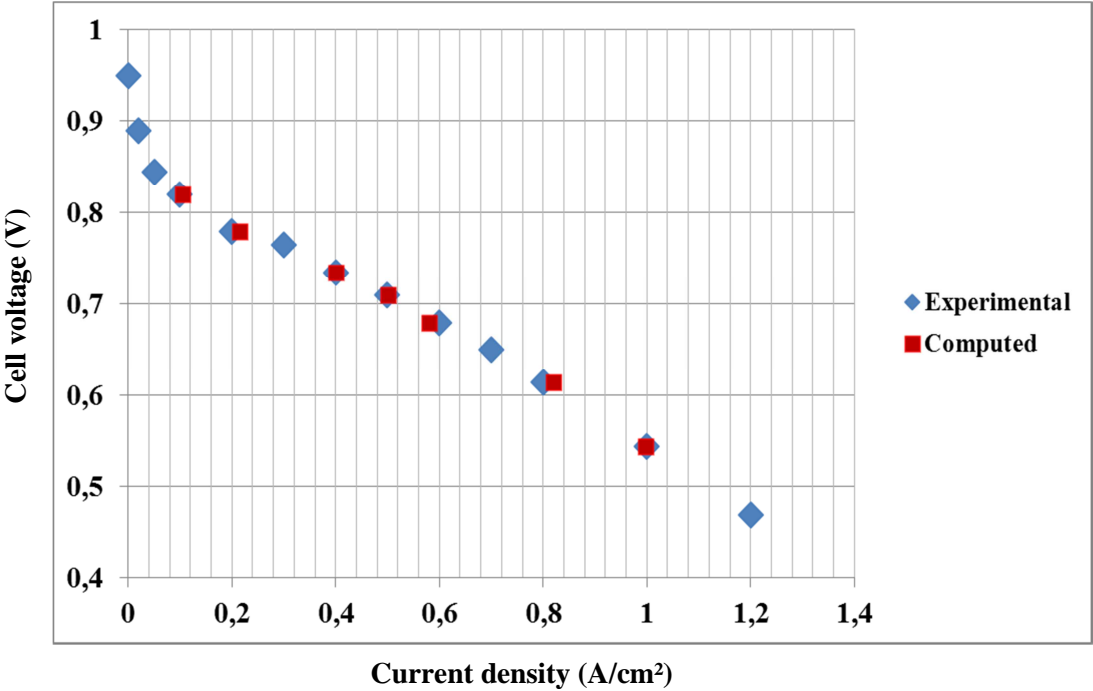
Figure IV.5 : Comparison of the computed results to the experimental polarization curve data

b) Local validation

For the local validation, a comparison between the computed current density in the MEA and the measured one with the sensor plate is made. Fig. IV.6 illustrates the comparison at a cell potential of 0.7V. An additional map of the interpolation of the simulated current density at the sensor plate current resolution is added for a better comparability.
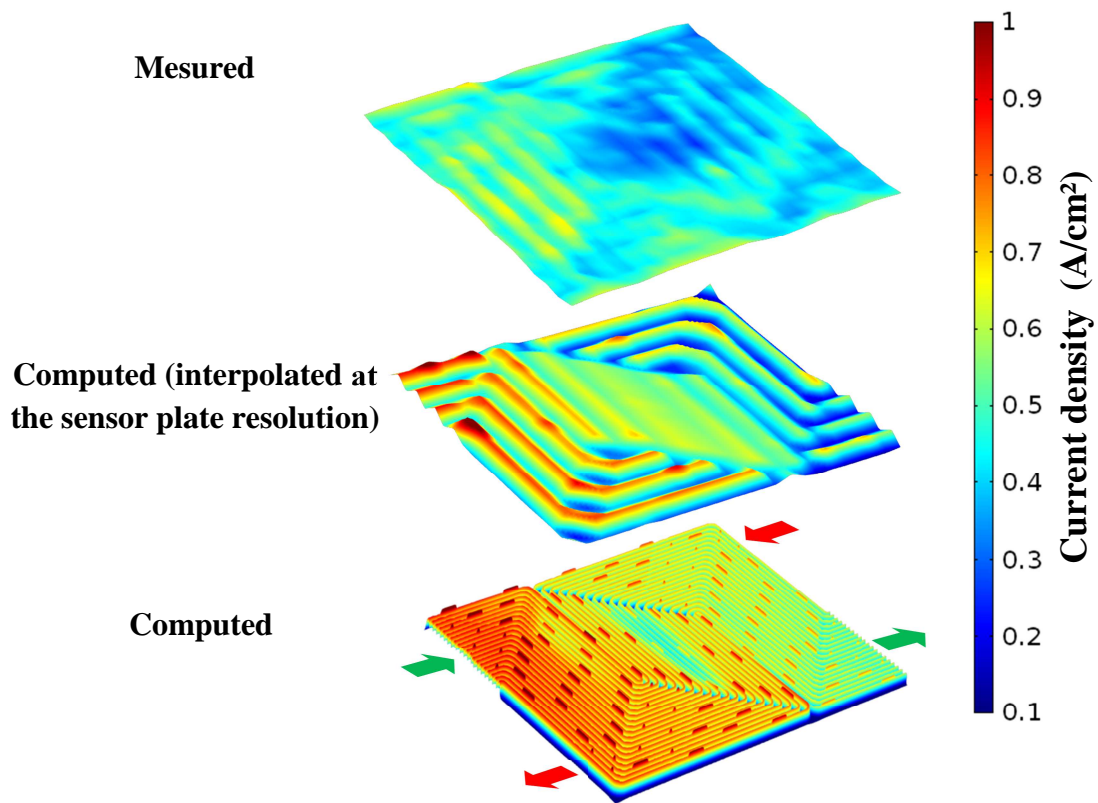
Figure IV.6 : Comparison of the measured and computed current density distributions. The arrows indicate the anode (red) and cathode (green) inlets and outlets.

In the both cases, the current is higher near the air inlet and lower near the air outlet in both experimental and simulated results. The relatively low current density at the center of the cell caused by the hot spot, which induces a local membrane drying, is captured by the model. Regarding the local values, it is not easy to make a precise conclusion because, contrary to the sensor plate, the model captures the channel/rib heterogeneities. Moreover, the local maxima of the current density distribution induced by the bipolar plates welding zones are captured by the model. Globally, it can be stated that a good agreement is observed between the simulated and the measured current densities in terms of general trends.

2.2. Thermal model validation

a) Global validation

A global validation is made by comparing the measured and simulated temperature increase of the cooling water between the inlet and outlet of the cell. Experimented and computed temperature

variations between the inlet and the outlet of the cell are respectively about 3 and 3.1 °C at a cell potential of 0.7 V. So the thermal model is validated globally with a ~ 3% error.

b) Local validation

In the multiphysics model, the configuration of the cell including the sensor plate (considered in Chapter III for the thermal model validation) is not considered. The thermal model can only be validated by comparing the BP simulated temperature to the one obtained from the sensor plate temperature measurement. It is worth mentioning that the temperature heterogeneities are smoothed by the sensor plate resolution (as observed in Chapter III). This comparison is presented in Fig.IV.7, with an additional interpolation of the BP simulated temperature at the sensor plate temperature resolution (regular grid of 120 elements).
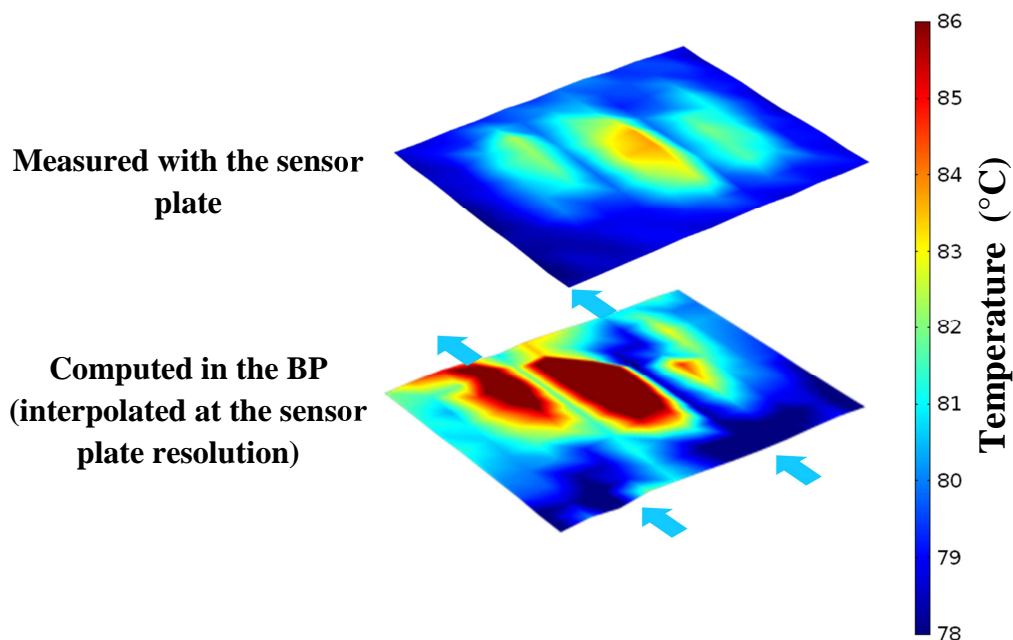
Figure IV.7 : Comparison of the measured temperature in the sensor plate and computed temperature in the bipolar plate. The arrows indicate the cooling water inlet and outlet

A good agreement is observed between the simulated and the measured temperatures regarding the general trends and localization of hot spots. Three hot zones are still observed on both the simulated and experimental temperatures, due mainly to the very low cooling water velocity in these zones (see Chapter 3, Fig.III.20). Furthermore, the observed temperatures in the hot zones close to air inlet are higher to those close to the air outlet due to the higher current density at the air inlet (Fig.IV.6).

So the heterogeneous temperature is well captured with a good localization of the hot zones over the cell surface. However, the magnitude of the temperature heterogeneities is not the same.

There are more heterogeneities in the real temperature distribution of the bipolar plate than the temperature measured by the sensor plate. The measured temperature in the sensor plate varies from ~ 78 to ~ 84 °C meanwhile the computed one in the bipolar plate ranges from ~ 78 to ~ 88 °C. These discrepancies agree with the temperature differences observed in the chapter 3 (section 4.4.a) with and without the sensor plate. Namely, the sensor plate just captures a part of the real temperature heterogeneities because of its in-plane thermal conduction and invasiveness. Moreover, in the multiphysics model, the heat sources are computed at the channel/rib level contrarily to the thermal model of the chapter 3, in which the heat sources heterogeneities were limited to the sensor plate resolution. Thus, the temperature distribution predicted with the multiphysics model presents higher heterogeneities than which ones observed in the Chapter 3.

3. Use of the model for the study of heat and water transport

Once the model is validated, it can be used to investigate the coupling effect between the electrochemical and the thermal behaviors in the cell. Due to the limitation in computational time for the simulations, in the following results, the cell discretization is limited to 6 subcomponents:

- ➢ Anode gas channels (aGC);
- ➢ Anode gas diffusion media (aGDM): combination of the anode GDL and MPL;
- ➢ Membrane Electrode Assembly;
- ➢ Cathode gas diffusion media (cGDM): combination of the cathode GDL and MPL;
- ➢ Cathode gas channels (cGC);
- ➢ Cooling channels.

3.1. Operation under nominal condition

The following simulations are performed in the same reference nominal conditions (0.7 V) used for the validation of the multiphysics model (presented in 2.1.a).

a) Water concentration distribution

The water mass concentration distribution (kg/m^3) in the cell components is presented in Fig.IV.8. Variations between   0.136 – 0.330, 0.147 – 0.356, 0.150 – 0.387 and 0.144 – 0.292 kg/m^3 are observed respectively in the anode gas channels, anode GDM, cathode GDM and cathode gas channels. The first conclusion is that the cumulative effect of reactant gases pre-humidification (at 50%), water production at the cathode due to the oxygen reduction reaction and electro-osmotic

flux from the anode to the cathode induce the highest water concentration in the cathode diffusion media. So the cathode GDM acts like a sponge which maintain a sufficient amount of water in the MEA.
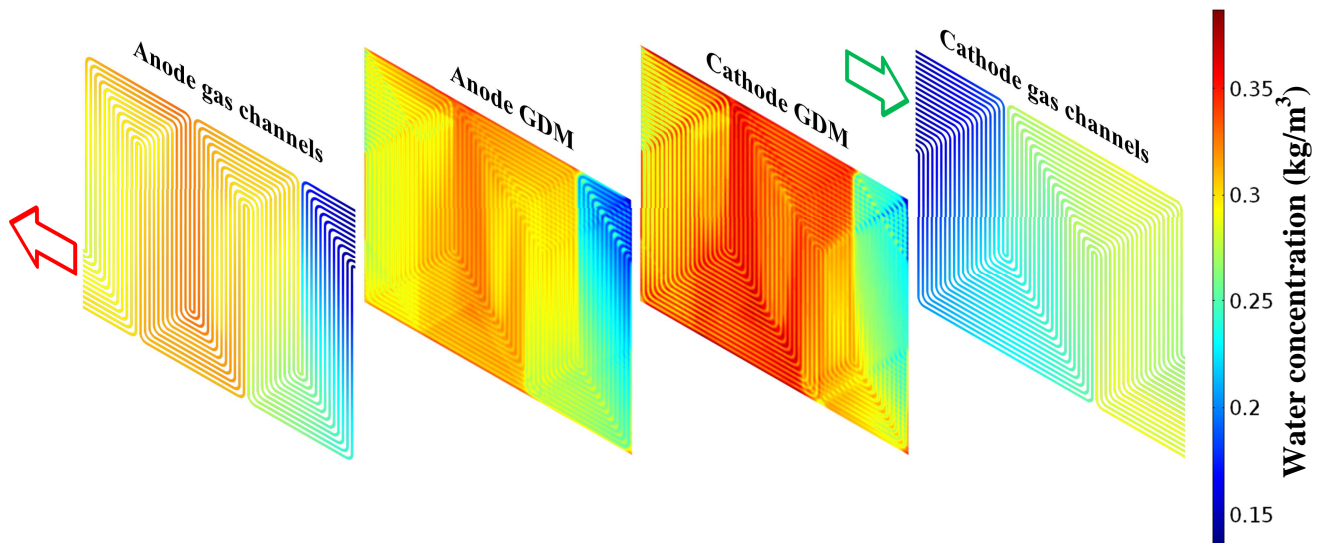
Figure IV.8 : Water mass concentration distribution in the cell components

A 1D plot at the reference cut-line at the middle of the cell is presented in Fig.IV.9. Close to the cathode inlet, the water concentration in the GDM is almost two times higher than the one in the gas channels. Contrary to the cathode gas channels, the water distribution in the anode gas channels is intrinsically coupled to the one in the anode GDM. This is due to the elevated convective transport in the cathode gas channels, compared to the anode gas channels.

Over the cathode flow field, the production of water due to the electrochemical reaction induces a progressive increase of water concentration either in the MEA, or in the channels. In particular, the water concentration in the second pass of the cathode flow field (2) is higher than the one in the first pass (1). Regarding the 3rd pass of the cathode flow field (3), water concentration becomes lower, due to the interaction with the dry flow of the hydrogen inlet. This drying effect is more emphasized in the first pass of the anode flow field (a), where the cell becomes much dryer. In this zones, the water concentration in the cathode compartment becomes higher than the one at the anode. This peculiar effect is due to the elevated flux of water from the cathode GDM to the anode compartment in order to humidify the anode gases (which are relatively dry), as it is shown in the next section.
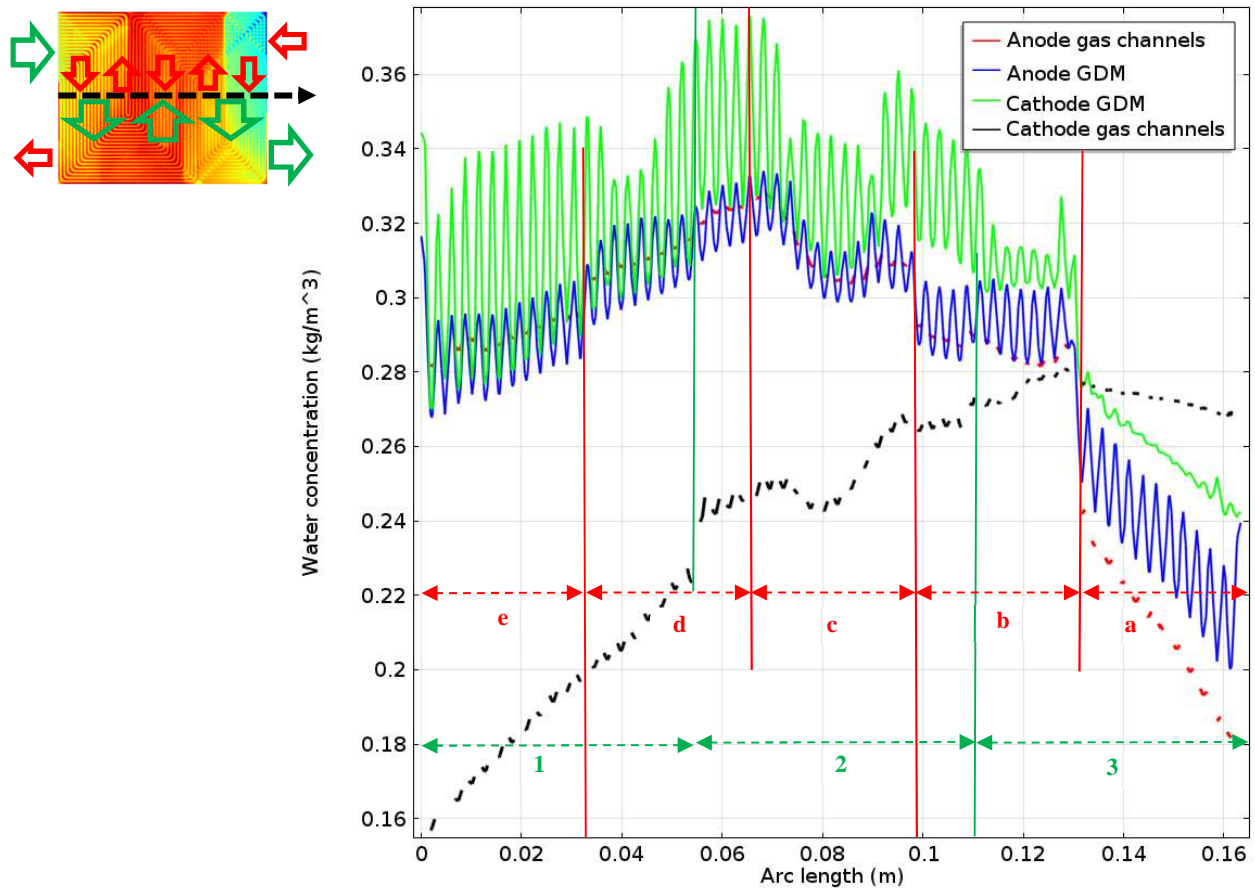
Figure IV.9 : Water mass concentration distribution in the cell components at the reference cut line. The vertical lines delimitate the different passes of the flow fields (red for the anode and green for the cathode)

As regards the channel/rib distribution, the water concentration is higher under the rib and lower under the channels with channel/rib variations about 0.02 kg/m³ for the anode GDM and 0.06 kg/m³ for the cathode GDM. Since water transport through the membrane takes place between the two GDMs, an accurate study of this phenomena may help getting more precise conclusions.

b) Water transport through the membrane

The water fluxes through the membrane, which are the result of the balance between electro-osmotic drag and molecular diffusion, is presented in Fig.IV.10. Positive fluxes (from 0 to ~ $1.71 \cdot 10^{-3} \, kg/m^2/s$) represent fluxes from cathode to anode meanwhile negative fluxes (from $\sim -1.38 \cdot 10^{-3}$ to 0 $kg/m^2/s$) are fluxes from cathode to anode. Positive fluxes mean electro-osmosis is predominating meanwhile negative fluxes mean diffusion is predominating. Accordingly to the water concentration distributions in the different components of the cell (see Fig.IV.8), water transport takes place from the anode toward the cathode close to the air inlet and conversely, from the cathode toward the anode close to the hydrogen inlet.

At the channel-rib level, the first observation is that electro-osmosis is predominant under the channels meanwhile diffusion is predominant under the ribs. It agrees with the elevated water accumulation of water which was observed under the rib due to the low water diffusion in that zone (see Fig.IV.8). The resulting water fluxes across the membrane are highly dependent on the cathode flow field design even if the first pass of the anode flow field can be distinguished. This results confirms the claim given in the previous section: the cell drying in front of the first pass of the anode flow field is related to the elevated diffusion of water from cathode to anode in this zone.
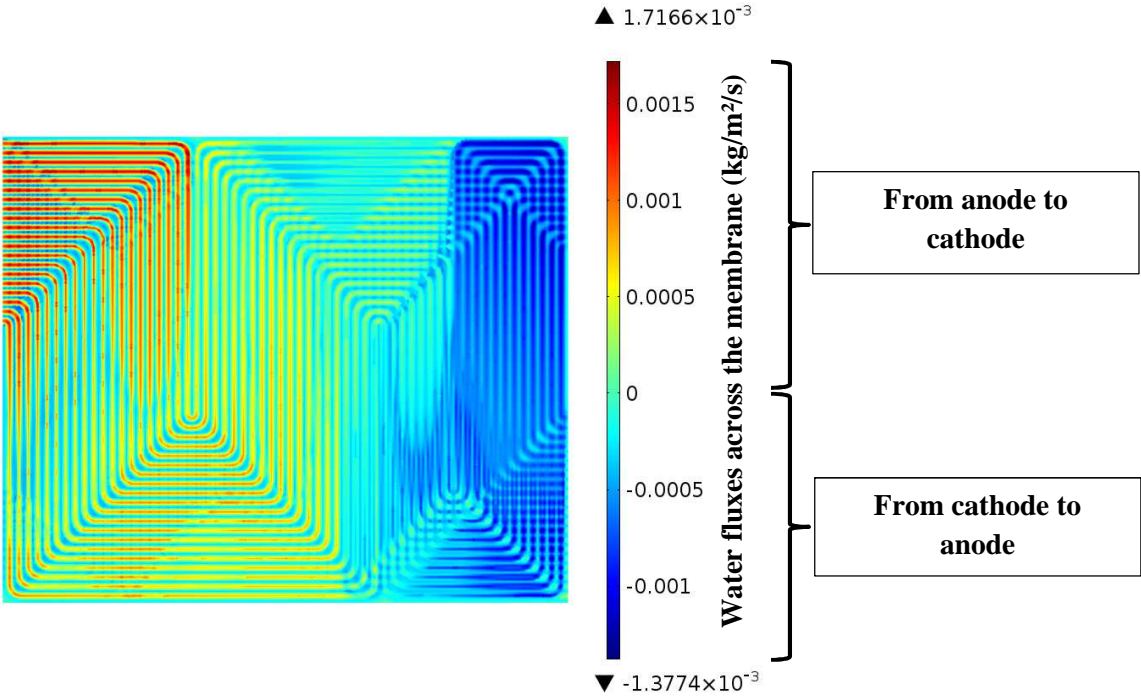
Figure IV.10 : Water fluxes across the membrane

It is also observed that hot spots induce higher fluxes from anode to cathode. This is due to the dependence of water diffusivity on water content, which is lower in the hot zones. This result is in good agreement with the observed decrease of water concentration in the cathode GDM in these zones, as presented if Fig.IV.8.

The distributions of the membrane water content, ionic conductivity, water diffusivity and electro-osmosis drag coefficient are presented in Fig.IV.11. The first observation is that the hot spots largely impact on the transport properties of the membrane. Water content, which is ~ 8 near the air inlet, reaches values < 4 in the hot spots. As a consequence, the membrane ionic conductivity is much lower in that zone, causing the lower current density observed in Fig.IV.11. The interpretation of water diffusivity is more complex since it depends on water content and temperature at the same time. Moreover, it increases with the temperature as well as with the

water content, following a non-monotonous law. The electro-osmosis drag coefficient remains quite constant ($a_{eo}=1$) in the operating conditions of the study.
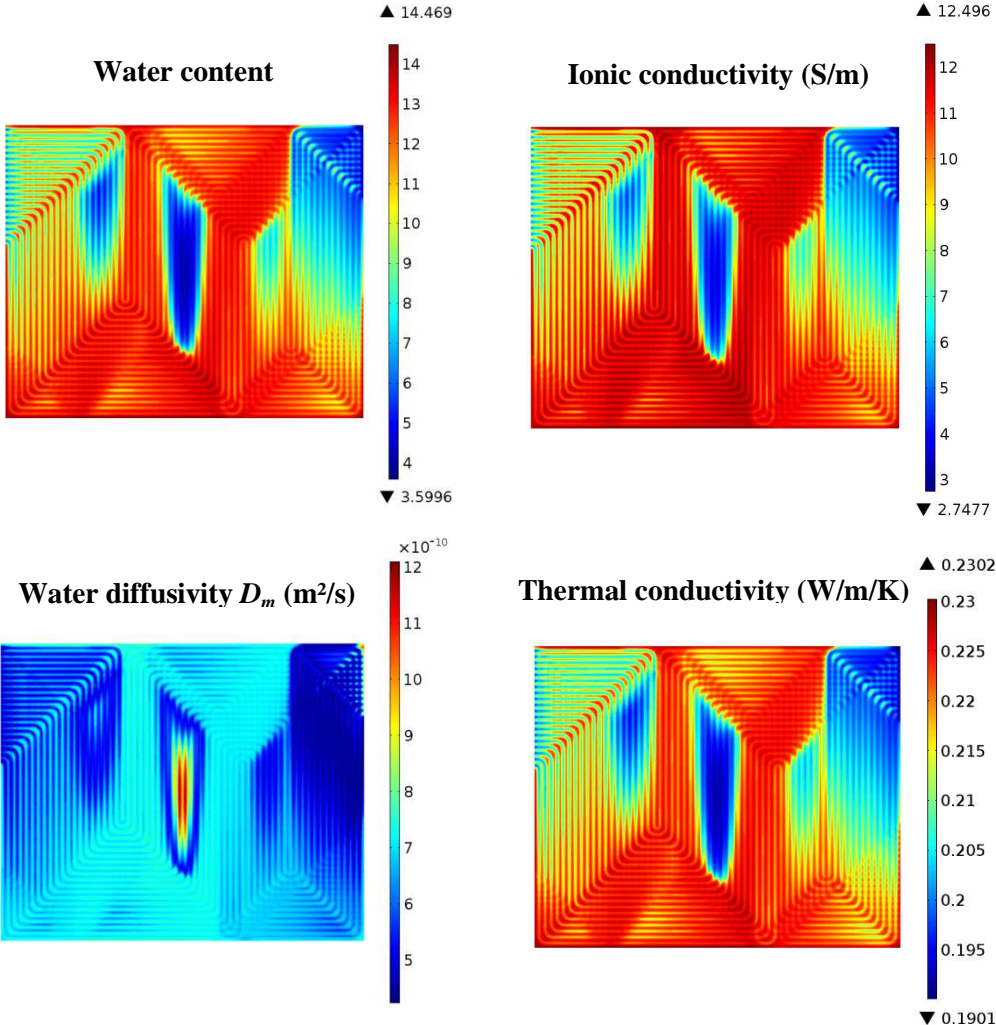
Figure IV.11 : Membrane water content, ionic conductivity, diffusivity and thermal conductivity

A representation of the water content evolution at the reference cut-line in presented in Fig.IV.12. This figure clearly highlights the impact of the three hot spots on the membrane water content. The channel/rib heterogeneities of the water content range from 0.5 to 3.5.
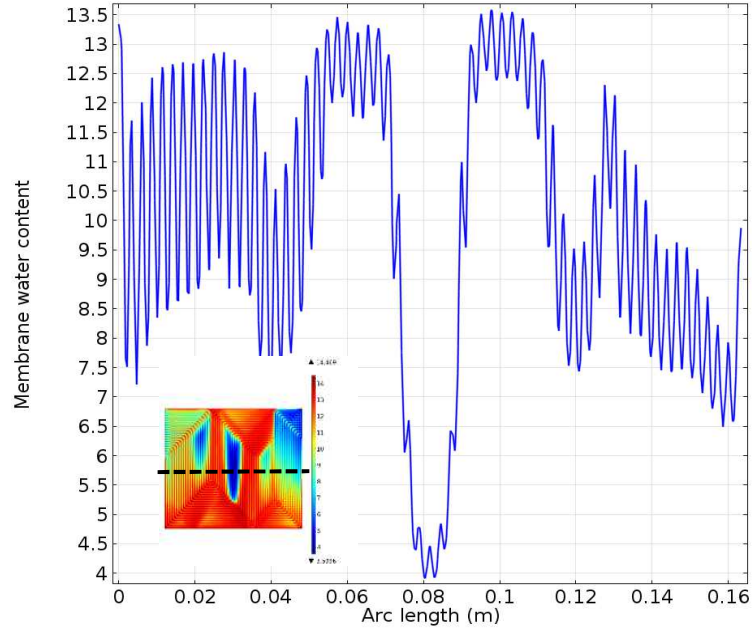
Figure IV.12 : 1D plot of the membrane water content at the reference cut line

c) Water saturation in the cell

The study of the humidity, defined as the ratio between the water vapor pressure and the water saturation pressure is more complex because of the coupled effects of temperature and water concentration distributions. Indeed, both temperature and water concentration are higher in the cathode catalyst layer where the electrochemical reaction takes place. The water vapor pressure has a linear dependence on water concentration while the water saturation pressure has an exponential dependence on temperature. The saturation (S) is defined in as:

$$S = \frac{P_{H_2O} - P_{sat}(T)}{\dfrac{\rho_l \cdot R \cdot T}{M_{H_2O}} - P_{sat}(T)}$$

[IV.42]

This saturation is defined only in the zones where there is liquid water. When there is no liquid water, its value is set to zero. At the equilibrium point, at which there is water condensation, the relative humidity is 1 and the saturation becomes higher than zero. Since in the model it is considered that the reactants are ideal gases and the liquid water flows with the same velocity as the gas, this definition of the saturation underestimates the quantity of liquid water in the gas channels. For two-phase fluid dynamics models, the liquid phase should be accurately computed with a separate density. Moreover, typical values of the velocity ratio between the gas/vapor and the liquid phase in the gas channels are between 100 and 1000 [155]. This ratio should be lower in the porous media. It is worth mentioning that the porosity as well as the fluid flow regime can also impacts on the water saturation. In few words, the saturation parameter aforementioned just

144

give qualitative results about the likely or unlikely presence of the liquid water in the cell. For appropriate quantitative results, an appropriate two-phase fluid dynamics model should be developed with the consideration of the interfacial effects as well as the capillary effects.

The distribution of such saturation in the gas channels and GDMs of the cell is presented in Fig. IV.13. It is observed that the saturation is higher in the cathode GDM despite its higher temperature. The maximal saturations are respectively $6.3 - 7.9 - 12.3$ and 3.0 (x 10^{-5}) respectively in the anode gas channels, aGDM, cGDM and cathode gas channels. The saturation distributions in the anode gas channels, aGDM and cGDM are highly coupled meanwhile the one in the cathode gas channels presents a particular evolution. This might be due to the coupled effects of high water transport via convection in the cathode gas channels and limited water transport from the cathode GDM to the cathode gas channels. The impact of the hot spots on water saturation is clearly highlighted, which means that heat and water management are highly coupled and should not be studied separately.
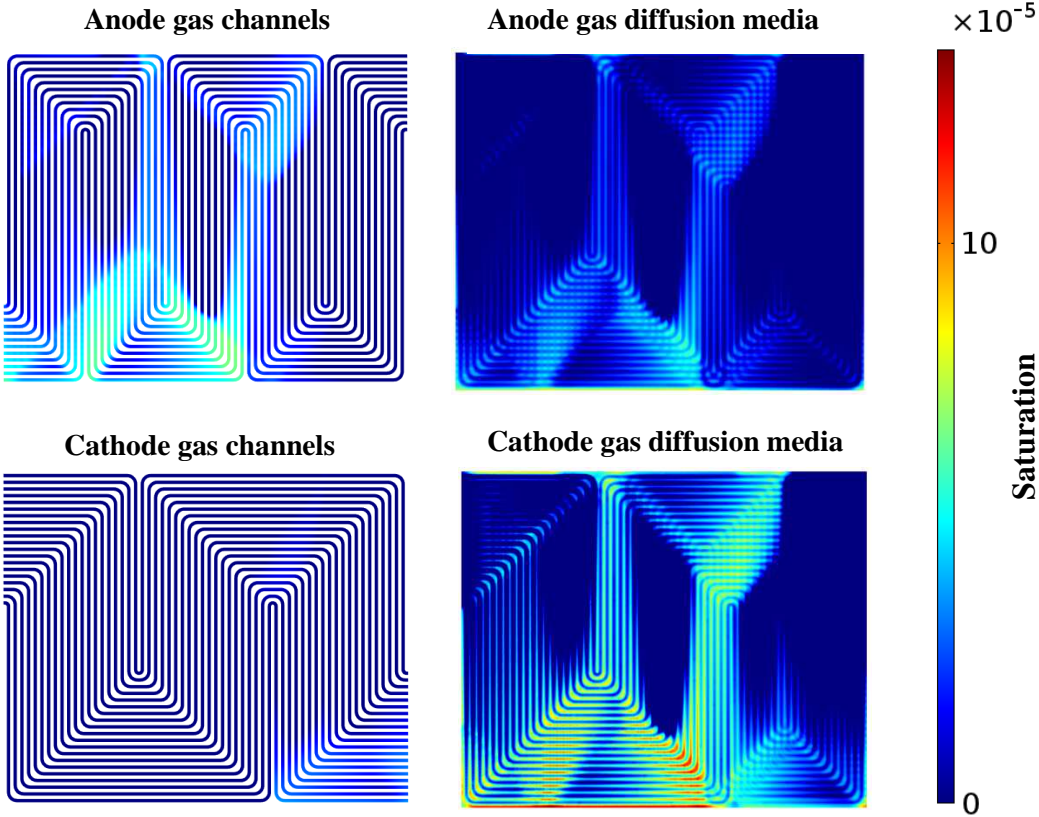
Figure IV.13 : Saturation in the different components of the cell

All the results and discussions presented above were related to the reference nominal operating conditions of the cell. In the following, the effect of the different operating parameters (current, temperature, relative humidity) on heat and water transport is studied.

3.2. Effect of the operating conditions on local parameters

a) Effect of the operating current

In this section, the impact of the operating current on the local parameters is studied. The operating conditions used for these simulations are the same as those presented in Tab.IV.7. So the flow rates and concentrations of the reactant gases at the inlet are imposed in order to produce the requested current still respecting the imposed stoichiometry. For the different current steps, the inlet temperature of the cooling water (T_{cw}^i) is set in order to maintain its outlet temperature (T_{cw}^o) at $80°C$. The cooling flow rate of the cell is set to $\dot{m} = 6\ g/s$ ($0.36\ l/min$). For example, in order to get an outlet temperature of the cooling water of 80°C with a cooling flow rate of $0.36\ l/min$, the inlet temperature of the cooling water is $\sim 79 - 77.8 - 76.2 - 74.4 - 73 - 71°C$ when the mean current density is respectively $0.1 - 0.2 - 0.4 - 0.6 - 0.8 - 1\ A/cm^2$. The distributions of the computed current densities, temperatures and water contents in the membrane at different operating currents are presented in Fig.IV.14.
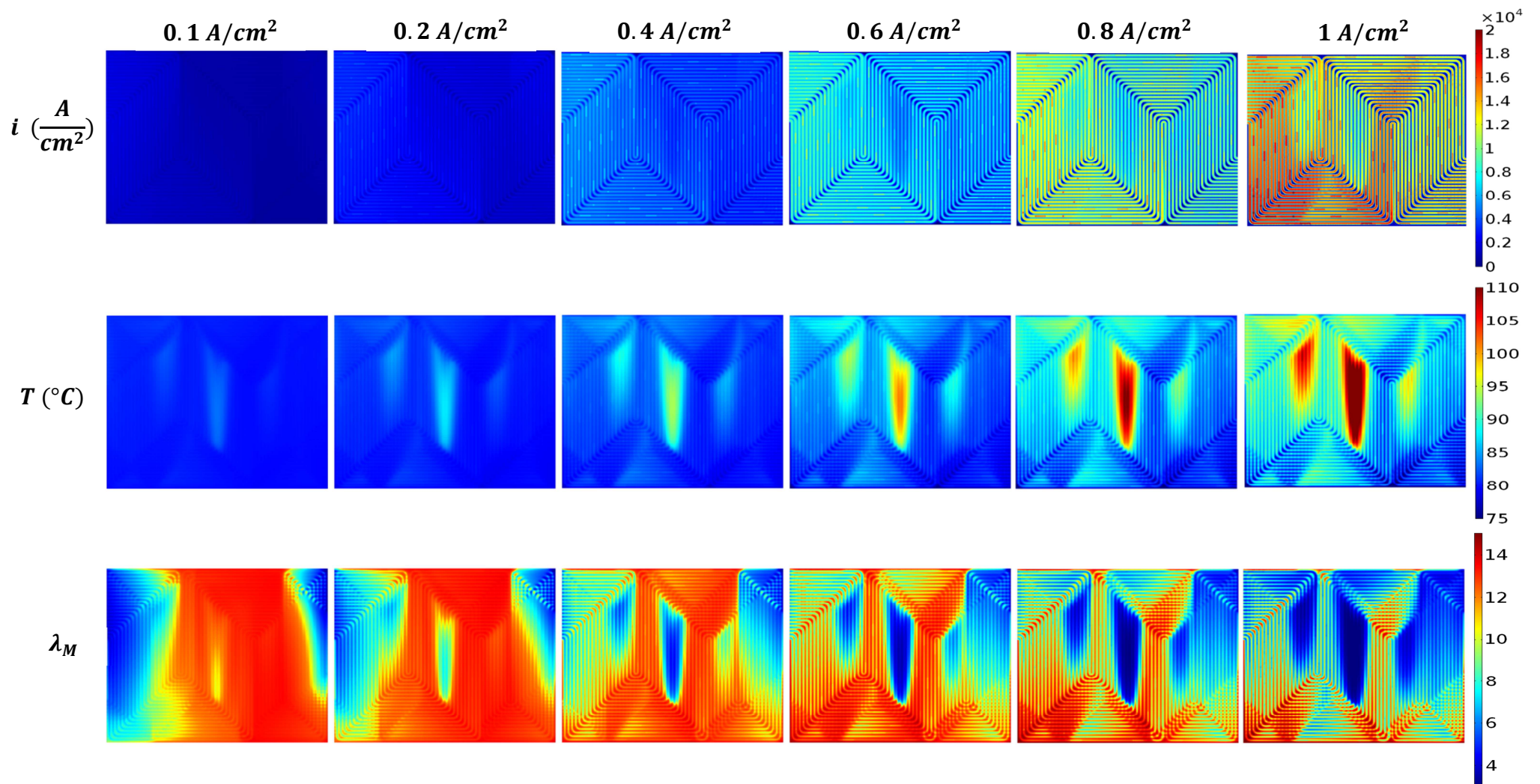
Figure IV.14 : Current density, temperature and water content in the membrane at the different operating currents

The heterogeneities of the current density, temperature and water content distribution increase when the total current increases. In the nominal operation conditions, the current density remains higher close to the air inlet. In these conditions, the membrane water content is enough to maintain a good ionic conductivity whatever the current. However, when the current achieves the highest value, this zone of higher current density progressively moves from the air inlet region to the cooling water inlet in the lower left corner (Fig.IV.14). This behavior results of the tradeoff between higher oxygen concentration and adequate cell temperature. Since the cooling water flow rate is fixed, the inlet temperature of the cooling water varies with the operating current in order to respect its outlet temperature set point. Simulations results highlights the significant dependence of the membrane water content with the membrane temperature. Namely, in the vicinity of the 3 hot zones observed at high current density (0.8, 1 A/cm²), the membrane water content is quite low. As a consequence, lower current densities are calculated because of the lower ionic conductivity of the membrane.

The increase of the current leads to higher temperature heterogeneities in the cell as observed on the temperature maps. In addition, as observed on the temperature plots, the hot spots due to the heterogeneities in the cooling flow velocity distribution (presented in Chapter 3) are more emphasized when increasing the operating current. Namely, the temperature variations over the membrane surface are respectively $\sim 4 - 9 - 17 - 26 - 38 - 48\,°C$ at $0.1 - 0.2 - 0.4 - 0.6 - 0.8 - 1\,A/cm^2$, even if the difference in cooling water temperature between the inlet and the outlet of the cell is only $\sim 1 - 2.2 - 3.8 - 5.6 - 7 - 9$ °C (Fig.IV.15).
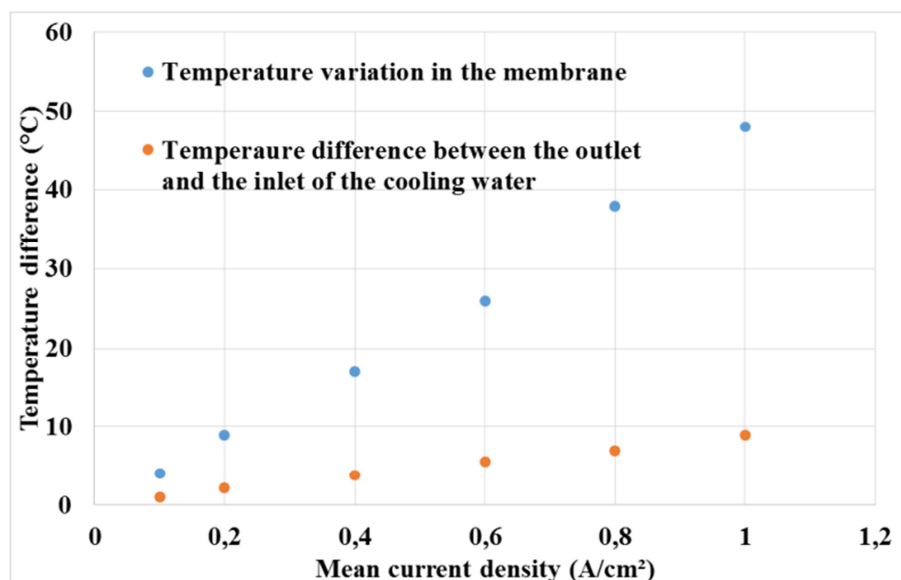
Figure IV.15: Effect of the current density on temperature heterogeneities

Furthermore, the current increase induces simultaneously more water production in the cell and higher temperature heterogeneities. These combined effects lead to much more water content

heterogeneities over the membrane surface. Since the membrane ionic conductivity linearly increase with the water content, the current density progressively moves towards the lower temperature and higher water concentration regions when the total current is increased.

Lower is the current, higher is the effect of the reactive gases inlets on the water content distribution. The effects of the air and hydrogen inlets on membrane drying can be clearly identified at 0.1 and $0.2\ A/cm^2$. At higher currents, the effect of the coolant flow field design becomes more and more significant. On the one hand, increasing current results in higher water production in the cell, and so higher water vapor pressures. On the other hand, increasing current results in higher heat production heterogeneities in the cell, with as a consequence higher water saturation pressures. The balance results in a decrease of the water content with the operating current. That means the effect of increasing temperature is predominating on the water content. To illustrate this, the evolutions of the mean, maximum and minimum values of the membrane water content with the current density are presented in Fig.IV.16. As for the temperature distribution, channel/rib heterogeneities of water content are more emphasized at higher current densities.
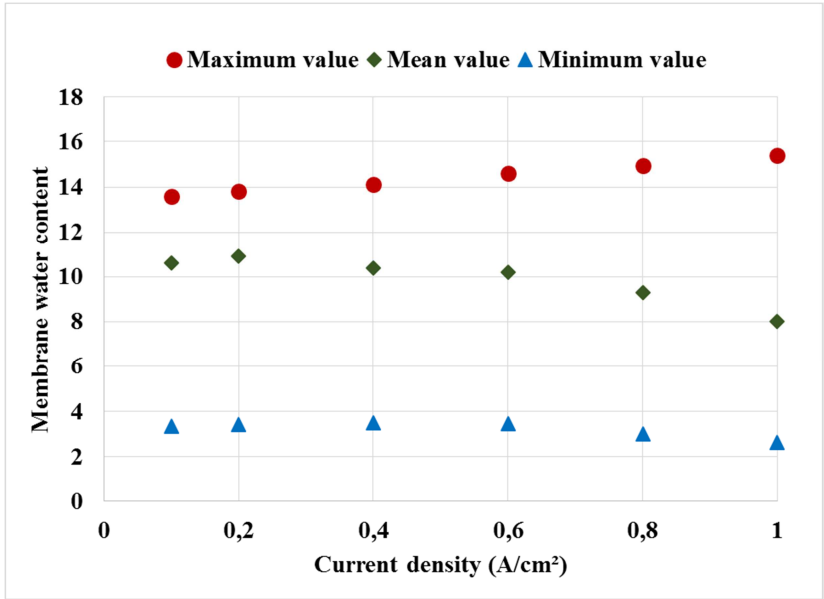
Figure IV.16 : Evolutions of the mean, maximum and minimum values of the membrane water content with current density

At the channel-rib scale, it is observed that increasing the operating current leads to more channel/rib heterogeneities, either for the current density distribution, or for the temperature and water content distributions. The 2D plot of the membrane temperature at the reference cut line presented in Fig.IV.17 highlights the emphasis of the channels/rib heterogeneities with the operating current. Typically, the channel/rib temperature variations about $0.4 - 0.8 - 1.8 - 3 - 4.5 - 6°C$ can be observed respectively at $0.1 - 0.2 - 0.4 - 0.6 - 0.8 - 1\ A/cm^2$. This evolution is

due to the higher channel/rib heat source heterogeneities at higher operating currents, mainly caused by the limitation of reactants species diffusion under the rib at high current densities.
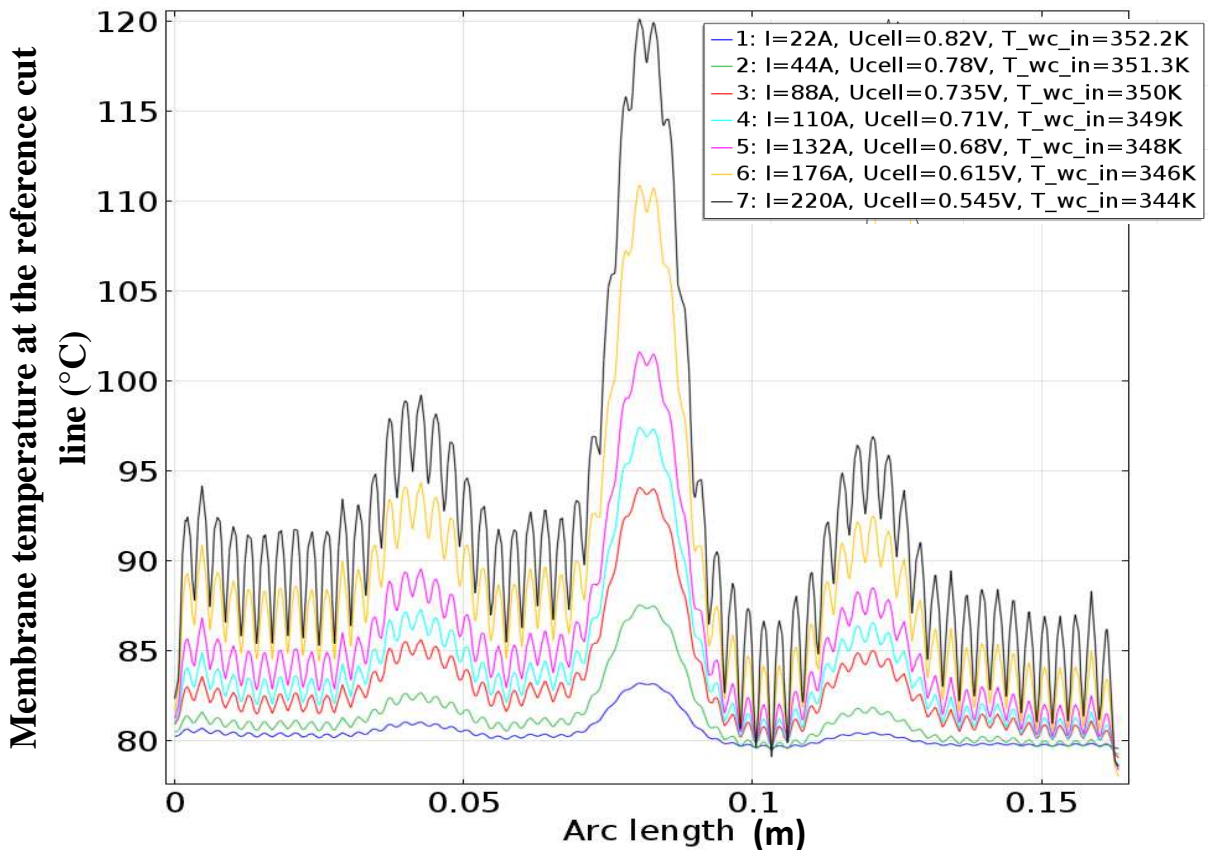
Figure IV.17: 2D plot of the membrane temperature at the reference cut line

The saturation distribution at different current densities in the channels and gas diffusion media of the cell is presented in Fig.IV.18. It is observed that the maximal saturation progressively increases with the current density. So the effect of the increased water production is predominant on the effect of the increased temperature. For each component, it is worth mentioning that increasing current leads to:

- More liquid water accumulation near the gas channels outlet;
- More accentuated impact of the coolant flow field design on the saturation distribution in the gas diffusion media;
- More Liquid water accumulation at the cathode gas diffusion media.

Liquid water accumulation in the gas diffusion media is partly related to the cold zone over the MEA surface area. Such a result highlights the effect of coolant flow-field design on the fuel cell flooding at high current density. Water accumulation at the anode compartment is related to the water diffusion through the membrane along the anode channel length. Nevertheless, water transport through the membrane results from a complex tradeoff between water electro-osmosis

150

and water diffusion (due to the higher gradient of water concentration across the membrane at the same time). So the study of water transport between both compartments is a complex and multiphysics phenomenon.
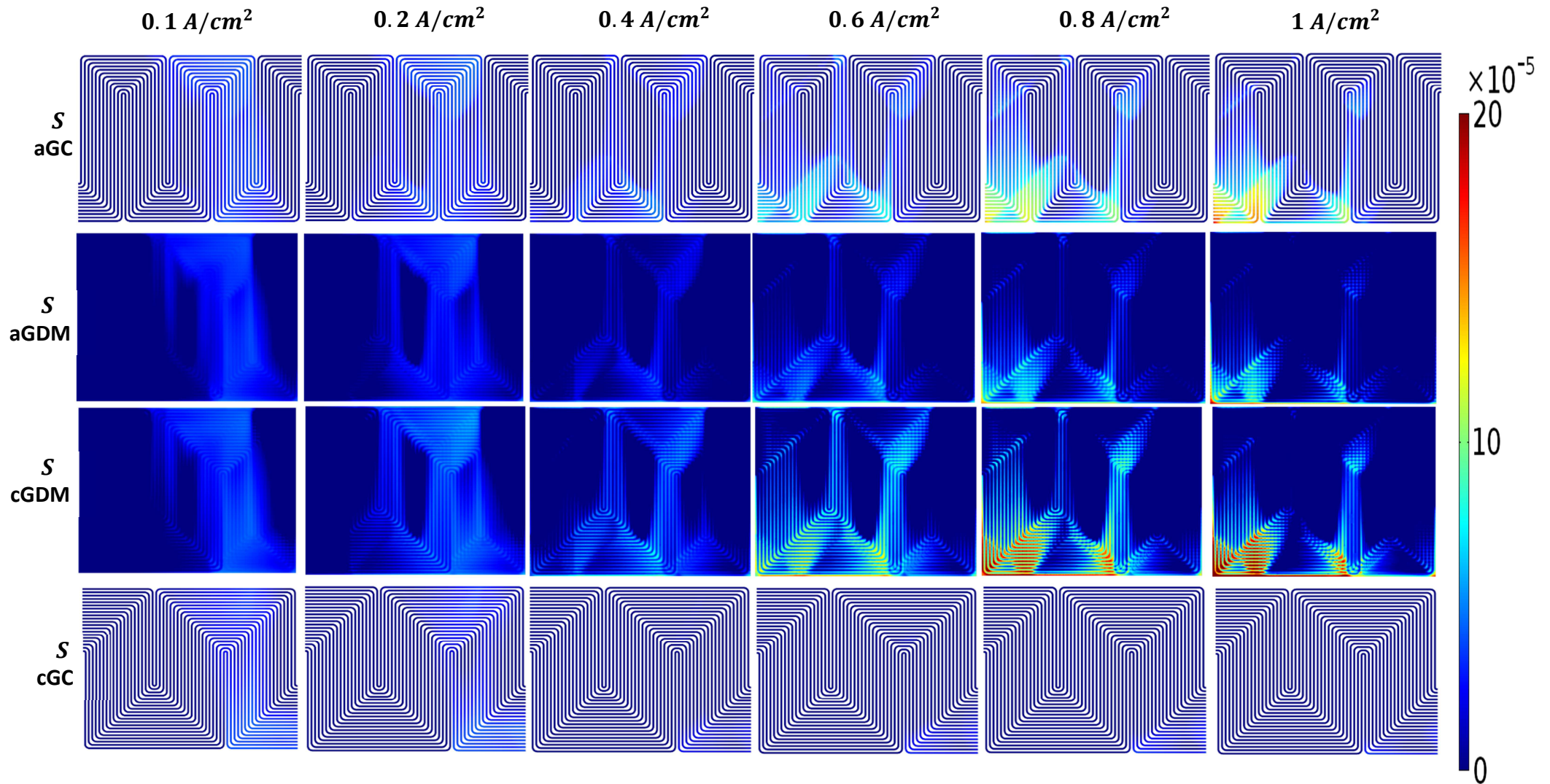
Figure IV.18: Saturation in the cell components at different operating currents

From a general point of view, there is more liquid water accumulation in the cold zones of the cathode GDLs and near the gas channels outlets in nominal operation conditions (Fig.IV.18). The saturation in the anode gas channels is intrinsically coupled to the one in the anode GDL while there is a significant difference between the cathode GDL and channels. This might be due to the water transport via convection in the cathode gas channels. The saturation evolution in the cathode GDL mainly depends both on the cathode and the coolant flow field designs. However, the first pass (of the 5-passes flow-field) of the anode is predominant over the last pass (of the 3-passes flow field) of the cathode due to the elevated water transport via diffusion from cathode to anode through the membrane.

For currents lower than $0.2\ A/cm^2,$ there is almost no presence of liquid water in the cell, even if the low cell temperature (79.5°C) induce low water saturation pressures. Indeed, in these conditions, the water removal via advection is completely predominant on the water production in the cell. At $0.4\ A/cm^2$, there is water condensation in the cold zones of the GDL and close to the air outlet of the cathode gas channels. In addition, there is a low liquid water accumulation after the central hot spot of the anode gas channels. At higher current densities ($> 0.6\ A/cm^2$), the distributions are quite the same, but with a maximal saturation which is progressively higher. At the same time, the saturation zones are progressively reduced. This is due to the competition between water and heat productions with current density increase. As a consequence, at high current densities the cell exhibits high humidity variations over the surface which could induce condensation and re-evaporation along the gas channels

At the channel/rib scale, it can be observed that increasing the operating current results in increasing at the same time the local water vapor concentration heterogeneities and the water saturation pressure heterogeneities. When the current increases, the water electro-osmosis fluxes mainly increase under the channels. At the same time, there is more water diffusion across the membrane under the ribs where there is more water accumulation. As a consequence, increasing current results in more channel/rib heterogeneities of water transport across the membrane.

b) Effect of the operating temperature

The effect of the operating temperature on the local parameters in presented in Fig.IV.19. The reference temperatures (outlet temperature of the cooling water) studied are 65, 80 and 95°C and the cell potential is set to 0.7 V. At the lower temperature of operation (65°C), higher currents are observed in the cell thanks to the higher membrane water content. In this operation condition, water condensation takes place at the cathode compartment that exhibits higher saturation. However, the water saturation in the cell is too high and the single phase model used for the fluid

flow should be questionable. Indeed, liquid water could fill the pores of the gas diffusion media, inducing higher diffusion resistances and even electrode flooding. Moreover, the accumulation of liquid water close to the gas channels outlet could block the channels, leading to reactants starvation. As a consequence, despite the high water content of the membrane which induce a good proton conductivity, the current should be lower than the one at 80°C.

At 95°C, the current density becomes lower due to the elevated temperature which induces membrane drying. In this condition, there is no presence of liquid water in the cell and it can be considered that the model accurately predicts the electrochemical and thermal behaviors of the cell. At 80°C which is the transition (and the reference temperature of this study), the current density is a slightly lower than the one at 65°C.The membrane water content is high enough to ensure a good proton conductivity.
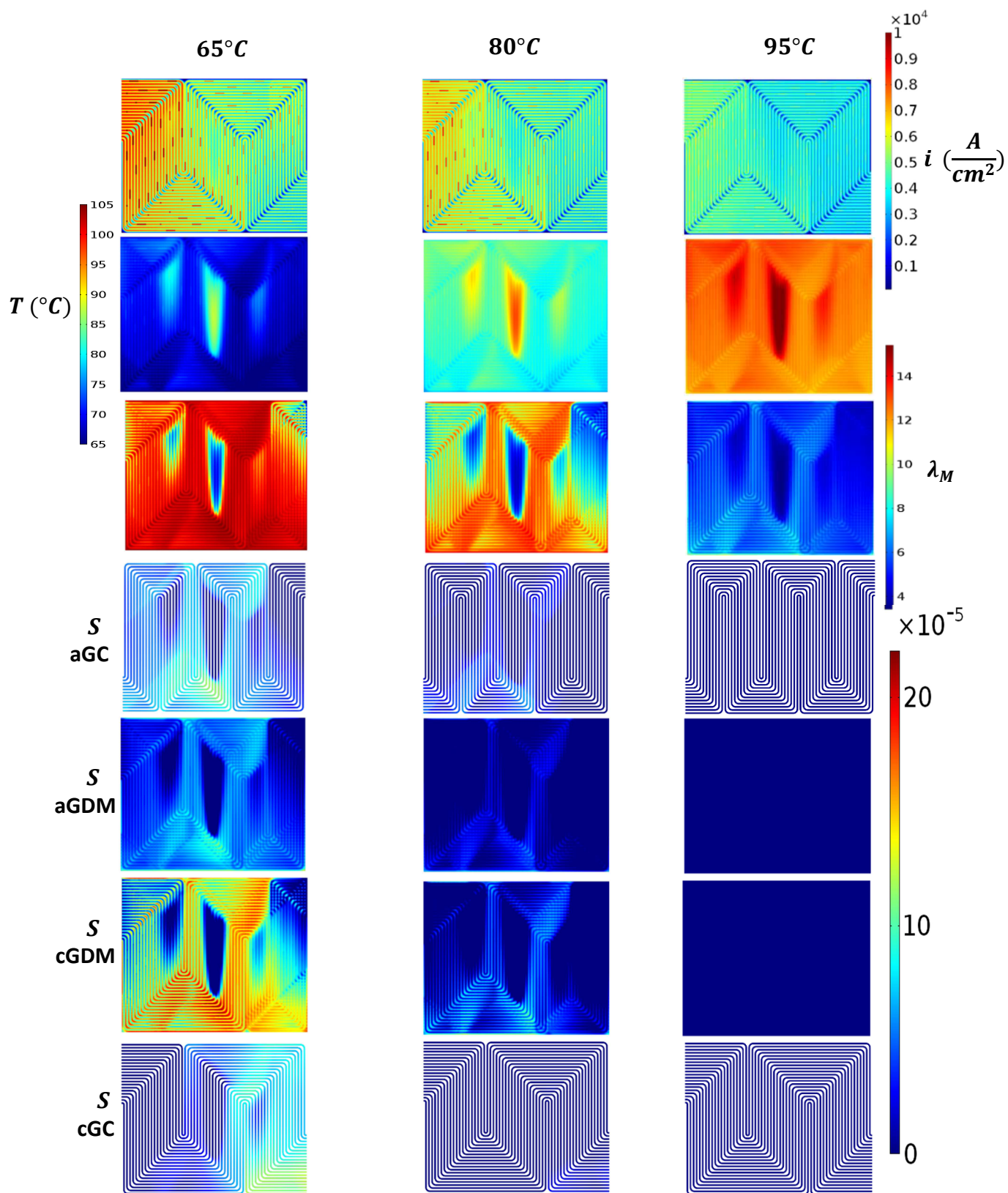
Figure IV.19: Effect of the operating temperature on local parameters

c) Effect of the relative humidity of the reactants

One of the main goals of the PEMFC industry is to reduce the pre-humidification of the reactant gases. The impact of the relative humidity (RH) of the reactants at the cell inlet on local parameters in presented in Fig.IV.20. The reference RH studied are 25, 50 and 75 %, and the cell potential is set to 0.7 V. The first observation is that increasing RH results in higher current densities close to the air inlet. At 25% (dry condition), the current density is more uniform along the MEA surface. In this condition, the production of water due to the electrochemical reaction is quite helpful for the membrane hydration. As a consequence, the increase of water content compensates in part the effect of the oxygen concentration depletion along the channels. At 75% (wet condition), the current density is much more heterogeneous with higher current close to the air inlet. Indeed, in this conditions, the high pre-humidification of the reactants induces a good proton conductivity in this zone. However, the high water saturation (especially in the gas diffusion media) can induce considerable deviation for the fluid dynamics model, due to the reasons aforementioned.
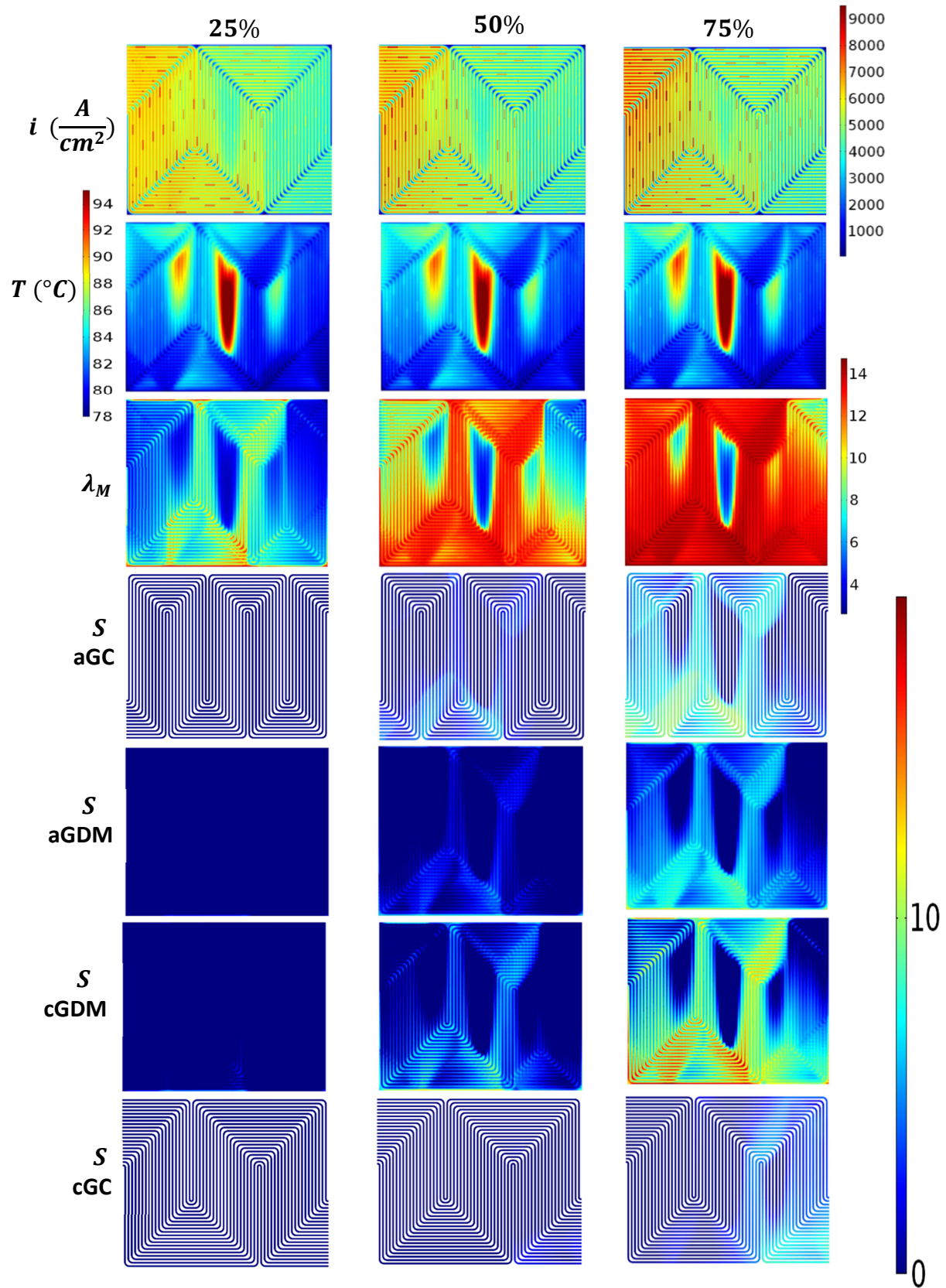
Figure IV.20 : Effect of the inlet RH on local parameters

d) Effect of the coolant flow rate

The coolant flow rate is a key factor for the thermal management that impacts not only the fuel cell stack, but also the fuel cell system (pump which moves the cooling water, radiator which evacuates the excessive heat, etc.). The study of the impact of such coolant flow rate on the membrane temperature and water content is presented in Fig.IV.21. Three coolant flow rates are studied: 2, 6 and 12 g/s.
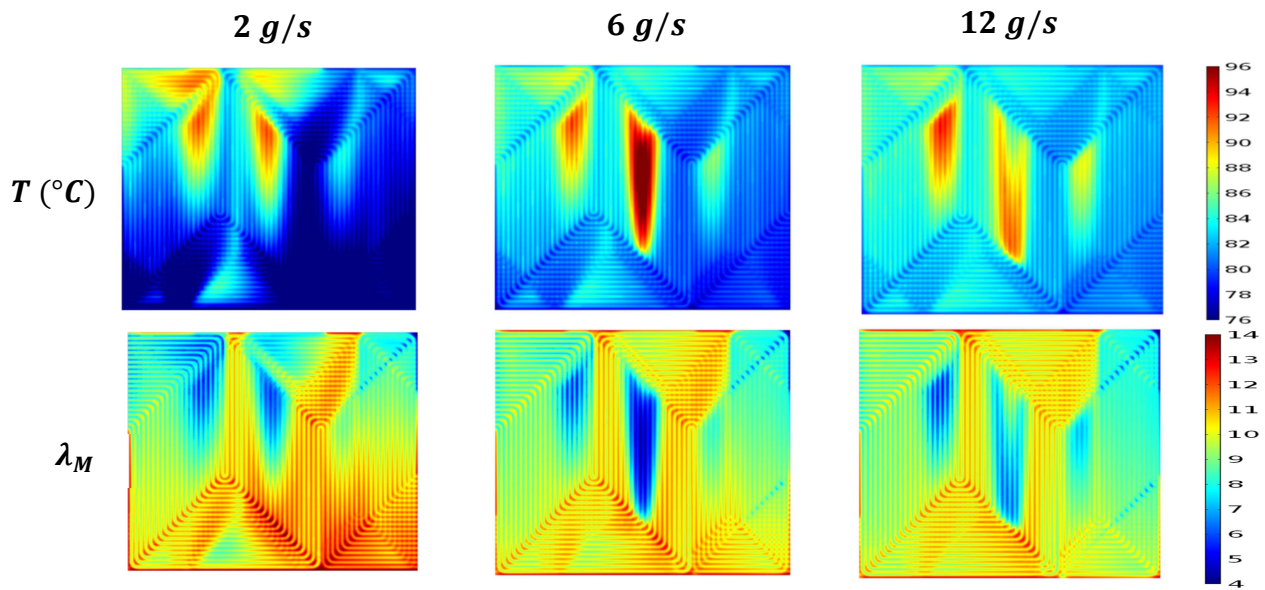
Figure IV.21 : Effect of the coolant flow rate on local parameters

Increasing the coolant flow rate ($\dot{m}_{cw}$) results in increasing the inlet temperature of the cooling water (T_{cw}^i) in order to respect the set point of the outlet temperature (T_{cw}^o), which is $80°C$. As a consequence, the global temperature becomes higher and more uniform over cell surface as presented in the Fig.IV.21. Because of the relationship between temperature and the membrane water content, the cell works in a dryer environment. At lower coolant flow rate, a displacement of the hot zone toward the coolant outlet is observed. Another consequence of the coolant flow rate increase is the higher singular pressure drop in the cross-flow zones of the cooling flow (as illustrated in Chapter 3, section 4.1.d). Since the singular pressure drops are directly related to the kinetic energy of the flow, the hot spots are emphasized when the coolant flow rate is increased. This effect is clearly observed between 2 and 6 g/s. However, at 12 $g/s,$ the global homogenization due to the lower temperature difference between the cooling water inlet and outlet partly masks the effect of the heterogeneous distribution of the coolant flow.

Conclusion

A pseudo-3D multiphysics model was developed in this chapter in order to study simultaneously, the electrochemical performances as well as the heat and water transports in the cell. The model was validated globally using the measured polarization data and locally using both the current density and temperature distributions over the cell surface measured with a sensor plate (S++). In the thermal model, the enthalpy of phase change was considered in the cell meanwhile single phase flows were assumed in the fluid dynamics model. The main conclusions that may be drawn from the study are:

- The temperature heterogeneities predicted using the multiphysics model are much higher than the ones predicted using the pseudo-3D thermal model developed in the chapter III. Indeed, the multiphysics model captures all the channel/rib heterogeneities of the heat sources in the cell (which was not the case in the thermal model). The significant impact of the temperature distribution on water saturation means that heat and water management are highly coupled and should not be studied separately.

- The water concentration is higher in the cathode gas diffusion media due to the cumulative effect of the oxygen reduction reaction and electro-osmotic flux from anode to cathode. The water distribution in the anode gas channels is intrinsically coupled to the one in the MEA, contrarily to the cathode gas channels.

- The water transport across the membrane is a complex phenomenon. Electro-osmosis is predominant under the channels meanwhile diffusion is predominant under the ribs, where there is more water accumulation. The BP design largely impact on the water fluxes across the membrane, especially as regards the diffusive fluxes. Moreover, the hot spots deeply impact on the transport properties of the membrane.

- The operating conditions of the cell greatly impact heat and water management. The increase of the operating current induces more global temperature heterogeneities, emphasizes the hot spots and reduces at the same time the impact of the reactive gases inlet on the humidity distribution. At a more local scale, the current increase leads to more channel/rib heterogeneities, either for the current density distribution, or for the temperature and water content distributions. The operating temperature mainly impacts the membrane water content, and so its proton conductivity. Increasing the relative humidity of the reactants leads to higher current densities close to the air inlet. Finally, the increase of the

coolant flow rate emphasizes the hot spots, even if it reduces the global temperature difference between the inlet and the outlet of the cooling water.

However, the model could be called into question in the following points. The important discrepancies in the parameters of membrane water transport (electro-osmosis drag and diffusivity) found in literature could considerably affect the water distribution in the cell. Moreover, the water saturation in the GDM could considerably impacts on its diffusive and thermal properties.

Globally, the model is an efficient tool for the study of the correlation between coupled heat and water management and degradations. Using appropriate degradation models, the model could be useful for the study of the long term performance of the cell components under different operating conditions. It is well known that the membrane swells when absorbing water, and even more when there is liquid-phase water. The highly heterogeneous distribution of temperature and humidity observed can induce high levels of hydrothermal stresses inside the membrane, and accelerate its degradation.

<div align="center">

Chapter V

CORRELATION BETWEEN TEMPERATURE, HUMIDITY AND DEGRADATIONS IN P.E.M. FUEL CELLS

Summary

</div>

Introduction

In Proton Exchange Membrane Fuel Cells, local temperature could be a driving force for many degradation mechanisms such as membrane hygrothermal deformation and creep, platinum dissolution, bipolar plates corrosion, etc. In order to investigate and quantify those effects, durability testing in automotive operating conditions were conducted as presented in the Chapter 2. During the ageing tests, the local performance and temperature were investigated using a printed circuit board inserted in the middle of the stacks. At the end of life, *post-mortem* analyses of the aged components were conducted in order to investigate their local microstructure and chemical composition. In parallel to those degradation studies, a thermal model was developed in the Chapter 3 in order to investigate the local temperature distribution inside the cell. This model was extended to a multiphysics full predictive model in the chapter 4, and used for the study of the impact of the operating conditions on coupled temperature and humidity distribution.

In this last part of the study, all the experimental and modeling tools presented in the previous parts are used simultaneously in order to investigate the correlation between local temperature and PEM fuel cells degradations in automotive application. The degradations observed during the ageing tests are presented and compared to the simulated thermal loading of the cell for the different tests. Those *on-line* studies are combined with the *post-mortem* analyses of the aged components in order to correlate at the same time the performance losses and the observed components degradation to the thermal conditions in the cell.

1. Study of the MEA degradations

The stationary ageing test is the reference test used in this study because the model used to predict the local thermal conditions in the cell is run in stationary conditions. The other tests are used in order to better investigate the impact of local parameters cycling on ageing conditions.

1.1. Global performance loss and degradation

The global continuous diagnosis, which consisted of polarization curves and electrochemical characterizations, were performed each 200 h from the beginning of test (BOT) to the end of test (EOT).

a) Polarization curves with potential degradation rates

Fig.V.1 shows the evolution of the polarization curves during the three ageing tests and the degradation rates of the singles cells at the reference current density of 0.5 A/cm².
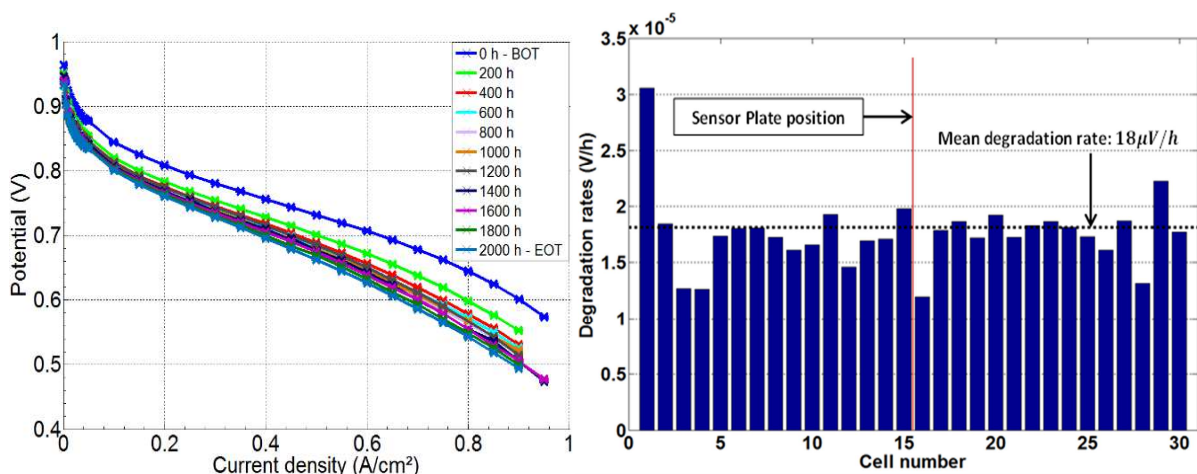
Figure V.1 : Evolution of the polarization curves and potential degradation rates during the ageing test

A high voltage drop is observed at the beginning of the test (during the firsts 200 hours). After that, the voltage drop becomes considerably slower. The mean degradation rate observed is $18 \ \mu V/h$. The voltage drop is quite homogeneous, except for the first cell which endured a degradation almost two times higher than the others. From a fluid dynamics point of view, the pressure drop at the stack inlet can induce an uneven distribution of the reactants gases and cooling water in the first cell. That could explain the higher degradations observed. The electrochemical characterizations may help in identifying the causes of potential loss.

b)   Electrochemical characterizations

Fig.V.2 shows the evolutions of the electrochemical active area ($m²$) and hydrogen permeation (mA/cm²) during the ageing test.
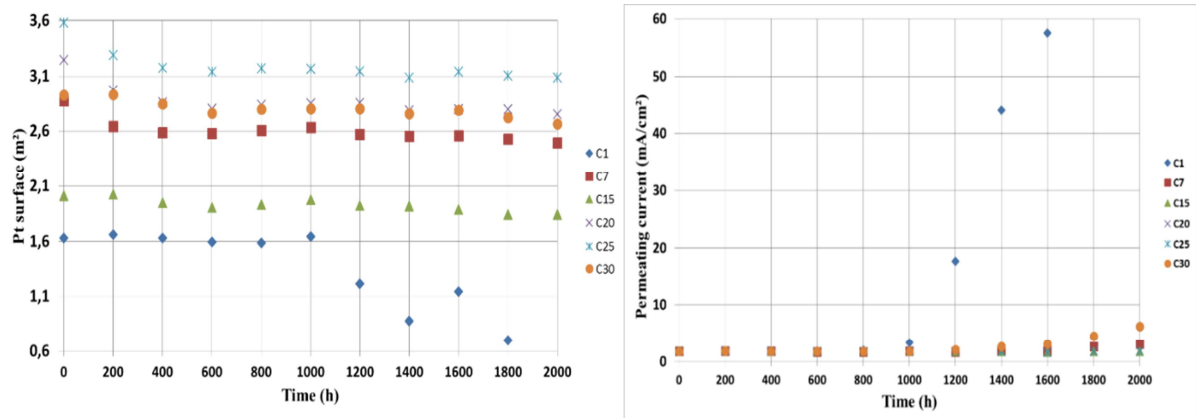
Figure V.2 : Evolution of the ECSA and permeation current

There are substantial electrochemical surface area losses during the first 200 hours. Regarding the hydrogen permeation, there is a zone where there is no considerable evolution at the beginning of the test, followed by a quite quadratic evolution from ~ 800 h. In the following, in order to eliminate the impacts of the edge-effects on the degradations observed, the cell 1 is excluded from the results. The mean evolutions of the rugosity factor of the electrochemical active area (*m²Pt/m² electrode*) and hydrogen permeation (mA/cm²), for the 5 remaining cells presented above, are presented in Fig.V.3.
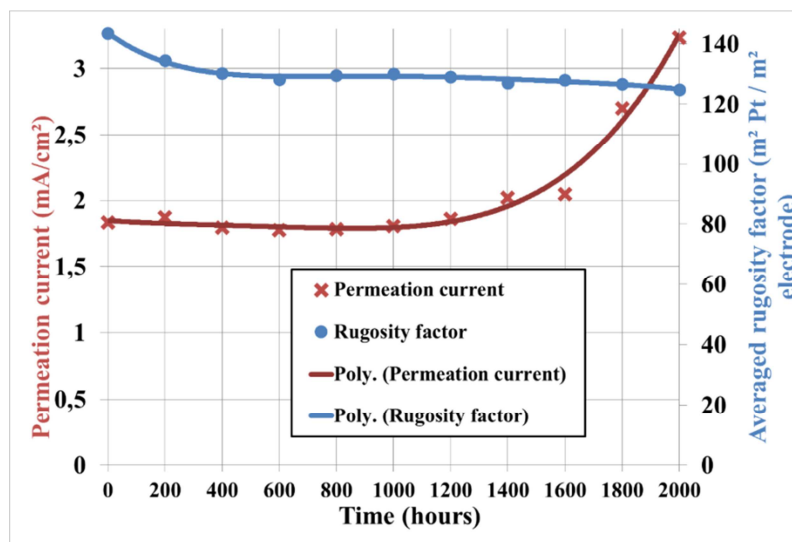
Figure V.3 : Mean evolutions of the permeation current and ECSA

The mean electrochemical surface area loss is very high during the firsts 200 h ($\sim 0.1\ m^2 Pt/m^2/h$) and becomes lower after ($\sim 5 \cdot 10^{-3} m^2 Pt/m^2/h$). These results agree with the polarization curves evolution which exhibit higher performance drop at the beginning of the test. It can be explained by an important effect of Ostwald ripening during

164

the first hours as reported by Holby et al. [156]. In addition, higher is the operating temperature, faster should be the growth of the particles [105]. In the zones where the temperature exceeds 100°C, the thermal oxidation of Pt/C in air should occurs, as observed by Stevens et al. [157].

Regarding the membrane degradation, the hydrogen permeation is almost stable during the first 800 hours of the ageing test, followed by a quite quadratic evolution from 800 h as it can be observed from the fitting curve. The acceleration of hydrogen permeation with time corresponds to membrane thinning and/or apparition of microcracks. The membrane thinning effect can related to the chemical degradation of the membrane induced by oxygen crossover as described by Inaba et al. [158]. The Fluoride-ion release rate (FRR) is an interesting method to investigate such chemical degradation of the membrane.

c)   Effluent water analysis

In order to investigate the membrane chemical degradation, FRR measurements of the effluent water was performed each 200 h. The results are presented in Fig.V.4. The measurements of the FRR at 1400 and 1600 h were not performed due to a problem on the data acquisition system.
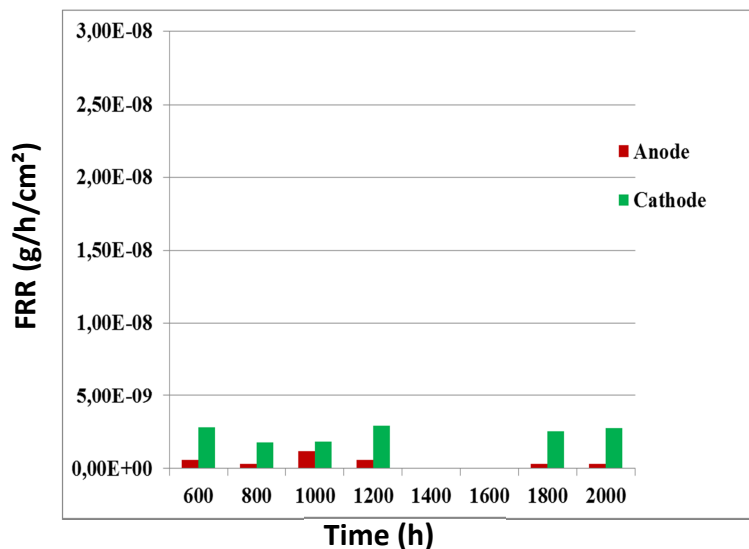
Figure V.4. Evolution of the FRR

First, it is observed that fluoride is mainly released in the cathode effluent water. There is no significant evolution of the FRR over time, despite the quadratic evolution of the hydrogen permeation across the membrane presented in Fig.V.3. Therefore, it can be stated that the main mechanism affecting the membrane permeation is not the chemical degradation. Investigations at a more local scale may help to better investigate the correlation between the local thermal conditions to the performance losses observed.

1.2. Local performance loss and degradation

Fig.V.5 shows examples of current density and temperature measured over the cell surface using the segmented printed circuit. The hot zones observed on the temperature map are related to the heterogeneities of the cooling flow field, as explained in the chapter III.
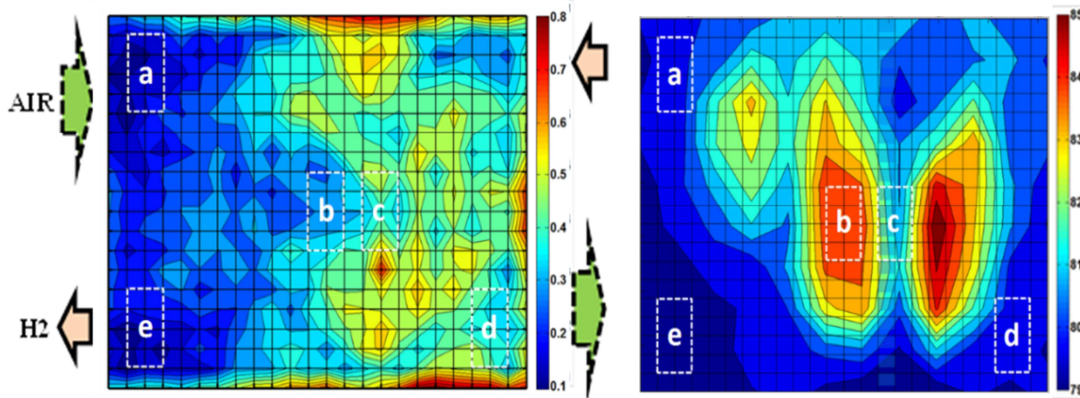
Figure V.5 : Measured current density (A/cm²) and temperature (°C) with the printed circuit board

For a detailed study of the correlation between local temperature and performance loss, five reference zones have been chosen in this study as indicated in Fig.V.5:

- **Zone a**: Medium temperature zone, with low water concentration (cathode inlet);
- **Zone b**: Hot zone, with relatively medium water concentration (center of the cell);
- **Zone c**: Cold zone, with relatively medium water concentration (center of the cell);
- **Zone d**: Cold zone, with high water concentration (cathode outlet);
- **Zone e:** Cold zone, with low water concentration (anode outlet).

8 current measurement segments are included in each zone in order to eliminate the side-effect of welding points of the bipolar plates on local current density heterogeneities. Fig.V.6 shows respectively the evolution of the current density and temperature during the stationary ageing test in the five reference zones.
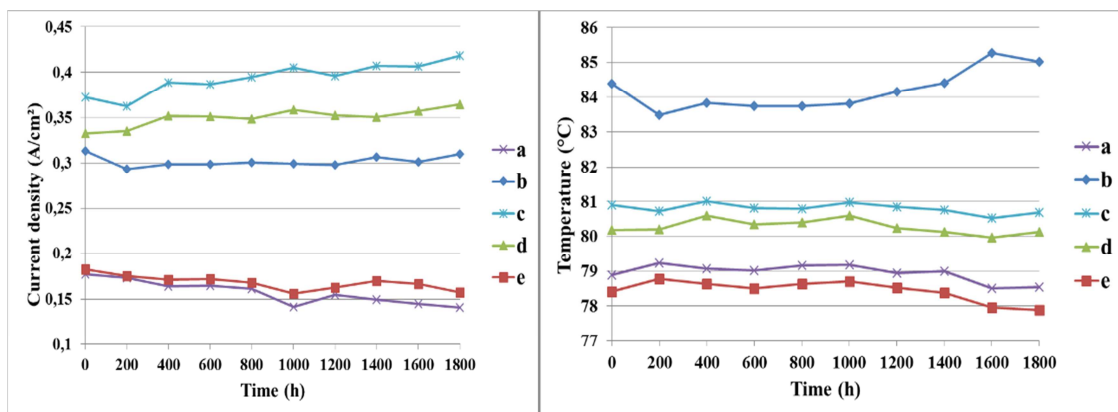
Figure V.6 : Evolution of the current density and temperature in the five reference zones

It is observed that there is no significant performance loss in the hot zone (b). However, there is a performance loss (about 14 %) close to the air inlet (low water concentration zones) and a performance rise (about 10 %) in the vicinity of the air outlet (high water concentration zones). Regarding temperature, no significant evolutions are found (~1.5 %) since temperature distribution is mainly controlled by the cooling flow field design. From this evolution of the local current density over time, it could be concluded that the main factor affecting the local performance loss is water concentration in the cell.

As a finding, it can be stated that the performance losses are mainly caused by the electrochemical active surface area loss at the beginning of the test and membrane mechanical degradations which is quite accelerated at the middle of test. Locally, the current density maximal values move from the air inlet towards the air outlet over time, suggesting that performance losses are related to the water concentration in the cell. A detailed examination of the aged components, especially the membrane, may help to understand the ageing mechanisms and their correlation with heat and water management.

1.3.   Post-mortem analyses

Once the aged stacks are disassembled, *post-mortem* analyses of the different components of the cell are performed. The *post-mortem* analyses protocol is composed of different steps. The first one is the investigation of the hydrophobicity loss of the GDLs, performed by immersing them in water and measuring the contact angle of the water droplets on their surfaces. The results showed no significant hydrophobicity degradations. The second one is study of the through-plane microstructure of the MEAs, using SEM. To this end, representative zones have been chosen depending on the local temperature and water concentration (zones a, b, c, d and e presented in section 3.1.b). The results showed no particular heterogeneities of the active layers thickness and microstructure, despite the high heterogeneities of temperature (see Appendix 5).

In the following section, local analyses of the MEA at different scales are presented. The results are simultaneously compared to the measured data during the continuous *on-line* diagnosis and discussed with the simulated results.

Fig.V.7 shows one aged membrane of the stationary test, separated from the catalyst layers. The separation is made using ethanol in which the MEA is immersed for few hours. Thus, the catalyst layers are easily detached from the membrane without external effort. By comparing the membrane structure to the simulated local parameters, some correlations were found with the membrane water content. For this reason, on the same figure, the plot of the

predicted membrane water content obtained via the pseudo-3D model is presented for comparison.
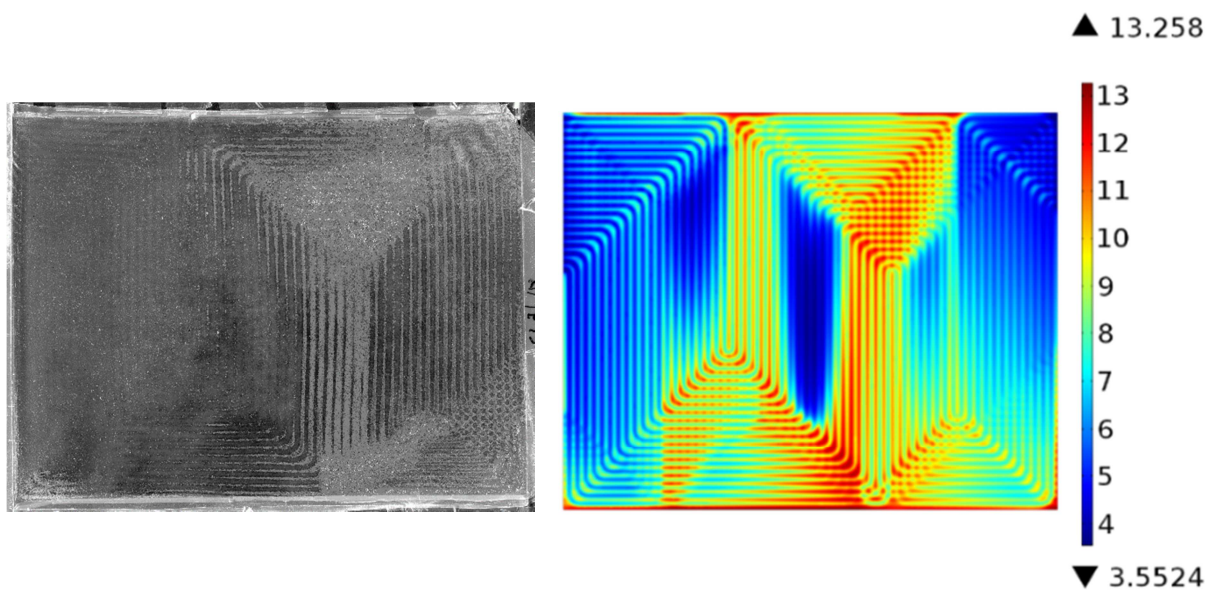
Figure V.7 : Comparison between the membrane structural degradations and the simulated water content

The first observation is the non-uniform printing of the reactive gases flow field on the membrane. There are some correlations between the water content distribution and the membrane structure. The transparent zones (black on the figure) are defect free. The opacification of the membrane (whitish zones on the figure) indicates structural changes. So higher is the water content, higher is the structural damage of the membrane. In particular, the degradations can be quantified as follows:

- When the water content λ_M is lower than 7, there is no visual observation of the membrane degradation;

- When the water content reaches 7, there is the emerging of degradations characterized by a slight swelling of the membrane with a delamination of a whitish color film. The film thickness is of a few microns;

- For $\lambda_M > 10,$ the delamination becomes more important, with the emerging of the intensification of the whitish color;

- For $\lambda_M > 11,$ there is a complete delamination of the film, with a considerable swelling. The intensification of the delamination causes superficial tears on the membrane.

Fig.V.8 show a local analysis of the membrane degraded zones via SEM. From the microscopic studies, it appears that the observed degradations are delaminations, mainly observed at the anode side of the membrane.

Under the channel

Under the rib
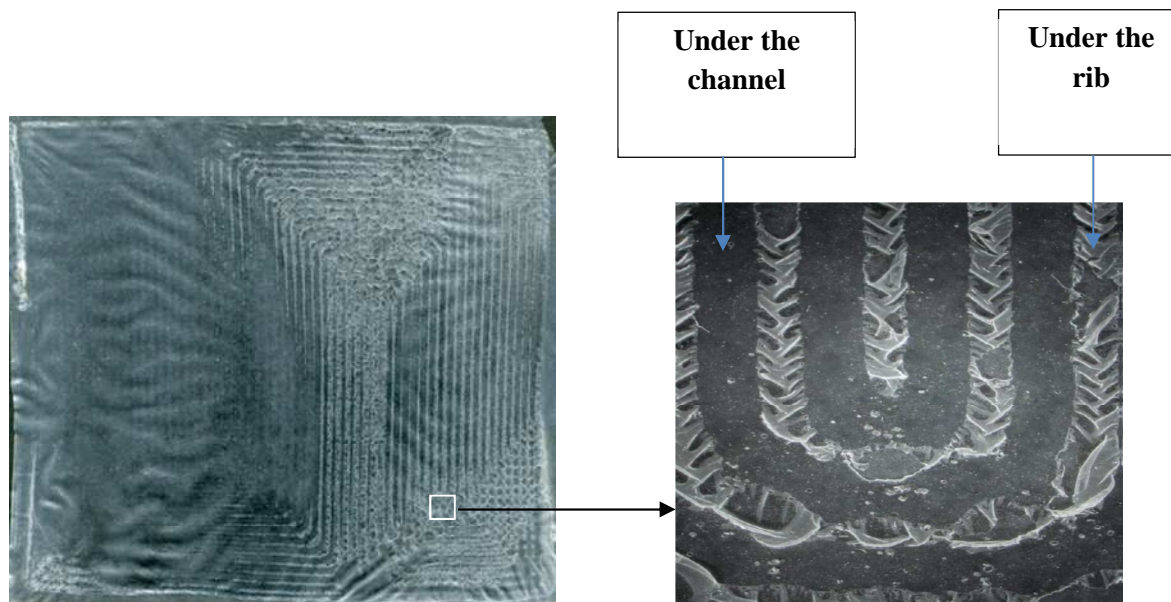
Figure V.8: Microscopic studies of the membrane degradations

The delaminations are coupled to the channel/rib geometry printing with a severity which depends on the local water content (see Fig.V.7). The anode flow field geometry printing is predominant close to the hydrogen inlet while the cathode flow field geometry printing is predominant in all the other parts. It is well known that the behavior of the Nafion is governed by irreversible thermodynamics. Majsztrik et al. [159] systematically investigated the hydrothermal behavior of Nafion and observed that: on one hand water acts like a Nafion plasticizer at lower temperatures; on the other hand, water acts like a Nafion Stiffener at temperatures above 90°C. It is not easy to make a conclusion about the observed degradations because only the irreversible (plastic) deformations are observed in detail using SEM. Moreover, the impact of the membrane separation protocol (immersion in ethanol for few hours) may induce structural changes. Curiously, the stack aged in NEDC/RH cycling conditions underwent a huge membrane degradation. The high increase of the membrane permeation led to an instantaneous loss of functionality for some cells of this stack.

1.4. Comparison of the membrane permeating currents

The evolutions of the rugosity factor (*m²Pt/m² electrode*) and hydrogen permeation (*mA/cm²*) during the stationary and NEDC/RH cycling tests are presented in Fig.V.9 for comparison.
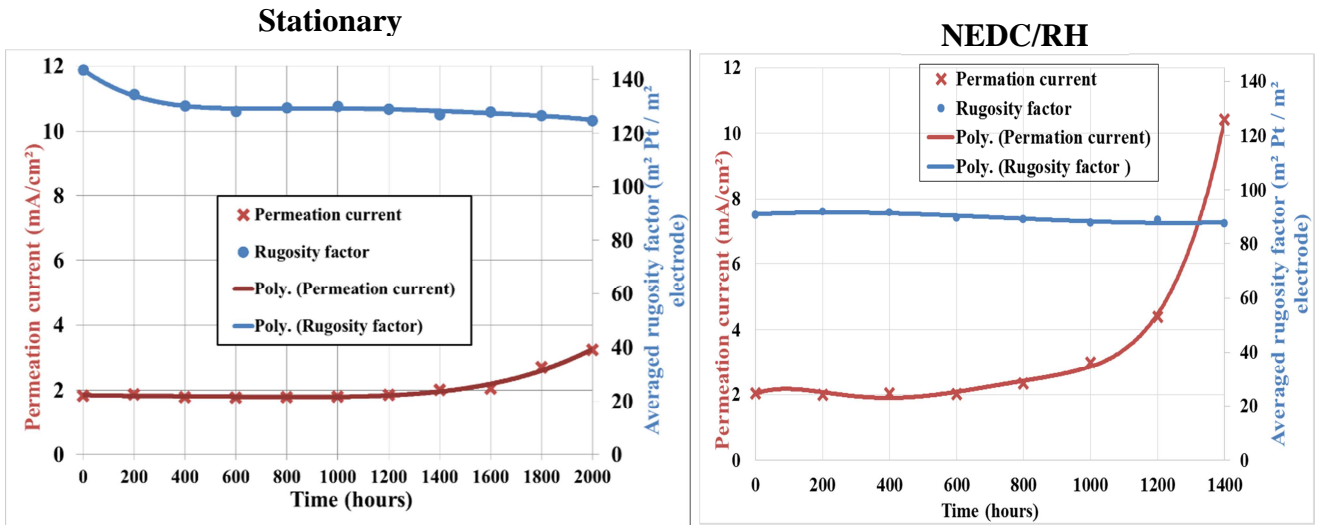
Stationary   **NEDC/RH**

Figure V.9 : Mean evolutions of the permeation current and ECSA

The ECSA loss of the NEDC cycle is very low compared to the stationary test one. Regarding the permeation current, there is a considerable increase for the NEDC/RH, compared to the stationary test. This makes think that the main effect of current and humidity cycling is an acceleration of the membrane degradation. The too high permeation (> 50 mA/cm²) of one cell of the stack (cell number 15) at 1400 h caused its loss of functionality. Therefore, at ~ 1500 h, the cell 15 was removed from the stack, leading to a 29 cells stack. Curiously, no gradual performance loss was observed on a specific zone of the active area. From the literature review, elevated potentials and temperatures are supposed to increase the membrane chemical degradation while RH cycling is supposed to increase its mechanical degradation. Therefore, the following study focuses on the study of the chemical and mechanical degradations of the membranes of the NEDC/RH cycling test.

1.5.   Comparison of the Fluoride Release Rates

The FRR measured at the outlet of the stack aged in NEDC/RH cycling conditions is presented in Fig.V.10 with the one of the stationary test for comparison.
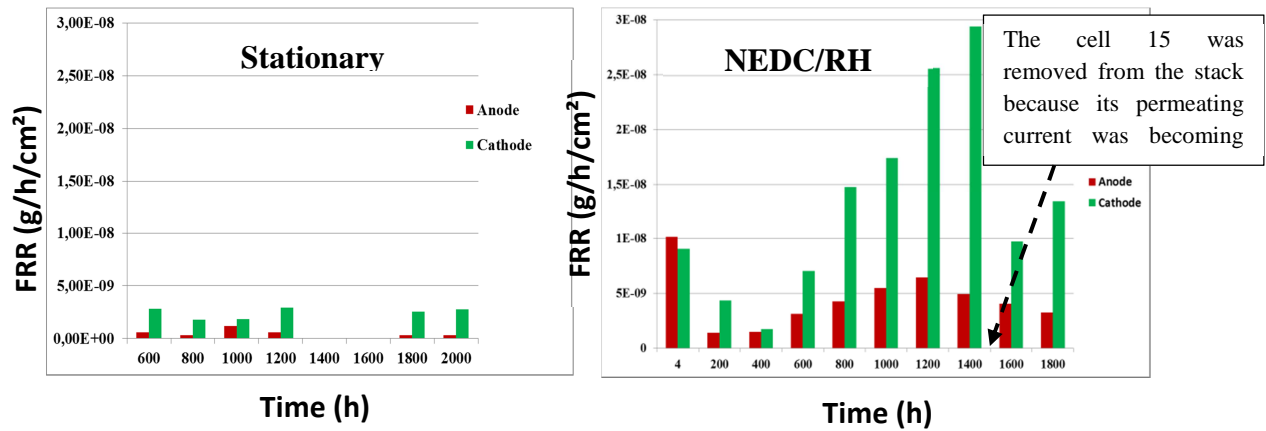
Figure V.10. Evolution of the FRR

It is observed that the during the NEDC/RH cycling, the FRR is almost 4 times higher than during the stationary test. This may be due to the higher mean operating potential and/or considerable hygrothermal loadings of the NEDC/RH cycling, compared to the stationary test. On the one hand, the membrane chemical degradation is more likely to occur at elevated potentials [160]. On the other hand, the operating temperature can also largely impact on the FRR [161]. According to Endoh et al. [162], reducing the humidification leads to an increase of the chemical degradation rate. The isolated effects of temperature and humidity on membrane chemical degradation can be studied by measuring the thickness of the membrane in the representative zones presented in section 1.3.a.

1.6. Effect of local parameters cycling on membrane chemical degradation

The measured temperature evolutions in the references zones during one cycle of the NEDC is presented in Fig.V.11. The reference zones are the same as presented in section 1.2.
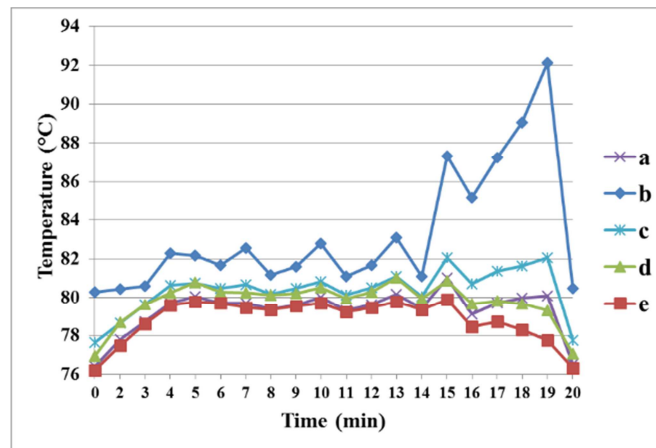
Figure V.11 : Evolution of the local temperature if the reference zones during the NEDC/RH cycle

It is clearly observed that the current cycling induce local temperature cycling in the cell, with different amplitudes between the zones. Higher is the temperature of the zone, higher is the amplitude of the temperature change. As a consequence, the hot zones (a) undergo a higher temperature cycling. Regarding the evolution of the cycles over time, there are not significant variations from the beginning to the end of test. The analysis of the membrane thickness in those zones via SEM showed no significant differences. That means local temperature and humidity are not the main factors affecting the membrane chemical degradation in this kind of cycle. As a consequence, the investigation has to be oriented towards mechanical degradation.

1.7. Effect of local parameters cycling on membrane mechanical degradation

In order to study the mechanical degradation, the IR camera with the hydrogen box presented in Chapter II, section 5.4 is used. This experimental technique is used to localize eventual pin-holes or local cracks of the membrane which are preferential paths for hydrogen permeation. For example, an infrared image of the MEA is presented in Fig. V.12 with the corresponding degradation point (red point) on the MEA. Whereas the mean temperature of

the MEA is ~ 20°C, a hot spot, where the temperature reaches 28°C, is observed in vicinity of the hydrogen outlet.
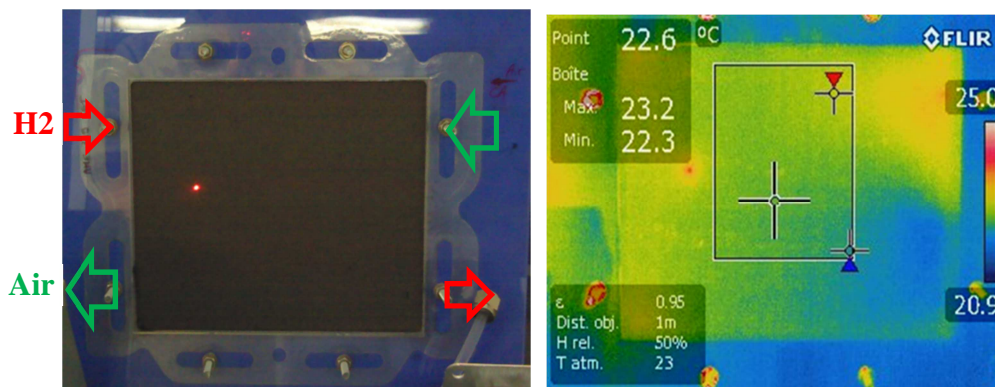
Figure V.12 : a) Aged MEA in the hydrogen box for the IR camera test

(b) Infrared image of the aged MEA

The figure V.13 shows the correlation between the maximal temperatures observed with the IR camera and the membrane permeation. Accordingly, there is a good correlation between the maximal temperature observed with the IR imaging and the permeation current measured. The maximal temperature of the IR camera seems to be a great indicator of the gas crossover through the membrane. The localization of the maximal temperature allows getting information about the preferential zones of gas crossover due to local pinholes and/or local membrane thinning.
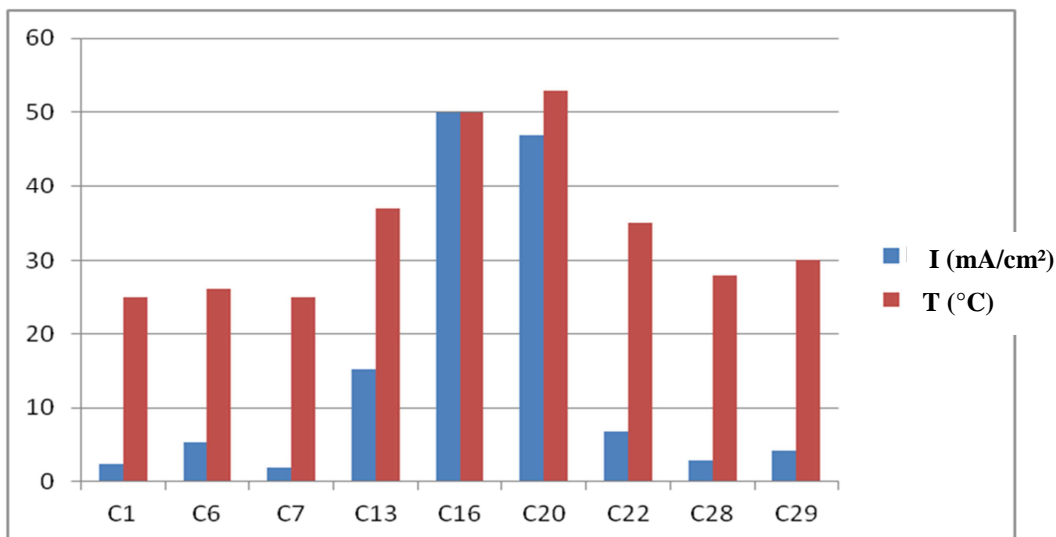
Figure V.13 : Correlation between the maximal temperatures observed with the IR camera and the membrane permeation

The IR images obtained for some cells of the aged stacks are presented in Fig.V.14. The preferential paths for hydrogen permeation (degraded zones) are mainly localized close to the anode outlet, except for the MEA 1, where it is located close to the hydrogen inlet.
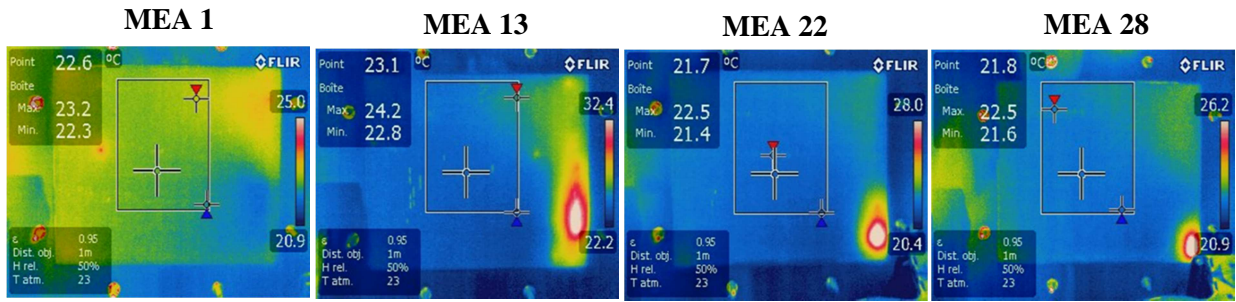
Figure V.14 : Infrared images of some aged MEA of the tests

The figure V.15 presents the simulated membrane water content at the minimum and maximal operating current points of the cycle as well as the water content evolution between these two points. Negative water content variations (from ~ -6.5 to 0) correspond to membrane shrinking while positive variations (from 0 to ~ 8) correspond to membrane swelling. For more detail, the global membrane water content evolution in the different operating conditions of the ageing tests are presented in Appendix 4.

The three zones indicated on the 2D plot of the water content difference with dashed black contours are the zones with the highest water content changes during the NEDC/RH cycling. In two of these three zones, significant membrane degradations are observed using the IR camera. Curiously, in the last zone (center of the cell), no significant degradation of the membrane is observed.
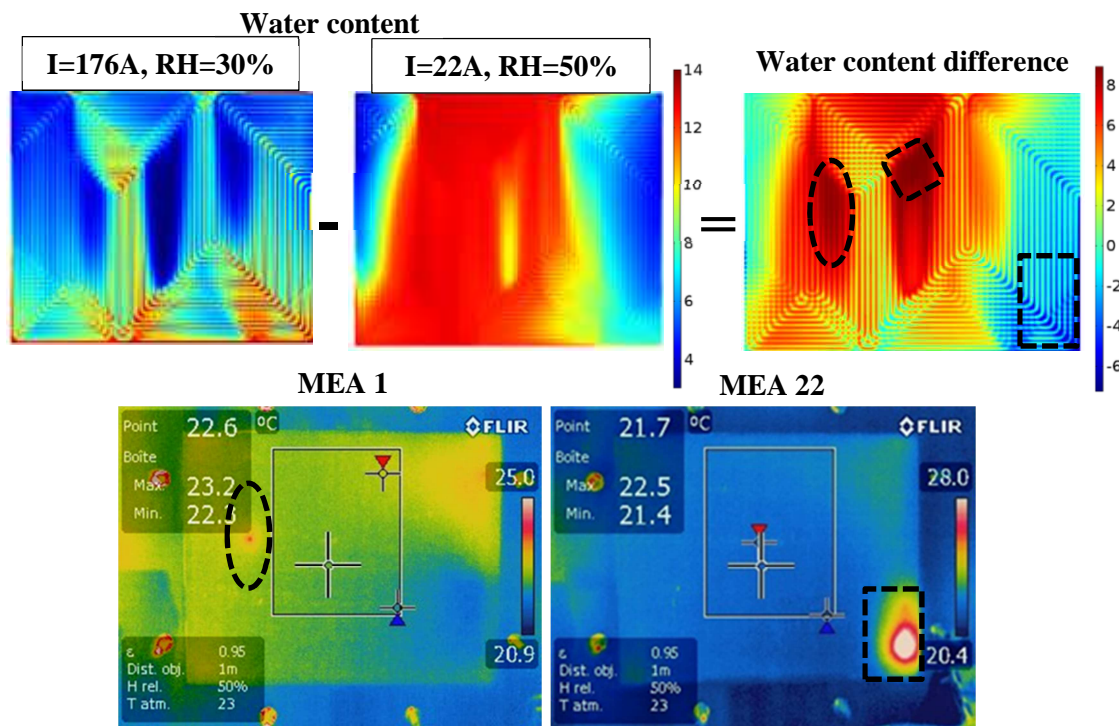
Figure V.15 : Correlation between the membrane degradations and the water content variations

174

On the whole, it can be stated that IR camera is useful technique to locate the pin-hole or local membrane thinning. The degraded zones of the membrane mainly correspond to the zones in which there are significant variations of membrane water content over time. Indeed, the variations of the membrane water content induce non-uniform membrane swelling and shrinking. As a consequence, there are non-uniform hygrothermal stresses in the membrane which can induce micro-cracks and pinholes where the gas crossover may intensify. These mechanical degradations can cause the fuel cell loss of functionality, even without gradual performance loss. However, further studies with huge humidity cycles are needed to better clarify this assertion since it is confirmed on only two zones among three.

2. Study of the Bipolar Plates degradations

2.1. Degradations cartography

Fig.V.16.a shows the cartography of cathode plate degradations for a cell aged in stationary conditions. Fig. V.10.b focuses on one cell of the stack (cell 25) and shows a localization and typology of the visual degradation observed by optical microscopy. The khaki color contrast is related to the severity of the degradations observed. The purple points, which indicate the welding zones of the bipolar plate, are not useful for this study.

a

Air inlet →

→ Air outlet

b

| Reference surface without degradations |

| Degraded surface |
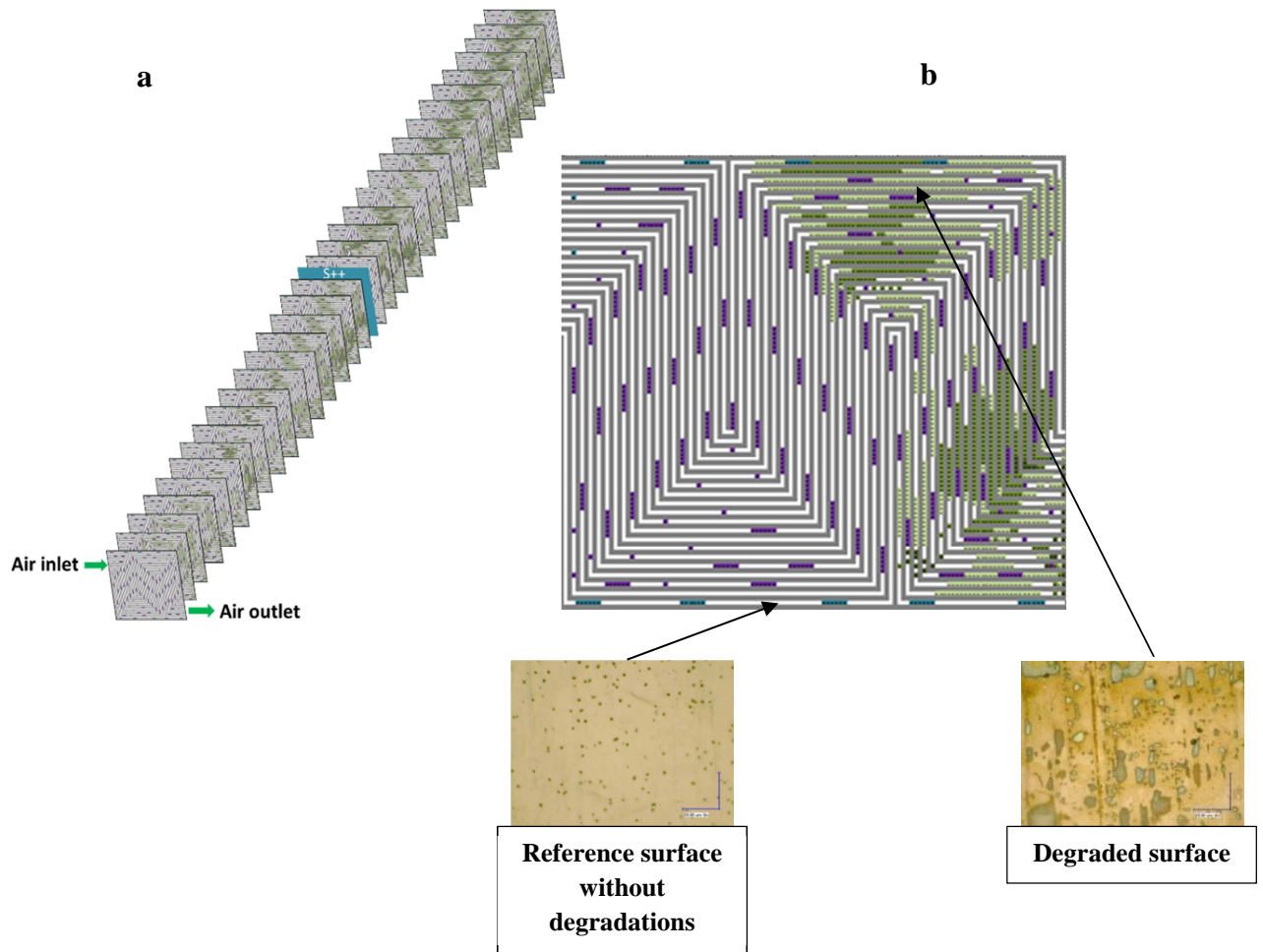
Figure V.16 : Cartography of the cathode plate degradations

The first observation is that the severity of the degradations observed is not homogeneous along the stack, but their localization over each cell is reproducible. When focusing on one single cell of the stack, different typologies of physical degradations are distinguished. The degradations are concentrated close to the air outlet, where the operating environment of the bipolar plate is wetter.

The same analyses are performed on the anode plates (see Fig.V.17). In this case, the severity of the observed degradations is indicated with the brown contrast. As for the cathode side, the degradations have the same localization on the anode plates, even if their severity is quite different.
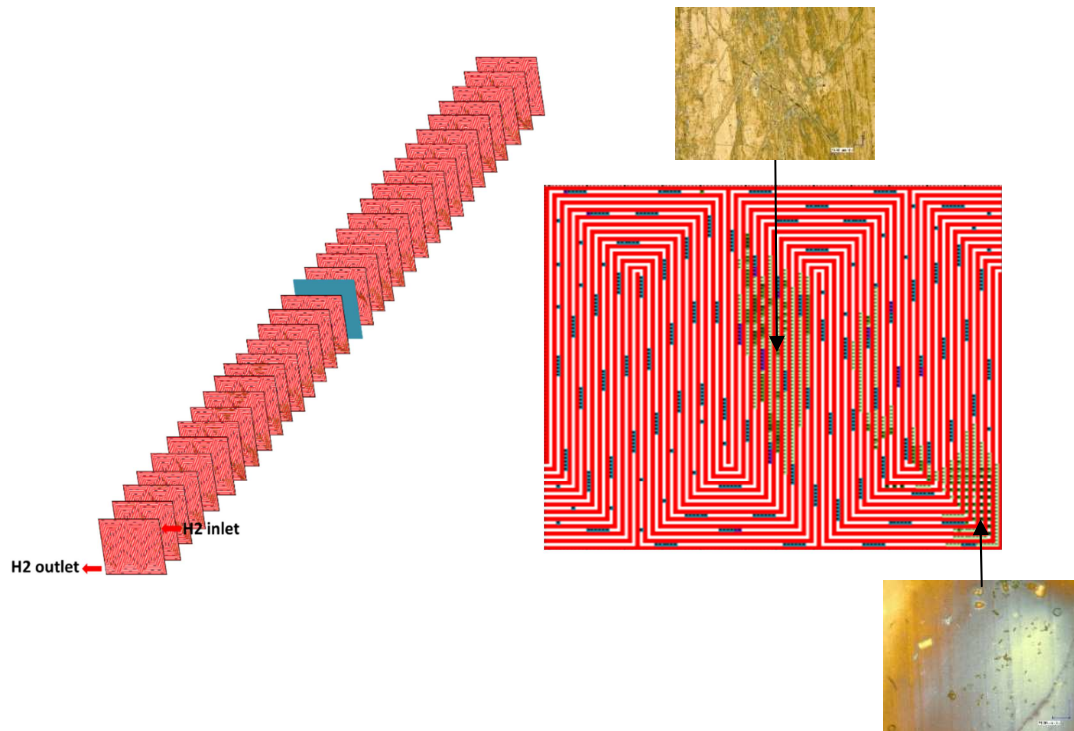
Figure V.17 : Cartography of the anode plate degradations

At the stack level, there is a linear evolution of the degradation severity from the first to the last cell. This could be caused by the heterogeneities of the cooling water distribution in the cells of the stack. Indeed, there is a progressive decrease of the coolant flow rate from the first to the last cell due to the pressure drop in the manifolds. This induces a progressive temperature increase from the first to the last cell. The degradations observed on the single cells are mainly located in the vicinity of hot spots of the cell, or close to the air outlet. Different types of physical degradations are identified via optical microscopy. For a deeper investigation of the observed degradations, Scanning Electron Microscopy is used.

2.2. Analysis via Scanning Electron Microscopy

When performing SEM on the aged bipolar plates (Fig.V.18), with a focus on the degraded zones, three main types of degradation can be distinguished:

- ➢ *Corrosion*. It is characterized by the bipolar plate surface chemical attack;
- ➢ *Fouling and deposits*. It is characterized by the accumulation of corrosion products and solid materials in the bipolar plate channels. Some SEM images of the deposits are presented in Fig.V.18.
- ➢ *Welding points attack.* The welding points are weakened by corrosion since they are at the same time preferential paths for current flow and chemically altered zones. The study of the welding points attack is an important challenge for mitigating the corrosion, but it is beyond the scope of this study.
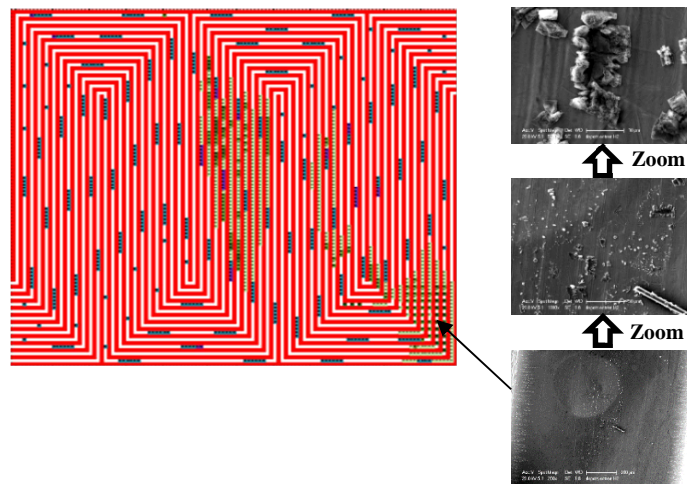
Figure V. 18: Example of degradations observed via SEM on the anode plate

Detailed analysis by X-ray Photoelectron Spectroscopy should allow identifying the chemical composition of the deposits and the state of oxidation of the BP surfaces.

2.3. Detailed analysis of the BP surface by XPS

a) Anode plate analysis

Fig.V.19 shows some results of the XPS spectrum analysis on some degraded zones of the anode plate.
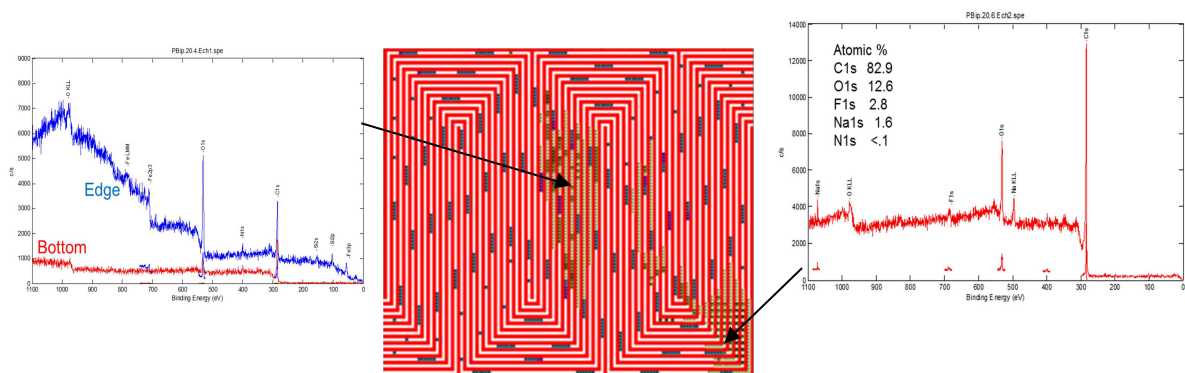
Figure V.19 : Example of XPS spectrum obtained on the anode plate

The first observation is that there is no passive layer on the BP surface. Deposits of corrosion products of the BP are observed in the hot zones. In particular, chromium oxide (Cr_2O_3), iron oxide (Fe_2O_3) and Silicon oxide (SiO_2) are observed in channels edge. In addition, graphite carbon is observed in the channels bottom. It may come either from the GDLs or from the BPs coating (on the land).

Deposits of CF_2, F, C and O are observed close to the hydrogen inlet. It is worth noting that F^- is very aggressive anion for the stainless steel and it should increase the potential risk of corrosion [110].

b) Cathode plate analysis

A passivation film of chromium oxides is observed on the cathode surface, excepted on the welding points, which are preferential zones of chemical attack. It agrees with what was observed by Davies et al. [163] and Wang et al. [164]. Corrosion products like chromium oxides, silicium oxides and iron oxides are observed in the channels. Pitting corrosion, coupled to an extremely localized depassivation is observed in some areas of BP, close to the air outlet.

2.4. Correlation between local temperature, humidity and BP degradations

Fig.V.20 shows the comparison between the anode plate degradations and the temperature in the gas channels.
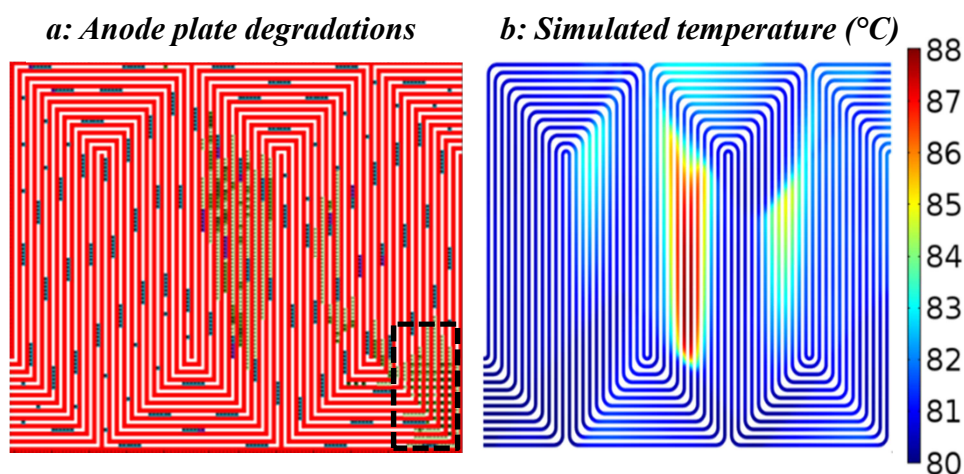
Figure V.20 : Comparison between the observed degradations on the anode plate and the local temperature

The first observation is that there is a deep correlation between the anode bipolar plate degradations and the temperature. The zones in which the anode bipolar plate temperature reaches extreme values (in which the saturation is lower) correspond to the zones where elevated degradations are observed. However, there are some degradations which don't really correspond to the hot zones as illustrated in dashed on Fig.V.20.a. XPS analyses showed that the fouling deposits in this zone are mainly composed of CF_2, F, C and O. The presence of O, CF_2 and F is likely related to a high oxygen permeation through the membrane, which cause its chemical attack by hydroxy and peroxy radicals. As a consequence, there is a considerable release of fluoride ions which are deposited on the bipolar plates since water is in vapor phase in this zone.

Fig.V.21.a shows the map of the observed degradations on the cathode plate and Fig.V.21.b shows the simulated relative humidity in the cathode gas channels.

a : Cathode plate degradations *b : RH in the gas channels*
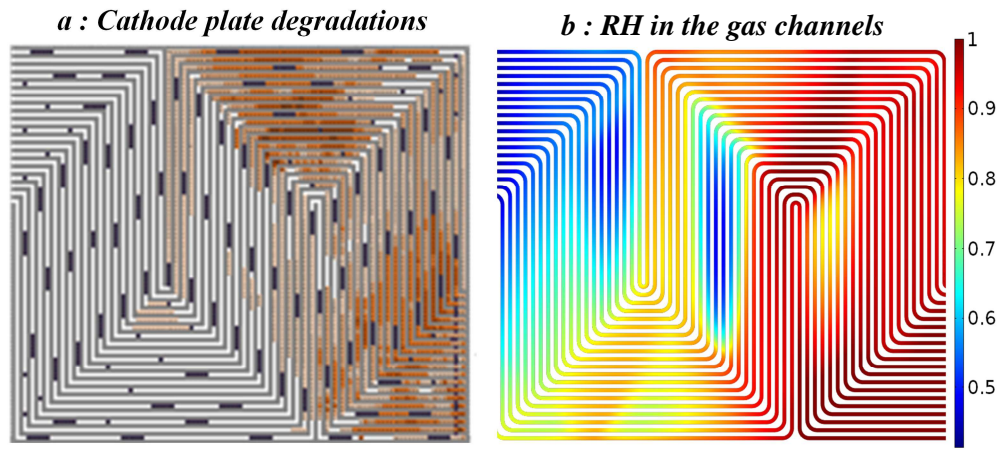
Figure V.21. Comparison between the observed degradations on the cathode plate and the local humidity

It is observed that there are some correlations between the humidity in the channels and the degradations. The observed degradations in the channels were classified in: dry corrosion, damp corrosion and deposits. In general, the main factors affecting the corrosion of stainless steel are the moisture on the surface, the water concentration and the temperature. Furthermore, the presence of contaminants and corrosive anions could increase the corrosion rate [145]. Fig.V.22 shows a global description of the correlation between heat, water management and the BPs degradations along one channel.
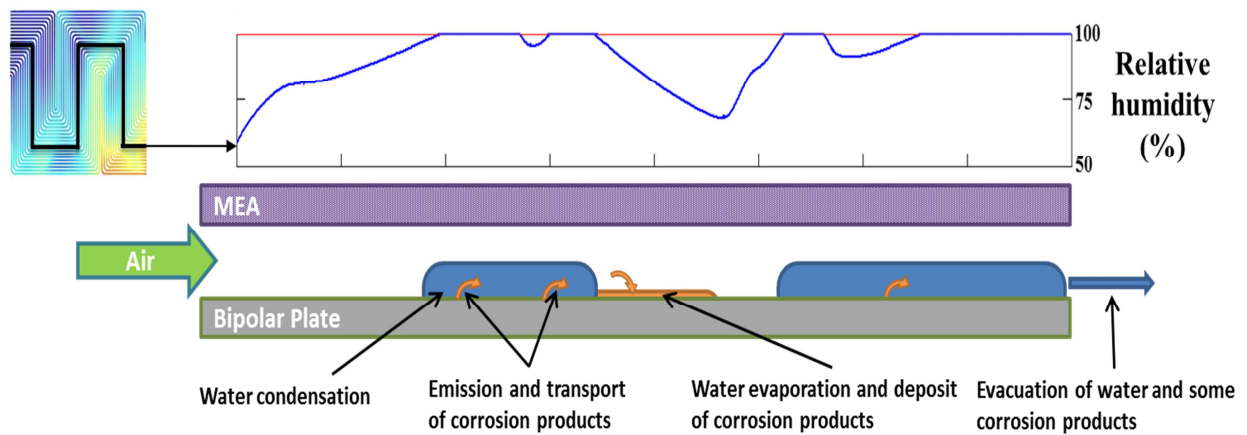
Figure V.22. Evolution of the water saturation along one channel - Description of the bipolar plates degradation mechanisms along the same channel

The electrochemical reaction induces a progressive increase of water concentration in the channel since the convective transport is predominant. From a certain water concentration threshold, there is water condensation on the bipolar plate surface, depending on local

temperature. The presence of liquid water increases the risk of corrosion. Farther in the gas channel, in the hot zones of the cell, the condensed water is evaporated again due to the increased water saturation pressure. This local evaporation increases the risk of deposits and fouling of the corrosion products on the bipolar plate surface.

Fouling, characterized by the accumulation of corrosion products and solid materials in the fuel cell environment, is mainly affected by temperature and phase change. During water evaporation (in the hot spots), the deposition of the dissolved materials is the major cause of fouling at the bipolar plates surface. The local flow velocity can also impact on fouling. At low flow rates, fouling is more probable due to the natural setting of suspended particles. The foulants pollute the reactive gases, increase the electrical resistance on the bipolar plate surface and they can be transported to the active layers by convection. The deposits can react with the coating layer and form other insoluble foulants, which can induce pollution of the MEA and even gas flows obstruction. Moreover, the corrosion products could cause ionic contamination of the membrane. Indeed, the membrane, which is an ionic conductor, may absorb the ionic impurities coming from metals corrosion and transported by liquid water droplets. As a consequence, its ionic conductivity would decrease, inducing a fuel cell performance drop.

Conclusion

In this study, a detailed investigation of the correlation between the coupled heat/water managements and PEMFCs degradations was conducted. Durability testing in automotive-related operating conditions was studied with different *in-situ* global and local experimental techniques. At the end of life, *post-mortem* analyses of the aged MEA and BP were performed. The main conclusion which can be drawn from this study are:

- The current density decreases over time in the dry zones and increases in the relatively wet zones.
- High values of water content in the membrane cause changes in physical structure, which can induce local delaminations. However, understanding the effect of the membrane delamination on performance loss remains a challenge.
- The membrane mechanical degradation is mainly affected by the water content variations over time. Cyclic variations of water content induce hydrothermal stresses in the membrane which lead to micro-cracks and pinholes.

- Dry and damp corrosion are observed in the bipolar plates. The main factor affecting the bipolar plates corrosion is the moisture on the surface and the temperature.

- Corrosion forms insoluble products that are transported by the flow and mixed with other degradation products (carbon from GDLs, CF_2 from membrane…). Those products can be either transported out of the cell through advection by the flow, or deposited in the fuel cell environment depending on local heat and water management. Phase change is mainly responsible for accumulation of corrosion products and fouling.

However, the study can be called into question on some points. The model used for the study of heat and water transport was calibrated for the MEA at the beginning of life. However, physical properties of the cell evolve with ageing: the electrochemical active surface area evolution is heterogeneous over the active area; the through-plane thermal conductivity of the GDLs increases with ageing as observed by Burheim et al. [134]. One perspective of the study is the modeling of the transport phenomena in the cell taking into account the evolution and degradation of the components. Appropriate degradation models should be developed and calibrated to this end. Indeed, the disparate time scale between real-time performances loss and various degradation mechanisms remains a great challenge. Moreover, the thermomechanical degradation of the coating layer of the bipolar plates was not taken into account in this study. The large difference in the coefficient of thermal expansion (CTE) between the base metal and the coating material may induce failure in the hot zones by separation, microcracks and pinholes [112].

CONCLUSION

The work presented in this thesis allowed to understand the temperature heterogeneities in a PEM Fuel Cell and to quantify the sources of these heterogeneities. The pseudo-3D approach developed appeared to be an efficient and low-cost method to study the heat and water transport phenomena at the cell scale, while taking into account the local heterogeneities induced by the bipolar plate design. Indeed, the model was accurately validated against measured data obtained via a sensor plate inserted in the middle of the stack. The pseudo-3D approach can easily be applied to other flow-field designs, for design and optimization purposes. Indeed, it appeared that the cooling flow field is a crucial factor for the heat management, and particular attention should be paid to its design. The reactive gases flow-field designs mainly impact on the water transport across the membrane, and consequently on the membrane water content. However, the phenomenon of water transport in the membrane, which represents the interface between the anode and cathode compartments, should be studied more carefully. Indeed, the elevated discrepancies in the water electro-osmosis drag and diffusivity models found in literature could induce non-negligible variations of the simulations, especially as regards temperature and water content distributions. The gas diffusion layer is also a crucial factor for the optimization of water management because it acts like a filter which maintains a considerable amount of the produced water in the MEA and contributes to smoothing the in-plane temperature heterogeneities.

The fact that a large part of the study was dedicated to modeling is justified by the correlations between heat/water management and degradations observed in Chapter V. Indeed, the simulations were useful in order to understand the components degradation, especially for the membrane. Without the simulation results, the observed mechanical degradation of the membrane could not be explained. Furthermore, in automotive conditions, the membrane is the most critical component of the cell in terms of durability. Nowadays, many researchers pay more attention to the electrochemical active surface area loss, which often leads to a gradual performance loss. Many efforts should be dedicated to the membrane, because its degradation often leads to an instantaneous functionality loss of the system, even without gradual performance loss. In the real automotive conditions, the global parameters cycling induces a non-uniform cycling of the local operating conditions, with can lead to a premature deterioration. From the correlation between the local water content and the membrane degradations found in this study, an empirical law can be deduced, for the

prediction of the membrane durability as a function of the value and/or oscillations of the local water content.

Experimental techniques are often limited in terms of reproducibility and invasiveness. Consequently, for fuel cells development, advanced models should be continuously developed with an appropriate choice of the physics, the dimensionality and the computation scale. Continuum-level modeling means making assumptions, which should be accurately borne in mind when analyzing the results. For example, in this study it was considered that the computed variables do not evolve along the thickness of each component. Moreover, one-phase flows were considered in the gas channels, and that may induce an uneven distribution of the saturation and phase change heat. The exact distribution of liquid water was measured by some researchers of the CEA and NIST using neutron radiography. They observed that the model developed in this study accurately predicts the localization of liquid water in the cell, excepted close to the air outlet, where there is a considerable amount of water condensation. But if the obtained results are post-treated taking into account the velocity ratio between the gas phase and the liquid phase, the coherence between the simulated and the measured distributions of liquid water becomes quite better close to the air outlet. In other words, the next step of this study should be the consideration of two-phase flows in the gas channels with the computation of different velocities for each phase. The resolution of the liquid phase can also be useful for the investigation of the bipolar plates degradations. Indeed, the accumulation of liquid water in the cell increases the probability of damp corrosion, especially in the cathode gas channels. The corrosion products are either transported out of the cell by the reactive gases flow, or deposited in the fuel cell environment depending on the local thermal conditions. The water evaporation is mainly responsible for the accumulation of the corrosion products in the gas channels.

For a proper study of the durability, the evolution of the thermal and electrical properties of the fuel cell components with ageing should be considered. Appropriate components degradation models should be proposed and calibrated to this end. Another perspective of the study is the detailed study of the structural damages observed in the membrane, which are greatly correlated to the water content. The membrane represents a crucial component towards which must be oriented the researches, with the purpose of an optimized heat and water management strategy for an improved durability. Furthermore, the industrial ambitions of increasing the fuel cell temperature and reducing the external humidification in the near future should induce additional constraints for the membrane durability studies.

REFERENCES

[1] N. Z. Muradov and T. N. Veziroglu. From hydrocarbon to hydrogen-carbon to hydrogen economy. *International Journal of Hydrogen Energy*, 30:225–237, 2005.

[2] World fossil fuel reserves and projected depletion. Technical report, The Colorado river commission of Nevada, 2002.

[3] R. Conrad and W. Seiler. Methane and hydrogen in seawater (Atlantic ocean). *Deep-Sea Research*, 35:1903–1917, 1988.

[4] Hydrogen production and storage. Technical report, International Energy Agency, 2006.

[5] National Hydrogen Association "Energy Evolution":
http://www.cleancaroptions.com/html/hydrogen_sources.html#WWTP

[6] Office of Air and Radiation. Technical support document for hydrogen production: Proposed rule for mandatory reporting of greenhouse gases. Technical report, U.S. Environmental Protection Agency, 2008.

[7] http://www.scientificamerican.com/article/has-the-time-finally-come-for-california-s-hydrogen-highway/

[8] http://fuelcellsworks.com/news/2014/07/30/jx-nippon-oil-to-build-100-hydrogen-stations-in-japan/

[9] http://media.daimler.com/dcmedia/0-921-656547-1-1636552-1-0-1-0-0-0-0-614316-0-1-@aj.a1.s177018-0-0-0-0.html

[10] http://cafcp.org/stationmap

[11] Fuel Cell Technical Team Roadmap 2013, U.S. DRIVE Partnership

[12] http://cleantechnica.com/2014/12/01/fuel-cell-economics-vs-batteries/

[13] M. J. Lampinen and M. Fomino. Analysis of free energy and entropy changes for half-cell reactions. *Journal of The Electrochemical Society*, 140(12):3537–3546, 1993.

[14] H. Ju, H. Meng and C-Y. Wang. A single-phase, non-isothermal model for PEM fuel cells. *International Journal of Heat and Mass Transfer*, 48:1303–1315, 2005.

[15] A. Z. Weber and J. Newman. Coupled thermal and water management in polymer electrolyte fuel cells. *Journal of The Electrochemical Society*, 153(12):A2205–A2214, 2006.

[16] N. Otmani. Détermination des contraintes mécaniques dans les membranes Nafion au cours du fonctionnement en pile à combustible. PhD Dissertation, *Grenoble Institute of Technology*, 2009.

[17] G. A. Luduena, T. D. Kuhne, and D. Sebastiani. Mixed grotthuss and vehicle transport mechanism in proton conducting polymers from ab initio molecular dynamics simulations. *Chemistry of Materials*, 2011.

[18] X. Yu, J. Yuan and B. Sundén. Review on the properties of nano-microstructures in the catalyst layer of PEMFC. *Journal of Fuel Cell Science and Technology*, 2011.

[19] A. Hermann, T. Chaudhuri and P. Spagnol. Bipolar plates for PEM fuel cells: A review. *International Journal of Hydrogen Energy*, 30:1297–1302, 2005

[20] M. Matsunaga, T. Fukushima and K. Ojima. Powertrain system of Honda FCX Clarity fuel cell vehicle. *World Electric Vehicle Journal*, 3, 2009.

[21] N. Konno, S. Mizuno, H. Nakaji and Ishikawa. Development of compact and high-performance fuel cell stack. *SAE International Journal of Alternative Powertrains*, 2015.

[22] G. Zhang and S. Kandlikar. A critical review of cooling techniques in proton exchange membrane fuel cell stacks. *International Journal of Hydrogen Energy*, 2012.

[23] B. Wu, M. Parkes, V. Yufit, L. De Benedetti, S. Veismann, C. Wirsching, F. Vesper, R. Martinez-Botas, A. Marquis, G. Offer and N. Brandon. Design and testing of a 9.5 kWe proton exchange membrane fuel cell-supercapacitor passive hybrid system. *International Journal of Hydrogen Energy*, 2014.

[24] Polymer electrolyte fuel cell (PEFC) technology road map. Technical report, New Energy and Industrial Technology Development Organization, 2007.

[25] D. Curtin, R. Lousenberg, T. Henry, P. Tangeman and M. Tisack. Advanced materials for improved PEMFC performance and life. *Journal of Power Sources*, 131:41–48, 2004.

[26] T. E. Springer, T. A. Zawodzinski and S. Gottesfeld. Polymer electrolyte fuel cell model. *Journal of The Electrochemical Society*, 138(8):2334–2342, 1991.

[27] D. M. Bernardi and M. W. Verbrugge. A mathematical model of the solid-polymer-electrolyte fuel cell. *Journal of The Electrochemical Society*, 139(9):2477–2491, 1992.

[28] T. Fuller and J. Newman. Water and thermal management in solid-polymer-electrolyte fuel cells. *Journal of The Electrochemical Society*, 140(5), 1993.

[29] H. Pei, Z. Liu, H. Zhang, Y. Yu, Z. Tu, Z. Wan and W. Liu. In situ measurement of temperature distribution in proton exchange membrane fuel cell in a hydrogen-air stack. *Journal of Power Sources*, 227:72–79, 2013.

[30] C-Y. Lee, W-J. Hsieh and G-W. Wu. Embedded flexible micro-sensors in MEA for measuring temperature and humidity in a micro-fuel cell. *Journal of Power Sources*, 181:237-243, 2008.

[31] C-Y. Lee, S-J. Lee, Y-M. Lo, and Y-M. Liu. Micro thermocouple and voltage sensor for fuel cell real time interior monitoring. *International Journal of Electrochemical Science*, 9:272–281, 2014.

[32] N. A. David, P. M. Wild, J. Jensen, T. Navessin and N. Djilali. Simultaneous in situ measurement of temperature and relative humidity in a PEMFC using optical fiber sensors. *Journal of The Electrochemical Society*, 157(8):B1173–B1179, 2010.

[33] G. Hinds, M. Stevens, J. Wilkinson, M. de Podesta and S. Bell. Novel in situ measurements of relative humidity in a polymer electrolyte membrane fuel cell. *Journal of Power Sources*, 186:52–57, 2009.

[34] S. Basu, M.W. Renfro and B.M. Cetegen. Spatially resolved optical measurements of water partial pressure and temperature in a PEM fuel cell under dynamic operating conditions. *Journal of Power Sources*, 162:286-293, 2006.

[35] S. Basu, M.W. Renfro, H. Gorgun and B.M. Cetegen. In situ simultaneous measurements of temperature and water partial pressure in a PEM fuel cell under steady state and dynamic cycling. *Journal of Power Sources*, 159:987-994, 2006.

[36] K. Inman, X. Wang and B. Sangeorzan. Design of an optical thermal sensor for proton exchange membrane fuel cell temperature measurement using phosphor thermometry. *Journal of Power Sources*, 195:4753-4757, 2010.

[37] M. Wang, H. Guo and C. Ma. Temperature distribution on the MEA surface of a PEMFC with serpentine channel flow bed. *Journal of Power Sources*, 157:181–187, 2006.

[38] A. Hakenjos, H. Muenter, U. Wittstadt and C. Hebling. A PEM fuel cell for combined measurement of current and temperature distribution, and flow field flooding. *Journal of Power Sources*, 131:213–216, 2004.

[39] B. Gould, R. Ramamurti, C. Osland and K. Swider-Lyons. Assessing fuel cell coolant flow fields with numerical models and infrared thermography. *International Journal of Hydrogen Energy*, 39:14061–14070, 2014.

[40] S. He, M. Mench and S. Tadigadapa. Thin film temperature sensor for real-time measurement of electrolyte temperature in a polymer electrolyte fuel cell. *Sensors and Actuators*, A125:170–177, 2006.

[41] G. Zhang, L. Guo, L. Ma and H. Liu. Simultaneous measurement of current and temperature distributions in a proton exchange membrane fuel cell. *Journal of Power Sources*, 195(11):3597–3604, June 2010.

[42] S++ Simulation Services, www.splusplus.com

[43] R. Lin, C. Cao, J. Ma, E. Gaslzow and K. A. Friedrich. In situ measurement of temperature

distribution within a single polymer electrolyte membrane fuel cell. *International Journal of Hydrogen Energy*, 37:11871 – 11886, 2012.

[44] S. Enz, T. A. Dao, M. Messerschmidt and J. Scholta. Investigation of degradation effects in polymer electrolyte fuel cells under automotive-related operating conditions. *Journal of power sources*, 274:521 – 535, 2015.

[45] Y-H. Lai and G. Fly. In-situ diagnostics and degradation mapping of a mixed-mode accelerated stress test for proton exchange membranes. *Journal of Power Sources*, 274:1162 – 1172, 2015.

[46] C.Y. Lee, C-H. Chen, C-L. Hsieh, K-F. Lin, S. Lee, T-L. Chen and Y-P. Huang. Flexible four-in-one micro sensor for reliability and 100-hour durability testing. *International Journal of Electrochemical Science,* 10:3185 – 3191, 2015.

[47] Y-S. Chen, H. Peng, D. Hussey, D. Jacobson, D. Tran, T. Abdel-Baset and M. Biernacki. Water distribution measurement for a PEMFC through neutron radiography. *Journal of Power Sources*, 170:376-386, 2007.

[48] G. Gebel, O. Diat, S. Escribano and R. Mosdale. Water profile determination in a running PEMFC by small-angle neutron scattering. *Journal of Power Sources*, 179:132-139, 2008.

[49] M. Gérard. Étude des interactions pile / système en vue de l'optimisation d'un générateur pile à combustible: interactions cœur de pile / compresseur - interactions cœur de pile / convertisseur. PhD thesis, *Université de Franche-Comté*, 2010.

[50] V. P. Schulz, J. Becker, A. Wiegmann, P. P. Mukherjee and C-Y. Wang. Modeling of two-phase behavior in the gas diffusion medium of PEFCs via full morphology approach. *Journal of The Electrochemical Society*, 154:B419–B426, 2007.

[51] P.P. Mukherjee, Q. Kanga and C.Y. Wang. Pore-scale modeling of two-phase transport in polymer electrolyte fuel cells - progress and perspective. *Energy & Environmental Science*, 4:346–369, 2010.

[52] P. Sinha and C-Y. Wang. Pore-network modeling of liquid water transport in gas diffusion layer of a polymer electrolyte fuel cell. *Electrochimica Acta*, 52:7936-7945, 2007.

[53] M. El Hannach, J. Pauchet and M. Prat. Pore network modeling: Application to multiphase transport inside the cathode catalyst layer of proton exchange membrane fuel cell. *Electrochimica Acta*, 56:10796 – 10808.

[54] B. Straubhaar and M. Prat. Water transport in gas diffusion layers of PEM fuel cells in presence of a temperature gradient. Condensation effect. *20th World hydrogen energy conference, WHEC, Gwangju Metropolitan City*, 2014.

[55] J. Park, M. Matsubara and X. Li. Application of lattice Boltzmann method to a micro-scale flow simulation in the porous electrode of a PEM fuel cell. *Journal of Power Sources*, 173:404–414, 2007.

[56] L. Hao and P. Cheng. Lattice Boltzmann simulations of anisotropic permeabilities in carbon paper gas diffusion layers. *Journal of Power Sources*, 186:104-114.

[57] P. Zhou and C.W. Wu. Numerical study on the compression effect of gas diffusion layer on PEMFC performance. *Journal of Power Sources*, 170:93–100, 2007.

[58] J. Elliott and S. Paddison. Modelling of morphology and proton transport in PFSA membranes. *Physical Chemistry Chemical Physics*, 2007.

[59] J. T. Wescott, Y. Qi, L. Subramanian and T. W. Weston Capehart. Mesoscale simulation of morphology in hydrated perfluorosulfonic acid membranes. *The Journal of Chemical Physics*, 124, 2006.

[60] D. Galperin and A. R. Khokhlov. Mesoscopic morphology of proton-conducting polyelectrolyte membranes of Nafion type: A self-consistent mean field simulation. *Macromolecular Theory and Simulations*, 15:137-146, 2006.

[61] N. Djilali and D. Lu. Influence of heat transfer on gas and water transport in fuel cells. *International Journal of Thermal Sciences*, 41:29–40, 2002.

[62]   J.G. Pharoah, O. S. Burheim, P. Vie and S. Kjelstrup, Thermal effects in PEMFCs, *Fundamentals and Development of Fuel Cells Conference* 2008.

[63]   J. Park, M. Matsubara and X. Li. Application of lattice Boltzmann method to a micro-scale flow simulation in the porous electrode of a PEM fuel cell. *Journal of Power Sources*, 173:404–414, 2007.

[64]   Y. Bultel, P. Ozil and R. Durand. Modelling of mass transfer within the PEM fuel cell active layer: limitations at the particle level. *Journal of Applied Electrochemistry*, 29:1025–1033, 1999.

[65]   J. Hwang and P. Chen. Heat/mass transfer in porous electrodes of fuel cells. *International Journal of Heat and Mass Transfer*, 49:2315-2327, 2006.

[66]   C. Siegel. Two-Dimensional, Non-Isothermal, Two-Phase Flow inside the Gas Diffusion Layer Unit of the Polymer-Electrolyte-Membrane Fuel Cell. *Proceedings of the COMSOL User Conference - Frankfurt,* 2006.

[67]   E. Birgersson, M. Noponen and M. Vynnycky. *Journal of The Electrochemical Society*, 152:A1021-A1034, 2005.

[68]   C-Y. Jung, H-S. Shim, S-M. Koo, S-H. Lee and S-C. Yi. Investigations of the temperature distribution in proton exchange membrane fuel cells. *Applied Energy,* 93:733-741, 2012.

[69]   S. Basu, C-Y. Wang and K. S. Chen. Phase Change in a Polymer Electrolyte Fuel Cell, *Journal of The Electrochemical Society*, 156(6):B748-B756, 2009.

[70]   Y. Shan, S. Choe and S. Choi, Unsteady 2D PEM fuel cell modeling for a stack emphasizing thermal effects. *Journal of Power Sources,* 165:196-209, 2007.

[71]   S. Shimpalee, S. Dutta. Numerical prediction of temperature distribution in PEM fuel cells**.** *Numerical Heat Transfer, Part A*, 38:111-128, 2000.

[72]   H. Ju, H. Meng and C-Y. Wang. A single-phase, non-isothermal model for PEM fuel cells. *International Journal of Heat and Mass Transfer*, 48:1303–1315, 2005.

[73]   M. Wang, H. Guo and C. Ma. Temperature distribution on the MEA surface of a PEMFC with serpentine channel flow bed. *Journal of Power Sources*, 157:181–187, 2006.

[74]   P. T. Nguyen, T. Berning and N.Djilali. Computational model of a PEM fuel cell with serpentine gas flow channels. *Journal of Power Sources*, 130(1-2):149–157, 2004.

[75]   A. Su, Y.M. Ferng, W.T. Chen, C.H. Cheng, F.B. Weng and C.Y. Lee. Investigating the transport characteristics and cell performance for a micro PEMFC through the micro sensors and CFD simulations. *International Journal of Hydrogen Energy* 37 : 11321-11333, 2012.

[76]   A. D. Le and B. Zhou. A general model of proton exchange membrane fuel cell. *Journal of Power Sources* 182:197-222, 2008.

[77]   S. S. Hwang, P. H. Lee, S. Hye Jo, C. L. Cha, S. W. Hong, S. S. Han and J. Y. Koo. Transient behavior of proton exchange membrane fuel cell under non-isothermal condition. *Renewable Energy* 42 : 54-59, 2012.

[78]   Z. Liu, Z. Mao, C. Wang, W. Zhuge and Y. Zhang. Numerical simulation of a mini PEMFC stack, *Journal of Power Sources* 160:1111-1121, 2006.

[79]   G. Inoue, Y. Matsukuma and M. Minemoto. Examination of optimal separator shape of polymer electrolyte fuel cell with numerical analysis including the effect of gas flow through gas diffusion layer, *Journal of Power Sources* 157 :153-165, 2006.

[80]   G. Inoue, T. Yoshimoto, Y. Matsukuma, M. Minemoto, H. Itoh and S. Tsurumaki. Numerical analysis of relative humidity distribution in polymer electrolyte fuel cell stack including cooling water, *Journal of Power Sources* 162 : 81-93, 2006.

[81]   T. Ishimoto and M. Koyama. A review of molecular-level mechanism of membrane degradation in the polymer electrolyte fuel cell. *Membranes*, 2:395–414, 2012.

[82]   X. Zhang, Y. Rui, Z. Tong, X. Sichuan, S. Yong and N. Huaisheng. The characteristics of voltage degradation of a proton exchange membrane fuel cell under a road operating environment.

International Journal of Hydrogen Energy, 39:9420–9429, 2014.

[83] R. E. Silva, R. Gouriveau, S. Jemei, D. Hissel, L. Boulon, K. Agbossou and N. Y. Steiner. Proton exchange membrane fuel cell degradation prediction based on adaptive neuro-fuzzy inference systems. *International Journal of Hydrogen Energy*, 39:11128 – 11144, 2014.

[84] C. Robin, M. Gerard, A.A. Franco and P. Schott. Multi-scale coupling between two dynamical models for PEMFC aging prediction. *International Journal of Hydrogen Energy*, 38(11):4675 – 4688, 2013.

[85] J. Pauchet, M. Prat, P. Schott and S. P. Kuttanikkad. Performance loss of proton exchange membrane fuel cell due to hydrophobicity loss in gas diffusion layer: Analysis by multiscale approach combining pore network and performance modelling. *International Journal of Hydrogen Energy*, 37(2):1628 – 1641, 2012.

[86] L. Dubau, L. Castanheira, F. Maillard, M. Chatenet, O. Lottin, G. Maranzana, J. Dillet, A. Lamibrac, J-C. Perrin, E. Moukheiber, A. ElKaddouri, G. De Moor, C. Bas, L. Flandin and N. Caqué. A review of PEM fuel cell durability: materials degradation, local heterogeneities of aging and possible mitigation strategies. *WIREs Energy Environnement*, 3:540-560, 2014.

[87] N-I. Kim, Y. Seo, K. B. Kim, N. Lee, J-H. Lee, I. Song, H. Choi and J-Y. Park. Post-mortem analysis of a long-term tested proton exchange membrane fuel cell stack under low cathode humidification conditions. *Journal of Power Sources*, 253:90–97, 2014.

[88] L. Guetaz, S. Escribano and O. Sicardy. Study by electron microscopy of proton exchange membrane fuel cell membrane-electrode assembly degradation mechanisms: Influence of local conditions. *Journal of Power Sources*, 212(0):169 – 178, 2012.

[89] P. Pei and H. Chen. Main factors affecting the lifetime of proton exchange membrane fuel cells in vehicle applications: A review. *Applied Energy*, 125:60–75, 2014.

[90] J. Wu, X. Z. Yuan, J. J. Martin, H. Wang, J. Zhang, J. Shen, S. Wu and W. Merida. A review of PEM fuel cell durability: Degradation mechanisms and mitigation strategies. *Journal of Power Sources*, 184(1):104 – 119, 2008.

[91] M. P. Rodgers, L. J. Bonville, H. R. Kunz, D. K. Slattery and J. M. Fenton. Fuel cell perfluorinated sulfonic acid membrane degradation correlating accelerated stress testing and lifetime. *Chemical Review*, 112:6075–6103, 2012.

[92] N. Ramaswamy, N. Hakim and S. Mukerjee. Degradation mechanism study of perfluorinated proton exchange membrane under fuel cell operating conditions. *Electrochimica Acta*, 53:3279-3295, 2008.

[93] V. Sethuraman, J. Weidner, A. Haug, A. Motupally and L. Protsailo. Hydrogen peroxide formation rate in a PEMFC anode and cathode. Effect of humidity and temperature. *Journal of The Electrochemical Society*, 155(1):B50–B57, 2008.

[94] W. Schmittinger and A. Vahidi. A review of the main parameters influencing long-term performance and durability of PEM fuel cells. *Journal of Power Sources*, 180:1–14, 2008.

[95] A. Kusoglu, A. Karlsson, M. Santare, S. Cleghorn and W. Johnson. Mechanical response of fuel cell membranes subjected to a hygrothermal cycle. *Journal of Power Sources*, 161:987–996, 2006.

[96] A. Kusoglu, A. Karlsson, M. Santare, S. Cleghorn and W. Johnson. Mechanical behavior of fuel cell membranes under humidity cycles and effect of swelling anisotropy on the fatigue stresses. *Journal of Power Sources*, 170:345-358, 2007.

[97] R. Solasi, Y. Zou, X. Huang, K. Reifsnider and D. Condit. On mechanical behavior and in-plane modeling of constrained PEM fuel cell membranes subjected to hydration and temperature cycles. *Journal of Power Sources*, 167:366–377, 2007.

[98] K. Panha, M. Fowler, X-Z. Yuan and H. Wang. Accelerated durability testing via reactants relative humidity cycling on PEM fuel cells. *Applied Energy*, 93:90-97, 2012.

[99] S. F. Burlatsky, M. Gummalla, J. O'Neill, V.V. Atrazhev, A.N. Varyukhin, D.V. Dmitriev and N.S. Erikhman. A mathematical model for predicting the life of polymer electrolyte fuel cell membranes

subjected to hydration cycling. *Journal of Power Sources*, 215:135–144, 2012.

[100] C. Lim, L. Ghassemzadeh, F. Van Hove, M. Lauritzen, J. Kolodziej, G.G. Wang, S. Holdcroft and E. Kjeang. Membrane degradation during combined chemical and mechanical accelerated stress testing of polymer electrolyte fuel cells. *Journal of Power Sources*, 257(0):102 – 110, 2014.

[101] R. Khorasany, E. Kjeang, G. Wang and R. Rajapakse. Simulation of ionomer membrane fatigue under mechanical and hygrothermal loading conditions. *Journal of Power Sources*, 279:55–63, 2015.

[102] S. Zhang, X. Yuana and H. Wang. A review of accelerated stress tests of mea durability in PEM fuel cells. *International Journal of Hydrogen Energy*, 34:388–404, 2009.

[103] W. Bi and T. F. Fuller. Temperature effects on PEM fuel cells Pt/C catalyst degradation. *Journal of The Electrochemical Society*, 155(2):B215–B221, 2008.

[104] T. Dam and F. de Bruijn. The stability of PEMFC electrodes. Platinum dissolution vs potential and temperature investigated by quartz crystal microbalance. *Journal of The Electrochemical Society*, 154:B494–B499, 2007.

[105] R. Borup, J. R. Davey, F. H. Garzon, D. L. Wood, and M. A. Inbody. PEM fuel cell electrocatalyst durability measurements. *Journal of Power Sources*, 163:76–81, 2006.

[106] R. Mukundan and R. Borup. Accelerated testing validation. Technical report, *Los Alamos National Laboratory*, 2014.

[107] K. Feng, G. Wu, Z. Li, X. Cai, and P. Chu. Corrosion behavior of SS316L in simulated and accelerated PEMFC environments. *International Journal of Hydrogen Energy*, 36:13032–13042, 2011.

[108] H. Wang and J. A. Turner. Electrochemical nitridation of a stainless steel for PEMFC bipolar plates. *International Journal of Hydrogen Energy*, 36:13008–13013, 2011.

[109] Y. Yang, L. Guo and H. Liu. Corrosion characteristics of SS316L as bipolar plate material in PEMFC cathode environments with different acidities. *International Journal of Hydrogen Energy*, 36:1654–1663, 2011.

[110] Y. Yang, L. Guo and H. Liu. Factors affecting corrosion behavior of SS316L as bipolar plate material in PEMFC cathode environments. *International Journal of Hydrogen Energy*, 37:1875–1883, 2012.

[111] P. Mani, A. Srinivasan and N. Rajendran. Effect of nitrides on the corrosion behaviour of 316L SS bipolar plates for proton exchange membrane fuel cell (PEMFC). *International Journal of Hydrogen Energy*, 40:3359–3369, 2015.

[112] A. S. Woodman, E. B. Anderson, K. D. Jayne, and M. C. Kimble, Development of Corrosion-Resistant Coatings for Fuel Cell Bipolar Plates, *AESF SUR/FIN '99 Proceedings,* 6/21-24, 1999.

[113] Q. Yan, H. Toghiani, Y-W. Lee, K. Liang and H. Causey. Effect of sub-freezing temperatures on a PEM fuel cell performance, startup and fuel cell components. *Journal of Power Sources*, 160:1242–1250, 2006.

[114] Q. Guo and Z. Qi. Effect of freeze-thaw cycles on the properties and performance of membrane-electrode assemblies. *Journal of Power Sources*, 160:1269-1274, 2006.

[115] I. Bloom, J. K. Basco, L. K. Walker, T. Malkow, G. DeMarco, A. Saturnio and G. Tsotridis. Fuel Cell Testing Protocols: An International Perspective, *ANL Technical Report* 2013.

[116] C. Carral and P. Mélé. A numerical analysis of PEMFC stack assembly through a 3D finite element model. *International Journal of Hydrogen Energy*, 39(9):4516–4530, 2014.

[117] A. Faghri and Z. Guo. Challenges and opportunities of thermal management issues related to fuel cell technology and modeling. *International Journal of Heat and Mass Transfer*, 48:3891-3920, 2005.

[118] M. Khandelwal and M.M. Mench. Direct measurement of through-plane thermal conductivity and

contact resistance in fuel cell materials. *Journal of Power Sources*, 161:1106-1115, 2006.

[119]   G. Karimi and P. Teertstra. Measurement of through-plane effective thermal conductivity and contact resistance in PEM fuel cell diffusion media. *Electrochimica Acta*, 55:1619-1625, 2010.

[120]   N. Alhazmi, M.S. Ismail, D.B. Ingham, K.J. Hughes, L. Ma and M. Pourkashanian. The in-plane thermal conductivity and the contact resistance of the components of the membrane electrode assembly in proton exchange membrane fuel cells. *Journal of Power Sources*, 241:136–145, 2013.

[121]   J. Yablecki, J. Hinebaugh and A. Bazylak. Effect of liquid water presence on PEMFC GDL effective thermal conductivity. *Journal of The Electrochemical Society*, 159 (12):F805–F809, 2012.

[122]   H. Sadeghifar, N. Djilali and M. Bahrami. Effect of polytetrafluoroethylene (PTFE) and micro porous layer (MPL) on thermal conductivity of fuel cell gas diffusion layers: Modeling and experiments. *Journal of Power Sources*, 248(0):632 – 641, 2014.

[123]   C. Choy, W. Wong, W. Yang and T. Kanamoto. Elastic modulus and thermal conductivity of ultradrawn polyethylene. *Journal of Polymer Science: Part B: Polymer Physics*, 37:3359-3367, 1999.

[124]   O. Burheim, P. Vie, J. Pharoah and S. Kjelstrup. *Ex situ* measurements of through-plane thermal conductivities in a polymer electrolyte fuel cell. *Journal of Power Sources*, 195:249–256, 2010.

[125]   O. Burheim, H. Su, H. Hauge, S. Pasupathi, and B. Pollet. Study of thermal conductivity of PEM fuel cell catalyst layers. *International Journal of Hydrogen Energy*, 39:9397–9408, 2014.

[126]   P. Vie and S. Kjelstrup. Thermal conductitivies from temperature profiles in polymer electrolyte fuel cells. *Electrochimica Acta*, 49:1069–1077, 2004.

[127]   A. Pfrang, D. Veyret and G. Tsotridis. Computation of thermal conductivity of gas diffusion layers of PEM fuel cells. *Convection and Conduction Heat Transfer*, 2011.

[128]   N. Zamel, X. Li, J. Shen, J. Becker and Andreas Wiegmann. Estimating effective thermal conductivity in carbon paper diffusion media. *Chemical Engineering Science*, 65:3994-4006, 2010.

[129]   A. Thomas, G. Maranzana, S. Didierjean, J. Dillet and O. Lottin. Thermal and water transfer in PEMFCs: investigating the role of the microporous layer. *International Journal of Hydrogen Energy*, 39:2649–2658, 2014.

[130]   O. Burheim, H. Su, S. Pasupathi, J. Pharoah and B. Pollet. Thermal conductivity and temperature profiles of the micro porous layers used for the polymer electrolyte membrane fuel cell. *International Journal of Hydrogen Energy*, 38:8437–8447, 2013.

[131]   Y. Wang and M. Gundevia. Measurement of thermal conductivity and heat pipe effect in hydrophilic and hydrophobic carbon papers. *International Journal of Heat and Mass Transfer*, 60:134-142, 2013.

[132]   T. Hottinen and O. Himanen. PEMFC temperature distribution caused by inhomogeneous compression of GDL. *Electrochemistry Communications*, 9:1047–1052, 2007.

[133]   H. Sadeghifar, N. Djilali and M. Bahrami. A new model for thermal contact resistance between fuel cell gas diffusion layers and bipolar plates. *Journal of Power Sources*, 266(0):51 – 59, 2014.

[134]   O. Burheim, G. Ellila, J.D. Fairweather, A. Labouriau, S. Kjelstrup and J.G. Pharoah. Ageing and thermal conductivity of porous transport layers used for PEM fuel cells. *International Journal of Hydrogen Energy*, 221:356–365, 2013.

[135]   T. Akiki. Modélisation de la dégradation de la production de puissance d'une pile à combustible suite aux sollicitations mécaniques. PhD Dissertation, *University of Technology of Belfort-Montbéliard*, 2011.

[136]   A. Raj and T. Shamim. Investigation of the effect of multidimensionality in PEM fuel cells. *Energy Conversion and Management*, 86:443-452, 2014.

[137]   G-S. Kim, P.C. Sui, A.A. Shah and Ned Djilali. Reduced-dimensional models for straight-channel proton exchange membrane fuel cells. *Journal of Power Sources*, 135:3240-3249, 2010.

[138]   R. Liu, M. Stremler, K. Sharp, M. Olsen, J. Santiago, R. Adrian, H. Aref and D. Beeb. Passive

mixing in a three-dimensional serpentine microchannel. *Journal of Microelectromechanical Systems*, 9:190–196, 2000.

[139] Y. Lasbet, B. Auvity, C. Castelain and H. Peerhossaini. A chaotic heat-exchanger for PEMFC cooling applications. *Journal of Power Sources*, 156:114–118, 2006.

[140] Y. Lasbet, B. Auvity, C. Castelain and H. Peerhossaini. Thermal and hydrodynamic performances of chaotic mini-channel: Application to the fuel cell cooling. *Heat Transfer Engineering*, 28(8-9):795–803, 2007.

[141] R. Sadasivam, R. Manglik and M. Jog. Fully developed forced convection through trapezoidal and hexagonal ducts. *International Journal of Heat and Mass Transfer*, 42:4321–4331, 1999.

[142] D. Venter and C. Du Toit, Friction factors and Nusselt numbers for laminar flow in ducts, Thesis (Mechanical Engineering), *North-West University, Potchefstroom Campus*, 2009.

[143] N. Damean and P. Regtien, Poiseuille number for the fully developed laminar flow through hexagonal ducts etched in <1 0 0> silicon, *Sensors and Actuators* A 90: 96-101, 2001.

[144] C. Chagny-Regardin, Mélange et chauffage de fluides complexes à l'aide d'un échangeur de chaleur à effet d'advection chaotique, PhD. Dissertation, *University of Nantes*, 2000.

[145] R. Antunes, M. C. Oliveira, G. Ett and V. Ett. Corrosion of metal bipolar plates for PEM fuel cells: A review. *International Journal of Hydrogen Energy*, 35:3632-3647, 2010.

[146] T-F. Cao, H. Lin, L. Chen, Y-L. He and W-Q. Tao. Numerical investigation of the coupled water and thermal management in PEM fuel cell. *Applied Energy*, 112:1115-1125, 2013.

[147] S. Hwang, P. Lee, S. Jo, C. Cha, S. Hong, S.Han and J. Ko. Transient behavior of proton exchange membrane fuel cell under non-isothermal condition. *Renewable Energy*, 42:54–59, 2012.

[148] F. Meier and G. Eigenberger. Transport parameters for the modelling of water transport in ionomer membranes for PEM-fuel cells. *Electrochimica Acta*, 49:1731–1742, 2004.

[149] T. Zawodzinski, J. Dawy, J. Valerio and S. Gottesfeld. The water content dependence of electro-osmotic drag in proton-conducting polymer electrolytes. *Electrochimica Acta*, 40:297–302, 1994.

[150] T. Fuller. Solid-polymer electrolyte fuel cells. PhD Dissertation, *University of California*, 1992.

[151] T. V. Nguyen and R. E. White. A water and heat management model for proton-exchange-membrane fuel cells. *Journal of The Electrochemical Society*, 140:2178–2186, 1993.

[152] T. Zawodzinski, M. Neeman, L. Sillerud and S. Gottesfeld. Determination of water diffusion coefficient in perfluorosulfonate ionomeric membranes. *The Journal of Physical Chemistry*, 95:6040–6044, 1991.

[153] S. Motupally, A. Becker and J. W. Weidner. Diffusion of water in Nafion 115 membranes. *Journal of The Electrochemical Society*, 147 (9):3171–3177, 2000.

[154] C. Fink and N. Fouquet. Three-dimensional simulation of polymer electrolyte membrane fuel cells with experimental validation. *Electrochimica Acta*, 56:10820–10831, 2011.

[155] M. Marchand. Gestion de l'eau dans les piles à combustibles. PhD Dissertation, *Grenoble Institute of Technology*, 1998.

[156] E. F. Holby, W. Sheng, Y. Shao-Horn and D. Morgan. Pt nanoparticle stability in PEM fuel cells: influence of particle size distribution and crossover hydrogen. *Energy & Environmental Science*, 2:865–871, 2009.

[157] D.A. Stevens and J.R. Dahn. Thermal degradation of the support in carbon-supported platinum electrocatalysts for PEM fuel cells. *Carbon*, 43:179-188, 2005.

[158] M. Inaba, T. Kinumoto, A. Kiriake, R. Umebayashi, A. Tasaka and Z. Ogumi. Gas crossover and membrane degradation in polymer electrolyte fuel cells. *Electrochimica Acta*, 51:5746–5753, 2006.

[159] P. W. Majsztrik. Mechanical and transport properties of Nafion® for PEM fuel cells; temperature and hydration effects. PhD thesis, *Princeton University*, 2008.

[160] K. H. Wong and E. Kjeang. Mitigation of chemical membrane degradation in fuel cells: Understanding the effect of cell voltage and iron ion redox cycle. *ChemSusChem*, 8:1072-1082,

2015.

[161]   J. Healy, C. Hayden, T. Xie, K. Olson, R. Waldo, M. Brundage, H. Gasteiger and J. Abbott. Aspects of the chemical degradation of PFSA ionomer used in PEM fuel cells. *Fuel Cells*, 5(2):302–308, 2005.

[162]   E. Endoh, S. Terazono, H. Widjaja and Y. Takimoto. Degradation study of MEA for PEMFC under low humidity conditions. *Electrochemical and Solid-State Letters*, 7 (7):A209–A211, 2004.

[163]   D. P. Davies, P. L. Adcock, M. Turpin and S. J. Rowen. Bipolar plate materials for solid polymer fuel cells. *Journal of Applied Electrochemistry*, 30:101-105, 2000.

[164]   H. Wang, M. A. Sweikart and J. A. Turner. Stainless steel as bipolar plate material for polymer electrolyte membrane fuel cells. *Journal of Power Sources*, 115:243-251, 2003.

[165]   B. Todd, J.B. Young. Thermodynamic and transport properties of gases for use in solid oxide fuel cell modelling. *Journal of Power Sources,* 110: 186–200, 2002.

[166]   C. R. Wilke. A viscosity equation for gas mixtures. The Journal of Chemical Physics, 18 :517-519, 1950.

[167]   M. Lindstrom, B.Wetton. A comparison of Fick and Maxwell-Stefan diffusion formulations in PEMFC cathode gas diffusion layers. Journal of Power Sources, 2013.

APPENDIX

APPENDIX 1: MOLECULAR DIFFUSIVITIES

The molecular diffusivities $D_{i,k}$ are temperature (T) and pressure (P) dependent following the empirical correlations:

D_{O_2,H_2O}	$4.26 \cdot 10^{-6} \cdot T^{2.334}/P$
D_{H_2,H_2O}	$2.14 \cdot 10^{-6} \cdot T^{2.334}/P$
D_{H_2,N_2}	$2.44 \cdot 10^{-4} \cdot T^{1.823}/P$
D_{O_2,N_2}	$6.43 \cdot 10^{-5} \cdot T^{1.823}/P$
D_{N_2,H_2O}	$4.45 \cdot 10^{-6} \cdot T^{2.334}/P$

APPENDIX 2: THROUGH-PLANE HEAT FLUXES

Solid/solid heat flux

For every component $\boldsymbol{a}$ of the system which exchange heat with an adjacent component $\boldsymbol{b}$ as represented in figure, the Fourier's law for the heat flux from $\boldsymbol{b}$ to $\boldsymbol{a}$ is:

$$\vec{\varphi} = -\lambda \frac{\partial \theta}{\partial z} \vec{u}$$

The through-plane heat flux integration leads to:

$$\phi_a = \frac{1}{e} \lambda_z \frac{\partial \theta}{\partial z}\bigg|_{z_2}$$

$$\nabla \cdot \phi_a = 0 \quad \leftrightarrow \lambda_z \frac{\partial \theta}{\partial z} = Constant$$

$$\leftrightarrow \quad \phi_a = \frac{\lambda_a}{e_a} \cdot [\theta(z_2^-) - \theta(z_1)] = \frac{1}{R_c} \cdot [\theta(z_2^+) - \theta(z_2^-)]$$

$$= \frac{\lambda_b}{e_b} \cdot [\theta(z_3) - \theta(z_2^+)]$$

$$\begin{cases} \theta(z_2^-) - \theta(z_1) = \phi_a \cdot \dfrac{e_a}{\lambda_a} \\[2mm] \theta(z_2^+) - \theta(z_2^-) = \phi_a \cdot R_c \\[2mm] \theta(z_3) - \theta(z_2^+) = \phi_a \cdot \dfrac{e_b}{\lambda_b} \end{cases}$$

$$\phi_a = \frac{1}{e_a} \cdot \frac{1}{\dfrac{e_a}{\lambda_a} + R_c + \dfrac{e_b}{\lambda_b}} [\theta(z_3) - \theta(z_1)]$$

$$T_a = \frac{\theta(z_1) + \theta(z_2^-)}{2} \quad \leftrightarrow \quad \theta(z_1) = 2 \cdot T_a - \theta(z_2^-)$$

$$T_b = \frac{\theta(z_2^+) + \theta(z_3)}{2} \quad \leftrightarrow \quad \theta(z_3) = 2 \cdot T_b - \theta(z_2^+)$$

The through-plane heat flux, considering heat conduction in both solids and a contact resistance (Rc) becomes:

$$\phi_a = \frac{1}{e_a} \cdot \frac{1}{\dfrac{e_a}{\lambda_a} + R_c + \dfrac{e_b}{\lambda_b}} [2 \cdot T_b - \theta(z_2^+) - 2 \cdot T_a + \theta(z_2^-)]$$

$$\phi_a = \frac{1}{e_a} \cdot \frac{1}{\dfrac{e_a}{\lambda_a} + R_c + \dfrac{e_b}{\lambda_b}} [2 \cdot T_b - 2 \cdot T_a - \phi_a \cdot R_c]$$

And definitely:

$$\phi_a = \frac{1}{e_a} \cdot \frac{1}{\dfrac{e_a}{2\lambda_a} + R_c + \dfrac{e_b}{2\lambda_b}} [T_b - T_a]$$

Analogously, the heat flux from *a* to *b* is:

$$\phi_b = \frac{1}{e_b} \cdot \frac{1}{\dfrac{e_a}{2\lambda_a} + R_c + \dfrac{e_b}{2\lambda_b}} [T_a - T_b]$$

Solid/fluid heat flux

The Fourier's law of heat conduction from z_1 to z_2 is:

$$\phi_e = \frac{1}{e} \lambda_z \frac{\partial \theta}{\partial z}\bigg|_{z_2} = \frac{\lambda_e}{e_e} \cdot [\theta(z_2) - \theta(z_1)]$$

The Newton's law of heat convection from z_2 to z_3:

$$\phi_e = h(T_f - \theta(z2))$$

Flux continuity at interface z_2 leads to::

$$\frac{\lambda_e}{e_e} \cdot [\theta(z_2) - \theta(z_1)] = h \cdot [T_f - \theta(z2)]$$

or

$$\leftrightarrow \quad \theta(z_1) = \frac{e_e}{\lambda_e} \cdot \left[\left(h + \frac{\lambda_e}{e_e} \right) \cdot \theta(z2) - h \cdot T_f \right]$$

Introducing the average temperature of the solid component:

$$T_e = \frac{\theta(z_1) + \theta(z_2)}{2}$$

Allows calculating $\theta(z_2)$:

$$\theta(z_2) = \frac{2T_e + \frac{h \cdot e}{\lambda} T_f}{2 + \frac{h \cdot e}{\lambda}}$$

It follows for the Newton's law of convection:

$$\phi_e = \frac{1}{e_e} \cdot h \cdot \left[T_f - \frac{2T_e + \frac{h \cdot e}{\lambda} T_f}{2 + \frac{h \cdot e}{\lambda}} \right]$$

$$\leftrightarrow \quad \phi_e = \frac{1}{e_e} \cdot \frac{1}{\frac{1}{h} + \frac{e}{2\lambda}} \cdot (T_f - T_e)$$

Analogously, the heat flux from the solid e to the fluid f is:

$$\phi_f = \frac{1}{e_f} \cdot \frac{1}{\frac{1}{h} + \frac{e}{2\lambda}} \cdot (T_e - T_f)$$

The heat fluxes $\phi_{i,j}$ at the interfaces of the different components of the cell are presented in Fig.III.12.a, which illustrates the 3D geometry at the channel scale. Figure III.12.b presents the corresponding pseudo-3D concept, which introduces a flattened configuration. Detailed through-plane heat fluxes.

Subsystem (Temperature)	$\Sigma\phi_i$	Q_s
Membrane (T_6)	$\dfrac{1}{e_6}\cdot\left(\dfrac{1}{\dfrac{e_5}{2\lambda_5}+\dfrac{e_6}{2\lambda_6}}\right)\cdot(T_5-T_6)+\dfrac{1}{e_6}\cdot\left(\dfrac{1}{\dfrac{e_7}{2\lambda_7}+\dfrac{e_6}{2\lambda_6}}\right)\cdot(T_7-T_6)$	$\dfrac{i^2}{\sigma_6}$
aCL (T_5)	$\dfrac{1}{e_5}\cdot\left(\dfrac{1}{\dfrac{e_6}{2\lambda_6}+\dfrac{e_5}{2\lambda_5}}\right)\cdot(T_6-T_5)+\dfrac{1}{e_5}\cdot\left(\dfrac{1}{\dfrac{e_4}{2\lambda_4}+\dfrac{e_5}{2\lambda_5}}\right)\cdot(T_4-T_5)$	$0\cdot\left(\dfrac{\Delta H_{tot}}{2\cdot F}-V_{cell}\right)\cdot i$ $+\dfrac{i^2}{\sigma_5}$
aMPL (T_4)	$\dfrac{1}{e_4}\cdot\left(\dfrac{1}{\dfrac{e_5}{2\lambda_5}+\dfrac{e_4}{2\lambda_4}}\right)\cdot(T_5-T_4)+\dfrac{1}{e_4}\cdot\left(\dfrac{1}{\dfrac{e_3}{2\lambda_3}+R_c+\dfrac{e_4}{2\lambda_4}}\right)\cdot(T_3-T_4)$	$\dfrac{i^2}{\sigma_4}$
aGDL (T_3)	$\dfrac{1}{e_3}\cdot\left(\dfrac{1}{\dfrac{e_4}{2\lambda_4}+R_c+\dfrac{e_3}{2\lambda_3}}\right)\cdot(T_4-T_3)+\dfrac{1}{e_3}\cdot\left(\dfrac{1}{\dfrac{e_1}{2\lambda_1}+R_c+\dfrac{e_3}{2\lambda_3}}\right)\cdot C_1$ $\cdot(T_1-T_3)$ $+\dfrac{1}{e_3}\cdot\left(\dfrac{1}{\dfrac{e_3}{2\lambda_3}+\dfrac{1}{h_2}}\right)\cdot C_2\cdot(T_2-T_3)$	$\dfrac{i^2}{\sigma_3}$
H2 Gas Channels (T_2)	$\dfrac{1}{e_2}\cdot\left(\dfrac{1}{\dfrac{e_3}{2\lambda_3}+\dfrac{1}{h_2}}\right)\cdot C_2\cdot(T_3-T_2)+\dfrac{1}{e_2}\cdot\left(\dfrac{1}{\dfrac{e_1}{2\lambda_1}+\dfrac{1}{h_2}}\right)\cdot C_3\cdot(T_1-T_2)$	0
aBP (T_1)	$\dfrac{1}{e_1}\cdot\left(\dfrac{1}{\dfrac{e_3}{2\lambda_3}+R_c+\dfrac{e_1}{2\lambda_1}}\right)\cdot C_1\cdot(T_3-T_1)+\dfrac{1}{e_1}\cdot\left(\dfrac{1}{\dfrac{1}{h_2}+\dfrac{e_1}{2\lambda_1}}\right)\cdot C_3$ $\cdot(T_2-T_1)+$ $\dfrac{1}{e_1}\cdot\left(\dfrac{1}{\dfrac{1}{h_{12}}+\dfrac{e_1}{2\lambda_1}}\right)\cdot C_3\cdot(T_{12}-T_1)+\dfrac{1}{e_1}\cdot\left(\dfrac{1}{\dfrac{e_{11}}{2\lambda_{11}}+R_c+\dfrac{e_1}{2\lambda_1}}\right)\cdot C_1$ $\cdot(T_{11}-T_1)$	$\dfrac{i^2}{\sigma_1}$
Cooling Water (T_{12})	$\dfrac{1}{e_{12}}\cdot\left(\dfrac{1}{\dfrac{e_1}{2\lambda_1}+\dfrac{1}{h_{12}}}\right)\cdot C_3\cdot(T_1-T_{12})+\dfrac{1}{e_{12}}\cdot\left(\dfrac{1}{\dfrac{e_{11}}{2\lambda_{11}}+\dfrac{1}{h_{12}}}\right)\cdot C_3\cdot(T_{11}-T_{12})$	0
cBP (T_{11})	$\dfrac{1}{e_{11}}\cdot\left(\dfrac{1}{\dfrac{e_1}{2\lambda_1}+R_c+\dfrac{e_{11}}{2\lambda_{11}}}\right)\cdot C_1\cdot(T_1-T_{11})+\dfrac{1}{e_{11}}\cdot\left(\dfrac{1}{\dfrac{1}{h_{12}}+\dfrac{e_{11}}{2\lambda_{11}}}\right)\cdot C_3$ $\cdot(T_{12}-T_{11})+$ $\dfrac{1}{e_{11}}\cdot\left(\dfrac{1}{\dfrac{1}{h_{10}}+\dfrac{e_{11}}{2\lambda_{11}}}\right)\cdot C_3\cdot(T_{10}-T_{11})+\dfrac{1}{e_{11}}\cdot\left(\dfrac{1}{\dfrac{e_9}{2\lambda_9}+R_c+\dfrac{e_{11}}{2\lambda_{11}}}\right)\cdot C_1$ $\cdot(T_9-T_{11})$	$\dfrac{i^2}{\sigma_{11}}$

Air Gas Channels (T_{10})	$\dfrac{1}{e_{10}} \cdot \left(\dfrac{1}{\frac{e_{11}}{2\lambda_{11}} + \frac{1}{h_{10}}}\right) \cdot C_3 \cdot (T_{11} - T_{10}) + \dfrac{1}{e_{10}} \cdot \left(\dfrac{1}{\frac{e_9}{2\lambda_9} + \frac{1}{h_{10}}}\right) \cdot C_2 \cdot (T_9 - T_{10})$	0
cGDL (T_9)	$\dfrac{1}{e_9} \cdot \left(\dfrac{1}{\frac{e_{11}}{2\lambda_{11}} + R_c + \frac{e_9}{2\lambda_9}}\right) \cdot C_1 \cdot (T_{11} - T_9) + \dfrac{1}{e_9} \cdot \left(\dfrac{1}{\frac{1}{h_{10}} + \frac{e_9}{2\lambda_9}}\right) \cdot C_2$ $\cdot (T_{10} - T_9)$ $+ \dfrac{1}{e_9} \cdot \left(\dfrac{1}{\frac{e_8}{2\lambda_8} + R_c + \frac{e_9}{2\lambda_9}}\right) \cdot (T_8 - T_9)$	$\dfrac{i^2}{\sigma_9}$
cMPL (T_8)	$\dfrac{1}{e_8} \cdot \left(\dfrac{1}{\frac{e_9}{2\lambda_9} + R_c + \frac{e_8}{2\lambda_8}}\right) \cdot (T_9 - T_8) + \dfrac{1}{e_8} \cdot \left(\dfrac{1}{\frac{e_7}{2\lambda_7} + \frac{e_8}{2\lambda_8}}\right) \cdot (T_7 - T_8)$	$\dfrac{i^2}{\sigma_8}$
cCL (T_7)	$\dfrac{1}{e_7} \cdot \left(\dfrac{1}{\frac{e_8}{2\lambda_8} + \frac{e_7}{2\lambda_7}}\right) \cdot (T_8 - T_7) + \dfrac{1}{e_7} \cdot \left(\dfrac{1}{\frac{e_6}{2\lambda_6} + \frac{e_7}{2\lambda_7}}\right) \cdot (T_6 - T_7)$	$1 \cdot \left(\dfrac{\Delta H_{tot}}{2 \cdot F} - V_{cell}\right) \cdot i$ $+ \dfrac{i^2}{\sigma_7}$

APPENDIX 3: THERMODYNAMIC PROPERTIES OF THE REACTIVE GASES

a) Thermodynamics and transport properties of the reactant gases

The transport properties of the reactant species, which depend on temperature, were calculated using the relationships proposed by Todd and Young [165]. These relations are given in appendix. For the reactive gases, which are a mixture of different species, the kinetic theory of the transport properties proposed by Van Der Waals was used. The heat capacity of the mixture is:

$$c_{p_{mix}} = \sum_i w_i c_{p_i}$$

The dynamic viscosity of the mixtures of ideal gases is given by the Wilke formulas [166]:

$$\mu_{mix} = \sum_i \frac{y_i \mu_i}{\sum_i y_j \Psi_{ij}}$$

Analogously, the thermal conductivity is:

$$k_{mix} = \sum_i \frac{y_i k_i}{\sum_i y_j \Psi_{ij}}$$

Where ψ_{ij} is given by:

$$\Psi_{ij} = \frac{\left[1 + \left(\frac{M_j}{M_i}\right)^{1/4}\left(\frac{\mu_i}{\mu_j}\right)^{1/2}\right]^2}{\sqrt{8\left(1 + \frac{M_i}{M_j}\right)}}$$

b) Diffusion coefficients

Fickian approximation is used in this model as illustrated in section 1.1.c, instead of the Stefan-Maxwell diffusion which is more adapted for the transport of more than two concentrated species. Lindstrom et al. [167] demonstrated that the use of the diagonal Fick diffusivity can be equivalent to the Maxwell-Stefan diffusion model, with variation by only a few percent, if an appropriate equivalent diffusion coefficient is used. For the PEM fuel cell application, they proposed the following value for the cathode equivalent diffusivity, which is used in the study:

$$D_0^c = 1.07 \cdot 10^{-5} \ m^2/s$$

At the anode compartment, the reference diffusion coefficient is the binary diffusivity between H_2 and H_2O:

$$D_0^a = 2.14 \cdot 10^{-6} \cdot \frac{T^{2.334}}{P}$$

In the Porous media, there is a Bruggeman correction to account for the impact of porous and tortuous structures on the effective molecular diffusivity:

$$D_{eff} = D_0 \cdot \frac{\varepsilon}{\tau}$$

c) Ideal gases approximation for the reactants

The hypothesis of ideal gases for the reactants, presented in 1.1., needs justification. This can be done by comparing the densities of ideal gas and water vapor at the fuel cell temperature and pressure operating ranges. In the reference operating conditions, the temperature ranges from ~ 78 to ~ 100°C and the water vapor partial pressure maximal ranges from ~ 0.2 to ~ 0.45 bar.

At T=80°C and P_{H_2O} =0.32 bar (anode reference nominal conditions):

- The water vapor density is: $\rho = 0.19757 \; kg/m^3$
- The ideal gas density is: $\rho = \dfrac{P \cdot MH2O}{R \cdot T} = 0.196 \; kg/m^3$

Thus, the error caused by the ideal gas approximation is about 0.8%.

At T=80°C and P_{H_2O} =0.23 bar (cathode reference nominal conditions):

- The water vapor density is: $\rho = 0.14175 \; kg/m^3$
- The ideal gas density is: $\rho = \dfrac{P \cdot MH2O}{R \cdot T} = 0.141 \; kg/m^3$

In this condition, the error caused by the ideal gas approximation is about 0.5%.

At T=80°C and $P_{H_2O} = P_{sat}(80°C)) = \; 0.47$ bar (saturation point):

- The water vapor density is: $\rho = 0.291 \; kg/m^3$
- The ideal gas density is: $\rho = \dfrac{P \cdot MH2O}{R \cdot T} = 0.288 \; kg/m^3$

Thus, the error caused by the ideal gas approximation reaches 1% at the saturation point. Then, it can be stated that the water vapor density satisfies the ideal gas law in all the operating range of the fuel cell.

APPENDIX 4: EVOLUTION OF THE LOCAL PARAMETERS DURING THE AGEING TESTS

During the stationary test, the cell is under prolonged thermal loading, with considerable spatial heterogeneities of temperature and water content along the active area. For the load/thermal cycling, there are also high temperature and water content heterogeneities along the active area, which also evolve with time. Significant variations of temperature (~15°C) and water content (~3) are observed over each cycle, leading to evolutions between moderately humidified and dry conditions. Regarding the NEDC/RH cycling, the hydrothermal conditions of the cell undergo noteworthy spatial and temporal variations, which should induce notable and non-uniform hygrothermal stresses in the membrane. The corresponding results of the simulations are presented in the following figure:
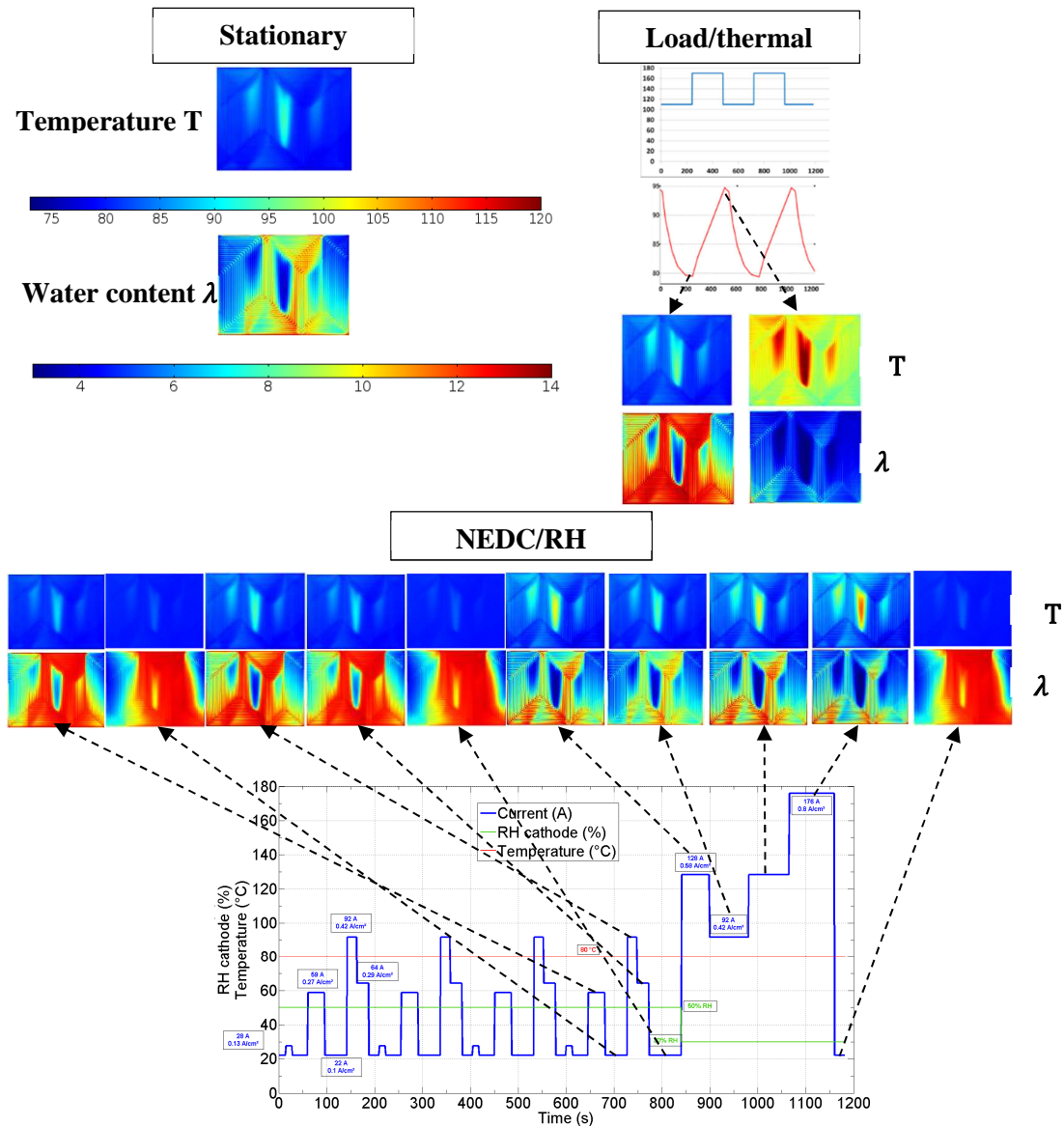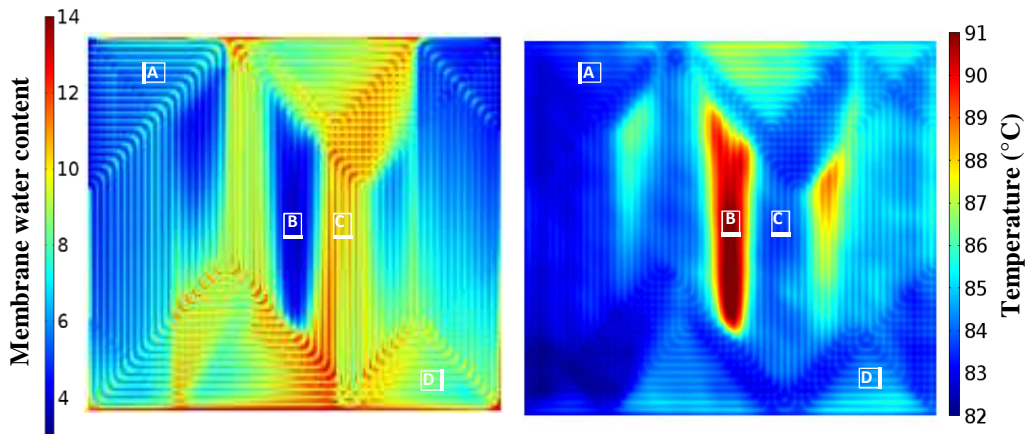

Simulated local operating conditions of the three reference ageing tests

APPENDIX 5: THROUGH-PLANE ANALYSIS OF THE AGED M.E.A.

a)   Analysis of the through-plane microstructure of the MEA

In order to study the local microstructure of the MEA, representative zones have been identified based on membrane local temperature and water content distributions predicted by the model. The figure presented below shows those cut zones (samples) for through-plane microscopic studies superposed on temperature and water content distributions. Those cut zones, which have different values of temperature and water concentration, are included in the reference zones *a, b, c* and *d* studied in section the 1.2 of the Chapter V.


Different cut zones superposed on water content and temperature distribution simulated over the membrane surface

The following table gives the mean hygrothermal operating conditions of the chosen zones.

| Zone	Mean water content	Mean temperature (°C)
A	8	83.5
B	4.5	90.5
C	10.5	84.5
D	11.5	84.7

Membrane water content and temperature in the reference zones

The following figure shows some optical microscopy results (x 2000) on the reference cut zones of the MEA 22 of the stack aged in stationary condictions. A micro-crack of the cathode catalyst layer, with a membrane creep inside the crack is observed in the main hot spot of the MEA (zone B). No significant degradation is observed in the other zones.
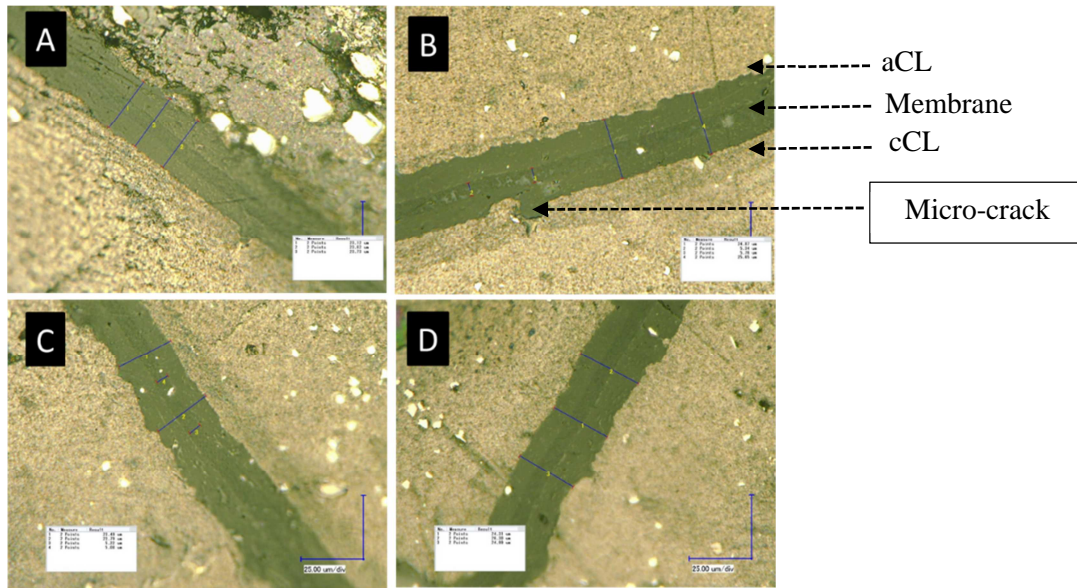
Optical microscopy images on the different zones (x 2000)

SEM analysis (obtained in back-scattered electrons) of the reference cut zones on the MEA 18 of the stack aged in stationary conditions:
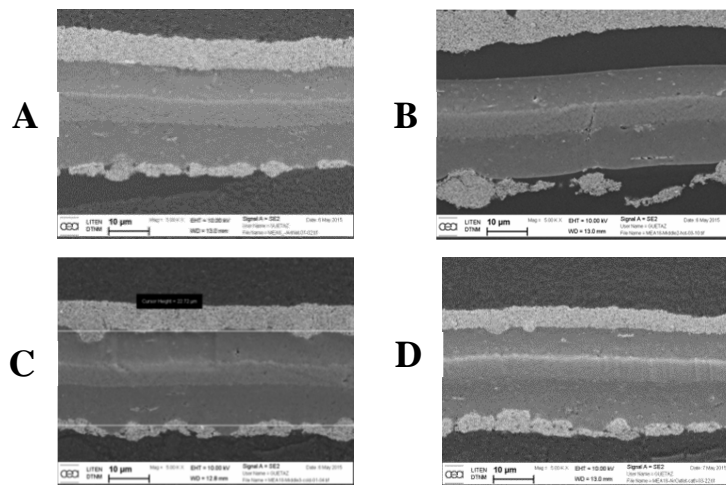
SEM images obtained in back-scattered electrons for the different samples

Local delaminations are observed between the different layers of the MEA. In particular, there are two different types of delamination. Some of them are located between the cathode catalyst layer and the membrane (zone B) and the others are between the anode catalyst layer and the microporous layer (zone A). The first ones are mainly located in the hot zones (B) where the temperature exceeded 90 °C. When the temperature reaches 90°C, the probability of thermal and mechanical degradation is highly increased due to the relatively low glass-transition temperature of hydrated Nafion. It is worth noting that the delaminations are very localized (length ~100 μm).

Combined to the reactive gases permeation, this delamination observed could induce local damage or shorting of the membrane despite of no gradual performance loss observation.